Potential Applications of Microtesla Magnetic Resonance Imaging Detected Using a Superconducting Quantum Interference Device

By

Whittier Ryan Myers

B. S. (Harvey Mudd College) 1999
M. A. (University of California, Berkeley) 2002

A dissertation submitted in partial satisfaction of the

requirements for the degree of

Doctor of Philosophy

in

Physics

in the

GRADUATE DIVISION

of the

UNIVERSITY OF CALIFORNIA, BERKELEY

Committee in charge:

Professor John Clarke, Chair
Professor Alessandra Lanzara
Professor David E. Wemmer

Spring 2006

Potential Applications of Microtesla Magnetic Resonance Imaging Detected Using a Superconducting Quantum Interference Device

Whittier Ryan Myers

Abstract

Potential Applications of Microtesla Magnetic Resonance Imaging Detected Using a Superconducting Quantum Interference Device

by

Whittier Ryan Myers

Doctor of Philosophy in Physics

University of California, Berkeley

Professor John Clarke, Chair

This dissertation describes magnetic resonance imaging (MRI) of protons performed in a precession field of 132 μT. In order to increase the signal-to-noise ratio (SNR), a pulsed 40-300 mT magnetic field prepolarizes the sample spins and an untuned second-order superconducting gradiometer coupled to a low transition temperature superconducting quantum interference device (SQUID) detects the subsequent 5.6-kHz spin precession.

Imaging sequences including multiple echoes and partial Fourier reconstruction are developed. Calculating the SNR of prepolarized SQUID-detected MRI shows that three-dimensional Fourier imaging yields higher SNR than slice-selection imaging. An experimentally demonstrated field-cycling pulse sequence and post-processing algorithm mitigate image artifacts caused by concomitant gradients in low-field MRI.

The magnetic field noise of SQUID untuned detection is compared to the noise of SQUID tuned detection, conventional Faraday detection, and the Nyquist noise generated by conducting biological samples.

A second-generation microtesla MRI system employing a low-noise SQUID is constructed to increase SNR. A 2.4-m cubic, eddy-current shield with 6-mm thick aluminum walls encloses the experiment to attenuate external noise. The measured noise is 0.75 fT $Hz^{-1/2}$ referred to the bottom gradiometer loop. Solenoids wound from 30-strand braided wire to decrease Nyquist noise and cooled by either liquid nitrogen or water polarize the spins. Copper wire coils wound on wooden supports produce the

imaging magnetic fields and field gradients. Water phantom images with 0.8 x 0.8 x 10 mm^3 resolution have a SNR of 6. Three-dimensional 1.6 x 1.9 x 14 mm^3 images of bell peppers and 3 x 3 x 26 mm^3 *in vivo* images of the human arm are presented.

Since contrast based on the transverse spin relaxation rate (T_1) is enhanced at low magnetic fields, microtesla MRI could potentially be used for tumor imaging. The measured T_1 of *ex vivo* normal and cancerous prostate tissue differ significantly at 132 μT. A single-sided MRI system designed for prostate imaging could achieve 3 x 3 x 5 mm^3 resolution in 8 minutes.

Existing SQUID-based magnetoencephalography (MEG) systems could be used as microtesla MRI detectors. A commercial 275-channel MEG system could acquire 6-minute brain images with $(4\ mm)^3$ resolution and SNR 16.

I dedicate this work to my parents,

Jean and Carl Myers.

They are the greatest blessing in my life.

Table of contents

Acknowledgements ..... **v**

Symbols ..... **viii**

1. Introduction **1**

1.1. SQUID detectors *3*
1.1.1. Flux quantization and Josephson junctions 3
1.1.2. SQUID current, voltage, and flux 4
1.1.3. The flux-locked loop 5
1.1.4. Untuned magnetometers and gradiometers 6

1.2. NMR and MRI *8*
1.2.1. Spin polarization and dynamics 8
1.2.2. Spin-echo NMR 9
1.2.3. Spatial resolution of one-dimensional MRI 10

1.3. Prepolarized SQUID-detected MRI *11*

1.4. First-generation microtesla SQUID MRI system *12*
1.4.1. SQUID and untuned gradiometer 13
1.4.2. Ultra low-noise cryostat 14
1.4.3. Magnetic field coils 15
1.4.4. Radiofrequency and 5.6 kHz magnetic shielding 17

2. Prepolarized low-field MRI pulse sequences and image reconstruction **20**

2.1. Projection-reconstruction *20*

2.2. Slice selection *23*

2.3. Fourier transform imaging *26*
2.3.1. Reciprocal space (*k*-space) in MRI 26
2.3.2. Resolution and field of view 27

2.4. Spin-warp imaging and reconstruction *28*

2.5. Other methods for scanning k-space *32*
2.5.1. Multiple echo sequences 32
2.5.2. Partial Fourier imaging 35
2.5.3. Interpolation of polar *k*-space points 37

2.6. Three-dimensional Fourier imaging *39*

2.7. Signal-to-noise ratio of a voxel *41*
2.7.1. Derivation of voxel SNR 41
2.7.2. SNR, resolution, and field-of-view 45
2.7.3. Optimal polarizing time 46
2.7.4. Voxel SNR of an acquired image 46

2.7.5. SNR of three-dimensional Fourier imaging versus slice selection....48

2.8. Image reconstruction from multiple detectors....49
2.8.1. Weighted image superposition algorithm....49
2.8.2. Application of weighted superposition....50
2.8.3. Sensitivity encoding (SENSE)....51

Appendix 2.A. Implementation details....54

3. Correction of concomitant gradient artifacts....55

3.1. Theory and algorithms....56
3.1.1. Effect of concomitant gradients on MR images....57
3.1.2. Reconstruction algorithm to correct distortion and blurring....60
3.1.3. Field cycling to eliminate phase-encoding concomitant gradient blurring....65

3.2. Experimental results....67

3.3. Limits of concomitant gradient correction....69

Appendix 3.A. MRI simulation algorithm....73

Appendix 3.B. Local image warping algorithm....73

4. Signal and Noise in SQUID MRI....76

4.1. Theoretical magnetic field noise of SQUID untuned detection....77
4.1.1. Flux noise of a bare SQUID....77
4.1.2. Magnetic field noise of a SQUID magnetometer....78

4.2. Measured magnetic field noise of SQUID untuned detection....83
4.2.1. Measurements of SQUID flux noise....84
4.2.2. Measurements of gradiometer magnetic field noise....94

4.3. Signal-to-noise ratio comparison of MRI detection modalities....100
4.3.1. Sample and detector geometry....100
4.3.2. Field noise of SQUID tuned detection....101
4.3.3. Field noise of conventional Faraday detection....115
4.3.4. Nyquist noise from a warm conducting sample....117
4.3.5. SNR comparison of detection modalities....119

5. Second-generation SQUID MRI system....125

5.1. Polarizing coils....125
5.1.1. Field strength....126
5.1.2. Cooling techniques....127
5.1.3. Magnetic field noise....129
5.1.4. Fabricated polarizing coils....133

5.2. Higher-balance, lower-inductance gradiometer....138

5.3. Second-generation aluminum shield....141
5.3.1. Physical description....141
5.3.2. Shielding performance....142

5.3.3. Eddy currents induced by the polarizing field 143

5.4. Second-generation magnetic field coils *145*
5.4.1. Cancellation field coils 147
5.4.2. Precession field coils 148
5.4.3. Image encoding gradient coils 150
5.4.4. Excitation coils 152
5.4.5. Eddy-current cancellation coil 152

5.5. Images taken with the second-generation MRI system *153*

6. Potential applications of microtesla SQUID-detected MRI 156

6.1. Comparison with conventional MRI *156*
6.1.1. Advantages of conventional MRI 157
6.1.2. Competing low-cost MRI technologies 158
6.1.3. Advantages of SQUID-detected microtesla MRI 160

6.2. Design of a single-sided imaging system *161*
6.2.1. Optimal gradiometer baseline and radius 162
6.2.2. Optimal polarizing coil geometry 164
6.2.3. Polarizing coil Nyquist noise 166
6.2.4. Cooling water spin precession amplitude 166
6.2.5. Calculated SNR 167

6.3. Detection or monitoring of prostate cancer *168*
6.3.1. Possible designs for a microtesla prostate MRI system 169
6.3.2. Low-field *in vitro* measurements of prostate tissue T_1 170
6.3.3. Prostate imaging pulse sequence 172
6.3.4. Calculated SNR and CNR of prostate images 176
6.3.5. Prospects for microtesla prostate MRI 178

6.4. Combined magnetoencephalography and MRI of the brain *179*
6.4.1. MEG gradiometer geometry and sensitivity 179
6.4.2. Polarizing coil geometry 181
6.4.3. NMR properties of brain tissue 182
6.4.4. Brain imaging pulse sequence 182
6.4.5. Calculated SNR and CNR of brain images 184
6.4.6. Prospects for combined MEG/MRI 184

Appendix 6.A. Spin noise of cooling water *185*

7. Future directions 188

7.1. MRI system upgrades *188*

7.2. Progress towards applications of microtesla MRI *190*

Acknowledgements

First, I want to thank John Clarke for his support over the years, which has included overall project guidance, detailed technical assistance with everything related to SQUIDs, and very helpful criticism of presentations and papers. I also appreciate his patience with the many mistakes I have made in the course of this research and his willingness to grant time off for spiritual retreat. I thank Ivo Souza and Jeffrey Reimer, who served on my qualifying exam, David Wemmer, who read my dissertation, and Alessandra Lanzara, who did both.

For my first two years in the Clarke group, I worked with Yann Chemla, Sherry Cho, Helene Grossman, and SeungKyun Lee to detect magnetically tagged *Listeria* bacteria with a high-T_c SQUID microscope. I particularly appreciate Sherry's meticulous instruction in high-T_c SQUID fabrication (don't talk to SQUIDs), Seung's perseverance in our attempt to make YBCO bridges with decent critical currents (chip #15 finally worked), and Helene's patient handling of the biological details of the experiment. These people also kept the lab clean.

The microtesla MRI project rests upon the shoulders of "McDermott and coworkers," which includes Robert McDermott, Andreas Trabesinger, SeungKyun Lee, Nathan Kelso, and Bennie ten Haken. They demonstrated that SQUID-detected microtesla MRI could work and paved the way for the calculations and system improvements described here. All low-noise SQUID-detected MRI past and future depends on Hugh Seton's innovative ultra low-noise cryostat, and we thank him for allowing us to use his patented design. Darrin Kinion stopped hunting for axions long enough to contribute his precision carpentry skills to build the first-generation wooden cube.

Seung taught me how to operate the MRI system when I started working on the project. In those days, we began taking data at 8 pm, it took over two hours to acquire an image, and we rotated the gradient fields by changing knobs on power supplies. When Michael Mößle arrived, he set to work automating this process and subsequently became master of the MRI cube. Michael spent hours futzing with the system in an attempt to compensate for the radiofrequency leaks in the first-generation aluminum shield. I felt somewhat guilty for calculating the SNR we would get if the system noise were as low as

it was two weeks ago, but I never did help him much with this process. For this reason, Michael acquired essentially all the phase-encoded images presented in this dissertation.

Micheal Mück and Vasili Semenov provided the SQUIDs measured in Chapter 4, and we installed two of Michael's SQUIDs in the MRI system. My measurements of Semenov's SQUID indicate that it is a truly excellent device, and I hope that he receives the credit he deserves for designing it.

Michael Hatridge designed the one-ton aluminum shield of the second-generation MRI system and managed to drill thousands of holes and install 10 50-kg aluminum plates without hurting anybody (the Safety Czar wasn't always looking). The first cube wasn't enough woodworking for Darin, so he used the new cube as an excuse to buy several shiny yellow DeWalt power tools and throw sawdust all over the southeast corner of Birge Hall. Sarah Busch and the undergraduates Adam Hunt, Peter Koo, and Salvador Barriga assisted Michael and Darin in their efforts. Katalin Markus cleaned up the mess outside after we forgot about it.

We never would have been able to measure the NMR properties of prostate tissue without the help of Marc Shuman, John Kurhanewicz, Jeffrey Simko, Kevin Chew, and Karen Chew. Lars Schmidt the Prostate King did most of the dirty work, and when he realized the low SNR of our experiment, he began cutting larger samples of tissue for us. Adam designed and built the temperature controller that maintained the tissue at 4 °C during the measurements.

Many aspects of this dissertation rely on advice from experts outside the Clarke group. I want to particularly thank Steve Conolly for his critical view of the market for MRI systems and Hugh Seton for additional information about his custom-made cryogenic capacitors and permission to reproduce Fig. 4.8. Ben Inglis acquired the image shown in Fig. 2.19(C) using the 4 T MRI system at the UCB Brain Imaging Center and is helping us to investigate methods for microtesla fMRI. Jiri Vrba and Robert Cropp provided the coordinates of the gradiometer array of the CTF 275 MEG system and gave me permission to publish the graphical depictions and SNR calculations of this system shown in Sec. 6.4. The Great Green Book by Haacke *et al*. provided valuable insights into the principles of magnetic resonance imaging.

Many people in the Physics Department provided important support for this work. Barbara Salisbury was always willing to help us navigate the LBL administrative maze, and I also enjoyed our conversations about the ups and downs of spiritual practice. May she find what she seeks. Nobody could get experiments done in Birge Hall without Eleanor Crump doing her best to keep this quirky building operating and its occupants safe. Several incidents occurred in the Clarke group during my tenure as Safety Czar, and I appreciate Eleanor's approachability and focus on what to do now rather than how things got this way. Anne Takizawa was always there to answer questions regarding the graduate school process. Finally, when the LBL researcher for whom I was working wouldn't pay my student fees for the Fall 2000 semester, the Physics Department (then chaired by Roger Falcone) used over $2,000 in discretionary funds to pay them. I would have paid them myself and didn't even ask. This place is serious about supporting its graduate students.

I have considered leaving graduate school several times over the past seven years, and a number of people contributed significant moral support to the completion of this degree. Despite the physical distance between us, my best friends Anne Sung and Lion Kimbro were there to talk with and provide a sounding board for my thoughts and plans. Anne introduced me to *The Pathfinder* by Nicholas Lore, which taught me the power of making commitments. During the 2003 Summer Surangama retreat at the City of Ten Thousand Buddhas, Rev. Heng Sure explained that keeping one commitment (finishing graduate school) creates the conditions for keeping future commitments (e. g. monastic training). I thank my spiritual teachers Sri Ecknath Easwaran, James Baraz, Rev. Kim Smith, Rev. Heng Sure, Ajahn Amaro, and Ajahn Pasanno for the ideals, insights, and encouragement they have shared with me. Finally, I thank my parents, to whom this work is dedicated, for their abiding, non-attached love for all these years.

Symbols

Variables and physical constants		SI units
a	Pickup coil radius	m
A_{eff}	Effective area of a SQUID magnetometer	m^2
A_p	Pickup coil area	m^2
α	Coupling coefficient between SQUID and input coil	
b	Gradiometer baseline	m
B_0	Precession field	T
B_p	Polarizing field	T
$\beta_\perp$	Geometrical detector response factor defined by Eq. (2.24)	m^{-1}
χ	Magnetic susceptibility	A m^{-1} T^{-1}
ε	Ratio of B_0 to the field generated by the gradient coils	
f_m	Modulation frequency of a flux-locked loop	Hz
ΔG_x	Phase-encoding gradient increment in the x-direction	T m^{-1}
Δl_x	Spatial resolution in the x-direction	m
Δk_x	Sampling period in k-space in the x-direction	m^{-1}
$\Delta\omega_l$	Spectral resolution	s^{-1}
Φ_0	Flux quantum ≡ $h/2e = 2.0678 \times 10^{-15}$	T m^2
$\mathbf{G}$	Applied gradient vector; components (G_x, G_y, G_z)	T m^{-1}
G_{freq}	The amplitude of the frequency encoding gradient	T m^{-1}
G_{phase}	The amplitude of the phase-encoding gradient	T m^{-1}
G_{ss}	The amplitude of the slice-selection gradient	T m^{-1}
$G_{x,max}$	The maximum phase-encoding gradient in the x-direction	T m^{-1}
γ	Proton gyromagnetic ratio = $2\pi \cdot 42.577482$	T^{-1} s^{-1}
$\hbar$	Plank's constant / $2\pi = 1.0546 \times 10^{-34}$	J s^{-1}
I_0	Critical current	A
J	Current density	A/m^2
$\mathbf{k}$	Reciprocal space vector	m^{-1}
k_B	Boltzmann's constant = 1.3807×10^{-23}	J K^{-1}
k_c	k-space filter cutoff	m^{-1}
k_{max}	The longest reciprocal space vector in k-space	m^{-1}
L	SQUID inductance	H
L_0	The inductance per turn squared of a transformer core	H / $turn^2$
L_x	Image field of view in the x-direction	m
L_i	SQUID input coil inductance	H
L_p	Pickup coil inductance	H
L_T	Total input circuit inductance (= $L_i + L_p$)	H
λ	Fraction of the polarizing coil volume which carries current	
M_i	Mutual inductance between SQUID and input coil	H
N_x	Number of phase encoding steps in x-direction	
ρ	Spin volume density	spins / m^3
ρ_{Cu}	Resistivity of copper = 1.7×10^{-8}	Ω m
R	Resistance of the SQUID shunt resistor	Ω

S_X	Noise spectral density (X: V voltage, J current, B magnetic field, Φ flux)	X^2 Hz^{-1}
S_{VJ}	Correlated spectral density of voltage and current noise	V A Hz^{-1}
t_{echo}	The time between the beginning of data acquisition and the echo top	s
T_1	Longitudinal spin relaxation time	s
T_2	Intrinsic transverse spin relaxation time	s
T_2'	Transverse spin relaxation time caused by field inhomogeneity	s
T_2^*	Measured transverse spin relaxation time; combination of T_2 and T_2'	s
T_d	Delay time between turning off polarizing field and 90° excitation pulse	s
T_N	Noise temperature of an amplifier	K
T_p	Polarizing time	s
T_{phase}	Time that the phase encoding gradient is applied	s
T_s	Data acquisition time (per sequence step)	s
T_{samp}	Sampling time	s
T_S	Sample temperature	K
T_T	Total sequence time	s
τ	Echo time – time between 90° and 180° excitation pulses	s
V_Φ	Maximum SQUID flux-to-voltage transfer function	V/(T m^2) or s^{-1}
V_{voxel}	Volume of the MRI voxel	m^3
ω_0	Spin angular precession frequency (= γB_0)	rad s^{-1}
Υ	Signal-to-noise ratio efficiency of a pulse sequence	

Abbreviations

CNR	Contrast-to-noise ratio
FLL	Flux-locked loop
fMRI	Functional magnetic resonance imaging
FWHM	Full-width-half-maximum (linewidth)
HWHM	Half-width-half-maximum (linewidth)
low-T_c	Low-transition temperature (superconductor)
MCG	Magnetocardiography
MEG	Magnetoencephalography
MRI	Magnetic resonance imaging
NMR	Nuclear magnetic resonance
QD	Quantum Design®
RCSJ	Resistively and capacitively shunted junction (model)
RMS	Root-mean-square
PSA	Prostate specific antigen
SNR	Signal-to-noise amplitude ratio
SQUID	Superconducting quantum interference device
voxel	Volume element; three-dimensional equivalent of pixel

1. Introduction

Since Grannell and Mansfield [1] first proposed *in vivo* magnetic resonance imaging (MRI) in 1975, this technique has become a critical tool in modern medicine and medical research. Clinical MRI is routinely used to diagnose brain disease and to image the musculoskeletal system, and the diagnosis of breast and prostate cancer using MRI is an active area of research. The signal-to-noise amplitude ratio (SNR) is a critical parameter in MRI. In conventional MRI, the SNR scales at least linearly with the strength of the precession field B_0. Because increased SNR can usually be traded for either increased spatial resolution or increased imaging speed, the precession fields employed in MRI over the past two decades have risen from ~0.1 T to the current 1.5 T clinical standard; research systems employ fields of up to 7 T. Despite its great successes, high-field MRI has drawbacks as well. A superconducting full-body MRI system costs approximately $1 million per tesla of precession field. This results in a cost per imaging session of over $1,000, which is prohibitively expensive for routine screening. In addition, many patients experience discomfort or claustrophobia in the narrow bore of superconducting MRI magnets.

For these reasons, there has recently been renewed interest in low-field MRI. In addition to reduced system costs, and more open coil geometries [2], low-field MRI also has the potential to reduce susceptibility artifacts [3] and increase contrast based on the proton longitudinal relaxation time (T_1-contrast) [4] relative to high field. In 2004, McDermott *et al*. [5] published MR images taken at $B_0 = 132$ μT. They used a combination of prepolarization with a pulsed magnetic field $B_p = 300$ mT and detection with an untuned gradiometer connected to a superconducting quantum interference device (SQUID) to achieve a SNR independent of B_0. Because their primary objective was to demonstrate the feasibility of SQUID-detected MRI at such low fields, McDermott *et al*. employed conceptually simple but sub-optimal pulse sequences and reconstruction mechanisms and did not quantify the SNR of their technique.

This dissertation extends the work of McDermott *et al*. in three ways. First, it applies the pulse sequences and techniques developed in high-field MRI to enhance and extend the capabilities of prepolarized SQUID-detected MRI. Second, it considers the feasibility of possible applications of SQUID-detected MRI and estimates the SQUID

noise level and prepolarization field that would be required to achieve adequate image SNR. Third, it describes the improvements to the Clarke group microtesla MRI system that have been made since Robert McDermott graduated from UC Berkeley.

The ultimate goal of this work is to discriminate between potential applications of low-field SQUID-detected MRI and appealing but unrealistic schemes. Because the behavior of prepolarizing coils, nuclear spins, and SQUID detectors can be adequately modeled using a computer, one can estimate the SNR, resolution, and imaging speed of an MRI system before it is built. Only the spin relaxation properties that determine tissue contrast must be determined from experiment. While this paper considers only a few of the possible applications of prepolarized SQUID-detected MRI, I hope that others will make models such as these before building MRI systems that cannot possibly live up to their hopes.

Section 1.1 describes the operation of SQUIDs and SQUID-based untuned magnetometers and gradiometers. Section 1.2 describes nuclear magnetic resonance (NMR) and the fundamentals of one-dimensional MRI. Starting with the Bloch equation, it derives the resolution of one-dimensional MRI and describes the spin-echo pulse sequence. Section 1.3 describes the advantages of low-field MRI and why the SNR of prepolarized MRI detected with an untuned superconducting pickup coil coupled to a SQUID is independent of B_0. The chapter concludes with Sec. 1.4, which describes the geometry and operation of the first-generation system built by McDermott and coworkers.

Chapter 2 introduces the fundamental concept of k-space in MRI reconstruction, describes pulse sequences for two- and three-dimensional images, and calculates the SNR of a volume element (voxel) in an MR image. Chapter 3 describes the problem of concomitant gradients which limits the minimum precession field that can be used for MRI; it goes on to develop reconstruction methods and pulse sequences to reduce the image distortion and blurring caused by concomitant gradients. Chapter 4 calculates the magnetic field noise of SQUIDs coupled to untuned gradiometers and the resulting voxel SNR. It then compares the SNR of SQUID untuned detection, SQUID tuned detection, and conventional Faraday detection as a function of precession frequency. Chapter 5 describes the design and construction of the second-generation Clarke group microtesla

MRI system. Chapter 6 considers the feasibility of limb imaging, MRI of the prostate for potential tumor detection, and performing MRI of the brain using the same SQUID arrays employed in magnetoencephalography.

1.1. SQUID detectors

Superconducting quantum interference devices (SQUIDs) made from low-transition temperature (low-T_c) superconductors are the most sensitive detectors of magnetic flux available. When coupled to an untuned superconducting magnetometer or gradiometer, they become extremely sensitive detectors of magnetic fields, achieving magnetic field noise on the order of 1 fT $Hz^{-1/2}$. Because understanding SQUID-detected MRI does not require a detailed understanding of SQUIDs themselves, I undertake only a heuristic description of SQUID dynamics. I defer detailed treatment of SQUID noise until Chapter 4.

1.1.1. Flux quantization and Josephson junctions

A Josephson junction consists of a thin insulating barrier between two superconductors. Cooper pairs tunnel across the junction producing a supercurrent

$$I = I_0 \sin(\gamma), \tag{1.1}$$

where I_0 is the junction critical current and γ is the phase difference of the superconducting wavefunction across the junction. A dc (direct current) SQUID consists of a loop of superconducting material interrupted by two Josephson junctions as shown in Fig. 1.1. Assuming identical junctions, the critical current of the SQUID is

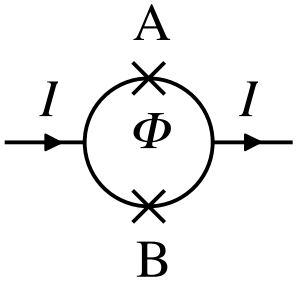

Figure 1.1: Diagram of a SQUID with Josephson junctions A and B threaded by total flux Φ.

$$I = I_0[\sin(\gamma_A) + \sin(\gamma_B)], \tag{1.2}$$

where γ_A and γ_B represent the phase difference across junctions A and B, respectively. Because the phase of the superconducting wavefunction must be continuous around the SQUID loop, the phase differences are constrained by [6]

$$\gamma_A - \gamma_B = 2\pi\Phi/\Phi_0, \tag{1.3}$$

where Φ is the total flux threading the SQUID and $\Phi_0 \equiv h/2e = 2.07 \times 10^{-15}$ Tm^2 is the flux quantum. The maximum critical current subject to this constraint is a periodic

function of flux. Thus the critical current reaches a maximum when $\Phi = n\Phi_0$ and goes to zero when $\Phi = (n+1/2)\Phi_0$, where n is an integer.

1.1.2. SQUID current, voltage, and flux

While the above discussion correctly predicts the periodic response of a SQUID to applied flux, it cannot describe SQUID behavior when the applied current exceeds I_{max} and a voltage develops across the SQUID. The resistively and capacitively shunted junction (RCSJ) model [7,8], shown in Fig. 1.2, accurately predicts the behavior of physical SQUIDs. In this model, the SQUID loop has inductance L, and each junction is

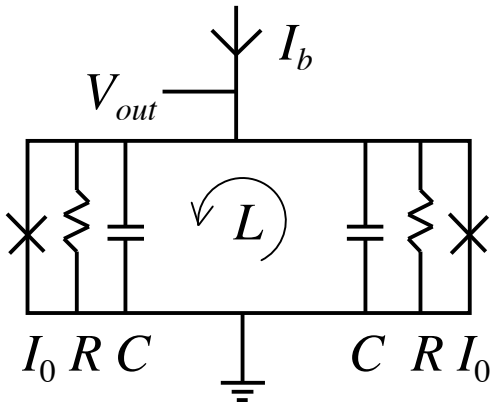

Figure 1.2: Resistively and capacitively shunted junction model of a SQUID.

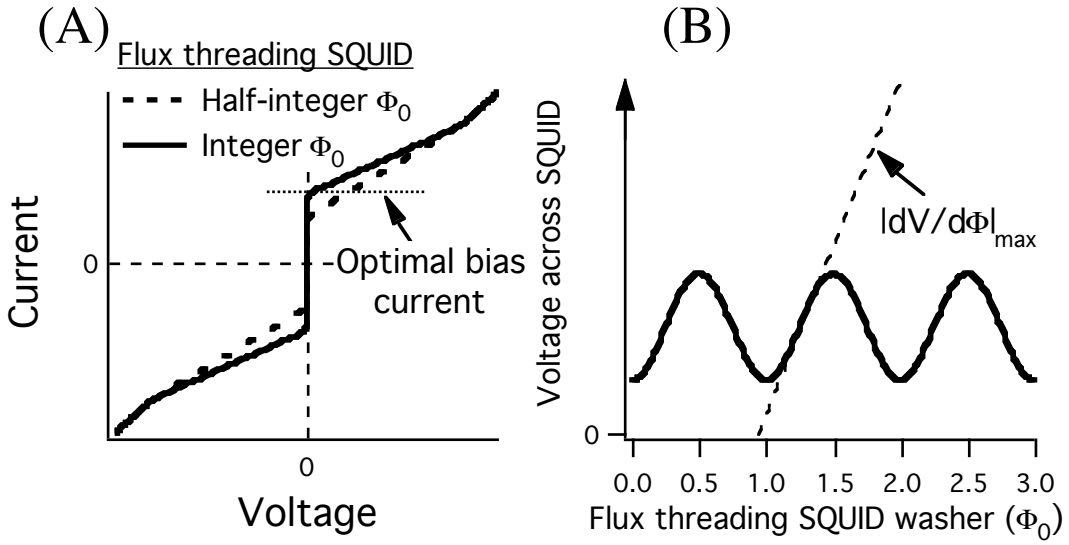

Figure 1.3: (A) SQUID current versus voltage across SQUID. (B) Voltage across the SQUID versus applied flux for a constant applied bias current.

shunted by an intrinsic capacitance C and a resistance R. For low-T_c SQUIDs, R generally represents the shunt resistors placed across the junctions to avoid hysteretic current-voltage characteristics. In typical operation, a SQUID is biased with a constant current I_b, and the voltage V_{out} across the SQUID responds to the applied flux. Figure 1.3(A) shows the current and voltage characteristics of the RSCJ model for optimized SQUID parameters. Like the simple model of Sec. 1.1.1, the critical current is

maximized for $\Phi = n\Phi_0$ and has a minimum when $\Phi = (n+1/2)\Phi_0$. Figure 1.3(B) shows the voltage across the SQUID plotted versus the applied flux for at the optimal bias current of Fig. 1.3(A). The maximum flux sensitivity occurs when the SQUID is flux-biased at $\Phi = (n+1/4)\Phi_0$; the slope of the voltage versus flux curve is at this point is $V_\Phi \equiv |dV/d\Phi|_{max}$.

1.1.3. The flux-locked loop

SQUID amplifiers are usually operated in a flux-locked feedback loop in order to produce a linear voltage response to applied flux. In this configuration, an oscillator applies an alternating flux bias to the SQUID with frequency f_m and peak-to-peak

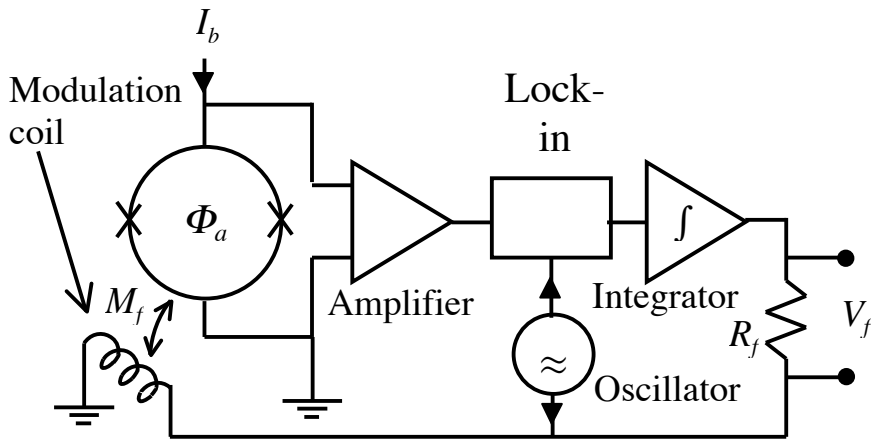

Figure 1.4: Schematic of a SQUID operated in a flux-locked loop.

amplitude $\Phi_0/2$. If the applied flux Φ_a is equal to an integer multiple of Φ_0, the voltage output of the SQUID will have only even Fourier components. However if Φ_a changes from this value, a Fourier component appears at frequency f_m. Feeding back the integrated output of a lock-in detector as a flux to the SQUID as shown in Fig. 1.4 maintains the total flux through the SQUID at an integer multiple of Φ_0. If the integrator output is connected through a resistor R_f to a modulation coil with mutual inductance M_f to the SQUID, the flux-locked loop maintains a voltage

$$V_f = \Phi_a R_f / M_f \tag{1.4}$$

across the resistor.

A flux-locked loop operating at frequency f_m can respond to signals at frequencies $\sim f_m/2$ and below; the signal propagation time between the SQUID and the flux-locking

electronics limits f_m to frequencies of a few megahertz. However, SQUIDs respond to magnetic flux at frequencies on the order of the Josephson frequency $f_J = V\Phi_0$; for a typical SQUID, V ~ 100 μV and f_J ~ 50 GHz. Since the flux-locked loop cannot follow them, frequency components of Φ_a above $f_m/2$ flux-average the SQUID voltage response shown in Fig. 1.3(B), lowering its effective amplitude and increasing the noise of the locked signal. SQUIDs therefore require radiofrequency shielding to maintain the total amplitude of high-frequency flux much smaller than Φ_0.

1.1.4. Untuned magnetometers and gradiometers

In order to measure external signals using a SQUID, the SQUID is inductively coupled to a superconducting input coil. In thin-film low-T_c SQUIDs, the input coil is patterned on top of the SQUID washer but separated from it by an insulating layer as shown in Fig. 1.5(A). In order to detect magnetic fields over an area larger than the SQUID washer, the input coil is connected to a superconducting pickup coil as shown in Fig. 1.5(B). In this configuration, the input coil of inductance L_i is coupled to the SQUID washer with mutual inductance M_i and connected to a superconducting wire-wound

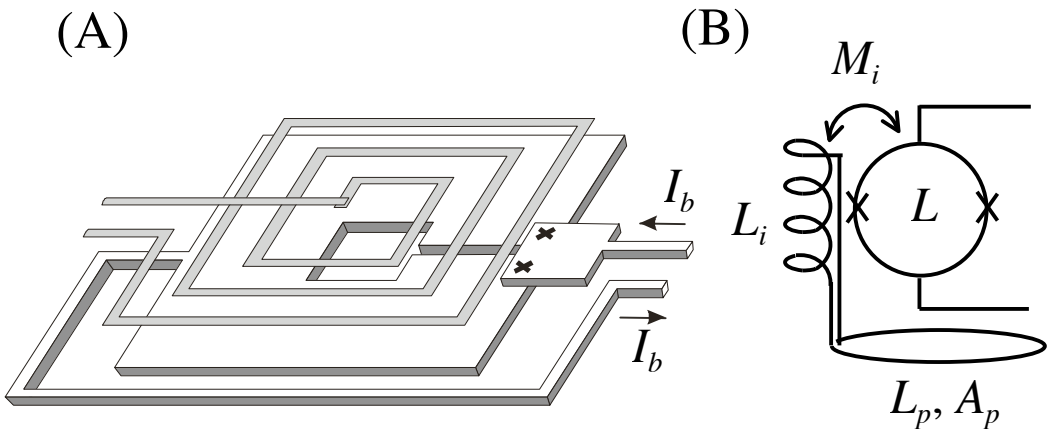

Figure 1.5: (A) Geometry of a square washer SQUID and input coil.
(B) Schematic of an SQUID untuned magnetometer.

pickup coil of inductance L_p and area A_p. A magnetic field B_a applied to the pickup coil will cause a supercurrent B_aA_p/L_T to flow in the input coil, where $L_T = L_i + L_p$ is the total inductance of the input circuit. This in turn couples a flux $B_aA_pM_i/L_T$ into the SQUID. Dividing this flux by the applied field yields the effective area

$$A_{eff} = A_pM_i/L_T \tag{1.5}$$

of the magnetometer. Connecting this device to the flux-locked loop described in the previous section yields an output voltage

$$V_f = \frac{R_f}{M_f} A_{eff} B_a = \frac{R_f}{M_f} \frac{M_i}{L_i + L_p} A_p B_a . \quad (1.6)$$

Unlike the voltage produced by Faraday induction, the voltage response of a SQUID coupled to an untuned magnetometer is independent of frequency.

Gradiometric detection operates on the same principle but replaces the single magnetometer pickup coil with multiple counter-wound pickup coils. Figure 1.6(A) shows a first-order axial gradiometer of diameter $2a$ and baseline b with the bottom loop a distance d above the sample. The counter-wound top and bottom loops cause the device to respond only to field gradients and not to uniform magnetic fields. Since the magnetic field from a dipole noise source a distance r from the gradiometer falls off as $1/r^3$ but the field gradient falls off as $1/r^4$, a gradiometer discriminates against distant noise sources. Figure 1.6(B) shows a device consisting of two first-order gradiometers that responds only to second-derivative magnetic fields. Because second-derivative fields fall off as $1/r^5$ from dipole sources, this second-order axial gradiometer eliminates external noise more effectively than the first-order gradiometer. For $d << b$, one can neglect the response of the upper loop(s) to magnetic fields produced by the sample and treat the signal and noise of the gradiometer as if it were a magnetometer consisting of only the bottom pickup loop.

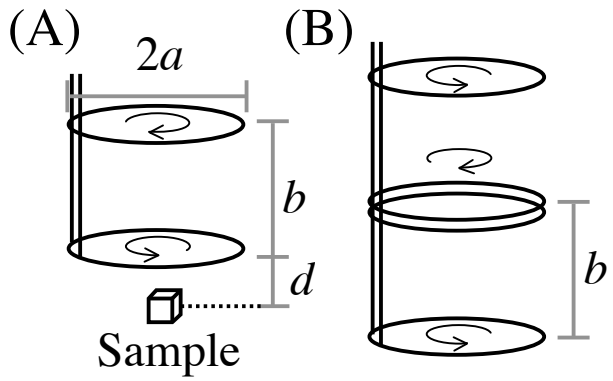

Figure 1.6: Superconducting axial gradiometers. (A) First-order. (B) Second-order. The arrows indicate the winding sense of each loop.

If the gradiometer loops do not have exactly the same area or are oriented at slightly different angles, the gradiometer will have a response to an externally applied uniform field as if it were a magnetometer with pickup loop area $A_{imbalance}$. The balance of a first-order gradiometer is defined as $A_p/A_{imbalance}$ and depends on the direction of the externally applied magnetic field. The balance of a second-order gradiometer against uniform

external fields is defined in the same way. Its balance against gradient fields could be defined as the response one its first-order gradiometers to an applied gradient divided by the response of the second order gradiometer; in practice it is difficult to produce sufficiently uniform gradients to measure this quantity. Because a gradiometer reduces the effect of uniform external noise fields by a factor of its balance compared to a magnetometer of equal area, a highly balanced gradiometer is required to realize a significant reduction in external noise.

1.2. NMR and MRI

1.2.1. Spin polarization and dynamics

An ensemble of spins of density ρ in equilibrium with a magnetic field B_0 have a magnetic moment

$$M_0 = \chi B_0 = \rho\gamma^2\hbar^2 B_0 / 4k_B T_S, \tag{1.7}$$

where χ is the magnetic susceptibility, γ is the gyromagnetic ratio, and T_S is the sample temperature. If these spins are tipped into the transverse plane, their subsequent dynamics obey the Bloch equation

$$\frac{d\mathbf{M}}{dt} = \gamma\mathbf{M}\times\mathbf{B} - \frac{1}{T_1}\left(M_z - \chi B_z\right)\hat{\mathbf{z}} - \frac{1}{T_2}\left(M_x\hat{\mathbf{x}} + M_y\hat{\mathbf{y}}\right), \tag{1.8}$$

where $\mathbf{M}$ is the net magnetization vector with components M_x, M_y, and M_z, $\mathbf{B}$ is the applied field, and T_1 and T_2 are the longitudinal and transverse spin relaxation times, respectively. This formulation of the Bloch equation assumes that B_z is much larger than B_x and B_y. The Bloch equation describes spin precession at angular frequency $\omega_0 = \gamma|\mathbf{B}|$ about the applied magnetic field, relaxation of the spins towards the equilibrium magnetization with time constant T_1, and dephasing of the spins with time constant T_2. The applied field in an MRI experiment can be described as

$$\mathbf{B}(\mathbf{r},t) = \left(B_0 + \Delta B(\mathbf{r})\right)\hat{\mathbf{z}} + B_1(t)\sin(\omega_1 t)\hat{\mathbf{x}} + \left(\mathbf{G}(t)\cdot\mathbf{r}\right)\hat{\mathbf{z}}, \tag{1.9}$$

where ΔB is the inhomogeneity in the static field B_0, B_1 represents the pulsed fields oscillating at angular frequency ω_1 used for resonant spin manipulation, and $\mathbf{G}$ represents the gradients employed for imaging. This dissertation considers only on-resonance magnetic field pulses for which $\omega_1 = \omega_0$.

1.2.2. Spin-echo NMR

Spin-echo NMR can be understood by considering the first two terms in Eq. (1.9). Applying a magnetic field $B_0\hat{\mathbf{z}} + B_1 \sin(\omega_0 t)\hat{\mathbf{x}}$ to spins which are polarized along the z-axis at time $t = 0$ causes the spins to rotate so that they form an angle [9]

$$\theta = \gamma B_1 t/2 \tag{1.10}$$

with respect to the z-axis. The most commonly used resonant pulses in MRI are those in which $\theta = \pi/2$ (90° pulse) and $\theta = \pi$ (180° pulse). If a 180° pulse is applied to spins which are already precessing in the transverse plane, it inverts the relative phase of these spins.

The effect of the field inhomogeneity term $\Delta B(\mathbf{r})$ is to make the spin precession frequency a function of position even in the absence of applied gradients. The spins will dephase under the influence of $\Delta B(\mathbf{r})$ so that their magnetization decays with a characteristic time T_2'. In order to simplify Eq. (1.9), T_2' and the intrinsic transverse relaxation time T_2 can be combined to form the measured transverse relaxation time T_2^*, where

$$1/T_2^* = 1/T_2 + 1/T_2'. \tag{1.11}$$

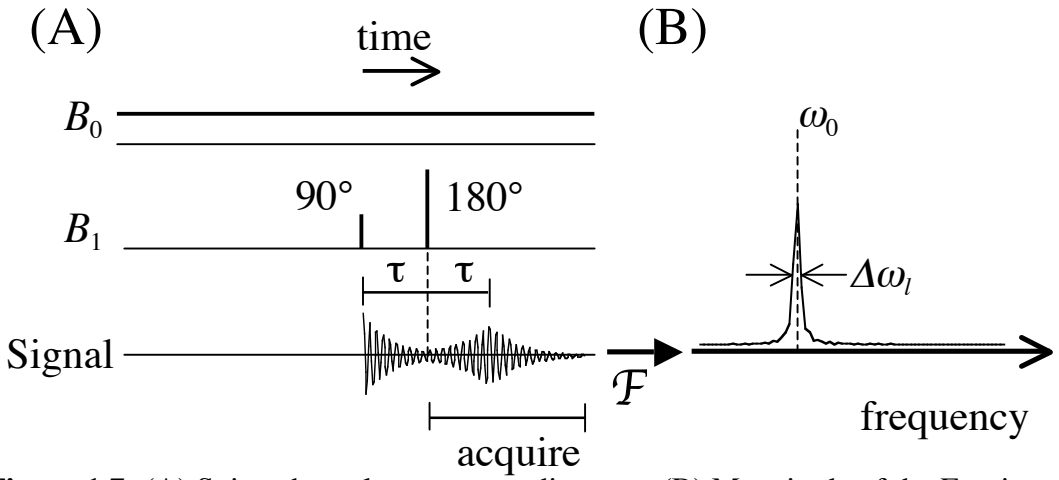

Figure 1.7: (A) Spin echo pulse sequence diagram. (B) Magnitude of the Fourier transform of the magnetic field measured at the detector.

Figure 1.7(A) shows the sequence diagram of the spin-echo pulse sequence. The spins are initially in equilibrium with the field $B_0\hat{\mathbf{z}}$. A 90° pulse tips the spins into the transverse plane and initiates spin precession. The transverse component of the magnetization dephases with time constant T_2^* for a time τ, after which a 180° pulse is

applied to invert the relative phase of the spins. The magnetic field inhomogeneity $\Delta B(\mathbf{r})$ now rephases the spins producing a spin echo a time τ after the 180° pulse (the intrinsic dephasing corresponding to T_2 is not rephased). A detector measuring one transverse component of the sample magnetization is activated after the 180° pulse. The magnitude of the Fourier transform of its output (shown in Fig. 1.7B) is centered at ω_0 with a full-width-half-maximum (FWHM) linewidth

$$\Delta\omega_l \approx 2/T_2^*. \tag{1.12}$$

1.2.3. Spatial resolution of one-dimensional MRI

When a magnetic field gradient is applied during an NMR experiment, the frequency spectrum of the measured signal reflects the geometry of the sample. For example, Fig. 1.8(A) shows a spin-echo pulse sequence with the addition of a gradient $\mathbf{G} = G_x \hat{\mathbf{x}}$ (dB_z/dx). If one applies this pulse sequence to two columns of water separated by a distance Δx as shown in Fig. 1.8(B), the magnitude of the Fourier transform is proportional to the spin density projected perpendicular to the x-direction; in this case two peaks separated by $\gamma G_x \Delta x$ as shown in Fig. 1.8(C). Assuming sufficiently thin

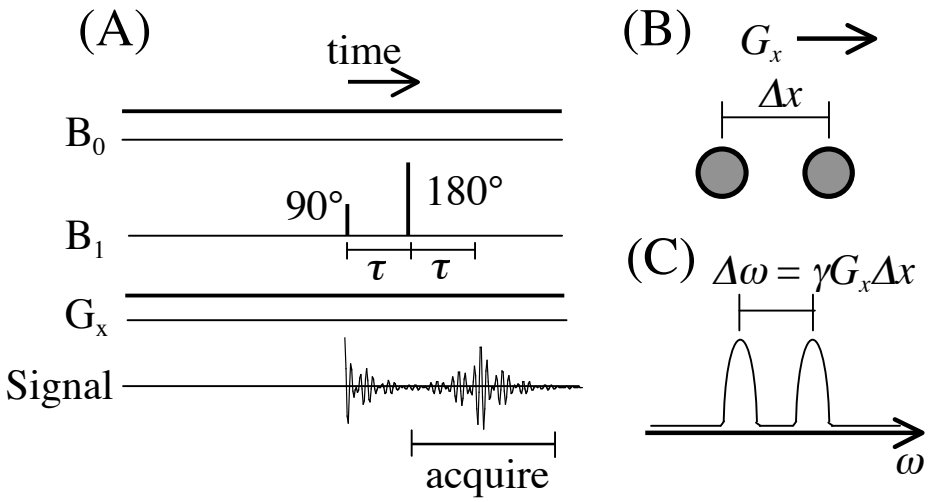

Figure 1.8: (A) Spin-echo pulse sequence with applied gradient G_x. (B) A sample of two columns of water separated by Δx. (C) The magnitude of the Fourier transform of the data acquired from the spin-echo pulse sequence of (A) performed on this sample.

columns, the FWHM spectral linewidth of each column will be $\Delta\omega_l$. In order to distinguish between the two columns, their spectral peaks must be separated by $\Delta\omega_l$, corresponding to a spatial resolution

$$\Delta l_x = \Delta\omega_l/\gamma G_x = 2/\gamma G_x T_2^*. \quad (1.13)$$

Thus the spatial resolution of MRI scales as the ratio of the NMR linewidth and the applied gradient.

If T_2^* is dominated by T_2, the resolution can be improved only by raising the applied gradient. However, if ΔB is the primary cause of dephasing, making B_0 more homogeneous will improve the resolution. In this case, if ΔB represents the difference between the minimum and maximum precession field inside each column in Fig. 1.8(B) with no applied gradient, each column will have linewidth $\Delta\omega_l = \gamma\Delta B$. The spatial resolution is then

$$\Delta l_x = \Delta B/G_x = B_0(\Delta B/B_0)/G_x. \quad (1.14)$$

Because magnet design determines the relative homogeneity $\Delta B/B_0$, Δl can be reduced either by improving the homogeneity of the magnet or by reducing B_0. Even when T_2 limits the resolution, a low-field MRI system will be able to employ less homogeneous magnets to obtain the same resolution as a high-field system.

1.3. Prepolarized SQUID-detected MRI

Equation (1.14) shows that low-field MRI can in principle achieve resolution equal to or higher than high-field MRI. However, Eq. (1.7) shows that the sample magnetization scales as linearly with the strength of the applied field. Furthermore, since the voltage generated by Faraday detection scales linearly with frequency, the signal detected by conventional MRI is proportional to B_0^2. While Sec. 4.3.3 describes the SNR of conventional MRI in more detail, the strong dependence on B_0 remains.

McDermott *et al.* [5] performed MRI with a SNR independent of B_0 by changing two elements of the MRI experiment. First, they detected the precessing spins using a SQUID connected to an untuned gradiometer; the output voltage of their detector obeys Eq. (1.6) rather than Faraday's law. Second, they prepolarized the spins using the pulse sequence shown in Fig. 1.9. The polarizing field $B_p >> B_0$ is applied for a time $T_p \geq T_1$, causing the spins to align along B_p. The polarizing field is then ramped down in a time longer than the spin precession period but much shorter than T_1. The spin magnetization adiabatically follows the direction of the applied field, so the spins end up aligned with B_0 with magnetization comparable to Eq. (1.7) in an applied field B_p. A 90° pulse initiates

spin precession and is followed by a standard spin-echo sequence. Thus the SNR of SQUID-detected prepolarized MRI is independent of B_0 but rather scales as B_p divided by the magnetic field noise of the SQUID.

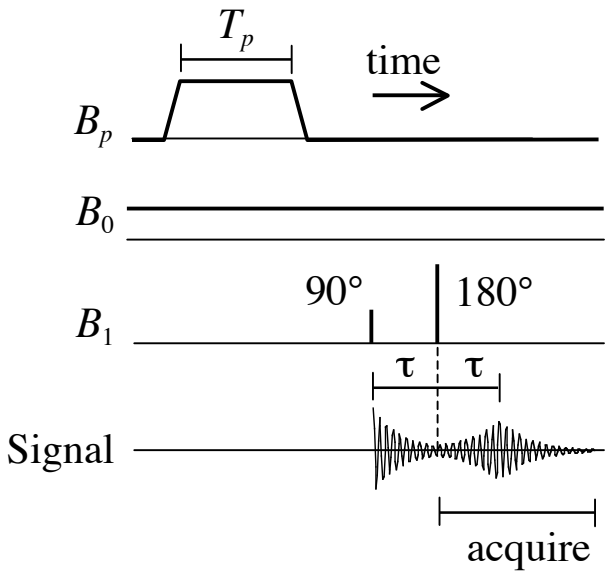

Figure 1.9: Prepolarized NMR pulse sequence.

Although B_0 no longer determines the SNR of such an MRI experiment, two factors prevent one from choosing an arbitrarily low precession frequency. First, the gradient terms in (1.9) do not obey Maxwell's equations, which state that variations in B_z must be accompanied by fields in the x and y directions. These so-called concomitant gradients can only be neglected when B_0 is much greater than the gradient strength times the sample size, setting a lower bound for B_0. Second, laboratories and hospitals are filled with electrical equipment that generates magnetic field noise. While enclosing the experiment in a conducting eddy current shield can reduce magnetic field noise, the required shielding thickness scales as the skin depth, which is proportional to $\omega_0^{-1/2}$.

1.4. First-generation microtesla SQUID MRI system

Considering the effects of concomitant gradients and taking advantage of a relatively low-noise band of the electromagnetic spectrum in Birge Hall, McDermott and co-workers chose a precession field $B_0 = 132$ μT corresponding to $\omega_0/2\pi = 5.6$ kHz. They built an MRI system [10] consisting of a SQUID connected to an untuned second-order gradiometer operated within a custom-built low-noise cryostat. Copper-wire coils supported by wooden frames provided the polarizing, precession, excitation (B_1), and gradient fields necessary for MRI. They enclosed the entire experiment in 3.2-mm thick aluminum plating to provide eddy-current shielding. A Tecmag Orion™ MRI console provided pulse sequence timing control and sampled the output of the SQUID flux-locked loop.

1.4.1. SQUID and untuned gradiometer

Figure 1.10 shows the gradiometer and sample configuration used in of the SQUID MRI system. The magnetic moment of the spins precessing about the applied field $B_0\hat{\mathbf{z}}$ couples flux into the bottom loop of the b = 75 mm, $2a$ = 65 mm second-order gradiometer. The resulting supercurrent couples flux into the SQUID. An array of Josephson junctions with I_c ~10 μA limits the current that flows in the input circuit in response to the polarizing field to prevent damage to the input coil. To prevent background fields from coupling flux directly into the SQUID washer, a superconducting shield encloses the SQUID, input coil, and current limiter.

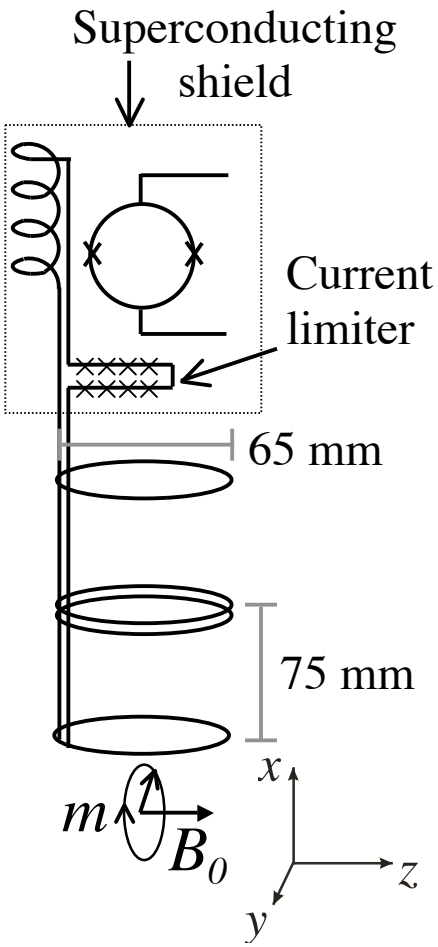

Figure 1.10: Schematic of SQUID, gradiometer, and sample for microtesla MRI.

A single loop of the gradiometer has inductance $L_1 = \mu_0 a[\ln(8a/\phi) - 2]$ = 0.28 μH, where 2ϕ = 75 μm is the diameter of the superconducting wire. In the first-generation system, the two turns of the middle loop of the gradiometer lie directly on top of each other, so I estimate their combined inductance to be $4L_1$, for a total gradiometer inductance of $L_p = 6L_1$ = 1.7 μH. The first-generation system employed a SQUID manufactured and packaged by Quantum Design, Inc. (San Diego). This device employed a cloverleaf pattern input coil [11] with inductance specifications L_i = 1.9 μH and M_i = 11 nH; when connected to the gradiometer and operated in a f_m = 2 MHz flux-locked loop, the SQUID had a flux noise of $S_\Phi^{1/2} = 6.0\ \mu\Phi_0\ \text{Hz}^{-1/2} = 1.2 \times 10^{-20}\ \text{T m}^2\ \text{Hz}^{-1/2}$. Since $A_p = \pi a^2$, the predicted effective area of the SQUID and gradiometer from Eq. (1.5) is 9.9×10^{-6} m^2; measurements using the technique described in Sec. 4.2.2.4 yield $A_{eff} = 7.1 \times 10^{-6}$ m^2. Using the measured value of the effective area, the magnetic field noise of the detector is $S_B^{1/2} = S_\Phi^{1/2}/A_{eff}$ = 1.7 fT Hz$^{-1/2}$ referred to the bottom loop of the

gradiometer. The gradiometer achieved a balance of ~100 against uniform fields in all directions.

1.4.2. Ultra low-noise cryostat

The potential of a low-noise detector can only be realized if the environmental noise can be reduced below the detector noise. Nyquist noise currents in the aluminized Mylar superinsulation used for thermal radiation shielding in liquid helium cryostats generates magnetic field noise; commercially available cryostats have a minimum magnetic field noise of ~4 fT $Hz^{-1/2}$. Because thermal shielding is located just below the pickup loop of the gradiometer, gradiometric detection does not reduce cryostat noise.

In order to reduce cryostat magnetic field noise in the context of SQUID-detected MRI, Seton, Hutchison, and Bussel [12] replaced the aluminized Mylar superinsulation with aluminized polyester. The weave of the polyester cloth breaks the aluminum film into small conducting islands. While still reflecting thermal insulation, these islands cannot sustain macroscopic Nyquist noise currents. In order to reduce the distance between the pickup loop and the room temperature sample while minimizing the helium boil-off rate and cryostat noise, they placed a non-conducting alumina plate in the vacuum space between the pickup coil and the sample. They attached alumina rods to the plate to thermally anchor it to the upper region of the cryostat cooled by escaping helium gas. Based on quality-factor measurements of a tuned coil in their cryostat, they estimate a cryostat magnetic field noise of 0.018 fT $Hz^{-1/2}$ [13]. Following their design, McDermott and co-workers constructed the dewar shown in Fig. 1.11. Used in all Clarke group MRI experiments to date, this cryostat achieves a d = 25 mm distance between the bottom loop of the gradiometer and the sample.

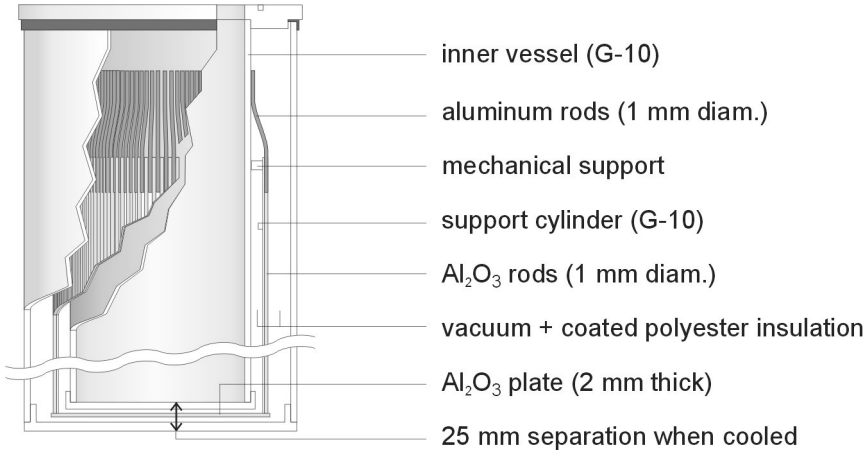

Figure 1.11: Cutaway view of the low-noise cryostat employed in the Clarke group microtesla SQUID MRI system. Further dimensions and details can be found in [10].

1.4.3. Magnetic field coils

Because metal near the gradiometer produces Nyquist noise that could limit the SNR, the magnetic field coils of the first-generation MRI system were wound on wooden coil forms. Figure 1.12 shows the geometry of the magnetic field coils, cryostat, and SQUID gradiometer of the first-generation microtesla MRI system. Three 1.8-m square coils cancel the unwanted components of the Earth's magnetic field; their coil frames form the infrastructure that supports the cryostat and other coils. A 1.15-m diameter Helmholz coil pair produces B_0 and a Maxwell pair of the same diameter generates a $G_z \equiv dB_z/dz$ field. Two sets of Golay coils produce $G_x \equiv dB_z/dx$ and $G_y \equiv dB_z/dy$ fields. Rectangular biplanar gradient coils (not shown in Fig. 1.12) provided the higher field gradients required for slice selective pulse sequences, which are described in Sec. 2.2. A smaller circular coil pair oriented along the x-axis produces B_1. Table 1.1 describes the detailed geometry of the first-generation coils. Mechanical relays are installed in series with many of the magnetic field coils; these relays are opened during data acquisition to minimize magnetic field noise coupled to the gradiometer unless the pulse sequence require that the coil be energized during this time.

The polarizing coil described in [10] consisted of a solenoid wound from 2-mm diameter copper wire; the sample was placed within the bore of the solenoid. While this coil could produce a field B_p = 300 mT in the center of its bore, it could only be operated for ~15 1-second pulses before requiring cooling for ~5 minutes. Such cooling was accomplished by conducting heat away from the coil windings with an array of 120

sections of 1-mm copper wire positioned vertically within the solenoid windings. These copper wires were soldered to and cooled by a copper tube below the polarizing coil containing flowing liquid nitrogen. Besides limiting the running time of MRI experiments, the polarizing coil also produced magnetic field noise. Although opening the relay between the polarizing coil and its amplifier during data acquisition eliminated much of the noise, Nyquist currents flowing within the cross-sections of the coil windings could not be eliminated in this way. Section 5.1 describes the improvements made to the polarizing coil in order to reduce its Nyquist magnetic field noise and improve coil cooling.

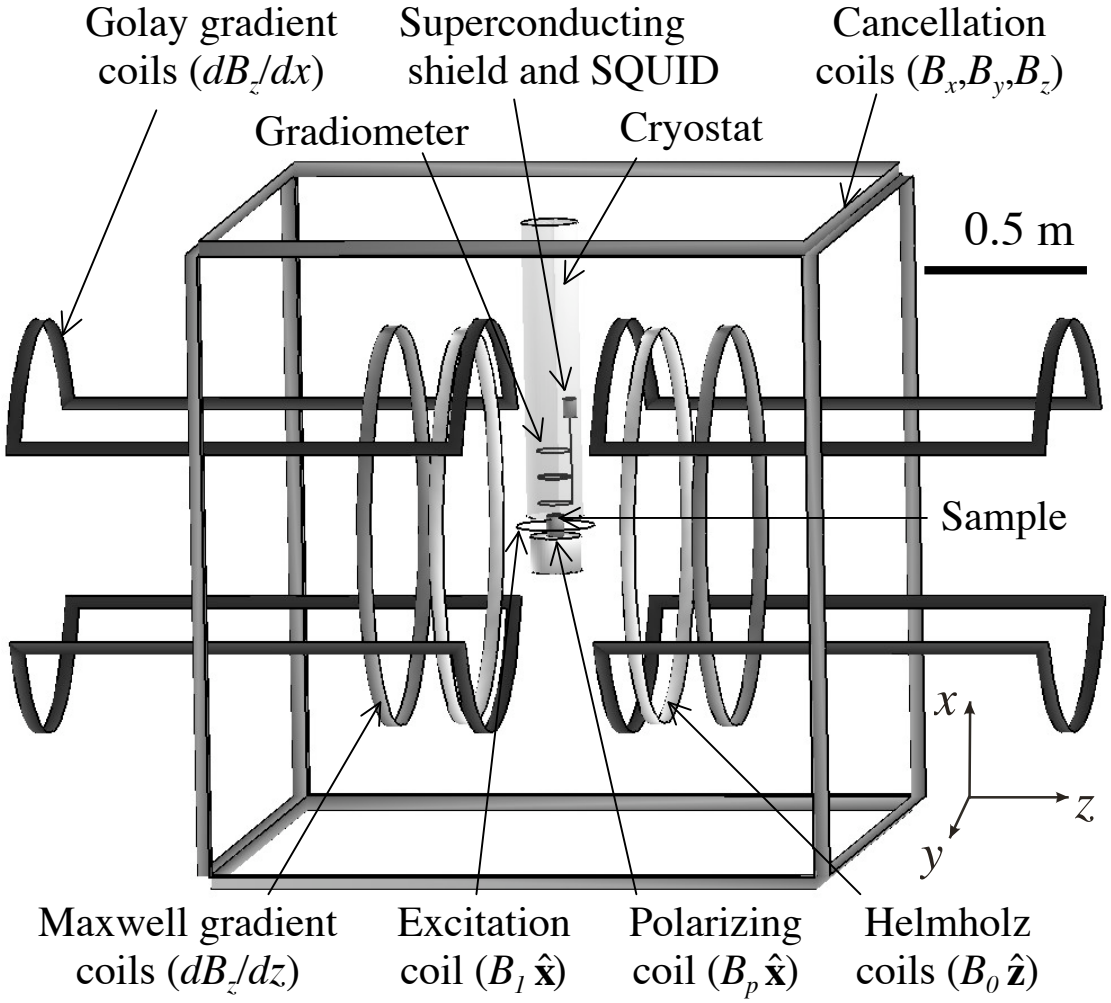

Figure 1.12: Coil geometry of the first-generation microtesla MRI system. The cryostat has been rendered translucent to reveal the superconducting shield containing the SQUID and the gradiometer. For clarity, the G_y Golay coils and slice selection gradient coils are not shown and the gradiometer radius is exaggerated.

Table 1.1: Coil geometry of first-generation system in September 2003. The coil function and typical fields reflect the pulse sequences in use at that time.

Function	Geometry	Turns, wire dia. Inductance Resistance	Typical field/ field gradient Current
Cancellation field B_x, B_y, B_z	Square coils on opposite sides of the 1.8 m cube	100, 1.0 mm 110 mH 30 Ω	25 μT 0.5 A
Precession field B_z	Helmholtz pair; radius 0.6 m	20, 1.0 mm 3.3 mH 3.7 Ω	132 μT 4.4 A
Excitation field B_x	Circular coil; 230 mm diameter	15, 0.8 mm 93 μH 0.8 Ω	33 μT 0.3 A
Polarization field B_x	Solenoid; height 90 mm, I. D. 57 mm, O. D. 137 mm	810, 2.0 mm 32 mH 1.4 Ω	300 mT 40 A
Shimming gradient dB_z/dx	Golay coil; radius of curvature 0.6 m	20, 0.8 mm 0.53 mH 2.4 Ω	5 μT/m 0.4 A
Encoding gradient dB_z/dy	Golay coil; radius of curvature 0.6 m	40, 0.8 mm 2.2 mH 3.8 Ω	100 μT/m 4 A
Encoding gradient dB_z/dz	Maxwell pair; radius 0.6 m	20, 1.0 mm 3.1 mH 3.5 Ω	100 μT/m 2 A
Slice selection gradient dB_z/dx	Biplanar coil; four 700 x 380 mm rectangular loops	20, 1.0 mm 3.1 mH 4.8 Ω	400 μT/m 2 A

1.4.4. Radiofrequency and 5.6 kHz magnetic shielding

In their initial experiments, McDermott and co-workers employed aluminum foil wrapped around the cryostat to shield the gradiometer to prevent it from coupling external radiofrequency noise to the SQUID. However, aluminum foil near the gradiometer coupled Nyquist noise into the gradiometer, so they did not wrap foil around the bottom half of the cryostat. While this aluminum reduced the effects of radiofrequency noise, it provided no shielding against external noise at the 5.6 kHz precession frequency.

Because such low-frequency external noise limited the sensitivity of their MRI experiments, McDermott and co-workers enclosed the entire assembly shown in Fig. 1.12 in 3.2-mm thick 5052 aluminum plate. Since this alloy has resistivity $\rho = 4.8 \times 10^{-8}$ Ωm,

it has a skin depth $\delta = (2\rho/\mu_0\omega_0)^{1/2} = 1.5$ mm at $\omega_0/2\pi = 5.6$ kHz, and the plates attenuate external 5.6 kHz noise by a factor of 8. In addition, they anticipated that the plates would form a Faraday cage that would screen external radiofrequency noise. However, because they attached the plates to a non-conducting wooden support frame and left gaps in the conducting connectors between the plates, they achieved less radiofrequency shielding than they had anticipated and the cryostat still had to be wrapped in aluminum foil. With this additional shielding, the system achieved a magnetic field noise of 3 fT $Hz^{-1/2}$ referred to the bottom loop of the gradiometer. McDermott and coworkers discovered that the additional noise above the 1.7 fT $Hz^{-1/2}$ SQUID noise originated from Nyquist currents flowing in the cross-sections of the polarizing coil windings.

The first two sections of Chapter 2 describe the pulse sequences that McDermott and coworkers employed to perform MRI using this system. The later sections of Chapter 2 describe the improved pulse sequences implemented since Robert McDermott received his Ph. D. Section 4.2 describes measurements of a lower-noise SQUID and its performance it the MRI system. The first section of Chapter 5 describes successive improvements in the polarizing coil to decrease its Nyquist noise and improve coil cooling. The remainder of Chapter 5 describes the design and construction of the second-generation microtesla MRI system.

---

[1] P. K. Grannell and P. Mansfield, Microscopy *in vivo* by nuclear magnetic resonance, *Phys. Med. Biol.* **20** (1975) 477.

[2] R. W. Mair, M. I. Hrovat, S. Patz, M. S. Rosen, I. C. Ruset, G. P. Topulos, L. L. Tsai, J. P. Butler, F. W. Hersman, R. L. Walsworth, He-3 lung imaging in an open access, very-low field human magnetic resonance imaging system, *Magn. Reson. Med.* **53** (2005) 745.

[3] C. H. Tseng, G. P. Wong, V. R. Pomeroy, R. W. Mair, D. P. Hinton, D. Hoffmann, R. E. Stoner, F. W. Hersman, D. G. Cory, R. L. Walsworth, Low-field MRI of laser polarized noble gas, *Phys. Rev. Lett.* **81** (1998) 3785.

[4] S-K. Lee, M. Mößle, W. Myers, N. Kelso, A. H. Trabesinger, A. Pines, and John Clarke, SQUID-detected MRI at 132 μT with T_1-weighted contrast established at 10 μT-300 μT, *Magn. Reson. Med.* **53** (2005) 9.

[5] R. McDermott, S-K. Lee, B. ten Haken, A. H. Trabesinger, A. Pines, John Clarke, Microtesla MRI with a superconducting quantum interference device, *Proc. Natl. Acad. Sci. USA* **101** (2004) 7857.

[6] M. Tinkham, *Introduction to Superconductivity*, 2nd ed., McGraw Hill, New York, 1996.

[7] W. C. Stewart, Current-voltage characteristics of Josephson junctions, *Appl. Phys. Lett.* **12** (1968) 277.
[8] D. E. McCumber, Effect of ac impedance on dc voltage-current characteristics of superconductor weak-link junctions, *J. Appl. Phys.* **39** (1968) 3113.
[9] E. M. Haacke, R. W. Brown, M. R. Thompson, R. Venkatesan, *Magnetic Resonance Imaging: Physical Principles and Sequence Design*, Wiley-Liss, New York, 1999.
[10] R. McDermott, N. Kelso, S-K. Lee, M. Mößle, M. Mück, W. Myers, B. ten Haken, H. C. Seton, A. H. Trabesinger, A. Pines, John Clarke, SQUID-detected magnetic resonance imaging in microtesla magnetic fields, *J. Low Temp. Phys.* **135** (2004) 793.
[11] M. B. Simmonds, US Patents 5,053,834 (1991) and 5,319,307 (1994).
[12] H. C. Seton, J. M. S. Hutchison, and D. M. Bussel, UK patents GB2331789 and GB2351549.
[13] H. C. Seton, J. M. S. Hutchison, and D. M. Bussel, Liquid-helium cryostat for SQUID-based MRI receivers, *Cryogenics* **45** (2005) 348.

2. Prepolarized low-field MRI pulse sequences and image reconstruction

Many of the fundamental advances in MRI have come not through hardware engineering but through pulse sequence design. As with early conventional MRI, the initial experiments of McDermott and co-workers employed conceptually simple projection-reconstruction pulse sequences to form two-dimensional images. They also employed slice selective pulse sequences to image two-dimensional slices of three-dimensional objects. Because heating of the polarizing coil limits the number of polarizing pulses that can be applied, efficient use of the available sample magnetization is essential to produce high-quality images. While projection-reconstruction and slice selection sufficed to produce the initial microtesla MR images, more efficient pulse sequences can substantially improve image quality using the same hardware. Because conventional MRI pulse sequences have undergone decades of development, finding appropriate pulse sequences for prepolarized SQUID detected MRI involves choosing between existing pulse sequences rather than inventing new ones.

Sections 2.1 and 2.2 describe projection-reconstruction and slice selection and the limitations of these techniques in the context of prepolarized microtesla MRI. Section 2.3 introduces the fundamental concepts of *k*-space and Fourier transform imaging. Section 2.4 describes the spin-warp pulse sequence and presents details of the image reconstruction algorithm. Section 2.5 describes modifications of the spin-warp pulse sequence that enhance image quality for either long or short T_2 relaxation times. Section 2.6 presents three-dimensional Fourier transform imaging including both pulse sequences and images. Section 2.7 derives an expression for the SNR of a voxel in Fourier transform imaging and demonstrates that three-dimensional Fourier transform imaging outperforms slice-selected imaging in prepolarized MRI. Finally, Sec. 2.8 describes sensitivity encoding (SENSE), a technique that employs the spatial selectivity of multiple sensors to reduce data acquisition time.

2.1. Projection-reconstruction

The projection-reconstruction pulse sequence consists of acquiring a series of projections of the sample in varying applied gradients as shown in Fig. 2.1(A); the magnitude of the Fourier transform of the acquired signal is proportional to the spin

density of the sample projected perpendicularly to the applied gradient. In this sequence, the applied gradient is constant in magnitude but rotated in the imaging plane by a fixed angle between each projection. The gradient must sweep out an angle of at least 180° to reconstruct an image of the sample. Fig. 2.1(B) shows the pulse sequence employed for prepolarized spin-echo projection-reconstruction MRI. While the magnetic field gradients need only be applied after the 90° pulse to influence spin evolution, the initial MRI experiments of McDermott and co-workers employed constant gradients to simplify sequence control.

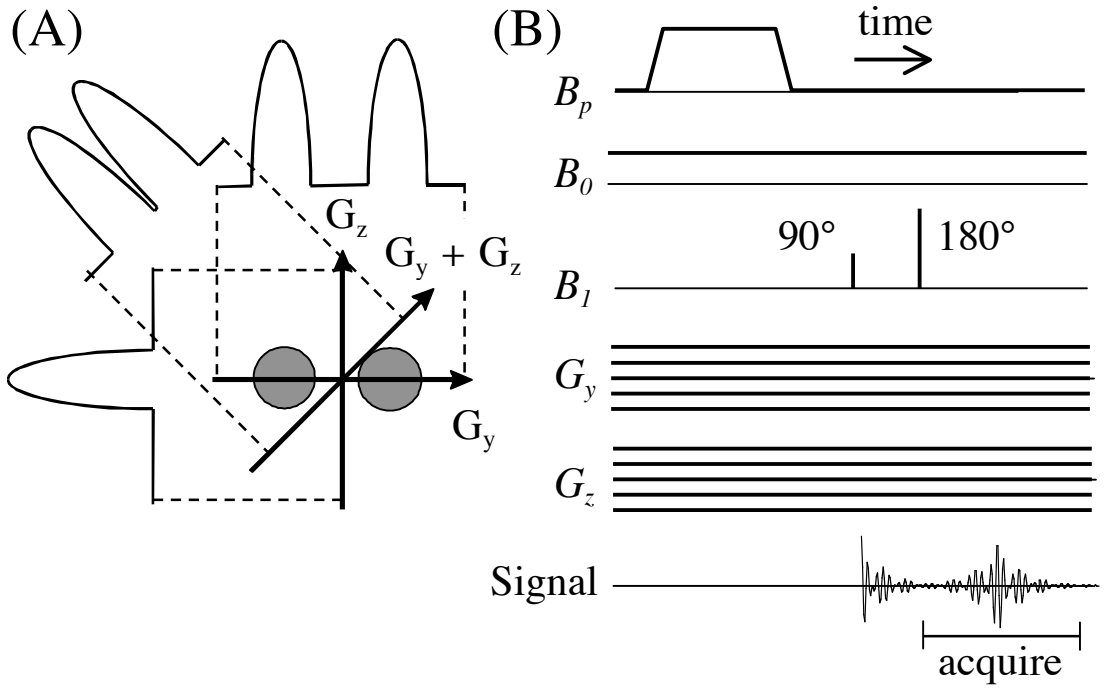

Figure 2.1: (A) Projections of a sample of two columns of water along an applied gradient at three different angles. (B) Pulse sequence diagram for prepolarized spin-echo projection-reconstruction MRI. The multiple lines shown for the G_x and G_y gradients indicate that the pulse sequence is repeated varying the values of these gradients.

McDermott and co-workers employed either filtered backprojection or *k*-space interpolation followed by Fourier reconstruction to form images from the data acquired from projection-reconstruction sequences. Backprojection reconstruction consists of superimposing the images generated by "painting" the projection generated from each data acquisition along the line perpendicular to the applied gradients. Figure 2.2 shows a four-angle backprojection reconstruction of the sample shown in Fig. 2.1(A). Although

the circles are beginning to take shape in this image, it also shows the streaked artifacts characteristic of backprojection reconstruction. It can be shown [1] that applying a filter to each projection before the backprojection operation can eliminate this streaking. The filter consists of taking the Fourier transform of each projection, multiplying each component by $|k|$, where $2\pi/k$ is the wavelength of the Fourier component, and then taking the inverse Fourier transform. Since this filter emphasizes the high-frequency components of the image, it tends to create artifacts of its own. Therefore, most implementations of filtered backprojection soften the edges of this filter and the algorithm used to reconstruct the images shown in this section replaces |k| with $|\sin^3(\pi k/2k_{\max})|/k^2$, where k_{max} is the highest frequency component in the projection.

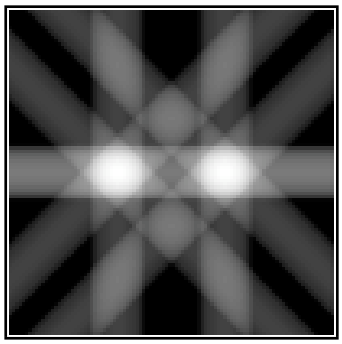

Figure 2.2: Backprojection reconstrucion of the sample of Fig. 2.1(A) using gradients applied at 0°, 45°, 90° and 135°.

Figure 2.3 shows projection-reconstruction MR images of 13 columns of mineral oil and a slice of bell pepper taken using the pulse sequence of Fig. 2.1(B). The samples were prepolarized in a field $B_p \approx 200$ mT and detected in a field $B_0 = 132$ μT using the SQUID untuned gradiometer. The images were reconstructed using filtered backprojection and display the correlated noise generally observed using this reconstruction technique. In addition, a brighter region surrounds the columns in Fig. 2.3(B); this artifact is not present in Fig. 2.3(D) nor the image produced from the same data set reconstructed using interpolated Fourier reconstruction [Fig. 2.17(A)].

Because interpolated Fourier reconstruction can be best understood after introducing the concept of *k*-space, I defer discussion of this algorithm until Sec. 2.5.3. This section also discusses the resolution and efficiency of projection-reconstruction imaging and its advantages and drawbacks.

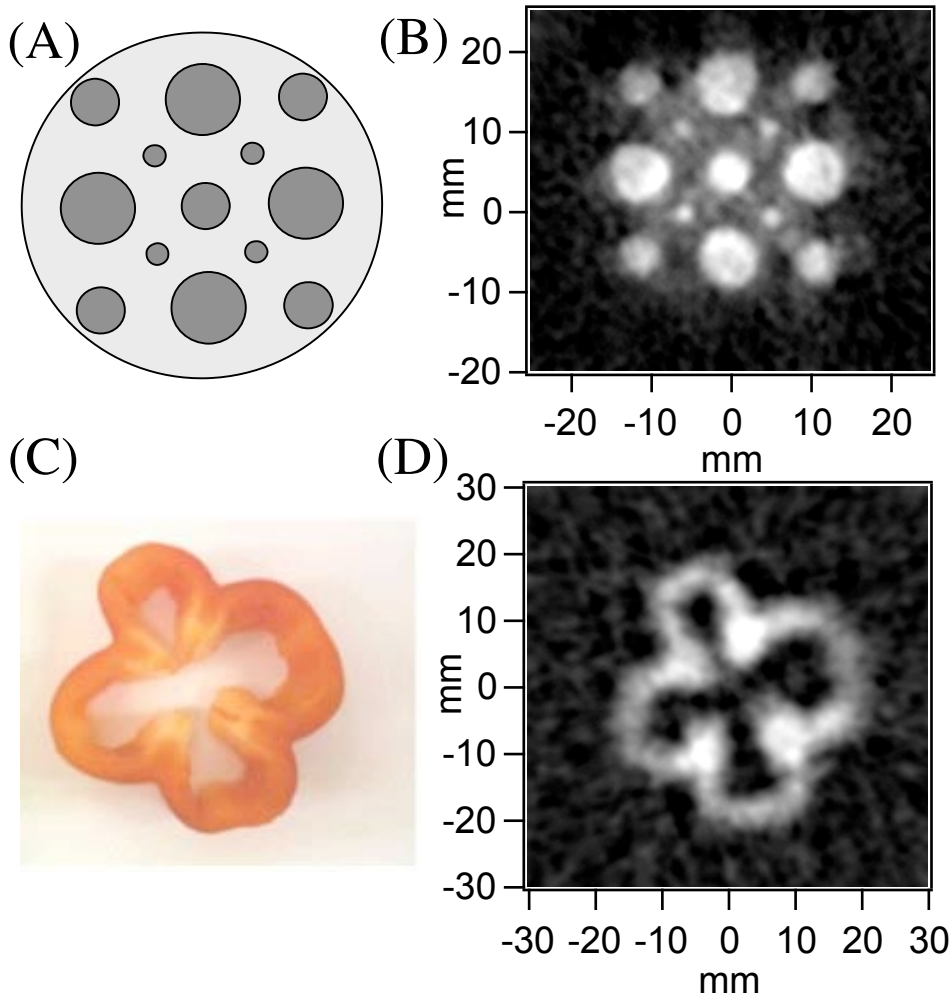

Figure 2.3: Objects and their microtesla MR images reconstructed using filtered backprojection. (A) A phantom of 13 cylindrical columns of mineral oil in Teflon®; the smallest column is 3 mm in diameter. (B) MR image of this phantom reconstructed from 48 projections taken in a 200 μT/m gradient; 16 averages were employed per projection. (C) A slice of red bell pepper. (D) Its MR image using 48 projections taken in a 100 μT/m gradient; 8 averages were employed per projection. While the total pulse sequence running time was 7.5 min for (B) and 5 min for (D), the images took ~2 hours to acquire because of the time spent waiting for the polarizing coil to cool between successive gradient steps.

2.2. Slice selection

Projection-reconstruction imaging can be extended to three dimensions by rotating the applied gradient vector **G** over the surface of a sphere rather than the circumference of a circle. However, McDermott and co-workers chose a simpler method to demonstrate the possibility of three-dimensional microtsela MRI: slice-selection. In this technique, a combination of applied gradients and narrow band excitation pulses cause only a two-

dimensional slice of the sample to contribute to the acquired MR signal. This slice is imaged in two dimensions, and then the excitation pulse is modified to select another slice of the sample.

Before introducing slice-selective excitation pulses, I review the broadband excitation pulses employed in other sequences. Figure 2.4(A) shows the broadband 90° pulse used in the pulse sequence of Fig. 2.1. Consisting of four cycles of a 5.6 kHz sine wave, it has FWHM bandwidth of 1.7 kHz. Since the spins in the 30-mm wide sample of Fig. 2.3(A) have a precession frequency bandwidth of only 260 Hz in the 200 μT/m applied gradient, this broadband pulse will tip all spins in the sample by ~90° despite the applied gradient. The 180° pulse employed in this sequence simply has twice the amplitude of the 90° pulse. In contrast, Fig. 2.4(B) shows a narrow-band excitation pulse with waveform

$$B_1(t) = B_{10}\sin(2\pi ft)\,\mathrm{sinc}(2\pi\Delta ft) = B_{10}\sin(2\pi ft)\sin(2\pi\Delta ft)/(2\pi\Delta ft), \qquad (2.1)$$

where B_{10} is the pulse amplitude, f is the center frequency of the pulse, and Δf = 150 Hz is the half-width half-maximum (HWHM) bandwidth of the excitation pulse. The Fourier transform of this waveform is a constant between f - Δf and f + Δf and zero elsewhere. However, because spin relaxation limits the waveform to only five lobes of the sinc function, the Fourier transform contains observable Gibbs ringing. Such ringing can be reduced by applying a filter to $B_1(t)$.

Figure 2.5 shows the slice-selective projection-reconstruction pulse sequence employed by McDermott and coworkers. After the polarizing pulse, the narrow-band 90° pulse of Fig. 2.4(B) is applied along with a gradient $G_x = G_{ss}$ for a time t_{ss}. This combination tips only spins between $x = (f - \omega_0/2\pi - \Delta f)/\gamma G_{ss}$ and $x = (f - \omega_0/2\pi + \Delta f)/\gamma G_{ss}$ into the xy plane to begin spin precession. Because G_{ss} also dephases the spins along the x-direction, a refocusing gradient $G_x \approx -G_{ss}/2$ rephases the spins after the 90° pulse. The remainder of the sequence follows the projection-reconstruction sequence of Fig. 2.1, except that the echo time τ is now measured between the application of the imaging gradients and the 180° pulse.

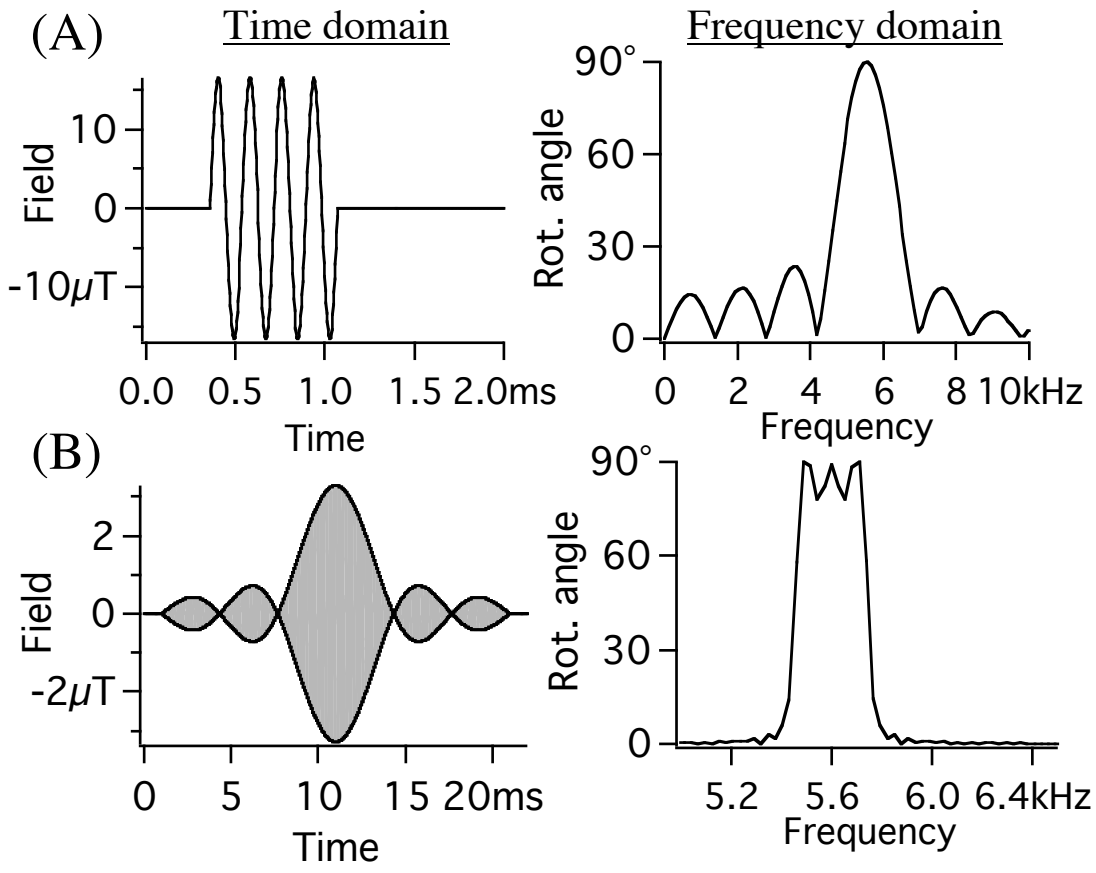

Figure 2.4: 90° excitation pulses for 5.6 kHz MRI. (A) Broadband pulse. (B) Five-lobe sinc pulse with 300 Hz FWHM bandwidth.

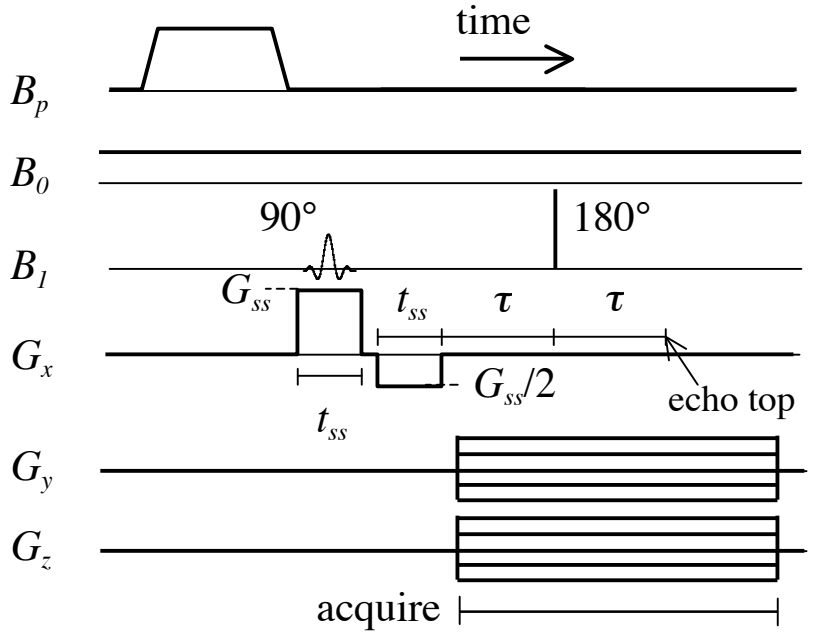

Figure 2.5: Slice-selective projection-reconstruction pulse sequence employed by McDermott and co-workers.

Figure 2.6(A) shows an MR image of an intact bell pepper taken with the sequence of Fig. 2.5 using G_{ss} = 350 μT/m to image a 20-mm thick slice. The image was reconstructed using Fourier interpolation (Sec. 2.5.3) from 24 projections taken in a 100 μT/m imaging gradient. Figure 2.6(B) shows a photograph of the bell pepper, sliced *after* the MR image was taken.

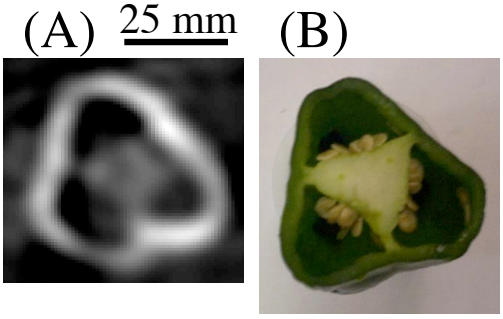

Figure 2.6: (A) A slice-selected image of an intact bell pepper. (B) A photograph of the bell pepper sliced after imaging.

2.3. Fourier transform imaging

Although filtered backprojection can be used to reconstruct MR images, there are two reasons to suspect that it may not be optimally efficient. First, this algorithm considers only the magnitude of the Fourier transform of the acquired data; the phase of the Fourier transform also contains information about the image. Second, projection-reconstruction techniques produce polar representations of the sample, which must then be mapped to rectangular representations for screen display. In this section, I describe the principles of Fourier transform reconstruction, an efficient, phase-sensitive imaging technique that can be used with rectangular sampling of reciprocal space.

2.3.1. Reciprocal space (*k*-space) in MRI

The principles underlying Fourier transform imaging begin with a simplified version of the Bloch equation. Combining Eqs. (1.8) and (1.9) and eliminating the relaxation, field inhomogeneity, and excitation terms, I obtain

$$\frac{d\mathbf{M}}{dt} = \gamma \mathbf{M} \times \left(B_0 + \mathbf{G}(t) \cdot \mathbf{r}\right)\hat{\mathbf{z}}. \tag{2.2}$$

This equation describes clockwise precession of the in-plane components of **M**, which can be described in complex notation as

$$M(\mathbf{r},t) = \exp\left[-i\gamma \int_0^t \left(B_0 + \mathbf{G}(t) \cdot \mathbf{r}\right) dt'\right], \tag{2.3}$$

where I have assumed that the spins begin aligned along the *x*-axis. Defining

$$\mathbf{k}(t) = \gamma \int_0^t \mathbf{G}(t) dt', \tag{2.4}$$

Eq. (2.3) becomes

$$M(\mathbf{r},t) = e^{-i\mathbf{k}(t)\cdot\mathbf{r}} e^{-i\gamma B_0 t}. \tag{2.5}$$

Equation (2.5) describes a spatial wave of spin angles with wavevector $\mathbf{k}(t)$ precessing with angular frequency γB_0. Assuming that the total spin magnetization in the xy plane at each point is $M(\mathbf{r})$, a detector that is equally sensitive to the x-component of each spin will measure a magnetic field

$$B_{det}(t) \propto \mathrm{Re}\left[\int_V M(\mathbf{r}) e^{-i\mathbf{k}(t)\cdot\mathbf{r}} d\mathbf{r} \;\; e^{-i\gamma B_0 t}\right], \tag{2.6}$$

where V is the sample volume. Demodulating $B_{det}(t)$ yields

$$s(\mathbf{k}) \propto \int_V M(\mathbf{r}) e^{-i\mathbf{k}\cdot\mathbf{r}} d\mathbf{r}, \tag{2.7}$$

the Fourier integral of the spin magnetization. If one measures $s(\mathbf{k})$ over a sufficient span of k-space, the spin magnetization can be reconstructed by taking the inverse Fourier transform of $s(\mathbf{k})$:

$$M(\mathbf{r}) \propto \int s(\mathbf{k}) e^{i\mathbf{k}\cdot\mathbf{r}} d\mathbf{k}. \tag{2.8}$$

Examining the time derivative of Eq. (2.4),

$$d\mathbf{k}/dt = \gamma\mathbf{G}(t), \tag{2.9}$$

shows that $\gamma\mathbf{G}$ is the "velocity" of the vector $\mathbf{k}$. Another operation commonly performed in Fourier imaging is the 180° excitation pulse, which inverts the relative phase of the spins, thereby mapping $\mathbf{k}$ to $-\mathbf{k}$. Thus Fourier imaging consists of applying a sequence of magnetic field gradients and 180° excitation pulses designed to trace out an optimal path in k-space, then reconstructing the image using the inverse Fourier transform of the acquired data.

2.3.2. Resolution and field of view

What is a "sufficient span" of k-space? This question can be answered by briefly reviewing the properties of the discrete Fourier transform in one dimension; the results can be generalized to two or three dimensions.

If one samples $s(k)$ at $2n$ points at intervals Δk over the span $-k_{max}$ to $k_{max} - \Delta k$, the discrete inverse Fourier transform

$$M(x) \propto \sum_{p=-n}^{n-1} s(p\Delta k) e^{ip\Delta k x} \tag{2.10}$$

is periodic in x with period $2\pi/\Delta k$. Therefore the field of view (FOV) of the image is given by

$$L = 2\pi/\Delta k. \tag{2.11}$$

If the sample is larger than L, it will appear aliased (overlapping itself) in the reconstructed image. The inverse of Eq. (2.10) is the discrete Fourier transform

$$s(k) \propto \sum_{q=-n}^{n-1} M(q\Delta x) e^{-i\Delta k q x}, \tag{2.12}$$

where the values of $M(x)$ are spaced by $\Delta x = \pi/k_{max}$. Therefore

$$\Delta l = \pi/k_{max} \tag{2.13}$$

is the best possible resolution available from the data $s(k)$. This resolution will only be achieved if the highest values of k contain signal and not just noise. For example, Eq. (2.4) indicates that it takes time to reach high values of k. If T_2 or T_2^* decay substantially reduces the signal amplitude during this time, the actual image resolution will be worse than that predicted by Eq. (2.13). Since the time available for spin manipulation and data acquisition is comparable to T_2^*, and the maximum applied gradient G_{max} sets the maximum k-space velocity, the resolution of Fourier transform imaging is approximately

$$\Delta l = \pi/k_{max} \approx \pi/(\gamma T_2^* G_{max}). \tag{2.14}$$

2.4. Spin-warp imaging and reconstruction

Spin-warp imaging is the simplest method to acquire k-space points on a rectangular grid. Figure 2.7(A) shows the pulse sequence diagram for two-dimensional spin-warp imaging, which consists of the spin-echo sequence of Fig. 1.8(A) with the addition of a G_z gradient pulse applied for a time T_{phase} between the 90° and 180° excitation pulses. Figure 2.7(B) shows the k-space trajectory of this pulse sequence. The k-space vector begins at the origin, and then moves out along a diagonal path under the influence of G_y and G_z. At a time τ after the 90° pulse, the 180° pulse inverts the k-space vector and the G_z gradient is turned off. During data acquisition, the k-space vector traverses the line $k_z = -\gamma\tau G_z$; the echo top occurs when $k_y = 0$. A rectangular grid of k-space points can be measured by repeating the sequence, incrementing the magnitude of the G_z gradient each time. In this sequence, the precession frequency of a spin depends on its y-coordinate, so G_y is called the frequency-encoding gradient G_{freq}. The phase of a

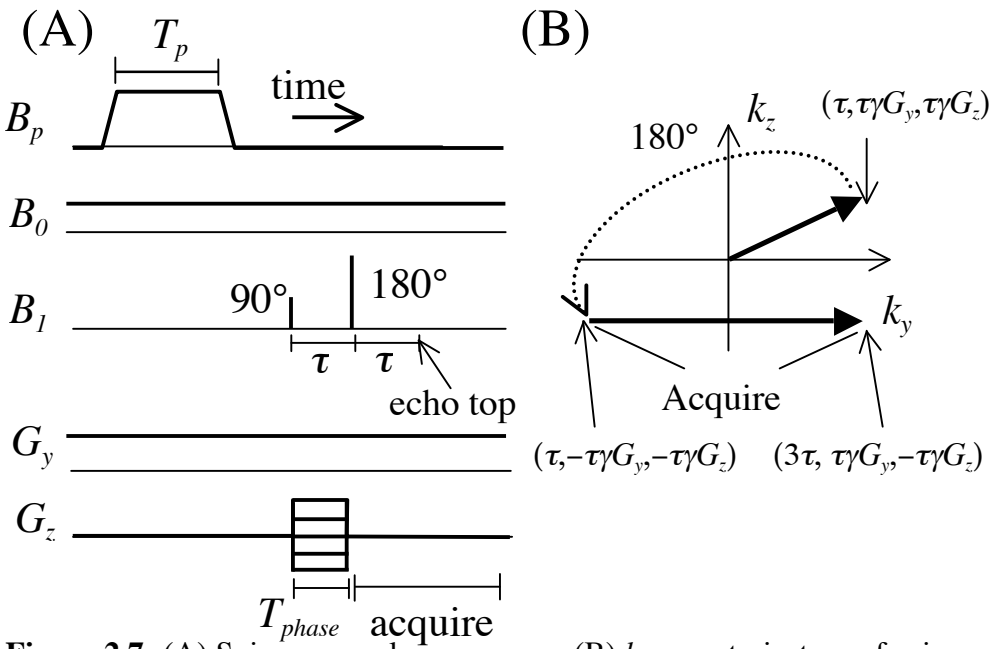

Figure 2.7: (A) Spin-warp pulse sequence. (B) *k*-space trajectory of spin-warp pulse sequence after the 90° pulse. Points along the trajectory are denoted as (time after 90° pulse, k_y, k_z).

spin at the echo top depends on its *z*-coordinate, so G_z is called the phase-encoding gradient G_{phase}.

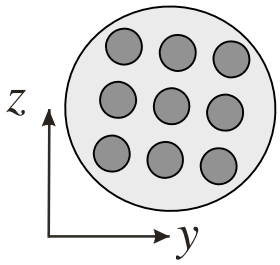

Figure 2.8: Nine-column water phantom used to demonstrate spin-warp imaging. Each column is 6.4 mm in diameter.

In order to demonstrate spin-warp imaging, I applied the pulse sequence of Fig. 2.7(A) to the phantom (MRI test sample) consisting of nine 6.4-mm diameter columns of water shown in Fig. 2.8. I employed $\omega_0/2\pi = 5593$ Hz, $B_p = 200$ mT, $T_p = 0.6$ s, $\tau = 135$ ms, $T_{phase} = 105$ ms, $G_y = 53$ μT/m and G_z ranging from –52 μT/m to 52 μT/m in $N_z = 37$ increments of $\Delta G_z = 2.9$ μT/m; the total sequence took 44 s to execute. The MRI console took 4,096 samples of the output of the flux-locked loop with a sampling time $T_{samp} = 50$ μs for a total data acquisition time of $T_s = 205$ ms. Figure 2.9 shows the data processing steps required to obtain *k*-space values. Figure 2.9(A) shows the magnetic field measured during the $G_z = 0$ sequence step; 60 Hz line noise and its harmonics dominate the detected field. Figure 2.9(B) shows the inverse Fourier transform of the measured field, which separates the 60 Hz noise from the 5.6 kHz signal. The projection of the nine columns along the *y*-axis is clearly visible. The information necessary to reconstruct the image is contained within an angular frequency band $\omega_0 \pm$

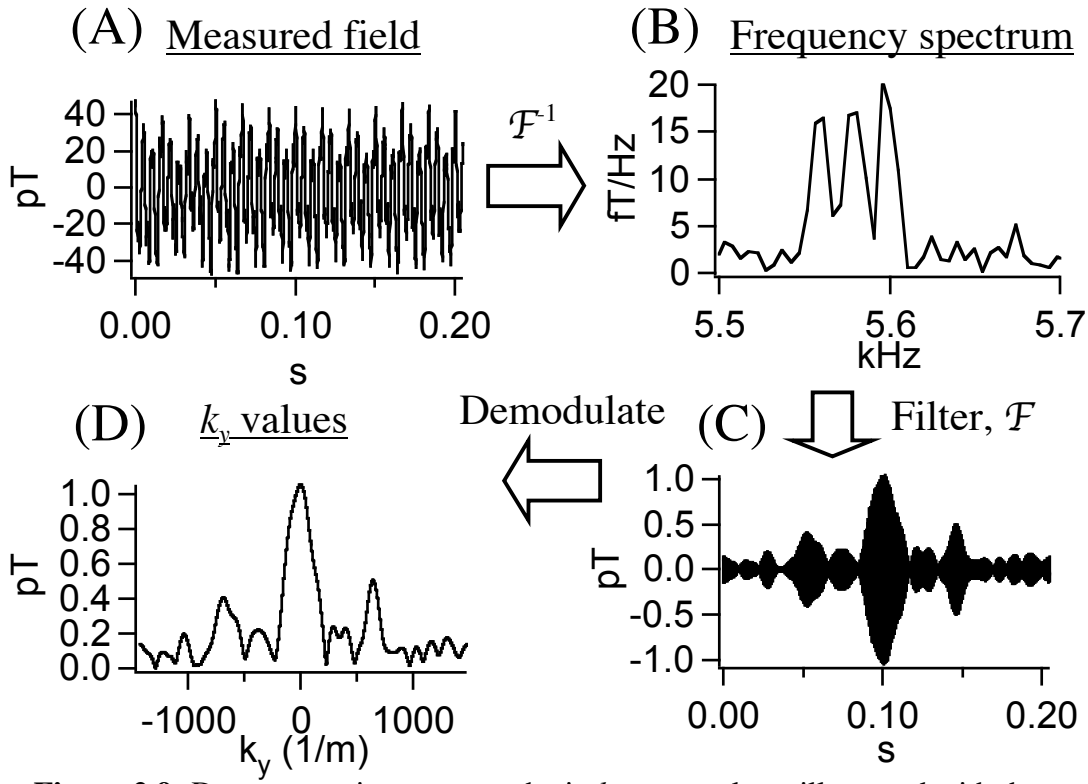

Figure 2.9: Data processing steps to obtain *k*-space values, illustrated with the data from the $k_z = 0$ step of spin warp imaging of the 9-column phantom. (A) The field detected by the SQUID. (B) The frequency spectrum. (C) The filtered magnetic field showing the echo top at 0.1 s. (D) The magnitude of the complex *k*-space values. $\mathcal{F}$ represents the Fourier transform.

$\gamma G_y L_y/2$, where L_y is the field of view in the *y*-direction. Choosing $L_y = L_z = 2\pi/\gamma \Delta G_z = 81$ mm, setting the Fourier components of the signal outside $\omega_0 \pm \gamma G_y L_y/2$ to zero, and taking the Fourier transform yields the filtered time trace shown in Fig. 2.9(C). The echo top appears a at time $t_{echo} = 0.1$ s after the beginning of data acquisition. To produce the line of *k*-space points required for image reconstruction, I demodulate the filtered data by shifting its center frequency from ω_0 to zero in inverse Fourier space. Finally, I transform from time to *k*-space coordinate using $k_y = (t - t_{echo})\gamma G_y$; Fig. 2.9(D) shows the magnitude of the resulting complex *k*-space values. The demodulation and filtering operation that takes the data shown in Fig. 2.9(A) and converts it to the demodulated *k*-space values in Fig. 2.9(D) can be described mathematically as

$$\mathrm{Demod}\left[\mathrm{B}_{det}(t)\right] \equiv 2\,\mathrm{Lowpass}\left[\mathrm{B}_{det}(t)e^{i\omega_0 t}\right] = s\left(\mathbf{k}(t)\right), \tag{2.15}$$

where Lowpass represents the operation of a low-pass filter with angular frequency bandwidth $\gamma G_y L_y/2$. Since

$$B_{\mathrm{det}}(t) = \mathrm{Re}\left[s(\mathbf{k}(t))e^{-i\omega_0 t}\right] = \frac{1}{2}\left[s(\mathbf{k}(t))e^{-i\omega_0 t} + s^*(\mathbf{k}(t))e^{i\omega_0 t}\right] \tag{2.16}$$

and the operation of the low-pass filter eliminates the term containing $e^{i\omega_o t}$, I insert a factor of 2 in Eq. (2.15) so that Demod[$B_{det}(t)$] has the same amplitude as $B_{det}(t)$.

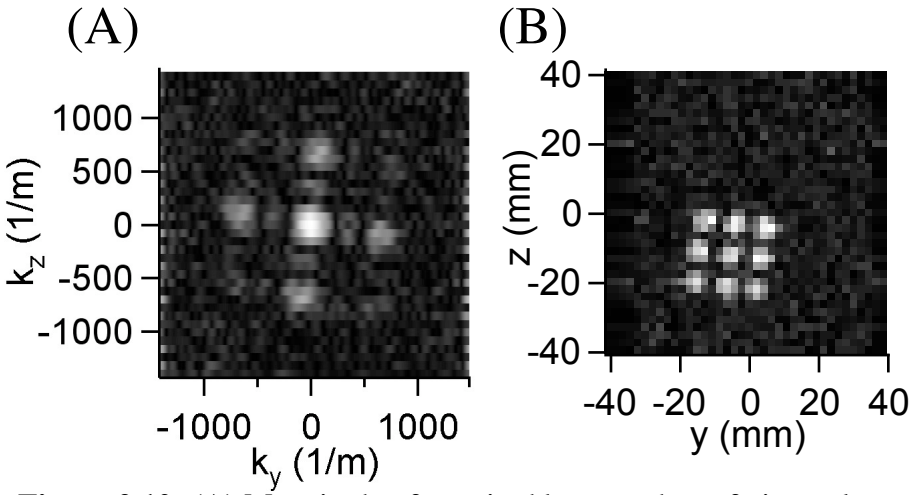

Figure 2.10: (A) Magnitude of acquired k-space data of nine-column phantom image. (B) Inverse Fourier transform of (A).

Figure 2.10(A) shows the magnitude of the *k*-space values generated by applying the process shown in Fig. 2.9 to the data acquired in all 37 steps of the imaging sequence. Because magnetic field values were sampled every T_{samp} = 50 μs, $\Delta k_y = \gamma G_y T_{samp}$, and taking the inverse Fourier tranform of this data set will produce a field of view $2\pi/\Delta k_y$ = 8.9 m. The filter applied to obtain Fig. 2.9(C) ensures that this unnecessarily large field of view contains no information outside the previously chosen field of view $L_y = L_z$. I therefore downsample the *k*-space values in Fig. 2.10(A) so that $\Delta k_y = \Delta k_z$ before taking the inverse Fourier transform to obtain the image shown in Fig. 2.10(B). As expected from Eq. (2.13), each pixel has dimensions $\pi/k_{y,max} \times \pi/k_{z,max}$ = 2.1 mm × 2.2 mm, where $k_{y,max}$ and $k_{y,max}$ are the maximum values of k_y and k_z, respectively.

Although Fig. 2.10(B) is a faithful representation of the nine-column phantom shown in Fig. 2.8, its appearance can be improved by further image processing. Fig. 2.11(A) shows an enlarged view of Fig. 2.10(B) which shows the clear pixilation of the image. The image can be interpolated by increasing $k_{y,max}$ and $k_{y,max}$ by adding zero values beyond the edges of measured *k*-space before performing the inverse Fourier transform. Figure 2.11(B) shows the image of the nine-column phantom after increasing the

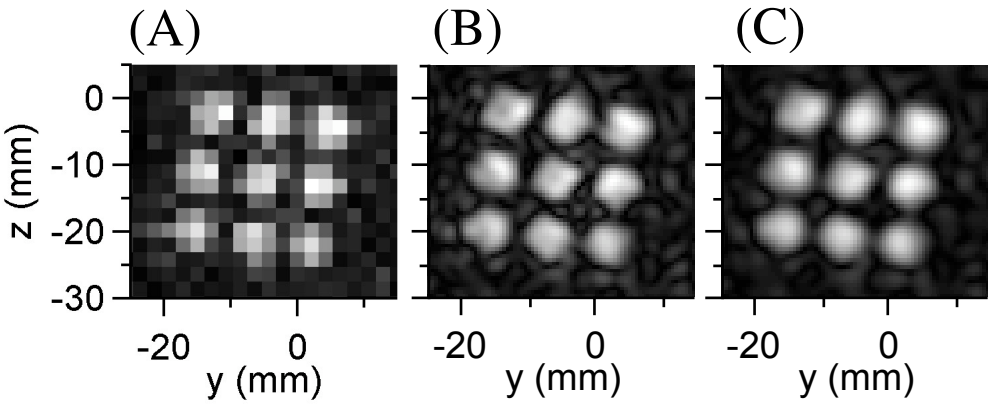

Figure 2.11: (A) Enlarged view of Fig. 2.10. (B) 4x interpolated image. (C) 4x interpolated image with filtered with a sqrt(cos) filter.

displayed image resolution by a factor of 4 using this procedure. Multiplying *k*- space by an envelope function that reduces the magnitude of high-*k* image components smoothes the image. I usually use the envelope function

$$f\left(|\mathbf{k}|\right) = \begin{cases} \sqrt{\cos\left(\pi|\mathbf{k}|/2k_c\right)}, & |\mathbf{k}| < k_c \\ 0, & |\mathbf{k}| \geq k_c \end{cases}, \tag{2.17}$$

where k_c is the *k*-space filter cutoff. I generally set k_c equal to the highest *k*-vector for which the MRI signal rises above the detector noise. Smoothing the nine-column phantom image using $k_c = 1730$ m^{-1} yields Fig. 2.11(C). Compared to Fig. 2.11(B), Fig. 2.11(C) has more regularly shaped columns, somewhat lower resolution and somewhat higher SNR.

2.5. Other methods for scanning *k*-space

This section considers more complex Fourier transform imaging schemes. To clarify the sequence timing definitions, Fig. 2.12 repeats the basic spin-echo sequence with the addition of the inevitable delays between each event that must be considered in detailed pulse sequence analysis.

2.5.1. Multiple echo sequences

Shortly after acquiring the image in Fig. 2.11, I realized that basic spin-warp imaging was not the optimal way to acquire images of water. To achieve optimal polarization, one must apply a polarizing pulse for a time $T_p \sim T_1$, but the data acquisition step of the spin-warp sequence described in Sec. 2.4 must be executed in a time comparable to T_2^* to minimize signal loss caused by spin dephasing. The tap water used

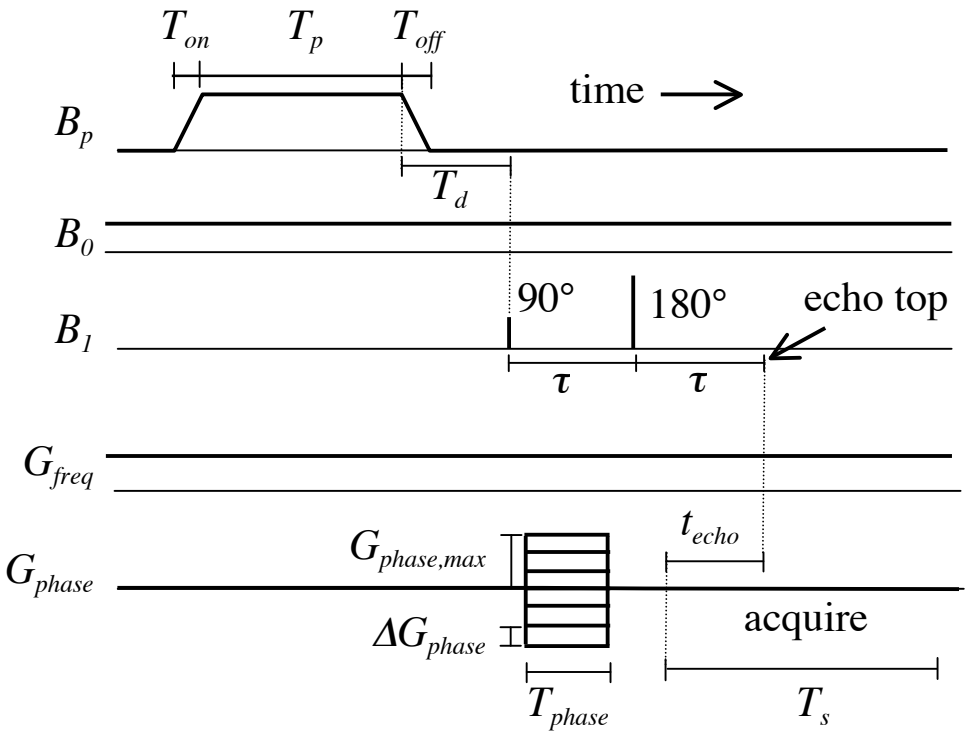

Figure 2.12: The detailed spin-warp sequence including time delays between events.

in these images had $T_1 = T_2 = 2.2$ s, but magnetic field inhomogeneity produced $T_2^* = 0.3$ s. With these relaxation times, the basic spin-echo sequence is inefficient because most of the sequence time is spent polarizing the spins. In order to lengthen the acquisition time, I added a sequence of 180° pulses to the end of the basic spin-warp sequence as shown in Fig. 2.13(A). These 180° pulses produce repeated echoes by repeatedly reversing the dephasing caused by field inhomogeneity. Figure 2.13(B) shows the effect of these echoes in *k*-space: the *k*-space trajectory begins at the origin, travels out along a diagonal line, and then traverses horizontal lines alternating between $k_z = -\gamma\tau G_z$ and $k_z = \gamma\tau G_z$. Echo tops occur when $k_y = 0$. Figure 2.13(C) shows eight echo tops acquired using the sequence of Fig. 2.13(A) in a gradient $G_y = 53$ μT/m. Although the spins dephase rapidly between echo tops under the action of both the applied gradient and the magnetic field inhomogeneity, the amplitude of each successive echo tops decays slowly with time constant $T_2 = 2.2$ s.

Since each step of this sequence measures both positive and negative values of k_z except for the $k_z = 0$ case, one must employ $(N_z + 1)/2$ steps to acquire N_z lines in *k*-space. In order to process the data from a sequence with $2M$ echoes, I first split the $(N_z + 1)/2$

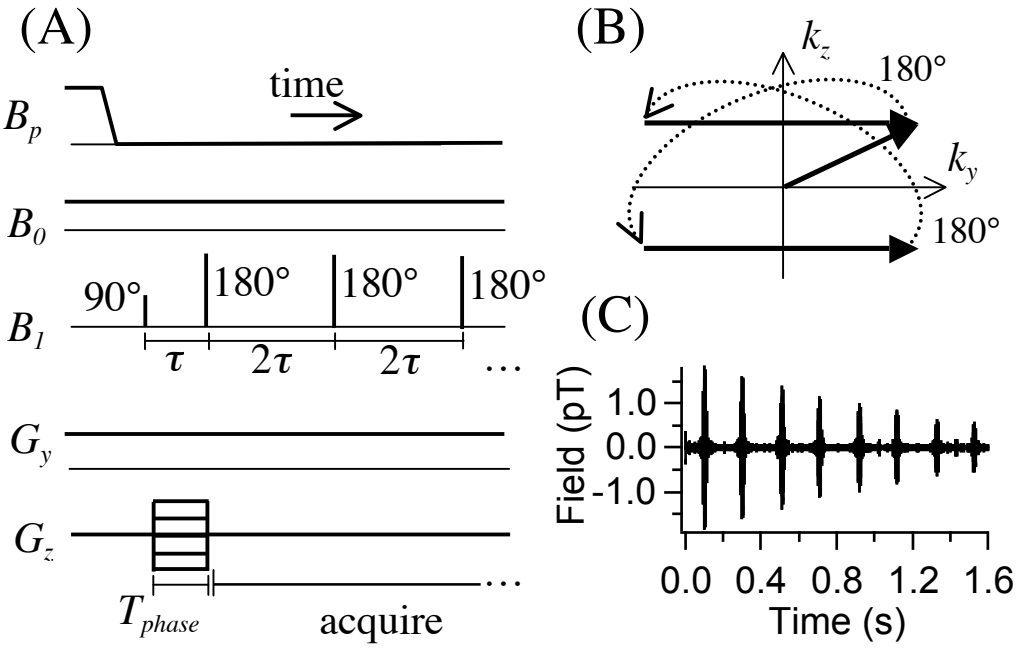

Figure 2.13: (A) Multiple echo Fourier transform imaging sequence. (B) *k*–space trajectory for this sequence. (C) Filtered magnetic field data showing eight echoes acquired using the sequence of (A) with $G_z = 0$.

acquisitions into individual echoes and process each of them as shown in Fig. 2.9 to obtain the demodulated time traces (Fig. 2.9(D) with the *x*-axis in time units). I estimate the echo top time for each of the 2*M* echoes as point at which the demodulated time trace of the $k_z = 0$ phase encoding step reaches its maximum magnitude. I then shift the demodulated time traces in time and phase to align the echo tops. The *M* odd-numbered echoes contain the $k_z < 0$ half of k-space, while the *M* even-numbered echoes contain the $k_z > 0$ half of k-space. Since T_2 relaxation reduces the amplitude of each successive echo top, the lowest noise estimate of $s(\mathbf{k})$ is obtained from a weighted sum of the echoes with the weighting function proportional to the amplitude of each echo. This weighted sum can be expressed as

$$s(\mathbf{k}) = \sum_{m=1}^{M} \frac{s_m(0)}{s_1(0)} s_m(\mathbf{k}), \tag{2.18}$$

where $s_m(\mathbf{k})$ is Fourier component with wavevector $\mathbf{k}$ acquired from the m^{th} odd or even echo as appropriate.

Figure 2.14 shows a $2M = 8$ echo image of the 13-column phantom shown in Fig. 2.3(A) filled with water. This image was produced using 32 $B_p = 200$ mT, $T_p = 1$ s polarizing pulses to obtain $N_z = 63$ *k*-space lines with frequency encoding gradient $G_y =$

75 μT/m and maximum phase encoding gradient $G_{z,max}$ = 79 μT/m; the total imaging time was 101 s. This image has higher SNR than the water image shown in Fig. 2.11 and has 1.5 x 1.3 mm resolution. Compared to the filtered backprojection image of the same phantom filled with oil shown in Fig. 2.3(B), Fig. 2.14 has substantially higher SNR, fewer artifacts, and higher resolution.

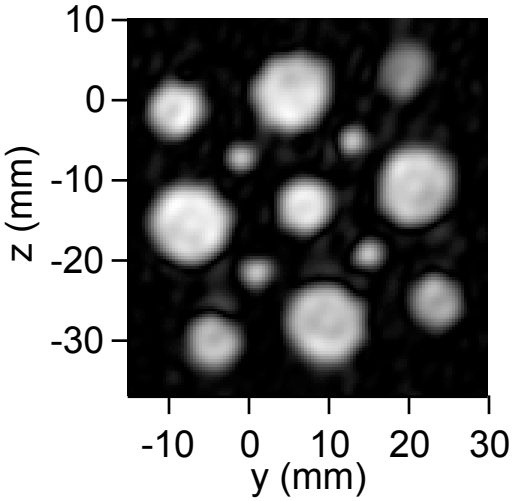

Figure 2.14: Eight-echo image of the 13-column phantom. The image uses 4x interpolation and sqrt(cos) filtering with k_c = 2200 m^{-1}. The top-right column was only half full.

2.5.2. Partial Fourier imaging

Multiple echo sequences enhance the SNR of images when $T_2 > T_2^*$. However, T_2 of most human tissue is much shorter than that of water. Table 2.1 shows approximate values of T_2 for various samples measured at B_0 = 132 μT. In Sec. 2.7.1, I demonstrate that the SNR of spin-echo MRI is proportional to the magnetization remaining at the echo top. Therefore sequences designed to image short-T_2 samples should be designed to reach the echo top as soon as possible while maintaining the desired resolution. From Eq. (2.13), the image resolution, sequence timing, and applied gradient strength are related by

Table 2.1: Measured T_2 values at 132 μT.

Sample	T_2 (ms)
Tap water	2200
Green pepper	80
Agarose gel (0.5% in water)	70
Mineral oil	60
Excised human prostate tissue	50
Fatty tissue in human arm	50
Muscle tissue in human arm	< 20

$$\Delta l_{freq} = \pi / k_{freq,max} = \pi / [\gamma (T_s - t_{echo}) G_{freq}] \tag{2.19}$$

in the frequency encoding direction and

$$\Delta l_{phase} = \pi / k_{phase,max} = \pi / (\gamma T_{phase} G_{phase,max}) \tag{2.20}$$

in the phase encoding direction, where Δl_{freq}, $k_{freq,max}$, Δl_{phase}, and $k_{phase,max}$ are the resolution and maximum reciprocal space value in the frequency- and phase-encoding directions, respectively, and $G_{phase,max}$ is the maximum applied phase encoding gradient. If data

acquisition begins immediately after the 180° pulse, then $t_{echo} = \tau$; if not, $t_{echo} < \tau$. So far, I have considered only pulse sequences in which $T_s = 2\tau$, yielding $\Delta l_{freq} = \pi/(\gamma\tau G_{freq})$. Such sequences acquire k-space points symmetrically between $-k_{freq,max}$ and $k_{freq,max}$. Equation (2.19) suggests that one could maintain high resolution in the frequency encoding direction while reducing τ to achieve high SNR of short-T_2 samples by choosing $t_{echo} \le \tau < T_s/2$. However this choice yields k-space points between $-\gamma t_{echo} G_{freq}$ and $\gamma(T_s - t_{echo})G_{freq}$, and the discrete inverse Fourier transform requires k-space points symmetric about the origin. The degree of asymmetry can be quantified as

$$\Xi = (T_s - 2t_{echo})/T_s, \tag{2.21}$$

where $\Xi = 0$ indicates symmetric data acquisition, while $\Xi = 1$ denotes data acquisition beginning at the echo top.

The solution to this problem relies upon the complex conjugate symmetry of k-space points. Because the spins are aligned along the x-axis after the 90° pulse, the initial magnetization M is a real quantity and

$$s(-\mathbf{k}) = C\int_V M(\mathbf{r})e^{i\mathbf{k}\cdot\mathbf{r}}d\mathbf{r} = \left(C\int_V M(\mathbf{r})e^{-i\mathbf{k}\cdot\mathbf{r}}d\mathbf{r}\right)^* = s^*(\mathbf{k}), \tag{2.22}$$

where C is the constant of proportionality in Eq. (2.7). Therefore, only half of k-space is required to perform the inverse Fourier transform. The simplest reconstruction algorithm for partial Fourier imaging simply discards the acquired data for $k_{freq} < 0$ and replaces them with values obtained from Eq. (2.22). However, this method discards good data and tends to produce image artifacts. Haacke *et al.* [2] describe an iterative reconstruction algorithm that uses all the acquired k-space data and produces much better results. For brevity, I omit the details of this algorithm.

Figure 2.15 shows a cross-sectional image of a human wrist acquired using 31 phase encoding steps with $\tau = 50$ ms, $T_{phase} = 35$ ms, $t_{echo} = 25$ ms, $G_{phase,max} = 80$ μT/m, and $G_{freq} = 60$ μT/m. The image is reconstructed using the iterative partial Fourier algorithm, 4x interpolation, and sqrt(cos) filtering with $k_c = 1250$ m^{-1}. Because the filter sets all k-space vectors beyond k_c to zero, the effective acquisition time is $t_{echo} + k_c\gamma/G_{freq} =$ 100 ms, and $\Xi = 0.5$. The image shows strong T_2-weighted contrast. The subcutaneous fat and fatty bone marrow of the radius and ulna have $T_2 \sim 50$ ms, so 11 averages of each phase encoding step yield a measurable signal at the echo top $2\tau = 100$ ms after the 90°

pulse. However, muscle has $T_2 < 20$ ms, so a vanishing signal from muscle remains at the echo top and muscle appears black in the image.

Because most of the initial magnetization in this sequence dephases before the echo top, image SNR could be substantially increased by further reducing τ and increasing Ξ. Two factors set a lower bound on τ. First, Eq. (2.20) indicates that the resolution scales inversely with $T_{phase}G_{phase,max}$, so for a given resolution, hardware limitations on gradient strength and image distortion caused by concomitant gradients (see Chapter 3) set a minimum value for T_{phase}. Second, if the flux-locked loop is activated too soon after switching either polarizing or gradient fields, magnetic fields generated by eddy currents induced by the switching will push the flux-locked loop beyond its dynamic range, thereby halting data acquisition. Michael Mößle and other members of the Clarke group have achieved substantial success in reducing these problems for later images. For example, the three-dimensional arm images presented in Sec. 2.6 have $\tau = 29$ ms, $T_{phase} = 17.5$ ms, and $\Xi = 0.65$.

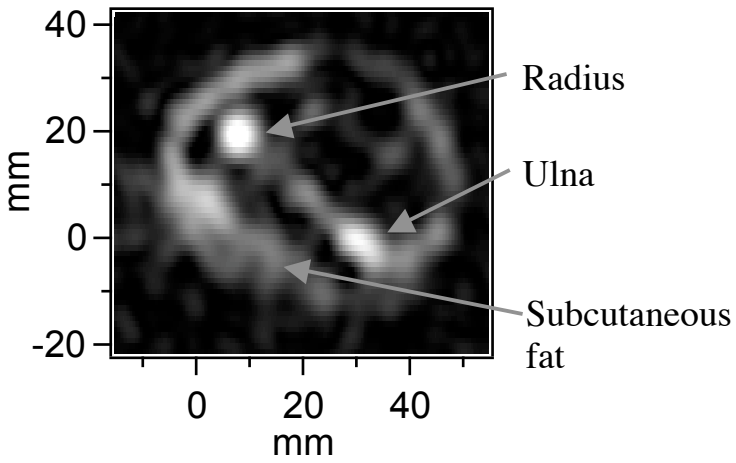

Figure 2.15: Cross-sectional image of a human wrist taken with $B_0 = 132$ μT, $T_p = 0.2$ s, and $B_p = 50$ mT. The total imaging time was ~200 s.

2.5.3. Interpolation of polar *k*-space points

New insight into projection-reconstruction imaging can be gained by applying the concepts of *k*-space to the projection-reconstruction sequence shown in Fig. 2.1(B). Figure 2.16(A) shows the *k*-space trajectory traced out by one step of this sequence when $G_y = G_z$. The *k*-space vector begins at the origin after the 90° pulse, travels along the diagonal line determined

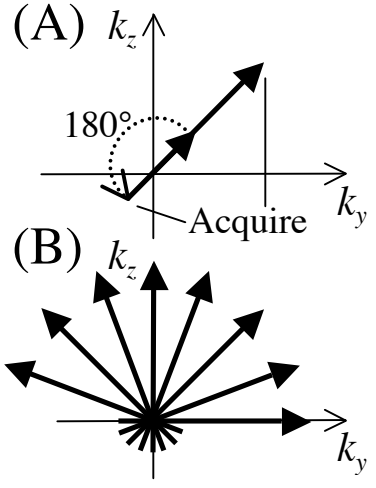

Figure 2.16: (A) *k*-space trajectory of a single projection-reconstruction step. (B) *k*-space data acquired from 8 such steps.

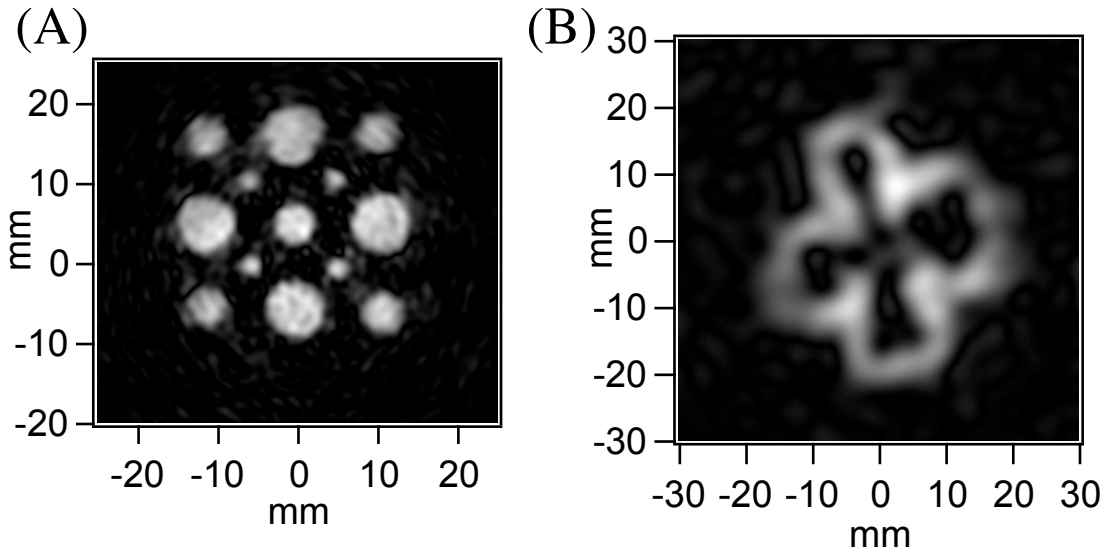

Figure 2.17: Fourier interpolation reconstruction of the data used to generate Fig. 2.3.

by the gradients, and is then inverted through the origin by the 180° pulse. Data is acquired as the *k*-space vector passes through the origin again and then retraces the same line. Heavily asymmetric data acquisition (as shown in the figure) is often used in projection-reconstruction imaging. Figure 2.16(B) shows the *k*-space data acquired from eight steps of this sequence.

The *k*-space diagram suggests an alternative to filtered backprojection reconstruction. All four quadrants of *k*-space can be filled by projection reconstruction steps using gradients rotated around a 180° angle by applying the methods of Sec. 2.5.2 to make each *k*-space trace symmetric about the origin. A rectangular grid of *k*-space values can then be formed by interpolating the polar *k*-space traces. The discrete inverse Fourier transform yields the reconstructed image. Figure 2.17 shows the results of Fourier interpolation applied to the same data sets used to reconstruct the images of Fig. 2.3. Because Fourier interpolation considers both the magnitude and phase of the acquired data whereas filtered backprojection uses only the magnitude data, Fourier interpolation images have higher SNR than their counterparts reconstructed with filtered backprojection. Fourier interpolation is also immune to some of the artifacts that plague filtered backprojection. For example, the brighter region around the columns in Fig. 2.3(B) is gone in Fig. 2.17(A). Because these images are reconstructed by discarding all $k < 0$ data and replacing it with $s^*(k)$, the resolution of images such as 2.17(B) produced from partially asymmetric pulse sequences is degraded compared to filtered

backprojection reconstruction. (Figure 2.17(A) was reconstructed from an almost completely asymmetric pulse sequence.) Using the iterative algorithm described in Sec. 2.5.2 to generate the missing *k*-space values would restore the missing resolution. However, because we now employ rectangular *k*-space methods almost exclusively, I have not added this feature to the reconstruction software.

Figure 2.17(A) has ~2-mm resolution, a SNR of 15, and took 420 s to acquire. In contrast, Fig. 2.14, the multiple-echo, spin-warp image of the same phantom filled with water instead of mineral oil, took only 100 s to acquire yet has 1.5 x 1.3 mm resolution and a SNR of 22. While some of this improvement was caused by the reduction in system noise caused by replacing the polarizing coil windings with Litz wire (Sec. 5.1.3), most of it can be attributed to improved pulse sequence design and the decision to image water instead of mineral oil. McDermott and co-workers filled their phantoms with mineral oil because it has substantially shorter T_1 than water and therefore requires shorter polarizing times. Without multiple echoes, they could only acquire data for $T_2 \sim T_2^*$, so they could not utilize the longer T_2 values of water. They therefore obtained higher image SNR with mineral oil phantoms. Using multiple echoes, we can now obtain better images of water than of mineral oil.

Although one could add multiple echoes to the projection-reconstruction sequence, polar *k*-space coverage is inherently less efficient than rectangular *k*-space coverage. To acquire a field of view L without aliasing, *k*-space points must be spaced by no more than $\Delta k = 2\pi/L$. Polar sampling of *k*-space up to k_{max} through a 180° angle requires $\pi k_{max}/\Delta k$ acquisitions to achieve the necessary spacing, while rectangular sampling requires only $(\pi k_{max}/\Delta k) + 1$ acquisitions yet covers a fraction $4/\pi$ greater *k*-space area. Thus it is better to sample *k*-space in a rectangular fashion whenever possible. The primary advantage of projection-reconstruction imaging is that it does not require ever-higher phase encoding gradients to achieve a given resolution as the echo time is decreased. Therefore, projection-reconstruction is able to take higher resolution images of samples with very short T_2 than spin-warp imaging.

2.6. Three-dimensional Fourier imaging

Fourier imaging can be easily extended to three dimensions by adding a second phase encoding gradient to the sequence shown in Fig. 2.12 that is perpendicular to both

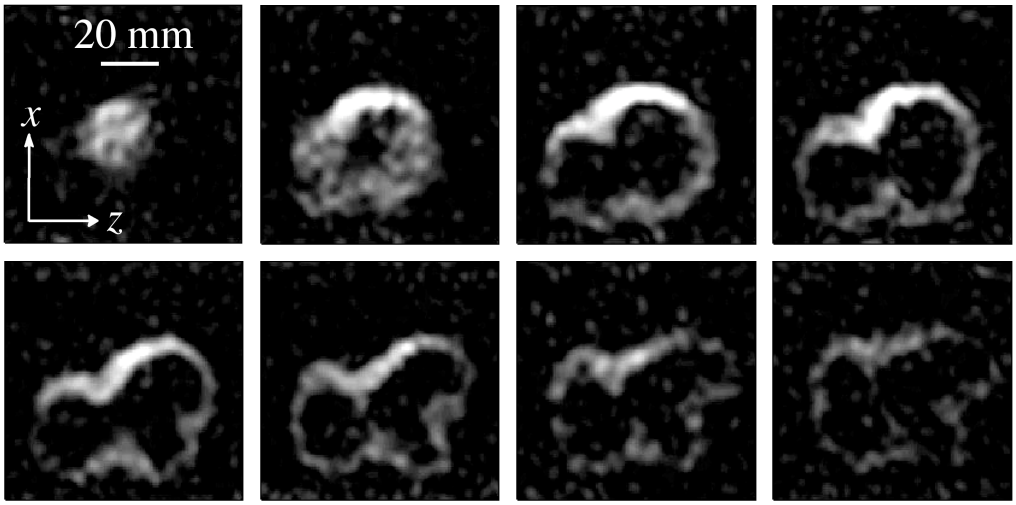

Figure 2.18: Eight 5-mm cross-sections of an image of a green pepper taken with B_0 = 132 μT, B_p = 60 mT, T_p = 0.5 s, τ = 41 ms, T_{phase} = 35 ms, $G_x = G_{freq}$ = 66 μT, N_y = 13, $G_{y,max}$ = 58 μT/m, N_z = 31, and $G_{z,max}$ = 120 μT/m. Each phase encoding step was measured only once (no averaging) for a total acquisition time of 5 minutes. A sqrt(cos) filter is applied with k_c = 1250 m^{-1}.

the frequency-encoding gradient and the first phase-encoding gradient. The three gradients are applied simultaneously during the time T_{phase} to reach the *k*-space vector $\gamma T_{phase}\left(G_x\hat{\mathbf{x}} + G_y\hat{\mathbf{y}} + G_z\hat{\mathbf{z}}\right)$. The two phase-encoding gradients (now taken to be G_y and G_z) are then turned off. After the 180° pulse, data is acquired as the *k*-space vector follows the line

$$\mathbf{k}(t) = \gamma\left[G_x\left(t - t_{echo}\right)\hat{\mathbf{x}} - T_{phase}G_y\hat{\mathbf{y}} - T_{phase}G_z\hat{\mathbf{z}}\right]. \tag{2.23}$$

The sequence requires a total of N_yN_z phase-encoding steps in which G_y ranges from $-N_y\Delta G_y/2$ to $(N_y - 1)\Delta G_y/2$ in steps of ΔG_y and G_z ranges from $-N_z\Delta G_z/2$ to $(N_z - 1)\Delta G_z/2$ in steps of ΔG_z. The FOV and resolution in the phase encoding directions are given by Eqs. (2.11) and (2.13), respectively, and need not be the same in both directions.

Figure 2.18 shows series of eight cross-sections of a three-dimensional image of a bell pepper. The images have an in-plane resolution of Δl_x = 3 mm by Δl_z = 3 mm, and each cross-section is Δl_y = 5 mm thick. Since the top (high *x*) regions of the image are closer to the gradiometer pickup loop, they couple more flux to the SQUID and therefore appear brighter than lower regions.

Figure 2.19(A) shows three 26-mm thick cross-sections of a three-dimensional microtesla MR image of a human wrist and forearm. The in-plane resolution is

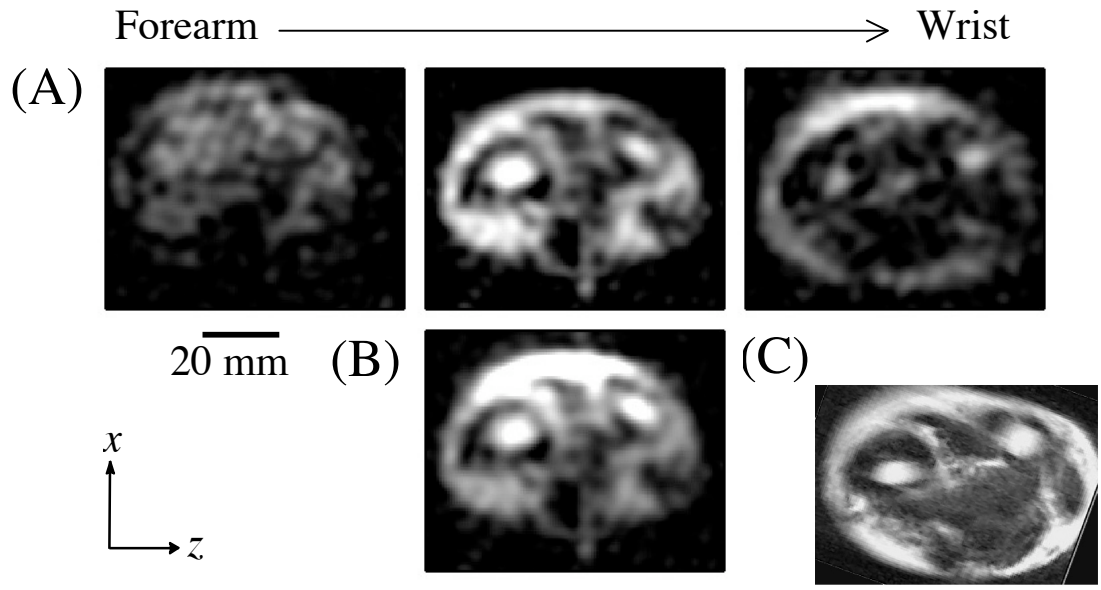

Figure 2.19: (A) Three 26-mm cross-sections of an image of a human forearm and wrist taken with B_0 = 132 μT, B_p = 50 mT, T_p = 0.2 s, τ = 29 ms, T_{phase} = 17.5 ms, $G_x = G_{freq}$ = 66 μT, N_y = 5, $G_{y,max}$ = 22 μT/m, N_z = 31, and $G_{z,max}$ = 240 μT/m. Each phase encoding step is averaged five times for a total acquisition time of 6.5 minutes. A sqrt(cos) filter is applied with k_c = 1400 m^{-1}. (B) The center image of (A) with image intensity corrected for the gradiometer response. (C) An image of the same forearm in the UCB Brain Imaging Center 4 T MRI system courtesy of Ben Inglis.

3 mm x 3 mm. As in Fig. 2.15, T_2-weighting causes muscle to appear black and subcutaneous fat and fatty bone marrow to appear white. These images exhibit the same intensity variation along the *x*-axis as is seen in Fig. 2.18. Figure 2.19(B) shows the second image of Fig. 2.19(A) corrected for this intensity variation by dividing the image intensity by the calculated gradiometer response. Figure 2.19(C) shows a T_2-weighted image of the forearm of the same subject taken with a 4 T conventional MRI system. The high-field MR image shows similar features with similar contrast, but the position of anatomical features differs between the two images because the forearm had to be placed in a different position to fit into the high-field MRI pickup coil (which was designed for brain imaging).

2.7. Signal-to-noise ratio of a voxel

2.7.1. Derivation of voxel SNR

I have now introduced all the tools necessary to derive the SNR of a voxel in a three-dimensional MRI image. The derivation is somewhat involved, but the end result is

intuitively clear. I assume a spin-warp sequence designed to give a resolution Δl_x x Δl_y x Δl_z in a field of view L_x x L_y x L_z, where $L_x = N_x \Delta l_x$, etc., and N_x, N_y, and N_z are even integers. For definiteness, I assume frequency encoding along the x-direction. Since spatial translation by a vector $\mathbf{a}$ is equivalent to multiplying k-space by $e^{-i\mathbf{k}\cdot\mathbf{a}}$ and changes neither signal nor noise, I calculate the SNR of the voxel centered at the origin.

The first step is to calculate the k-space corresponding to this voxel when it is filled with spins of magnetization M. According to a reciprocity principle of electromagnetism, the flux through a loop of wire from a dipole moment $\mathbf{m}$ is

$$\Phi(t) = \left[\mu_0 \boldsymbol{\beta}(\mathbf{r})/4\pi\right] \cdot \mathbf{m}(\mathbf{r},t), \tag{2.24}$$

where $\mu_0 \boldsymbol{\beta}(\mathbf{r})/4\pi$ is the field produced per unit current flowing through the loop at the location of the dipole. We can apply this principle to calculate the coupling of the precessing spins in a voxel to the pickup loop. In this case, $\mathbf{m}(\mathbf{r},t)$ rotates in the horizontal plane perpendicular to B_0, so the amplitude of the flux coupled into the pickup loop depends on $\beta_\perp$, the component of $\boldsymbol{\beta}$ perpendicular to B_0. Integrating Eq. (2.24) over the central voxel volume and dividing by the pickup coil area A_p yields the detected magnetic field

$$B_{det}(t) = \frac{\mu_0}{4\pi A_p} \int_{V_{voxel}} \beta_\perp(\mathbf{r}) M(\mathbf{r},t) d\mathbf{r}. \tag{2.25}$$

For a uniformly magnetized voxel that is small compared to the detector dimensions, $\beta_\perp$ and M do not depend on $\mathbf{r}$. The detected magnetic field can be expressed in complex k-space notation as

$$s(\mathbf{k}) = \frac{\mu_0 \beta_\perp M}{4\pi A_p} \int_{V_{voxel}} e^{-i\mathbf{k}\cdot\mathbf{r}} d\mathbf{r} = \frac{\mu_0 \beta_\perp M}{4\pi A_p} \int_{-\Delta l_x/2}^{\Delta l_x/2} e^{-ik_x x} dx \int_{-\Delta l_y/2}^{\Delta l_y/2} e^{-ik_y y} dy \int_{-\Delta l_z/2}^{\Delta l_z/2} e^{-ik_z z} dz, \tag{2.26}$$

where I have assumed negligible T_2^* decay. Since

$$\int_{-\Delta l_x/2}^{\Delta l_x/2} e^{-ik_x x} dx = \frac{2}{k_x} \sin\left(\frac{k_x \Delta l_x}{2}\right), \tag{2.27}$$

$$s(\mathbf{k}) = \frac{\mu_0 \beta_\perp M}{4\pi A_p} \frac{8}{k_x k_y k_z} \sin\left(\frac{k_x \Delta l_x}{2}\right) \sin\left(\frac{k_y \Delta l_y}{2}\right) \sin\left(\frac{k_z \Delta l_z}{2}\right). \tag{2.28}$$

The next step is to calculate the magnetic field signal corresponding to the voxel when reconstructed using the inverse discrete Fourier transform:

$$B_{voxel}(\mathbf{r}) = \sum_{p=-N_x/2}^{N_x/2-1} \sum_{q=-N_y/2}^{N_y/2-1} \sum_{r=-N_z/2}^{N_z/2-1} s\left(p\Delta k_x \hat{\mathbf{x}} + q\Delta k_y \hat{\mathbf{y}} + r\Delta k_z \hat{\mathbf{z}}\right) e^{i\left(p\Delta k_x x + q\Delta k_y y + r\Delta k_z z\right)}, \quad (2.29)$$

where $\Delta k_x = \pi/L_x$, etc. Since I have chosen the central voxel, $x = y = z = 0$, and the exponential in Eq. (2.29) becomes unity. The reconstructed signal is therefore

$$B_{signal} = \frac{\mu_0 \beta_\perp M}{4\pi A_p} \sum_{p,q,r} \frac{8}{p\Delta k_x q\Delta k_y r\Delta k_z} \sin\left(\frac{p\Delta k_x \Delta l_x}{2}\right) \sin\left(\frac{q\Delta k_y \Delta l_y}{2}\right) \sin\left(\frac{r\Delta k_z \Delta l_z}{2}\right), \quad (2.30)$$

where I have omitted the summation ranges for brevity. This equation contains the product of three sums of the form

$$\sum_{p=-N_x/2}^{N_x/2-1} \frac{2}{p\Delta k_x} \sin\left(\frac{p\Delta k_x \Delta l_x}{2}\right) = \frac{2N_x \Delta l_x}{\pi} \sum_{p=-N_x/2}^{N_x/2-1} \frac{1}{p} \sin\left(\frac{\pi p}{2N_x}\right) \quad (2.31)$$

where I have substituted $\Delta k_x = \pi/L_x = \pi/N_x \Delta l_x$. In the limit of large N_x, the sum over p in Eq. (2.31) goes to 1.518; it reaches 99.9% of this value for $N_x = 8$. Approximating the value of this sum by $\pi/2$ introduces a 3.5% error, but greatly simplifies the solution. Using this approximation, Eq. (2.30) becomes

$$B_{signal} = \frac{\mu_0 \beta_\perp}{4\pi A_p} M \Delta l_x \Delta l_y \Delta l_z N_x N_y N_z = \frac{\mu_0 \beta_\perp}{4\pi A_p} M V_{voxel} N_x N_y N_z, \quad (2.32)$$

where V_{voxel} is the voxel volume.

Now that the voxel signal has been established, I turn to the voxel noise. The uncertainty of a single point in k-space can be calculated by applying the Demod operation described by Eq. (2.15) to a source of magnetic field noise $B_{noise}(t)$ with spectral density S_B. The real component of this point has root-mean-square (RMS) noise

$$\delta \mathrm{Re}\left[s(\mathbf{k}(t))\right] = \sqrt{\left\langle \mathrm{Re}^2\left\{\mathrm{Demod}\left[B_{noise}(t)\right]\right\}\right\rangle} = \sqrt{\left\langle \left\{2\,\mathrm{Lowpass}\left[B_{noise}(t)\cos(\omega_0 t)\right]\right\}^2\right\rangle}. \quad (2.33)$$

Since $B_{noise}(t)$ is not time-correlated with $\cos(\omega_0 t)$, the average square of their product is the product of their average squares, and Eq. (2.33) becomes

$$\delta \mathrm{Re}\left[s(\mathbf{k})\right] = S_B^{1/2}\sqrt{2BW} = S_B^{1/2}\sqrt{\gamma G_x L_x/2\pi} = S_B^{1/2}\sqrt{\gamma G_x/\Delta k_x} = S_B^{1/2}\sqrt{N_x/T_s}, \quad (2.34)$$

where $BW = \gamma G_x L_x/4\pi$ is the low-pass filter bandwidth in frequency units, and I have substituted $L_x = 2\pi/\Delta k_x$ and then $\Delta k_x = \gamma G_x T_s/N_x$, where T_s is the data acquisition time of each frequency-encoding step. Since the imaginary component of $s(\mathbf{k})$ has the same

uncertainty as the real component, the uncertainty in the magnitude of each *k*-space point is

$$\delta\left|s(\mathbf{k})\right| = S_B^{1/2}\sqrt{2N_x/T_s}\,. \tag{2.35}$$

The uncertainty in the complex magnitude of the voxel can be calculated by propagating this uncertainty through the sum in Eq. (2.29). Since the individual *k*-space uncertainties are uncorrelated and have random phase, all voxels have identical magnitude uncertainty

$$\delta\left|B_{voxel}\right| = S_B^{1/2}N_x\sqrt{N_yN_z/T_s}\,. \tag{2.36}$$

Because MR images usually display the complex magnitude of each voxel, $\delta\left|B_{voxel}\right|$ determines the noise in the displayed image. The SNR of the central voxel is therefore

$$SNR_{voxel} = B_{signal}\big/\delta\left|B_{voxel}\right| = \frac{\mu_0\beta_\perp}{4\pi A_p S_B^{1/2}}\,MV_{voxel}\sqrt{N_yN_zT_s/2}\,. \tag{2.37}$$

This equation assumes that the spin magnetization does not decay during the measurement. This assumption can be relaxed by noting that evaluating $s(\mathbf{k} = 0)$ for an arbitrary precessing spin density $M(\mathbf{r},t)$ yields

$$s(\mathbf{k}=0) = \frac{\mu_0\beta_\perp}{4\pi A_p}\int_{V_{FOV}} M(\mathbf{r},t_{echo})d\mathbf{r}\,, \tag{2.38}$$

where V_{FOV} represents the image field of view and t_{echo} is the time when $\mathbf{k} = 0$. Since the average image intensity scales as $s(\mathbf{k} = 0)$, the image SNR, and by extension, the voxel SNR also scale as $s(\mathbf{k} = 0)$. This suggests that M in Eq. (2.37) should be replaced by M_{echo}, the magnetization at the echo top. For the sequence timing shown in Fig. 2.12,

$$M_{echo} = M_0\left\{1-\exp\left[-T_p/T_1(B_p)\right]\right\}\exp\left[-T_d/T_1(B_0)\right]\exp\left(-2\tau/T_2\right), \tag{2.39}$$

where M_0 is given by Eq. (1.7) evaluated at the field B_p and $T_1(B_p)$ and $T_1(B_0)$ are the longitudinal relaxation times at magnetic fields B_p and B_0, respectively. Allowing for N_{av} averages of each acquisition step, I obtain

$$SNR_{voxel} = \frac{\mu_0\beta_\perp}{4\pi A_p S_B^{1/2}}\,M_{echo}V_{voxel}\sqrt{N_{av}N_yN_zT_s/2}\,. \tag{2.40}$$

Comparing Eqs. (2.25) and (2.40) shows that SNR_{voxel} is the magnetic field detected at the pickup loop from the voxel divided by the magnetic field noise and multiplied by the square root of the total sequence acquisition time. Displaying the real amplitude of each

voxel instead of its magnitude would eliminate the factor of $1/\sqrt{2}$ but requires that all voxels have the same phase.

2.7.2. SNR, resolution, and field-of-view

A careful examination of Eq. (2.40) reveals much about MRI sequence design. First, since SNR_{voxel} scales linearly with V_{voxel}, higher resolution (smaller voxel size) always comes at the expense of reduced SNR. Using Eqs. (2.19) and (2.20) to express V_{voxel} in terms of sequence parameters, I obtain

$$V_{voxel} = \Delta l_x \Delta l_y \Delta l_z = \frac{\pi}{\gamma(T_s - t_{echo})G_x} \frac{\pi}{\gamma T_{phase} N_y \Delta G_y} \frac{\pi}{\gamma T_{phase} N_z \Delta G_z}. \quad (2.41)$$

In order to improve the resolution in the frequency-encoding direction, one can either increase G_x or T_s. At first glance, one should always increase T_s, since SNR_{voxel} scales as G_x^{-1} but only as $T_s^{-1/2}$. However, although the image voxel size will keep decreasing with increasing T_s, Eq. (1.13) shows that T_2^* decay limits the resolution to $2/\gamma G_x T_2^*$. If $T_s - t_{echo}$ becomes larger than $\pi T_2^*/2$, T_2^* decay will reduce the amplitude of the high-k_x components of reciprocal space, leading to correlations between the voxels in the x-direction and producing an effective resolution $2/\gamma G_x T_2^*$. In order to improve the resolution in the phase-encoding direction y, one can either increase T_{phase} or ΔG_y, thereby reducing the FOV or increase N_y, thereby increasing the imaging time. In the first two cases, SNR scales as Δl_y; in the third case, SNR scales as $\Delta l_y^{1/2}$ and the imaging time scales as Δl_y^{-1}.

While increasing the image resolution is costly in terms of SNR, increasing the image FOV is relatively cheap. Since $\Delta k_x = G_x T_{samp}$, the frequency-encoding FOV can be increased by simply decreasing T_{samp} and increasing N_x accordingly. Equation (2.40) shows that there is no SNR penalty for this operation; therefore until one reaches the detector bandwidth limit, frequency-encoding FOV is free. The FOV in the phase-encoding direction y is $L_y = N_y \Delta l_y$. If one increases N_y while reducing ΔG_y to maintain constant Δl_y, L_y increases as N_y and SNR_{voxel} increases as $N_y^{1/2}$. If $N_{av} > 1$, one can increase N_y and reduce N_{av} accordingly to maintain the same imaging time and SNR while increasing L_y.

2.7.3. Optimal polarizing time

Because SNR can always be increased through additional signal averaging, the most useful metric to compare the SNR of different pulse sequences is given by the SNR efficiency

$$\Upsilon = \frac{SNR_{voxel}}{\sqrt{T_T}} = \frac{SNR_{voxel}}{\sqrt{N_{av}N_yN_zT_R}}, \tag{2.42}$$

where T_T is the total sequence running time and T_R is the repetition time of each sequence step. Using the sequence timing described in Fig. 2.12,

$$T_R = T_{on} + T_p + T_d + 2\tau + T_s - t_{echo}, \tag{2.43}$$

and the SNR efficiency of three-dimensional spin-warp Fourier imaging is

$$\Upsilon = \frac{\mu_0\beta_\perp}{4\pi A_p S_B^{1/2}} M_{echo} V_{voxel} \sqrt{\frac{T_s}{2\left(T_{ramp} + T_p + T_d + 2\tau + T_s - t_{echo}\right)}}. \tag{2.44}$$

Since optimal sequence design requires $T_p \sim T_1(B_p)$ (to achieve adequate polarization) and $T_s \sim T_2^*$ (to prevent loss of resolution), and relaxation dynamics ensure $T_1(B_p) \geq T_1(B_0) \geq T_2$, T_p is usually the longest step in the sequence. Substituting Eq. (2.39) into Eq. (2.44) shows that Υ depends on B_p as

$$\Upsilon \propto \left\{1 - \exp\left[-T_p / T_1(B_p)\right]\right\} \Big/ \sqrt{T_p + T_{other}}, \tag{2.45}$$

where $T_{other} = T_{on} + T_d + 2\tau + T_s - t_{echo}$. The maximum of Eq. (2.45) with respect to T_p cannot be expressed analytically, but Fig. 2.20 plots the optimal polarizing time $T_{p,opt}$ as a function of $T_1(B_p)$ and T_{other}.

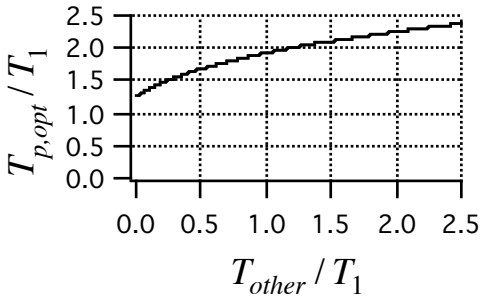

Figure 2.20: Optimal polarizing time versus T_{other}.

2.7.4. Voxel SNR of an acquired image

To ascertain the validity of Eq. (2.40), I evaluate SNR_{voxel} for the water phantom image shown in Fig. 2.14, consisting of 3-mm, 6-mm, and 9-mm diameter columns; each column is 48 mm deep. For a spin a distance h below a pickup coil of radius a = 32.5 mm,

$$\beta_\perp = 2\pi a^2 \Big/ \left(a^2 + h^2\right)^{3/2}. \tag{2.46}$$

The phantom was placed flush against the bottom of the cryostat such that the pickup coil was 25 mm above the top of the phantom. Integrating Eq. (2.46) over the length of the

sample yields the average value $\beta_\perp = 40$ m^{-1}. The top of the Litz wire polarizing coil described in Sec. 5.1.4.2 was also placed flush with the bottom of the cryostat. In this configuration, it provided an average field of $B_p = 0.21$ T over the sample. This field produces an equilibrium magnetization of

$$M_0 = \rho\gamma^2\hbar^2 B_p / 4k_B T_S = 6.8 \times 10^{-4} \text{ A m}^{-1}, \tag{2.47}$$

where $\rho = 6.69 \times 10^{28}$ protons/m^3 is the spin density of water and $T_S = 298$ K is the sample temperature. The sequence timing parameters are $T_p = 1$ s, $T_d = 46$ ms, and $\tau = 137$ ms; the latter echo tops are separated by $2\tau' = 226$ ms. Evaluating Eq. (2.39) for the m^{th} echo using the field-independent relaxation times $T_1 = T_2 = 2.2$ s, I obtain

$$M_{echo} = \left(1 - e^{-T_p/T_1}\right) e^{-T_d/T_1} e^{-2\tau/T_2} \left(e^{-2\tau'/T_2}\right)^{m-1} M_0 = 0.32(0.90)^{m-1} M_0. \tag{2.48}$$

I calculate $S_B^{1/2} = 4.6$ fT Hz$^{-1/2}$ by computing the RMS field amplitude of the measured data in the two 100-Hz bands on either side of the frequencies used for imaging. This noise was substantially above the 1.7 fT Hz$^{-1/2}$ SQUID noise and came primarily from external sources. The remaining parameters required to evaluate Eq. (2.40) are $A_p = \pi a^2 = 3.3 \times 10^{-3}$ m^2, $V_{voxel} = 1.5$ mm x 1.3 mm x 48 mm $= 9.4 \times 10^{-8}$ m^3, $N_{av} = 1$, $N_y = 63$, $N_z = 1$, and $T_s = 205$ ms. [I have set the frequency-encoding direction to x to match Eq. (2.40)].

I first calculate the SNR of an image generated from only the first two echoes. In this case, half of k-space is filled from the first echo and half from the second echo yielding an average echo top magnetization of $M_{echo} = 0.30M_0$ and $SNR_{voxel} = 12.7$. I reconstructed an image from the first two echoes and measured a voxel SNR of 14.4, 13% higher than predicted.

Examining Eq. (2.48) reveals that the SNR of images calculated from latter echo pairs decline by $(0.90)^2$ for each successive pair. If k-space values are combined using the weighting algorithm of Eq. (2.18), the SNR of images reconstructed from multiple echo pairs adds in quadrature. The calculated SNR of the eight-echo image shown in Fig. 2.14 is 19.7; the actual image has a SNR of 21.6, 10% higher than predicted. The sqrt(cos) filter decreases image noise at the expense of smoothing the sharpest features of the image; this effect could explain why the measured SNR is somewhat higher than predicted. Alternately, the differences are small enough to be explained by the uncertainties in the values used to calculate SNR_{voxel}. In any case, the close agreement

between measured and calculated SNR confirms Eq. (2.40) and demonstrates that one can calculate the SNR of a SQUID-detected MRI system from the NMR properties of the sample, system geometry, magnetic field noise, polarizing field strength, and pulse sequence.

2.7.5. SNR of three-dimensional Fourier imaging versus slice selection

Both three-dimensional Fourier imaging and slice selection followed by two-dimensional Fourier imaging can be used to acquire three-dimensional MR images. Section 2.7.1 computes the SNR of three-dimensional Fourier imaging. How does the SNR of slice-selected imaging compare?

For slice-selection along the z-direction, the narrow-bandwidth 90° pulse and the simultaneously applied G_z gradient initiate precession of spins only in a slice of thickness Δl_z. A total of $N_y = L_y/\Delta l_y$ phase encoding steps result in a two-dimensional image. The SNR of a voxel in this image can be calculated from Eq. (2.40) with $N_z = 1$ and $V_{voxel} = \Delta l_x \Delta l_y \Delta l_z$. One must acquire a total of N_z such two-dimensional images in order to form the entire three-dimensional image. Since three-dimensional Fourier imaging and slice-selected imaging both take a total time $T_T = N_y N_z T_R$ to acquire a three-dimensional image, the ratio of their SNR efficiencies is

$$\Upsilon_{3D} / \Upsilon_{SS} = \sqrt{N_z} \,. \tag{2.49}$$

Three-dimensional imaging produces substantially higher SNR because it acquires signal from the entire sample during each step, whereas slice measures only a minority of the polarized spins during each step. In either case, one must wait until the next polarizing pulse to measure again. In contrast, conventional MRI polarizes the spins in the static field B_0 and can rapidly measure successive slices of spins because each slice has repolarized during the time elapsed since it was last measured.

Although prepolarized slice selective imaging is inherently inefficient, spatially-selective excitation pulses could be used to eliminate the signal originating from unwanted regions of the sample. One could then reduce the FOV in the phase-encoding directions, thereby reducing the minimum required imaging time to obtain a given resolution.

2.8. Image reconstruction from multiple detectors

Some potential applications of SQUID-detected low-field MRI would employ SQUID arrays presently used to detect biomagnetic signals as MRI detectors. Because these SQUID arrays can contain dozens to hundreds of SQUIDs, understanding image reconstruction from multiple detectors is essential to evaluating the feasibility of these techniques.

2.8.1. Weighted image superposition algorithm

Many methods of image reconstruction from N_d detectors begin by reconstructing one image from each detector. Since the position of objects in an MRI image depends on the frequency and phase of its spins and not on the location of the detector, the objects will appear in the same position in each of the N_d images, assuming the FOV is large enough to encompass the entire sample. Simply summing the N_d separate images would produce an approximation of the sample, but the resulting image would be shaded by the detector response. If the geometrical response factor for the n^{th} detector at a voxel located at point $\mathbf{r}$ is $\beta_{\perp,n}(\mathbf{r})$, and the reconstructed magnetic field from the n^{th} detector originating from this voxel is $B_{voxel,n}(\mathbf{r})$, the best estimate of the voxel magnetiztion at $\mathbf{r}$ from this detector can be obtained by solving Eq. (2.32) for M to obtain

$$M_n(\mathbf{r}) = \frac{4\pi A_{p,n}}{\mu_0 \beta_{\perp,n}(\mathbf{r}) V_{voxel} N_x N_y N_z} B_{voxel,n}(\mathbf{r}), \tag{2.50}$$

where $A_{p,n}$ is the pickup loop area of the n^{th} detector. The uncertainty in $M_n(\mathbf{r})$ is proportional to $A_{p,n} S_{B,n}^{1/2} / \beta_{\perp,n}(\mathbf{r})$, where $S_{B,n}^{1/2}$ is the magnetic field noise of the n^{th} detector. Assuming uncorrelated detector noise, the best estimate of the voxel magnetization can be obtained from a weighted sum of $M_n(\mathbf{r})$, with the contribution of each detector weighted by the inverse square of its uncertainty:

$$M(\mathbf{r}) = \left(\sum_{n=1}^{N_d} \frac{\beta_{\perp,n}^2(\mathbf{r}) M_n(\mathbf{r})}{A_{p,n}^2 S_{B,n}} \right) \Bigg/ \left(\sum_{n=1}^{N_d} \frac{\beta_{\perp,n}^2(\mathbf{r})}{A_{p,n}^2 S_{B,n}} \right) \propto \left(\sum_{n=1}^{N_d} \frac{\beta_{\perp,n}(\mathbf{r}) B_{voxel,n}(\mathbf{r})}{A_{p,n}^2 S_{B,n}} \right) \Bigg/ \left(\sum_{n=1}^{N_d} \frac{\beta_{\perp,n}^2(\mathbf{r})}{A_{p,n}^2 S_{B,n}} \right). \tag{2.51}$$

The uncertainty in $M(\mathbf{r})$ scales as

$$\delta M(\mathbf{r}) \propto \sqrt{\sum_{n=1}^{N_d} \frac{A_{p,n}^2 S_{B,n}}{\beta_{\perp,n}^2(\mathbf{r})}}. \tag{2.52}$$

Comparing this expression for $N_d = 1$ with Eq. (2.40) shows that the voxel SNR of MR images acquired with multiple detectors is

$$SNR_{voxel}(\mathbf{r}) = \frac{\mu_0}{4\pi}\sqrt{\sum_{n=1}^{N_d}\frac{\beta_{\perp,n}^2(\mathbf{r})}{A_{p,n}^2 S_{B,n}}}M_{echo}(\mathbf{r})V_{voxel}\sqrt{N_{av}N_y N_z T_s/2}\,, \tag{2.53}$$

where I have explicitly indicated the dependence of M_{echo} on $\mathbf{r}$.

2.8.2. Application of weighted superposition

The Clarke group MRI system has only one gradiometer, in part because simulations show that replacing the single gradiometer with multiple co-planar gradiometers would not substantially increase the SNR of samples within our imaging region. However, adding additional gradiometers of the same size could be used to image larger samples. Because the effects of concomitant gradients scale with the square of the sample dimensions, I wanted to measure a large phantom to demonstrate the concomitant gradient correction algorithm described in Chapter 3. Rather than building a larger cryostat to accommodate nine gradiometers, I took nine images of the phantom using the same pulse sequence but moving the cryostat between each image. The image reconstruction procedure is exactly the same as if I had acquired data from nine gradiometers simultaneously.

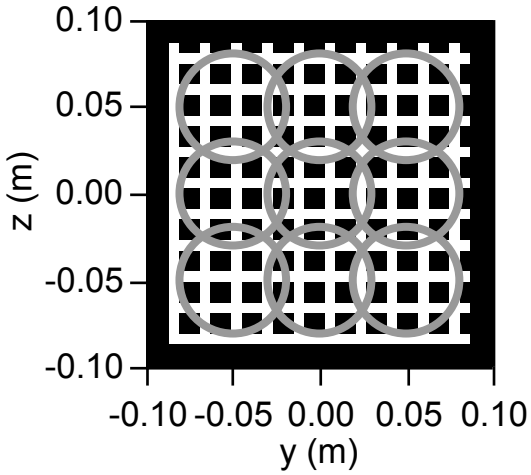

Figure 2.21: The nine positions of the gradiometer pickup loop above the water grid phantom.

Figure 2.21 shows a schematic of the 10 x 10 grid filled with water used to demonstrate concomitant gradient correction in Chapter 3. The nine gray circles represent the different positions of the gradiometer pickup loop above the sample. Figure 2.22(A) shows the nine images reconstructed with the detector in each of these positions. Figure 2.22(B) shows the nine images combined using weighted superposition. Because the same detector is used to acquire each image, $S_{B,n}$ and $A_{p,n}$ drop out of Eq. (2.51). However, because none of the detectors is sensitive to spins near the edge of the image, the denominator in Eq. (2.51) becomes small in this region, thereby emphasizing the noise in the image. To reduce this effect, I generate Fig. 2.22(B) from

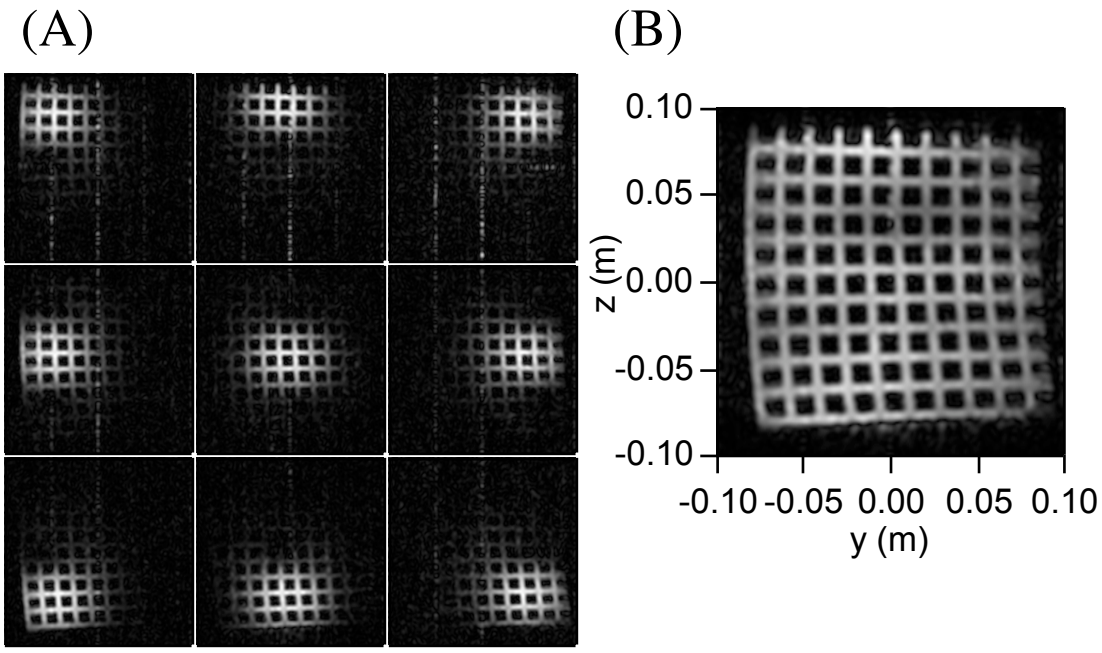

Figure 2.22: Images of the water grid phantom shown in Fig. 2.21. (A) The individual images measured with the gradiometer pickup coil at each of the locations shown in Fig. 2.21. Frequency encoding is performed along *y* and phase encoding along *z*. (B) The image generated from the weighted superposition of the images in (A).

$$B_{voxel}(\mathbf{r}) = \left(\sum_{n=1}^{N_d} \beta_{\perp,n}(\mathbf{r}) B_{voxel,n}(\mathbf{r})\right) \Bigg/ \max\left(\sum_{n=1}^{N_d} \beta_{\perp,n}^2(\mathbf{r}), \frac{\beta_{\perp}^2(\mathbf{r}_0)}{C_M}\right), \tag{2.54}$$

where $\beta_{\perp}^2(\mathbf{r}_0)$ is the geometrical response factor at a point on the sample in centered on the gradiometer pickup loop, and $C_M = 2$ is the maximum correction factor allowed in the image. The distortion in Fig. 2.22(B) comes from a combination of inhomogeneity of the background field and the effects of concomitant gradients; concomitant gradients also cause the blurring at the left and right edges of the image. Chapter 3 presents an algorithm that corrects for these image artifacts.

2.8.3. Sensitivity encoding (SENSE)

The weighted image superposition algorithm requires that each image be acquired with a FOV sufficient to encompass the entire sample. One could decrease the total sequence time while maintaining the same resolution by increasing Δk_{phase}, but this procedure reduces the FOV and results in an aliased image in which magnetization at multiple spatial locations contributes to the same voxel. Figure 2.23 shows a simulated image of the spin grid with L_z a factor of ~2 smaller than the grid size. Using a single

detector, there is no way to "unfold" this aliased image. However, it is possible to use the spatial selectivity of detectors at different spatial positions to determine the location of the ambiguous magnetization. Although other methods exist, I focus on the sensitivity encoding (SENSE) algorithm developed by Pruessman *et al.* [3] for reconstructing images with rectangular *k*-space sampling.

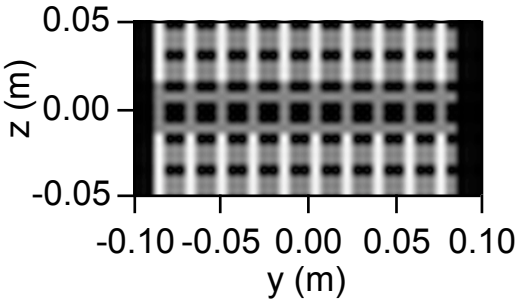

Figure 2.23: A simulated image of the spin grid shown in Fig. 2.21 with a reduced FOV in the *z*-direction.

As in the weighted superposition algorithm, Pruessman *et al.* begin by reconstructing N_d images of the sample, one for each detector. Because the sample size is larger that the image FOV, spins from N_p different physical locations contribute to the intensity of a single voxel in these images. N_p need not be the same at each point in the reduced-FOV images. If a_n is the measured magnetization of this voxel (a complex quantity) from detector n, Pruessman *et al.* show that v_m, the reconstructed voxel magnetization at the m^{th} physical location $\mathbf{r}_m$, can be expressed in vector notation as

$$\mathbf{v} = \mathbf{U}\,\mathbf{a}, \tag{2.55}$$

where the unfolding matrix $\mathbf{U}$ is given by

$$\mathbf{U} = \left(\mathbf{S}^{\mathrm{H}}\boldsymbol{\Psi}^{-1}\mathbf{S}\right)^{-1}\mathbf{S}^{\mathrm{H}}\boldsymbol{\Psi}^{-1}. \tag{2.56}$$

Here, $\mathbf{S}_{m,n} = \beta_{\perp,n}(\mathbf{r}_m)/A_{p,n}$ proportional to the response of detector n to spins at $\mathbf{r}_m$, $\boldsymbol{\Psi}_{n,p}$ is the noise correlation matrix between detectors n and p, and $\mathbf{S}^{\mathrm{H}}$ represents the conjugate transpose of $\mathbf{S}$. If the detectors have uncorrelated noise of equal magnitude, $\boldsymbol{\Psi}$ can be replaced by the identity matrix. If $N_p = 1$ and the detector noise is uncorrelated, Eq. (2.55) reduces to Eq. (2.51). Because Eq. (2.55) splits the measured signal among N_p different voxels, the voxel SNR using SENSE is at least a factor of $N_p^{1/2}$ lower than that of the image reconstructed with the full FOV. Since reducing the image FOV reduces N_y and/or N_z, the voxel SNR predicted by Eq. (2.53) need not be modified, but now describes the best possible SNR. Pruessman *et al.* [3] derive expressions for the actual voxel SNR achieved using SENSE reconstruction.

In order to demonstrate the feasibility of employing SENSE to reduce the imaging time of SQUID-detected low-field MRI, I artificially reduced the FOV of the images

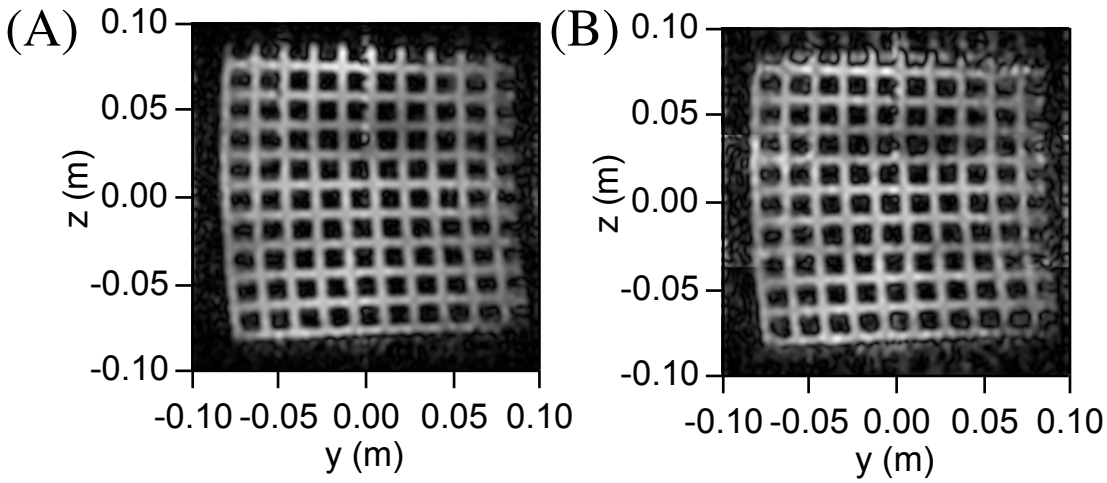

Figure 2.24: SENSE reconstruction of the image of the grid phantom with the phase-encoding FOV reduced by a factor of N_p. (A) $N_p = 2$. (B) $N_p = 3$.

shown in Fig. 2.22(A) by a factor of N_p by reconstructing them using only every N_p^{th} phase-encoding step. I then combined these images using SENSE, employing the same $C_M = 2$ maximum correction factor as in Fig. 2.22(B). Figure 2.24(A) shows the resulting image for $N_p = 2$, while Fig. 2.24(B) shows $N_p = 3$. Figure 2.24(A) can barely be distinguished from Fig. 2.22(B), the same image without SENSE reconstruction, but Fig. 2.24(B) shows artifacts caused by SENSE reconstruction. Table 2.2 shows the measured voxel SNR of these images compared to the best-case $N_p^{-1/2}$ dependence. The $N_p = 2$ case achieves nearly the best-case SNR, but the $N_p = 3$ case achieves only 69% of the best-case SNR.

Table 2.2: Voxel SNR of images reconstructed using SENSE.

Figure	2.22(B)	2.24(A)	2.24(B)
FOV reduction factor (N_p)	1	2	3
Voxel signal (a. u.)	22.3	11.3	6.9
Voxel noise (a. u.)	1	0.74	0.77
Voxel SNR	22.3	15.1	8.9
Predicted best voxel SNR ($\propto N_p^{-1/2}$)	22.3	15.7	12.9

The excellent performance of the SENSE algorithm in the $N_p = 2$ case and the poorer performance in the $N_p = 3$ case can be explained by the fact that reducing the FOV in the images reconstructed from the individual sensors [Fig. 2.22(A)] by a factor of 2 barely causes these images to overlap themselves. In contrast, a FOV reduction factor of 3 causes substantial overlap. Thus the SENSE algorithm can easily distinguish between ambiguous voxels in the $N_p = 2$ case and is substantially less sensitive to errors in the

detector response matrix **S** than in the $N_p = 3$ case. Pruessman *et al*. demonstrate successful SENSE reconstruction of images for up to $N_p = 4$, but they start with higher initial SNR and measure (rather than calculate) **S**. Based on the results of this section, I conclude that SENSE reconstruction will produce artifact-free images with SNR given by Eq. (2.53) when the FOV is large enough so that the images produced by the individual sensors do not overlap themselves. SENSE reconstruction might still work when this criterion is not met, but additional calculations would be required to ascertain the resulting image degredation.

Appendix 2.A. Implementation details

All the reconstruction algorithms described in this chapter are implemented in the IGOR Pro® template file `NTNMRimport.pxt`. Most of them are accessible through the menu bar, but a few, such as those generating simulated MRI images and SENSE reconstruction, can be executed only on the command line.

The IGOR Pro® discrete Fourier transform routines `fft` and `ifft` use different conventions than those described in this chapter. The IGOR Pro® routine `fft` is defined as

$$I(x) \propto \sum_{p=0}^{n-1} f(p\Delta k) e^{2\pi i p \Delta k x}, \tag{2.57}$$

which is equivalent to the inverse discrete Fourier transform [Eq. (2.10)] with the summation range changed to 0 to n – 1 and Δk replaced by $2\pi\Delta k$. The `NTNMRimport` code therefore uses the inverse of the transforms described in this chapter and defines **k** as

$$\mathbf{k}(t) = \gamma/2\pi \int_0^t \mathbf{G}(t)dt'. \tag{2.58}$$

All related quantities such as k_c are scaled accordingly.

---

[1] E. M. Haacke, R. W. Brown, M. R. Thompson, R. Venkatesan, *Magnetic Resonance Imaging: Physical Principles and Sequence Design*, Wiley-Liss, New York, 1999 p. 320.
[2] Haacke *et al*. p. 296.
[3] K. P. Pruessman, M. Weiger, M. B. Scheidegger, P. Boesiger, SENSE: Sensitivity encoding for fast MRI, *Magn. Reson. Med*. **42** (1999) 952.

3. Correction of concomitant gradient artifacts*

Magnetic resonance imaging requires magnetic field gradients to map the spatial position of a given spin onto its precession frequency or phase. An ideal imaging gradient would establish a linear relationship between position and precession frequency over the entire sample volume. However, Maxwell's equations prohibit unidirectional magnetic field gradients. Any physical gradient contains unwanted fields orthogonal to and of the same magnitude as the desired imaging gradient. Such concomitant gradients cause the precession frequency to be a nonlinear function of position, distorting the resulting MR image. Norris and Hutchison [1] first brought the issue of concomitant gradients to the attention of the MRI community in 1990. More recently, Yablonskiy *et al*. [2] quantified the impact of concomitant gradients by demonstrating that concomitant gradients warp planes of constant precession frequency into cylinders of radius $R_c = B_0/G$, where G is the strength of the applied gradient; concomitant gradient distortion becomes significant when R_c becomes comparable to the field of view L. The parameter $\varepsilon = L/R_c$ characterizes the severity of concomitant gradient distortion. For typical high-field MRI, $B_0 \sim 1$ T and $G \sim 10$ mT/m, so that $R_c \sim 100$ m, and the effects of concomitant gradients can be neglected for human-sized objects using conventional sequences. In contrast, Fig. 2.3(B) shows an MR image taken with $B_0 = 132$ μT and $G = 200$ μT/m, yielding $R_c = 0.7$ m. While the resulting image distortion cannot be seen in this image of a 35-mm phantom, concomitant gradient distortion would almost certainly be observable in an image of a human brain, roughly 0.2 m across, using the same imaging parameters.

A number of different schemes have been proposed to mitigate the effects of concomitant gradients in MRI. Radical schemes include alternating the direction of the precession field [3], applying higher order gradients along with the imaging gradient [4], and employing a train of 180° pulses and stroboscopic acquisition [5]. These methods require substantial modifications of MRI hardware and pulse sequences and have not been demonstrated in practice. Other methods focus on fast imaging sequences at 1.5 T and above. Weisskoff *et al*. [6] apply "prewarping" frequency-encoding gradients before

---

* This chapter was originally published as "Correction of Concomitant Gradient Artifacts in Experimental Microtesla MRI" in the *Journal of Magnetic Resonance* **177** (2005) p. 274-284. I thank Elsevier and my co-authors Michael Mößle and John Clarke for permission to adapt this article for my dissertation.

the 180° pulse in echo-planar imaging to reduce the average amplitude of the concomitant phase. Bernstein, Zhou, and coworkers [7-9] demonstrate phase correction algorithms that reduce concomitant gradient distortion in spiral and echo-planar images. These algorithms correct only the first-order perturbation of precession frequency by concomitant gradients and have not been shown to work at low fields. Volegov *et al.* [10] compute the higher-order effects of concomitant gradients on the point spread function in low-field MRI when the gradient switching time is much shorter than the precession period, but do not provide details of a correction algorithm.

This chapter considers the effects of concomitant gradients on MR images of human-scale objects in microtesla magnetic fields in the limit of slow gradient switching. One motivation for this work is the possibility of combining low-field MRI with existing magnetoencephalography (MEG) systems. Such systems contain about 300 SQUIDs in a helmet placed over the head of the subject and are used to detect the magnetic fields produced by neuronal currents in the brain. Needless to say, these techniques could be applied to other applications of low-field MRI.

Section 3.1.1 presents simulations of the acquisition of a MR image of a 0.175-m two-dimensional grid of spins using a pulse sequence with $B_0 = 66$ μT, a 57 μT/m frequency-encoding gradient, and a 280 μT/m maximum phase-encoding gradient. The concomitant terms of the frequency-encoding gradient distort the image, while the concomitant terms of the phase-encoding gradient cause image blurring. Section 3.1.2 develops a non-perturbative phase correction algorithm that can also correct for inhomogeneous magnetic fields and demonstrates this correction algorithm on the simulated images. Section 3.1.3 introduces a new technique that raises B_0 during phase encoding to mitigate image blurring caused by concomitant phase-encoding gradients. Section 3.2 applies both these correction techniques to experimental images generated using comparable sequence parameters. Finally, Sec. 3.3 concludes by considering the limits of these correction techniques and the constraints that concomitant gradients place on low-field MRI hardware and the design of pulse sequences.

3.1. Theory and algorithms

For simplicity, this chapter considers only the case of two-dimensional MRI with B_0 pointing in the z-direction and the sample in the yz-plane. Frequency encoding is

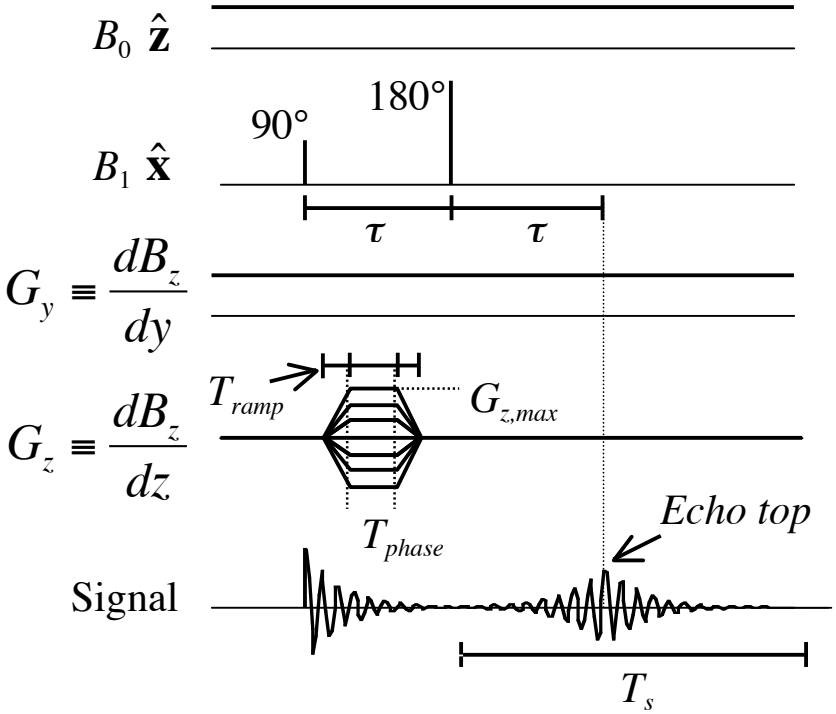

Figure 3.1: Spin-echo pulse sequence employed in the simulations and experiments described in this chapter. Data acquisition begins after the 180° pulse, and the echo top occurs a time τ after the 180° pulse.

performed along the *y*-direction, phase encoding along the *z*-direction. The results can be generalized to alternate geometries and to three dimensions.

3.1.1. Effect of concomitant gradients on MR images

Figure 3.1 shows an encoding sequence for standard spin-echo MRI with echo time 2τ and data acquisition time T_s. The phase-encoding gradient is ramped up for a time T_{ramp}, held constant for T_{phase}, and then ramped down for T_{ramp}. Ignoring the requirements of Maxwell's equations, the ideal phase-encoding magnetic field is

$$\mathbf{B}_{phase}^{ideal} = \left(B_0 + yG_y + zG_z\right)\hat{\mathbf{z}} \tag{3.1}$$

where G_y and G_z are the magnitude of the frequency and phase-encoding gradients, respectively. Similarly, the ideal magnetic field during data acquisition (frequency encoding) is

$$\mathbf{B}_{freq}^{ideal} = \left(B_0 + yG_y\right)\hat{\mathbf{z}}. \tag{3.2}$$

For these fields, the spin precession angular frequency $\gamma|\mathbf{B}|$ is a linear function of position. Therefore, the image can be reconstructed as the inverse Fourier transform of *k*-space. However, Maxwell's equations require $\nabla \cdot \mathbf{B} = 0$ and $\nabla \times \mathbf{B} = 0$ for static magnetic

fields in free space. Thus the physical magnetic fields used in MRI must contain additional concomitant gradient terms. Assuming no field inhomogeneity and using a cylindrically symmetrical coil to generate G_z, the physical fields can be expressed as (Eq. (A10) with $\alpha = 1/2$ in [11])

$$\mathbf{B}_{phase}^{phys} = \mathbf{B}_{phase}^{ideal} + zG_y\hat{\mathbf{y}} - \frac{1}{2}xG_z\hat{\mathbf{x}} - \frac{1}{2}yG_z\hat{\mathbf{y}}, \tag{3.3}$$

$$\mathbf{B}_{freq}^{phys} = \mathbf{B}_{freq}^{ideal} + zG_y\hat{\mathbf{y}}. \tag{3.4}$$

To illustrate the effect of these concomitant gradient terms, the spin-precession angular frequency during phase and frequency encoding can be expanded in the yz-plane to second order as [11]

$$\omega_{phase}^{phys} = \gamma\left|\mathbf{B}_{phase}^{phys}\right| = \gamma\left[B_0 + G_y y + G_z z + \frac{G_y^2}{2B_0}z^2 + \frac{G_z^2}{8B_0}y^2 - \frac{G_y G_z}{2B_0}yz + O\left(\frac{G^3}{B_0^2}\right)\right] \tag{3.5}$$

and

$$\omega_{freq}^{phys} = \gamma\left|\mathbf{B}_{freq}^{phys}\right| = \gamma\left[B_0 + G_y y + \frac{G_y^2}{2B_0}z^2 + O\left(\frac{G_y^3}{B_0^2}\right)\right]. \tag{3.6}$$

The additional concomitant gradient terms cause the precession frequency to be a nonlinear function of position. Linearity is restored in the limit in which the magnetic field $GL/2$ generated by the gradient coils at the edge of the sample is much smaller than B_0 ($\varepsilon/2 \equiv GL/2B_0 << 1$) [2].

Because the mathematical properties of Eqs. (3.3) and (3.4) have been adequately explored elsewhere [2,11], this chapter focuses on the effects of concomitant gradients on MR images. Figure 3.2(A) shows a simulated MR image of a 175 mm x 175 mm grid of spins using the pulse sequence of Fig. 3.1 and the idealized magnetic fields of Eqs. (3.1) and (3.2). The grid is the approximate size of a human brain. I choose $B_0 = 66$ μT, $G_y = 57$ μT/m and the area under the phase-encoding gradient to match the experimental sequences presented in Sec. 3.2. A detailed description of the simulation algorithm is reserved for Appendix 3.A. Figure 3.2(B) shows a simulated image using the same sequence and the physical magnetic fields from Eqs. (3.3) and (3.4). Concomitant gradients distort Fig. 3.2(B) by bending the vertical edges of the image towards $+y$, by stretching the vertical scale for $y < 0$, and by compressing the vertical scale for $y > 0$. Figure 3.2(C) shows a simulated image that employs a phase-encoding gradient seven

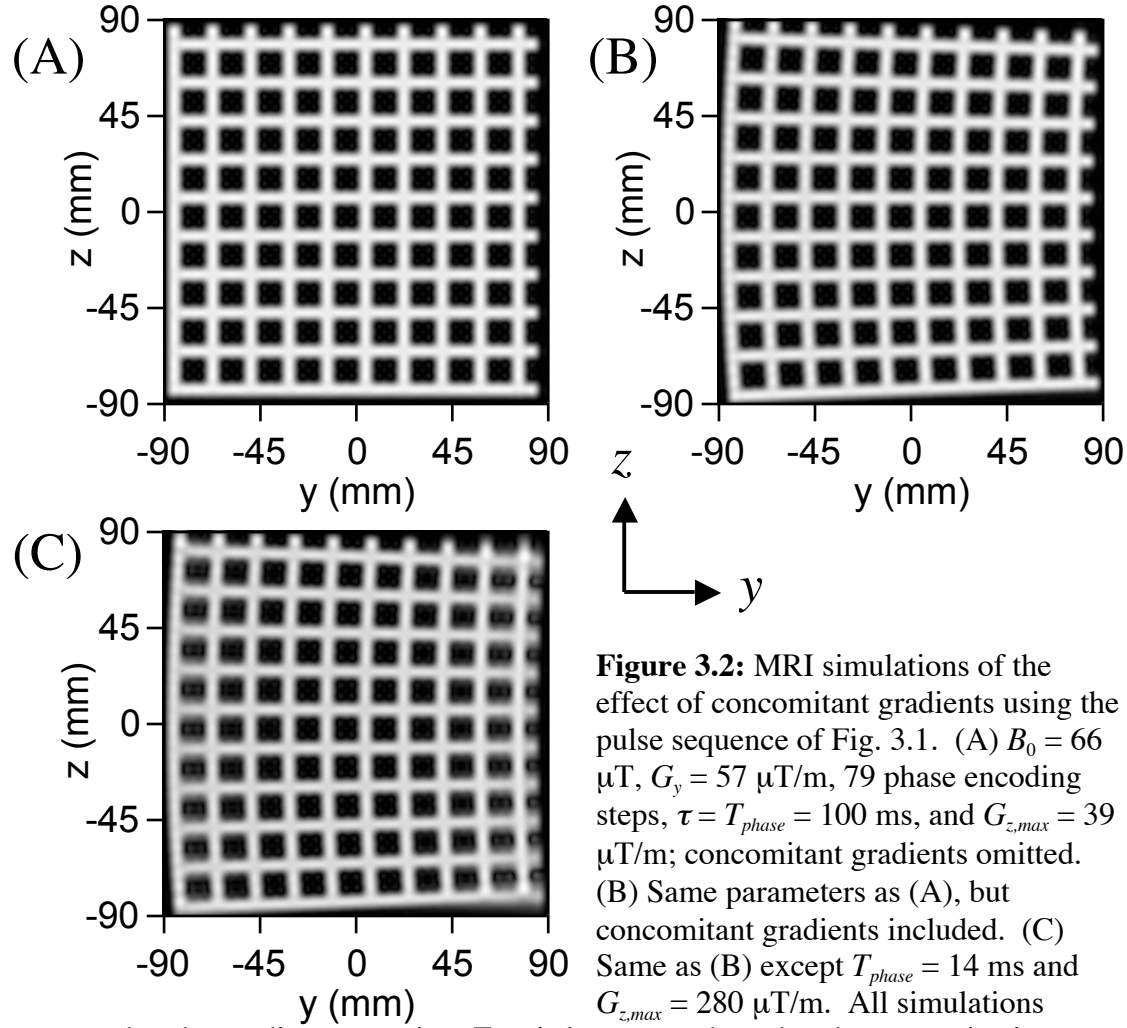

Figure 3.2: MRI simulations of the effect of concomitant gradients using the pulse sequence of Fig. 3.1. (A) B_0 = 66 μT, G_y = 57 μT/m, 79 phase encoding steps, $\tau = T_{phase}$ = 100 ms, and $G_{z,max}$ = 39 μT/m; concomitant gradients omitted. (B) Same parameters as (A), but concomitant gradients included. (C) Same as (B) except T_{phase} = 14 ms and $G_{z,max}$ = 280 μT/m. All simulations assume that the gradient ramp time T_{ramp} is long enough so that the magnetization adiabatically follows the direction of the applied field ($\gamma B_0 T_{ramp} >> 1$ [2]), but short enough to neglect the phase accumulated during gradient ramping.

times higher than Fig. 3.2(B) and correspondingly shorter T_{phase}; short phase-encoding times are desirable because they prevent signal loss caused by spin relaxation during phase encoding. In addition to the distortion present in Fig. 3.2(B), Fig. 3.2(C) shows vertical blurring at the horizontal edges of the image.

The image distortion and blurring in Figs. 3.2(B) and 3.2(C) can be explained using Eqs. (3.5) and (3.6). The apparent position of a spin in the frequency-encoding direction to second order is given by

$$y_{MRI} = \frac{\omega_{freq}^{phys} - \gamma B_0}{\gamma G_y} \approx y + \frac{G_y}{2B_0} z^2. \tag{3.7}$$

Thus spins with large $|z|$ appear shifted towards +y, as seen in Fig. 3.2(B). The apparent position of a spin in the z-direction depends on its phase at the echo top

$$\phi_{echo}^{phys} = -\omega_{phase}^{phys} T_{phase} - \omega_{freq}^{phys}\left(\tau - T_{phase}\right) + \omega_{freq}^{phys}\tau = -\left(\omega_{phase}^{phys} - \omega_{freq}^{phys}\right)T_{phase}, \tag{3.8}$$

according to the relation

$$z_{MRI} = \frac{-\phi_{echo}^{phys}}{\gamma G_z T_{phase}} \approx \left(1 - \frac{G_y}{2B_0} y\right) z + \frac{G_z}{8B_0} y^2; \tag{3.9}$$

terms higher than second order have again been neglected and $T_{ramp} = 0$. The term in parenthesis describes the vertical scale distortion seen in Fig. 3.2(B). Because each phase-encoding step employs a different value of G_z, z_{MRI} takes on different values in the same image, and images employing high G_z [such as Fig. 3.2(C)] will be blurred at large $|y|$.

3.1.2. Reconstruction algorithm to correct distortion and blurring

Although the distortion caused by frequency-encoding concomitant gradients shown in Fig. 3.2(B) could be corrected by undoing the spatial shifts described in Eqs. (3.7) and (3.9) (or their higher-order counterparts) after image reconstruction, the blurring caused by phase-encoding concomitant gradients demonstrated in Fig. 3.2(C) cannot be corrected after reconstruction. Here I present a post-acquisition, pre-reconstruction phase correction algorithm to correct for image distortion and blurring caused by concomitant gradients. Our algorithm applies the concepts developed by Du *et al*. [9] in the context of high-field echo-planar imaging to low-field spin-echo imaging and extends their algorithm beyond second-order correction. I show that it can be further extended to correct for systematic image distortions caused by magnetic field inhomogeneity.

I begin by separating the spin precession angular frequency during the frequency-encoding step into two parts:

$$\omega_{freq}^{phys} = \gamma\left|\mathbf{B}_{freq}^{ideal}\right| + \Delta\omega_{freq}^{c} = \omega_{freq}^{ideal} + \Delta\omega_{freq}^{c}, \tag{3.10}$$

where $\Delta\omega_{freq}^{c}$ is the change in angular precession frequency caused by concomitant gradients. I next generalize Eq. (3.8) to allow for the possibility of non-negligible T_{ramp}:

$$\phi_{echo}^{phys} = -\gamma\int_0^{\tau}\left|\mathbf{B}_{phase}^{phys}(t)\right|dt + \omega_{freq}^{phys}\tau, \tag{3.11}$$

where $\mathbf{B}_{phase}^{phys}(t)$ is the magnetic field including concomitant gradients at a time t after the 90° pulse. Although $\mathbf{B}_{phase}^{phys}(t)$ changes direction while the gradient is ramped, the precessing spins remain perpendicular to $\mathbf{B}_{phase}^{phys}(t)$ in the adiabatic gradient switching regime $\gamma B_0 T_{ramp} >> 1$ [2]. In this regime, the precession frequency depends on the magnitude of $\mathbf{B}_{phase}^{phys}(t)$ rather than its components and the spin phase remains well defined during gradient ramping. I separate ϕ_{echo}^{phys} into two parts:

$$\phi_{echo}^{phys} = \left(-\gamma \int_0^{\tau} \left| \mathbf{B}_{phase}^{ideal}(t) \right| dt + \omega_{freq}^{ideal} \tau \right) + \Delta\phi_{echo}^{c} = \phi_{echo}^{ideal} + \Delta\phi_{echo}^{c}. \tag{3.12}$$

Here $\mathbf{B}_{phase}^{ideal}(t)$ is defined analogously to $\mathbf{B}_{phase}^{phys}(t)$, and $\Delta\phi_{echo}^{c}$ is the change in the spin phase at the echo top caused by concomitant gradients.

The magnetic field measured at the detector for a given phase-encoding gradient G_z can be computed by integrating the contribution of each spin over the volume of the sample:

$$B_{det}(t;G_z) \propto \int_V M(\mathbf{r}) \cos\left(\omega_{freq}^{ideal} t + \phi_{echo}^{ideal} + \Delta\omega_{freq}^{c} t + \Delta\phi_{echo}^{c} \right) d\mathbf{r}\,. \tag{3.13}$$

Here $M(\mathbf{r})$ is the magnetization at point $\mathbf{r}$, and t is defined relative to the echo top. The four terms inside the parenthesis are implicit functions of $\mathbf{r}$; ϕ_{echo}^{ideal} and $\Delta\phi_{echo}^{c}$ depend on the phase-encoding gradient G_z as well. One can formally eliminate the contributions of concomitant gradients near a specific point $\mathbf{r_0}$ by defining a scaled time

$$t' = \left(\frac{\omega_{freq}^{ideal}}{\omega_{freq}^{ideal} + \Delta\omega_{freq}^{c}} \right) \left(t - \frac{\Delta\phi_{echo}^{c}}{\omega_{freq}^{ideal}} \right). \tag{3.14}$$

Here, ω_{freq}^{ideal}, $\Delta\omega_{freq}^{c}$, ϕ_{echo}^{ideal}, and $\Delta\phi_{echo}^{c}$ are evaluated at $\mathbf{r} = \mathbf{r_0}$ so that t' depends on $\mathbf{r_0}$ and G_z. I then evaluate Eq. (3.13) by inserting t' in place of t to obtain a rescaled detected field

$$B'_{det}(t;G_z) = B_{det}(t';G_z) \propto \int_V M(\mathbf{r}) \cos\left(\omega_{freq}^{ideal} t + \phi_{echo}^{ideal} \right) d\mathbf{r}\,, \tag{3.15}$$

which eliminates the terms $\Delta\omega_{freq}^{c}$ and $\Delta\phi_{echo}^{c}$. By recording $B_{det}(t;G_z)$ for each value of G_z, I can turn this formal manipulation into a prescription for correcting concomitant gradients by first breaking the image up into regions, each centered on a particular value of $\mathbf{r_0}$. For each value of $\mathbf{r_0}$, I interpolate the acquired data to obtain $B'_{det}(t;G_z)$, evaluating

Eq. (3.14) at the position $\mathbf{r_0}$. Subsequently I demodulate and combine $B'_{det}(t;G_z)$ to obtain a *k*-space representation of the image. The inverse Fourier transform of this *k*-space will be corrected for concomitant gradients in the vicinity of $\mathbf{r_0}$. Finally, I splice together the images obtained for each value of $\mathbf{r_0}$; the resulting image will be globally corrected for concomitant gradient distortion and blurring. An equivalent algorithm can be performed directly on the *k*-space representation of the distorted image. Demodulation of $B_{\text{det}}(t;G_z)$ can be accomplished by applying Eq. (2.15) to obtain

$$s\left(k_y,k_z\right) = 2\,\text{Lowpass}\left\{B_{det}\left(\frac{k_y}{\gamma G_y};G_z\right)\exp\left(i\frac{B_0 k_y}{G_y}\right)\right\}, \tag{3.16}$$

where *s* represents the complex *k*-space, $k_y = \gamma G_y t$, $k_z = -\gamma\int_0^\tau G_z dt$, and Lowpass represents the action of a low-pass filter. I define $k'_y = \gamma G_y t'$ to find

$$s'\left(k_y,k_z\right) = s\left(k'_y,k_z\right) = 2\,\text{Lowpass}\left\{B_{\text{det}}\left(\frac{k'_y}{\gamma G_y};G_z\right)\exp\left(i\frac{B_0 k'_y}{G_y}\right)\right\}. \tag{3.17}$$

The inverse Fourier transform of $s'\left(k_y,k_z\right)$ will be corrected for concomitant gradients in the vicinity of $\mathbf{r_0}$; a globally corrected image can be created by splicing locally corrected images together.

To demonstrate this phase correction algorithm, I applied it to the *k*-space data generated by the MRI simulation used to produce the distorted and blurred image in Fig. 3.2(C). To reconstruct the image, I divided the field of view into equally spaced square regions. I evaluated Eq. (17) to compute $s'\left(k_y,k_z\right)$ for each region, choosing $\mathbf{r_0}$ at the center of that region. Figure 3.3(A) shows the results of this algorithm using 8 x 8 square regions. The blurring is eliminated, and the grid lines are globally straight; the only remaining artifacts are discontinuities at the boundaries of the correction regions. I can eliminate these discontinuities by reducing the size of the correction regions as shown in Fig. 3.3(B), which employs 24 x 24 square regions. Alternately, I can apply the post-reconstruction local image-warping algorithm described in Appendix 3.B; Fig. 3.3(C) shows the results of this algorithm applied to Fig. 3A. Figure 3.3(C) has a few remaining artifacts, but the image-warping algorithm is substantially faster than increasing the grid density because it requires fewer reconstruction regions to eliminate discontinuities,

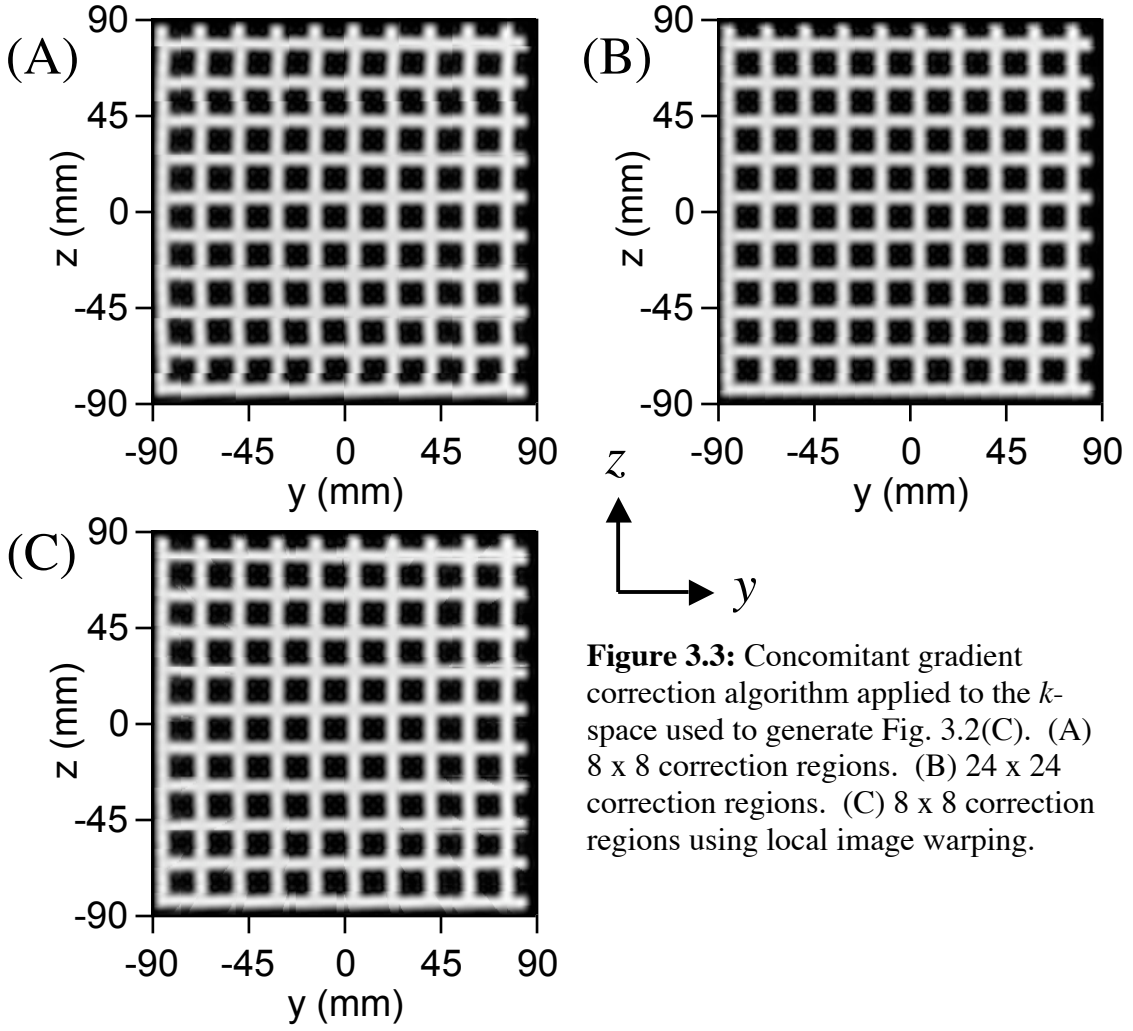

Figure 3.3: Concomitant gradient correction algorithm applied to the *k*-space used to generate Fig. 3.2(C). (A) 8 x 8 correction regions. (B) 24 x 24 correction regions. (C) 8 x 8 correction regions using local image warping.

thereby reducing the number of interpolation and Fourier transform steps. It takes about 30 s to reconstruct Fig. 3.3(C) using unoptimized code running on a 1.6 GHz PowerPC G5. Since each region can be reconstructed independently of the others, this algorithm could be easily adapted for parallel processing.

In order to estimate the accuracy of the phase correction algorithm, I consider a spin located at a point $\mathbf{r_0} + \mathbf{\Delta r} = (y_0 + \Delta y, z_0 + \Delta z)$ in the vicinity of $\mathbf{r_0}$. The combined effect of concomitant gradients and phase correction shifts the detected frequency to

$$\omega_{freq}^{corr} = \left(\frac{\omega_{freq}^{phys}(\mathbf{r_0} + \mathbf{\Delta r})}{\omega_{freq}^{phys}(\mathbf{r_0})} \right) \omega_{freq}^{ideal}(\mathbf{r_0}) = \gamma B_0 \frac{\sqrt{(1 + \chi_y + \Delta\chi_y)^2 + (\chi_z + \Delta\chi_z)^2}}{\sqrt{(1 + \chi_y)^2 + \chi_z^2}} (1 + \chi_y), \quad (3.18)$$

where $\chi_y = G_y y_0 / B_0$, $\chi_z = G_y z_0 / B_0$, $\Delta\chi_y = G_y \Delta y / B_0$, and $\Delta\chi_z = G_y \Delta z / B_0$. Factoring the denominator out of the numerator yields

$$\omega_{freq}^{corr} = \gamma B_0 \sqrt{1 + \frac{\Delta\chi_y\left(2 + 2\chi_y + \Delta\chi_y\right) + \Delta\chi_z\left(2\chi_z + \Delta\chi_z\right)}{\left(1 + \chi_y\right)^2 + \chi_z^2}}\left(1 + \chi_y\right). \tag{3.19}$$

In Sec. 3.3, I show that the concomitant gradient correction algorithm requires $G_y L/B_0 < 1$, so that χ_y and χ_z must always be less than 1/2. If I employ a 10 x 10 or larger grid of correction regions, $\Delta\chi_y$, and $\Delta\chi_z$ will be much smaller than χ_y and χ_z. Assuming χ_y, χ_z, $\Delta\chi_y$, and $\Delta\chi_z$ are all much smaller than unity, I can expand Eq. (3.19) to first order in $\Delta\chi$ and second order in χ as

$$\omega_{freq}^{corr} = \gamma B_0\left(1 + \chi_y + \Delta\chi_y + \chi_z\Delta\chi_z - \chi_y\chi_z\Delta\chi_z - \chi_z^2\Delta\chi_y + O\left(\chi^3\right)\right). \tag{3.20}$$

The apparent position of the spin can be computed by substituting ω_{freq}^{corr} for ω_{freq}^{phys} in Eq. (3.7):

$$y_{MRI}^{corr} \approx y_0 + \Delta y + \frac{G_y}{B_0} z_0\Delta z - \frac{G_y^2}{B_0^2} y_0 z_0\Delta z - \frac{G_y^2}{B_0^2} z_0^2\Delta y. \tag{3.21}$$

The first two terms in Eq. (3.21) are the physical location of the spin, and the latter terms represent the remaining concomitant gradient distortion. Comparing the third term in Eq. (3.21) to the second term in Eq. (3.7), the leading error term now scales as $z_0\Delta z$ instead of z^2; concomitant gradient correction will therefore be effective when $\Delta z << z_0$. This third term in Eq. (3.21) describes the discontinuities in the vertical lines in Fig. 3.3(A) at large values of $|z|$. These discontinuities can be corrected either by reducing Δy and Δz by reducing the size of the correction regions [Fig. 3.3(B)] or by employing the local image-warping algorithm that corrects for terms linear in Δy and Δz [Fig. 3.3(C)]. There is a similar but more complicated analysis for the phase-encoding direction.

This phase correction algorithm can be extended to correct distortions arising from known field inhomogeneities in addition to concomitant gradients by simply adding the appropriate field terms to Eqs. (3.3) and (3.4). Inhomogeneities in B_0, the background field, and the frequency-encoding gradient G_y should be added to both Eq. (3.3) and Eq. (3.4), while inhomogeneity in the phase-encoding gradient G_z should be added to Eq. (3.3) only. I apply software correction for background field inhomogeneity to experimental images in Sec. 3.2.

3.1.3. Field cycling to eliminate phase-encoding concomitant gradient blurring

Concomitant gradients can also be mitigated in low-field MRI by employing pulse sequences that cannot be implemented with high-field superconducting magnets. These pulse sequences can supplement or replace the software correction algorithm described above and must be tailored to fit specific applications. For example, consider the possibility of combining MEG with MRI by detecting MR signals with the array of SQUIDs used to measure magnetic fields in MEG. Because neuronal currents in the brain change on a timescale of 1 ms or slower, the bandwidth of existing MEG systems is typically 1-2 kHz, thereby limiting the potential MRI readout frequency. In the MRI sequence shown in Fig. 3.1, one must choose $T_{phase} << T_2$ (the transverse spin relaxation time) to minimize signal losses caused by relaxation; for brain tissue, T_2 ranges from 60 ms to 100 ms [12]. Choosing T_{phase} = 10 ms and resolution Δz = 2 mm requires a maximum phase-encoding gradient $G_{z,max} = \pi/\gamma T_{phase}\Delta z$ = 590 μT/m. Since this gradient corresponds to a field of 59 μT at the edges of the 0.2 m field of view required for head imaging, one requires $B_0 >$ 59 μT (2.5 kHz) simply to maintain the one-to-one relation between spatial position and precession frequency; the results of Sec. 3.3 suggest that B_0 must be at least twice this field for successful software correction of concomitant gradient distortion. Protons precessing at the frequencies associated with these fields would not be detected by existing MEG systems.

The solution to this problem makes use of the fact that substantially lower gradients are required to achieve a given resolution in the frequency-encoding direction than in the phase-encoding direction. The resolution in the frequency-encoding direction depends on the acquisition time after the echo top, $(T_s - \tau)$; one requires $(T_s - \tau) \sim T_2$ and $\tau << T_2$ to maximize the SNR. Choosing $(T_s - \tau)$ = 60 ms requires a frequency-encoding gradient $G_y = \pi/\gamma(T_s - \tau)\Delta y$ = 98 μT/m to achieve a resolution Δy = 2 mm. I can therefore employ the pulse sequence shown in Fig. 3.4, in which I increase the precession field to $B_{0,phase}$ to reduce the effects of concomitant gradients during phase encoding, and then lower it during data acquisition to allow detection of the precessing spins in a limited bandwidth.

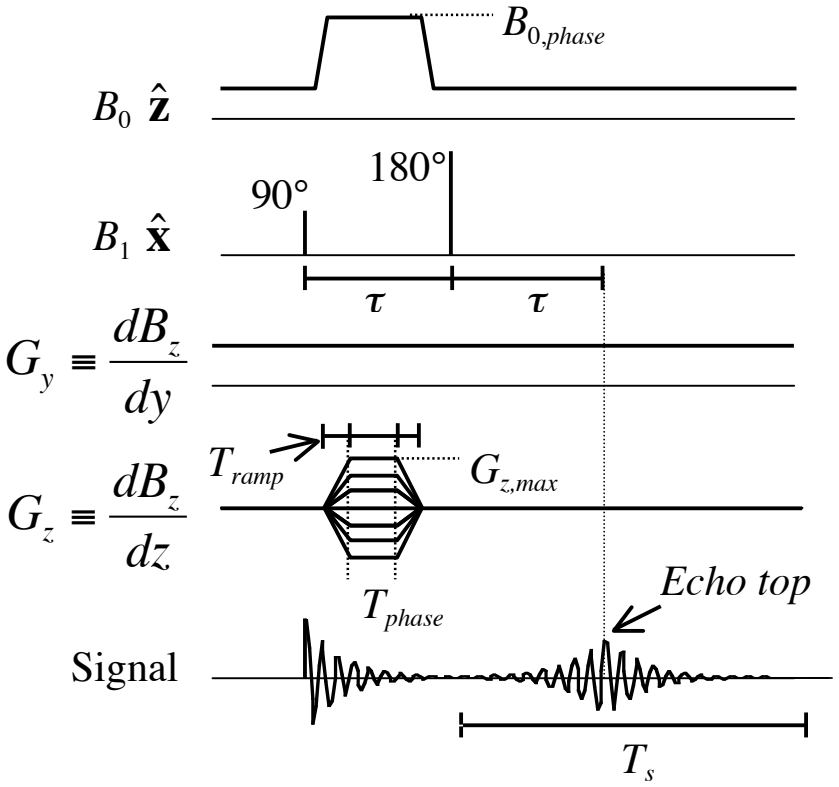

Figure 3.4: Field-cycling pulse sequence for MRI at readout frequencies below 2 kHz.

Figure 3.5 shows a simulated MR image generated with the pulse sequence of Fig. 3.4 applied to the grid of Fig. 3.2. The sequence parameters are the same as Fig. 3.2(C) except that B_0 has been increased by a factor of four during the phase-encoding step. The blurring at the edges of Fig. 3.2(C) caused by concomitant gradients during phase encoding has vanished; Fig. 3.5 is essentially identical to Fig. 3.2(B), in which the maximum phase-encoding gradient is seven times smaller. The remaining distortion can be corrected using either the methods of Sec. 3.1.2 or post-reconstruction image-warping algorithms.

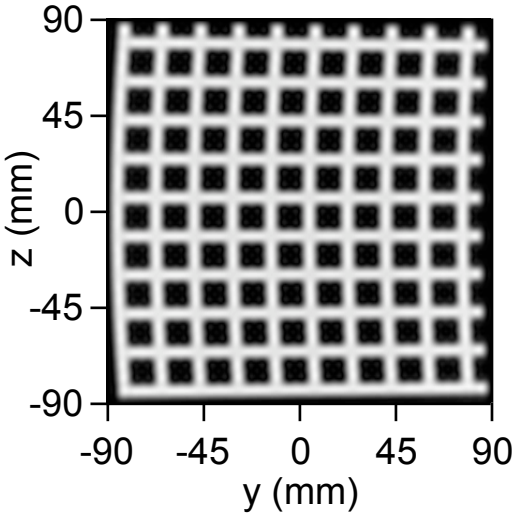

Figure 3.5: MRI simulation of the pulse sequence of Fig. 3.4 with $B_{0,phase}$ = 264 μT; all other parameters as in Fig. 3.2(C).

3.2. Experimental results

In order to observe the distortion and blurring caused by concomitant gradients in experimental images, I created a physical analogue of the pattern of spins shown in Fig. 3.2(A) by machining 20 5-mm wide, 165-mm long, 14-mm deep grooves in a sheet of plastic and filling them with water. I placed this grid on top of the polarizing coil and suspended the liquid helium cyrostat containing the gradiometer and SQUID above the grid. Because the 65-mm gradiometer pickup loop restricted the available field of view, I could not acquire the entire image with one pulse sequence. I therefore acquired a series of nine images, moving the gradiometer after each image to span the entire grid as shown in Fig. 2.21. The center of the gradiometer occupied positions y = 0, ±60 mm and z = 0, ±60 mm relative to the center of the grid. I employed the techniques described in Sec. 2.8.1 to merge the nine images into a single composite image and compensate for the inhomogeneous sensitivity of the gradiometer.

I applied the pulse sequence of Fig. 3.1 with $B_0 = 66$ μT and $G_y = 57$ μT/m to image the grid. Because the experimental gradients have nonzero rise times, whereas the MRI simulation algorithm assumes $T_{ramp} = 0$, the experimental phase-encoding gradient waveform differed from that used to generate Fig. 3.2(C). Since the area under the phase-encoding gradient waveform determines the resolution of the image and the time-integrated square of the gradient determines the first-order concomitant gradient effects, I matched these quantities in the simulated and experimental pulse sequences. Figure 3.6(A) shows the resulting image. Concomitant gradients cause distortion and blurring comparable to that seen in Fig. 3.2(C), but Fig. 3.6(A) contains asymmetric distortion not present in Fig. 3.2(C). This distortion originates from inhomogeneity in the Earth's magnetic field that I believe is caused by steel reinforcing rods in the floor of the laboratory. Rather than construct additional gradient shimming coils to cancel this inhomogeneous field, I measured its influence on the spin precession frequency at the center, edges, and corners of the grid. The precession frequency differed by 25 Hz at opposite corners of the grid. I fitted a two-dimensional quadratic function to this data and used the phase correction algorithm to correct the distortion caused by the inhomogeneous field. The resulting image, shown in Fig. 3.6(B), has distortion and blurring nearly identical to Fig. 3.2(C). I then applied both the empirical field correction

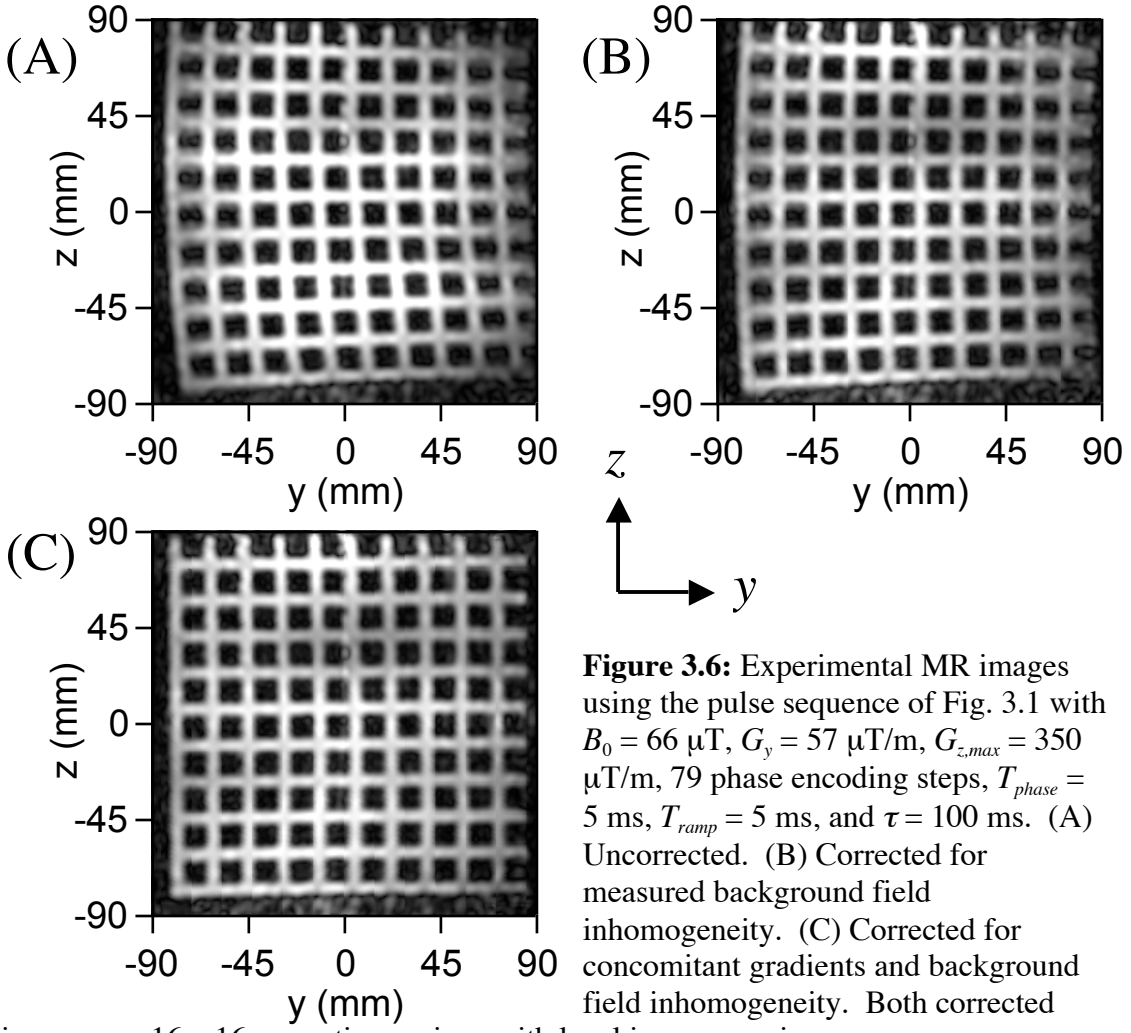

Figure 3.6: Experimental MR images using the pulse sequence of Fig. 3.1 with B_0 = 66 μT, G_y = 57 μT/m, $G_{z,max}$ = 350 μT/m, 79 phase encoding steps, T_{phase} = 5 ms, T_{ramp} = 5 ms, and τ = 100 ms. (A) Uncorrected. (B) Corrected for measured background field inhomogeneity. (C) Corrected for concomitant gradients and background field inhomogeneity. Both corrected images use 16 x 16 correction regions with local image warping.

and the concomitant gradient correction to obtain the image shown in Fig. 3.6(C). The combination of these corrections eliminates the blurring and produces an image that is nearly distortion-free.

I also investigated the effect of raising the precession field during phase encoding on concomitant gradient blurring. Figure 3.7(A) shows an enlarged view of the top-left corner of Fig. 3.6(A), and Fig. 3.7(B) shows the same corner imaged with the same pulse sequence except that I raised B_0 to $B_{0,phase}$ = 264 μT during phase encoding. The blurring caused by concomitant phase-encoding gradients in Fig. 3.7(A) is not present in Fig. 3.7(B), consistent with the simulation shown in Fig. 3.5. I attempted to expand the field of view by combining field-cycling images from different gradiometer positions, but was not able to do so because none of the available amplifiers could both cycle B_0 up to

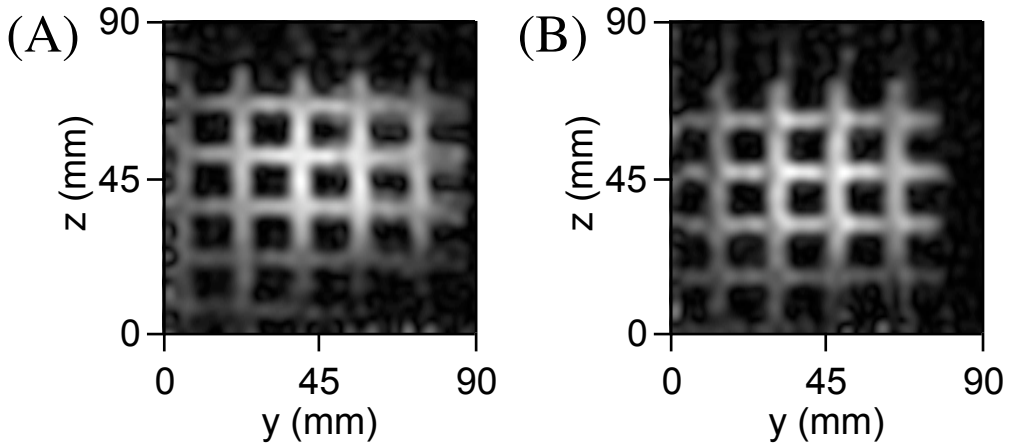

Figure 3.7: Experimental MR images demonstrating correction for phase encoding concomitant gradient blurring using field cycling. Top right corner of the grid imaged with (A) the pulse sequence of Fig. 3.1 with parameters given in Fig. 3.6, (B) the field-cycling pulse sequence of Fig. 3.4 with $B_{0,phase}$ = 264 μT and all other parameters as in Fig. 3.6. I applied the phase correction algorithm to both images to correct for the inhomogeneity in the earth's field but not for concomitant gradients.

264 μT for phase encoding and maintain a stable measurement field of 66 μT for the duration of the experiment without coupling excess field noise into the gradiometer.

3.3. Limits of concomitant gradient correction

So far, I have only considered cases in which the phase correction algorithm or B_0 field cycling successfully eliminates distortion and blurring caused by concomitant gradients. However, these correction techniques must fail for arbitrarily low B_0. If one reduces B_0 sufficiently, the field generated by the gradient coils will become comparable to B_0 and the total magnetic field will have a minimum within the image field of view. Spins on either side of this minimum cannot be distinguished by their precession frequencies, and neither correction technique accounts for this situation. This criterion restricts the allowable fields and gradients during both frequency and phase encoding.

During frequency encoding, the z-component of the magnetic field is weakest and the perpendicular y-component strongest at the points $(y,z) = (-L/2,\pm L/2)$, where L is the image field of view. The magnitude of the magnetic field at this point is

$$\left|\mathbf{B}_{freq}^{phys}\right| = \sqrt{\left(B_0 - \frac{1}{2}LG_y\right)^2 + \left(\frac{1}{2}LG_y\right)^2} = B_0\sqrt{\left(1 - \frac{1}{2}\varepsilon_y^{freq}\right)^2 + \left(\frac{1}{2}\varepsilon_y^{freq}\right)^2}, \qquad (3.22)$$

where $\varepsilon_y^{freq} = G_y L/B_0$. Since Eq. (3.22) has a minimum at $\varepsilon_y^{freq} = 1$, I require $\varepsilon_y^{freq} < 1$ to keep the minimum of the magnetic field outside the field of view. During phase

encoding when $G_z = G_{z,max}$, the z-component of the magnetic field is weakest at the point ($-L/2$,$-L/2$). At this point,

$$\begin{aligned}\left|\mathbf{B}_{phase}^{phys}\right| &= \sqrt{\left(B_{0,phase} - \frac{1}{2}LG_y - \frac{1}{2}LG_{z,max}\right)^2 + \left(-\frac{1}{2}LG_y + \frac{1}{4}LG_{z,max}\right)^2} \\ &= B_{0,phase}\sqrt{\left(1 - \frac{1}{2}\varepsilon_y^{phase} - \frac{1}{2}\varepsilon_z^{phase}\right)^2 + \left(-\frac{1}{2}\varepsilon_y^{phase} + \frac{1}{4}\varepsilon_z^{phase}\right)^2}\end{aligned}, \qquad (3.23)$$

where $\varepsilon_y^{phase} = G_y L/B_{0,phase}$ and $\varepsilon_z^{phase} = G_{z,max} L/B_{0,phase}$. To keep the minima of Eq. (3.23) outside the field of view one requires $\partial\left|\mathbf{B}_{phase}^{phys}\right|/\partial\varepsilon_y^{phase} < 0$ and $\partial\left|\mathbf{B}_{phase}^{phys}\right|/\partial\varepsilon_z^{phase} < 0$, which translate into the conditions $\varepsilon_y^{phase} + \varepsilon_z^{phase}/4 < 1$ and $\varepsilon_y^{phase}/4 + 5\varepsilon_z^{phase}/8 < 1$. While these expressions describe analytical limits beyond which concomitant gradient correction will fail, more stringent conditions may be required to produce acceptable image quality.

In order to investigate the limits of concomitant gradient correction further, I simulate the effect of progressively lowering B_0 in the 2-mm resolution pulse sequence for combined MEG/MRI described in Sec. 3.1.3. Figure 3.8(A) shows the grid image reconstructed from this pulse sequence with $B_0 = B_{0,phase} = 35$ μT (1490 Hz), $G_y = 98$ μT/m and $G_{z,max} = 590$ μT/m; because B_0 is lower and the gradients are higher than in the experimental pulse sequence, concomitant gradient distortion and blurring are greater than in Fig. 3.2(C) or Fig. 3.6(B). In this sequence, the 80 ms acquisition time is substantially longer than $\tau = 20$ ms, where 2τ is the echo time, and I therefore employ the iterative algorithm to reconstruct the image from the resulting partial k-space as described in Sec. 2.5.2. Figure 3.8(B) shows the results of the same sequence except with $B_{0,phase} =$ 100 μT. In this case, raising B_0 during phase encoding only partially corrects the blurring caused by concomitant phase-encoding gradients. Applying the phase correction algorithm to the k-space used to generate Fig. 3.8(B) yields Fig. 3.8(C); 24 x 24 reconstruction regions and local image warping are required to generate an artifact-free image. I repeated this procedure with $B_0 = 23.5$ μT (1000 Hz) to obtain Fig. 3.9, but the resulting image is unacceptably distorted and blurred despite field cycling to 100 μT and applying the phase correction algorithm. Field cycling to 200 μT does not appreciably change the image. I therefore conclude that a precession field of at least 35 μT during data acquisition is required to achieve 2-mm resolution of head-sized objects using this sequence; the electronics of a combined MEG/MRI system would have to be capable of

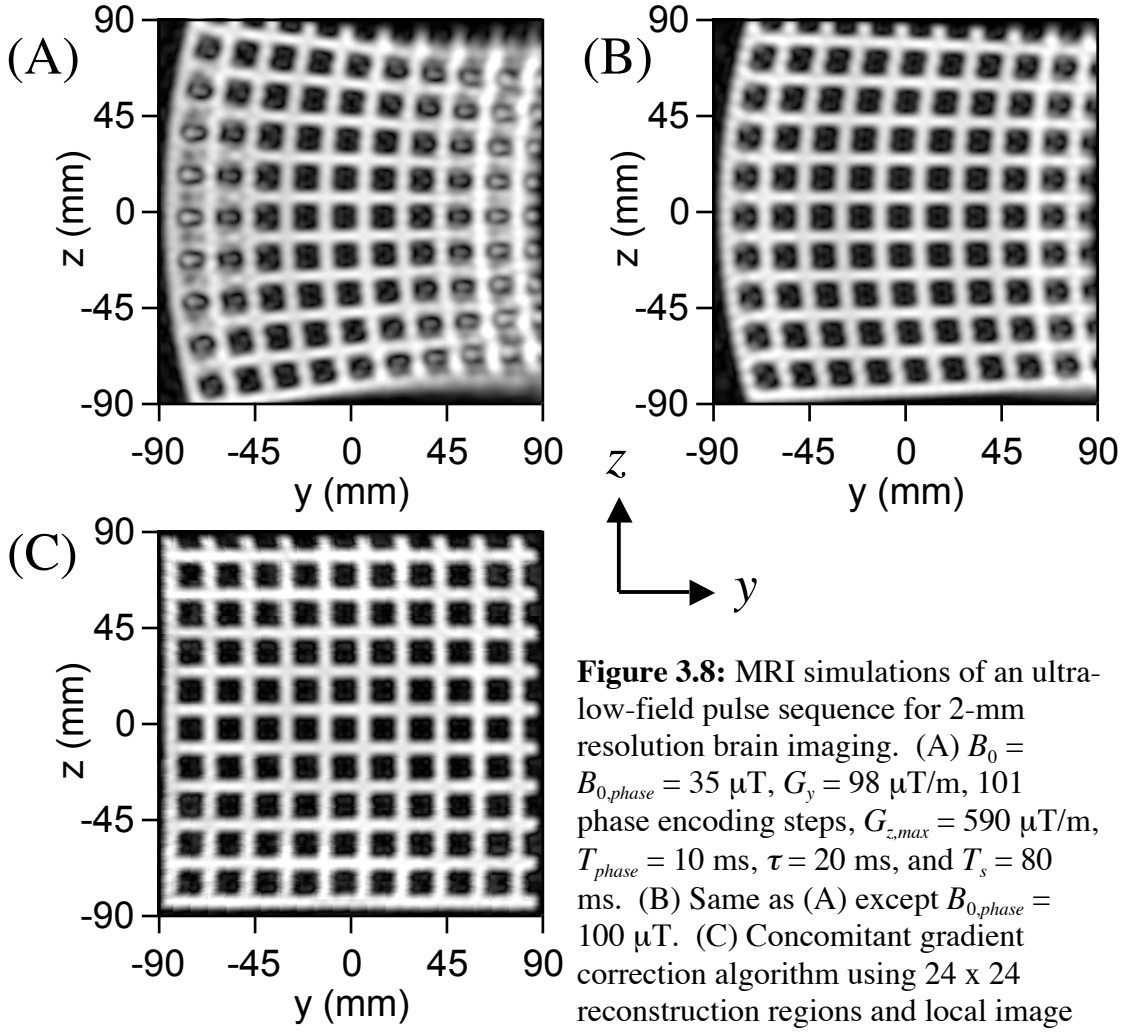

Figure 3.8: MRI simulations of an ultra-low-field pulse sequence for 2-mm resolution brain imaging. (A) B_0 = $B_{0,phase}$ = 35 μT, G_y = 98 μT/m, 101 phase encoding steps, $G_{z,max}$ = 590 μT/m, T_{phase} = 10 ms, τ = 20 ms, and T_s = 80 ms. (B) Same as (A) except $B_{0,phase}$ = 100 μT. (C) Concomitant gradient correction algorithm using 24 x 24 reconstruction regions and local image warping applied to the *k*-space used to generate (B).

detecting the 1490 ± 420 Hz signal band of the precessing spins (assuming L = 0.2 m). Because the external noise in our laboratory increases rapidly below 2.5 kHz and the effectiveness of the aluminum eddy-current shield surrounding our system decreases at low frequencies, I was unable to perform experimental MRI below 2.8 kHz to test these results.

In addition to the limitations on B_0 and gradient strength discussed above, the phase

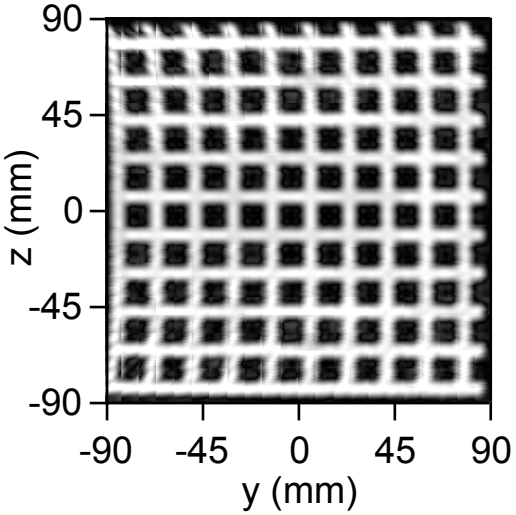

Figure 3.9: The same pulse sequence and concomitant gradient correction as Fig. 3.8(C) except B_0 = 23.5 μT.

correction algorithm requires $\gamma B_0 T_{ramp} >> 1$ to ensure that the spins remain perpendicular to the direction of the total magnetic field during gradient ramping. For $B_0 = 35$ μT, one requires $T_{ramp} >> 0.1$ ms, a small fraction of the 10 ms phase-encoding time used for Fig. 3.8.

Table 3.1: Sequence parameters and correction algorithms

Image	Figures	Encoding step	B_0 (μT)	G_y or $G_{z,max}$ (μT/m)	$\varepsilon = GL/B_0$ [a]	Required con. grad. correction
Simulated grid image	3.2(B), 3.2(C), 3.3	frequency	66	57	0.15	Phase correction
	3.2(B)	phase	66	39	0.10	
	3.2(C), 3.3	phase	66	280	0.74	
Experimental grid image	3.6	frequency	66	57	0.14	Phase correction
	3.6	phase	66	280[b]	0.70	
Simulated limits of con. grad. correction	3.8(B), 3.8(C)	frequency	35	98	0.49	Phase correction and B_0 field cycling
	3.8(B), 3.8(C)	phase	100	590	1.03	
Uncorrectable con. grad.	3.9	frequency	23.5	98	0.73	Correction fails
	3.9	phase	100	590	1.03	

[a] For the simulated images, $L = 175$ mm; for the experimental images, $L = 165$ mm.
[b] Root mean square gradient. Maximum phase-encoding gradient is 350 μT/m.

Table 3.1 summarizes the fields and gradients of the experimental (Fig. 3.6) and simulated (Figs. 3.2, 3.3, and 3.8) images presented in this paper. The phase correction algorithm alone is enough to correct the concomitant gradient distortion and blurring seen in Figs. 3.2(C) and 3.6(B). In contrast, the lower B_0 and higher gradients employed in Fig. 3.8 require both increasing B_0 during phase encoding and post-acquisition correction. Reducing B_0 still further as shown in Fig. 3.9 results in concomitant gradient artifacts that cannot be corrected even with both techniques. Although they cannot reconstruct images in arbitrarily low precession fields, these techniques enable distortion-free MRI in regimes in which ε becomes comparable to unity, thereby extending the potential of low-field MRI. In particular, they should enable the acquisition of MR images of the brain within the limited bandwidth of existing MEG systems.

Appendix 3.A. MRI simulation algorithm

I created the simulated MR images employed in this paper by calculating the signal detected by SQUID gradiometer as a function of time from a given object and pulse sequence and then processing these simulated traces with our image reconstruction software. I assume that the distance between the object and the bottom loop of the gradiometer is much smaller than the gradiometer baseline, so that the gradiometer effectively operates as a magnetometer. I employed the following algorithm to generate the time traces:

1. Divide the simulated object into squares of constant spin density. I employ $\Delta y = \Delta z = 6$ mm squares for the grid images presented in this paper; 3-mm squares produce nearly identical images.

2. Calculate the magnetic field at the center of the square during frequency and phase-encoding steps and the resulting values of ω_{freq}^{phys} and ϕ_{echo}^{phys} using Eqs. (3.3), (3.4), and (3.8) for each value of G_z.

3. Calculate the contribution of the n^{th} square to the field detected by the SQUID as

$$B_n(t) \propto \rho_n \int_{-\Delta y/2}^{\Delta y/2} \int_{-\Delta z/2}^{\Delta z/2} \cos\left[\left(\omega_{freq}^{phys} + \gamma y' G_y\right)\left(t - T_{phase}\right) + \phi_{echo}^{phys} - \gamma z' G_z T_{phase}\right] dz' dy', \quad (3.24)$$

where ρ_n is the spin density of the nth square and the 180° pulse occurs at $t = 0$. This equation assumes the slow gradient ramping regime ($\gamma B_0 T_{ramp} >> 1$) in which the precessing spins remain perpendicular to the total magnetic field at all times and the accumulated phase scales with the time integral of the total field. It also ignores spin relaxation and assumes uniform detector response over the sample. I solve this integral analytically, then evaluate with numerical values.

4. Sum $B_n(t)$ for all squares to obtain $B_{det}(t)$ for this value of G_z.

Appendix 3.B. Local image warping algorithm

The phase correction algorithm ensures that the image intensity at the correction point $\mathbf{r_0}$ corresponds to the true spin density at that point. However, Fourier transform image reconstruction assumes uniform frequency and phase-encoding gradients over the entire image. Concomitant gradients modify the local gradient values, causing image distortion and discontinuities at the boundaries of the correction regions as seen in Fig.

3.3(A). One can eliminate these artifacts by increasing the number of correction regions, as in Fig. 3.3(B), but the time to run the phase correction algorithm scales with the number of regions required. Alternatively, one can reduce or eliminate these discontinuities without substantially increasing the run time by applying a linear transformation to each corrected region based on the calculated gradients at $\mathbf{r_0} = (y_0,z_0)$. By examining Eqs. (3.7) and (3.9), one can express the apparent position in the locally corrected image (y_{MRI},z_{MRI}) in terms of the true spin position (y,z) to first order as

$$y_{MRI} - y_0 = \frac{1}{\gamma G_y}\left[\frac{\partial \omega_{freq}^{phys}}{\partial y}(y - y_0) + \frac{\partial \omega_{freq}^{phys}}{\partial z}(z - z_0)\right] \tag{3.25}$$

and

$$z_{MRI} - z_0 = \frac{-1}{\gamma G_z T_{phase}}\left[\frac{\partial \phi_{echo}^{phys}}{\partial y}(y - y_0) + \frac{\partial \phi_{echo}^{phys}}{\partial z}(z - z_0)\right]. \tag{3.26}$$

The inverse linear transformation can be obtained by solving these equations to obtain $y(y_{MRI},z_{MRI})$ and $z(y_{MRI},z_{MRI})$; applying this transform to each locally corrected image corrects for first-order gradient variation. The partial derivatives of ω_{freq}^{phys} and ϕ_{echo}^{phys} can be evaluated either analytically or numerically. Equation (3.26) should be evaluated using a small value of G_z since local image warping cannot correct distortion from concomitant phase-encoding gradients. Figure 3.3(C) shows the results of this algorithm applied using 8 x 8 square correction regions; all subsequent applications of the phase correction algorithm in this chapter employ local image warping.

---

[1] D. G. Norris, J. M. S. Hutchison, Concomitant magnetic field gradients and their effects on imaging at low magnetic field strengths, *Magn. Reson. Imaging* **8** (1990) 33.

[2] D. A. Yablonskiy, A. L. Sukstanskii, J. J. H. Ackerman, Image artifacts in very low magnetic field MRI: The role of concomitant gradients, *J. Magn. Reson.* **174** (2005) 279.

[3] T. Classen-Vujcic, J. Slotboom, A. F. Mehlkopf, Reduction of the concomitant field gradient effects by main magnetic field alteration, *Proc. Soc. Mag. Reson.* **3** (1995) 56.

[4] T. Classen-Vujcic, J. Slotboom, A. F. Mehlkopf, Hardware corrections of concomitant field gradients, *Proc. Intl. Soc. Mag. Reson. Med.* **5** (1997) 110.

[5] C. A. Meriles, D. Sakellariou, A. H. Trabesinger, V. Demas, A. Pines, Zero- to low-field MRI with averaging of concomitant gradient fields, *Proc. Natl. Acad. Sci. USA* **102** (2005) 1840.

[6] R. M. Weisskoff, M. S. Cohen, R. R. Rzedzian, Nonaxial whole-body instant imaging, *Magn. Reson. Med.* **29** (1993) 796.
[7] X. J. Zhou, Y. P. Du, M. A. Bernstein, H. G. Reynolds, J. K. Maier, J. A. Polzin, Concomitant magnetic-field-induced artifacts in axial echo planar imaging, *Magn. Reson. Med.* **39** (1998) 596.
[8] K. F. King, A. Ganin, X. J. Zhou, M. A. Bernstein, Concomitant gradient field effects in spiral scans, *Magn. Reson. Med.* **41** (1999) 103.
[9] Y. P. Du, X. J. Zhou, M. A. Bernstein, Correction of concomitant magnetic field-induced image artifacts in nonaxial echo-planar imaging, *Magn. Reson. Med.* **48** (2002) 509.
[10] P. L. Volegov, J. C. Mosher, M. A. Espy, R. H. Kraus Jr., On concomitant gradients in low-field MRI, *J. Magn. Reson.* **175** (2005) 103.
[11] M. A. Bernstein, X. J. Zhou, J. A. Polzin, K. F. King, A. Ganin, N. J. Pelc, G. H. Glover, Concomitant gradient terms in phase contrast MR: Analysis and correction, *Magn. Reson. Med.* **39** (1998) 300.
[12] H. W. Fischer, P. A. Rinck, Y. van Haverbeke, R. N. Muller, Nuclear relaxation of human brain gray and white matter: analysis of field dependence and implications for MRI, *Magn. Reson. Med.* **16** (1990) 317.

4. Signal and Noise in SQUID MRI

In addition to concomitant gradients, the other major challenge facing low-field magnetic resonance imaging is achieving adequate resolution, voxel SNR, and imaging speed. In Chapter 2, I showed that either decreasing the magnetic field noise or increasing the polarizing field increases the voxel SNR and that this increased SNR can often be traded for either increased resolution or decreased imaging time. Since these three parameters (combined with tissue contrast, cost, and ease of use) will determine the clinical relevance of SQUID-detected low-field MRI, it is essential to understand the noise limits of SQUID gradiometers and the field limits of polarizing coils. This chapter focuses on the intrinsic noise of the detector and sample; I defer the treatment of external noise and polarizing coils to Chapter 5. Because the flux from the MRI sample couples almost exclusively to the bottom loop of the second-order gradiometer, the bottom loop of the gradiometer functions essentially as a magnetometer; the upper loops serve only to cancel noise. Therefore the figure of merit for this gradiometer is the field noise referred to the bottom pickup loop; I frequently refer to this simply as the field noise of the gradiometer.

Section 4.1 focuses on the theoretical noise limits of SQUID untuned gradiometers and the practical challenges to achieving these limits. I begin by summarizing the results of computer simulations of SQUID voltage, current, and flux noise. I then combine these results with the work of Martinis and Clarke [1] to calculate the theoretical magnetic field noise of SQUID untuned magnetometers and gradiometers, taking into account the correlation between current and voltage noise. These calculations indicate that a field noise as low as 0.1 fT $Hz^{-1/2}$ (referred to the bottom loop of the gradiometer) might be achieved. Since this is substantially lower than the 1.7 fT $Hz^{-1/2}$ obtained using the Quantum Design SQUID as described in Chapter 1, I began to search for a replacement SQUID. I measured the noise of several SQUIDs with 60-turn input coils specially fabricated by Michael Mück to match the inductance of the gradiometer. Section 4.2 describes the measurement process, the parameters of the SQUIDs, and the results obtained when we replaced the Quantum Design SQUID with a lower noise 60-turn SQUID.

Section 4.3 compares SQUID untuned detection to two other MRI detection modalities: a SQUID coupled to a tuned superconducting gradiometer and a room-temperature amplifier coupled to a tuned copper coil (conventional MRI detection). In particular, it asks the question: over what range of precession frequencies does each modality yield the highest SNR? I begin by defining a common sample and pickup coil geometry with which to compare the three detection modalities and estimating the required MRI bandwidth. The magnetic field noise of SQUID untuned detection is independent of frequency and is calculated Sec. 4.1.2. In the case of SQUID tuned detection, the high intrinsic quality factor of the superconducting gradiometer must be damped to obtain the required bandwidth. The simplest approach is to insert a cold resistor in series with the gradiometer, but this introduces substantial Nyquist noise. In a more sophisticated approach, Seton and coworkers [2] provide damping while introducing much less noise by applying the phase-shifted output of the SQUID electronics as a flux to the gradiometer. I show that at frequencies below 2 MHz, the magnetic field noise of SQUID tuned detection decreases with increasing precession frequency and calculate the frequency above which tuned detection provides lower noise than untuned detection. However, the stray capacitance of the superconducting pickup coil and its leads constrain the number of turns on the pickup coil and the SQUID input coil, causing the noise to increase above 2 MHz. Furthermore, warm conducting samples (such as the human body) generate magnetic field noise with a power spectrum nearly independent of frequency [3]. Therefore, at precession frequencies for which the magnetic field noise becomes negligible compared to the sample noise, conventional detection and SQUID tuned detection are equally sensitive. In order to estimate these frequencies, I calculate the radiofrequency resistance of the copper pickup coil and the sample noise of conducting cylindrical phantoms approximating human tissue. I conclude by plotting the SNR of a 1 mm^3 voxel as a function of precession frequency for all three detection modalities.

4.1. Theoretical magnetic field noise of SQUID untuned detection

4.1.1. Flux noise of a bare SQUID

I begin by summarizing the results obtained by Tesche and Clarke [4] for the theoretical voltage and flux noise of a SQUID in the absence of a superconducting pickup

loop. They performed computer simulations of the resistively shunted junction model (Fig. 4.1) of the SQUID with $\beta_L = 2LI_0/\Phi_0 = 1$ and $\Gamma = 2\pi k_B T/I_0\Phi_0 = 0.05$, where L is the loop inductance of the SQUID and I_0 is the single junction critical current. They neglected the effects of the junction capacitance C, but assumed that a sufficiently low-valued shunt resistor R had been placed in parallel with each junction to prevent hysteresis ($\beta_C = 2\pi I_0 R^2 C/\Phi_0 < 1$). They obtained a maximum flux-to-voltage transfer coefficient

$$V_\Phi \equiv \left|\partial V/\partial\Phi\right| \approx R/L \qquad (4.1)$$

at a bias current $I_b \approx 2I_0$ and at a flux bias of $(2m+1)\Phi_0/4$, where m is an integer. At the optimum bias point, the voltage noise V_N across the SQUID had spectral density $S_V \approx 16k_BTR$ and the circulating noise current J_N around the SQUID had spectral density $S_J \approx 11k_BT/R$, where T = 4.2 K is the SQUID temperature. The voltage and current noises were substantially correlated with $S_{VJ} \equiv \langle V_N J_N \rangle / BW \approx 12k_BT$, where BW is the noise measurement bandwidth. While the current noise will induce noise currents in an input coil coupled to the SQUID, in the absence of such coupling, the flux noise of the SQUID is computed from the voltage noise alone. The spectral density of the flux noise is thus

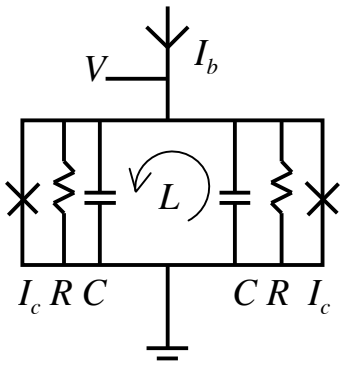

Figure 4.1: The resistor-capacitor shunted junction model of the SQUID. Claude and Tesche assume $1/C \rightarrow 0$.

$$S_\Phi = S_V / V_\Phi^2 \approx 16k_BTL^2/R. \qquad (4.2)$$

For typical parameters L = 400 pH and R = 10 Ω, V_Φ = 50 μV/Φ_0, $S_V^{1/2}$ = 0.1 nV Hz$^{-1/2}$, and $S_\Phi^{1/2}$ = 2 μΦ_0 Hz$^{-1/2}$. While later theoretical work [5] accounts for the junction capacitance and considers a larger range of β_L and Γ, I will use the simple results of Tesche and Clarke to estimate the sensitivity of SQUID magnetometers.

4.1.2. Magnetic field noise of a SQUID magnetometer

Although bare SQUIDs are excellent detectors of magnetic flux, their small size (≤ 1 mm) limits their magnetic field sensitivity. A superconducting flux transformer, shown schematically in Figure 4.2, can dramatically increase the field sensitivity of the SQUID. This device consists of a superconducting multi-turn input coil of inductance L_i

coupled to the SQUID washer with mutual inductance M_i and connected to a superconducting wire-wound pickup coil of inductance L_p and area A_p. A magnetic field B applied to the pickup coil will cause a supercurrent $I_p = BA_p/L_T$ to flow in the input coil, where $L_T = L_i + L_p$ is the total inductance of the input circuit. This in turn couples a flux BA_pM_i/L_T into the SQUID. Dividing this flux by the applied field yields the effective area

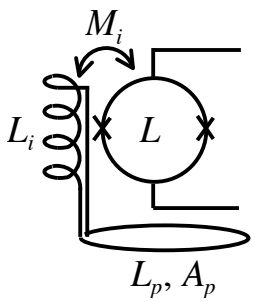

Figure 4.2: Schematic of a superconducting flux transformer. The SQUID RC shunt is omitted for clarity.

$$A_{eff} = A_pM_i/L_T \tag{4.3}$$

of the magnetometer. For an N-turn input coil patterned directly on top of the superconducting washer of the SQUID, $L_i = \alpha^2N^2L$ and $M_i = \alpha\sqrt{L_iL} = \alpha^2NL$, where $\alpha \le 1$ is the coupling coefficient. In order to calculate the magnetic field noise of a SQUID connected to a flux transformer, one must make assumptions about the interaction between the SQUID and the input coil.

4.1.2.1. SQUID parameters unaffected by input coil

I begin with the simplest assumption: the only effect of the input coil is to apply a magnetic flux I_pM_i to the SQUID. In this case, the flux noise of the SQUID is the same as that of a bare SQUID and is given by Eq. (4.2). The magnetic field noise is thus

$$S_B^{1/2} = \frac{S_\Phi^{1/2}}{A_{eff}} = \frac{S_V^{1/2}}{V_\Phi}\frac{L_T}{A_pM_i} = \frac{S_V^{1/2}}{V_\Phi}\frac{\left(\alpha^2N^2L + L_p\right)}{\alpha^2NA_pL}. \tag{4.4}$$

The magnetic field noise is minimized when $N = \sqrt{L_p/L}\,/\alpha$ and $L_i = L_p$, yielding a magnetic field noise of

$$S_B^{1/2} = \frac{S_V^{1/2}}{V_\Phi}\frac{2}{\alpha A_p}\sqrt{\frac{L_p}{L}} \approx \sqrt{\frac{16k_BT}{R}}\frac{2}{\alpha A_p}\sqrt{LL_p}\,. \tag{4.5}$$

Using the SQUID parameters L = 400 pH and R = 10 Ω, the parameters of the 65-mm diameter second-order gradiometer $A_p = 3.3 \times 10^{-3}$ m^2 and L_p = 1.7 μH and assuming $\alpha = 0.9$ (Ketchen and Jaycox [6] measured 0.93; Hilbert and Clarke [7] measured 0.84), the optimal field noise is $S_B^{1/2} = 0.17$ fT Hz$^{-1/2}$ (referred to the bottom loop of the pickup coil) obtained with N = 72 input coil turns and $A_{eff} = 23$ mm^2. The second-generation gradiometer described in Sec. 5.2 separates the two center gradiometer coils by 2.5 mm, thereby reducing its self-inductance to L_p = 1.3 μH. With this gradiometer, the optimal

field noise is $S_B^{1/2} = 0.15$ fT Hz$^{-1/2}$ obtained with $N = 63$ input coil turns and $A_{eff} = 26$ mm^2. I will use $L_p = 1.3$ μH in all subsequent calculations in this chapter.

The initial assumption of this section is unphysical. If a current flowing in the input coil couples flux into the SQUID, a current flowing in the SQUID will induce flux in the pickup coil. This back-action can be divided into two parts. First, the low-frequency circulating current and current noise in the SQUID produce currents in the input coil that in turn couple flux back to the SQUID. Second, this same phenomenon occurs at the Josephson frequency (~10 GHz), thereby influencing the dynamics of the SQUID itself. While the first effect occurs for all SQUIDs coupled to input coils, the high-frequency currents that produce the second effect can be absorbed by parasitic capacitance in the input coil. Rather than attempting to estimate the parasitic capacitance of the input coil, I will estimate the magnetic field noise in the two extreme cases of parasitic capacitance sufficient to damp all high-frequency oscillations and negligible parasitic capacitance. Since Martinis and Clarke [1] have already calculated the voltage response and voltage noise of a SQUID tuned amplifier in both limits, I will simply extend their treatment to a SQUID untuned magnetometer.

4.1.2.2. Large parasitic capacitance/no high-frequency oscillations

Martinis and Clarke consider the SQUID tuned amplifier shown in Fig. 4.3; the input coil of the SQUID is connected to a voltage $V_i(\omega)$ in series with a resistor R_i, a capacitor C_i, and an inductor L_p. A current J circulates around the SQUID loop and a flux Φ threads it. In the case of complete damping of high-frequency current fluctuations in the input coil, they compute a voltage

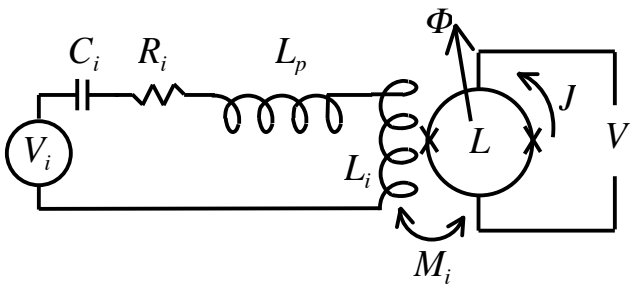

Figure 4.3: A generalized SQUID tuned amplifier.

$$V(\omega) = V_N(\omega) + M_i V_\Phi \frac{V_i(\omega) - j\omega M_i J_N(\omega)}{Z_T(\omega) + j\omega M_i^2 J_\Phi} \tag{4.6}$$

measured across the SQUID, where $Z_T(\omega) = R_i + j\omega(L_i + L_p) - j/\omega C_i$, $V_N(\omega)$ and $J_N(\omega)$ are the Fourier transforms of the time-dependent voltage noise and circulating current noise, respectively, and $J_\Phi = (\partial J/\partial \Phi)$ is the response of the circulating current to an

applied flux. In the case of an untuned magnetometer, $R_i = 1/C_i = 0$ and $V_i(\omega) = j\omega A_p B(\omega)$, where $B(\omega)$ is the field applied to the pickup loop. In this case, Eq. (4.6) becomes

$$V(\omega) = V_N(\omega) + V_\Phi \frac{M_i A_p B(\omega) - M_i^2 J_N(\omega)}{L_T + M_i^2 J_\Phi}. \tag{4.7}$$

Hilbert and Clarke [7] performed analog simulations of SQUID dynamics and calculated J_Φ in terms of the SQUID parameters as

$$J_\Phi = -\eta/L - j\omega\xi/R; \tag{4.8}$$

at a flux bias of $(2m+1)\Phi_0/4$, η ranges from -0.05 to 0.3 and ξ ranges from 0.1 to 1.25 depending on the bias current. Since the inductive term dominates J_Φ at the SQUID readout frequency, I neglect the resistive term. The inductive term changes the effective area to

$$A'_{eff} = A_p M_i / \left(L_T - \eta M_i^2/L\right) = A_p M_i / L'_T, \tag{4.9}$$

where $L'_T = L_i + L_p - \eta M_i^2/L$. The flux noise can be expressed by dividing Eq. (4.7) with no applied field by V_Φ to obtain

$$\Phi_N(\omega) = \frac{V_N(\omega)}{V_\Phi} - \frac{M_i^2 J_N(\omega)}{L'_T}. \tag{4.10}$$

Taking into account the correlation between the voltage and circulating current noises, the spectral density of the flux noise is

$$S'_\Phi = \left\langle \Phi_N^*(\omega)\Phi_N(\omega)\right\rangle / BW = \frac{S_V}{V_\Phi^2} - \frac{2M_i^2 S_{VJ}}{V_\Phi L'_T} + \frac{M_i^4 S_J}{L_T'^2}, \tag{4.11}$$

where BW represents the bandwidth of the noise measurement which is included in the spectral densities in the rightmost expression. The spectral density of the magnetic field noise is thus

$$S'_B = \frac{S'_\Phi}{A'^2_{eff}} = \frac{1}{A_p^2}\left(\frac{L_T'^2 S_V}{M_i^2 V_\Phi^2} - \frac{2L'_T S_{VJ}}{V_\Phi} + M_i^2 S_J\right). \tag{4.12}$$

Substituting the estimates of V_Φ, S_V, S_J, and S_{VJ} from Section 4.1.1 and taking the square root, I obtain the magnetic field noise

$$S_B'^{1/2} \approx \frac{1}{A_p}\sqrt{\frac{16k_B TL}{R}}\sqrt{\frac{\left[\left(1-\eta\alpha^2\right)L_i + L_p\right]^2}{\alpha^2 L_i} - \frac{3}{2}\left[\left(1-\eta\alpha^2\right)L_i + L_p\right] + \frac{11}{16}\alpha^2 L_i}. \tag{4.13}$$

For comparison, substituting the same values into Eq. (4.4) yields

$$S_B^{1/2} \approx \frac{1}{A_p}\sqrt{\frac{16k_BTL}{R}}\sqrt{\frac{\left(L_i+L_p\right)^2}{\alpha^2 L_i}} \tag{4.14}$$

for the magnetic field noise neglecting interactions between the SQUID and input coil. Since $L_i < L_i + L_p \approx \left(1-\eta\alpha^2\right)L_i + L_p$, the effect of these interactions is to lower the magnetic field noise. I will estimate the magnitude of this reduction after treating the case of negligible parasitic capacitance.

4.1.2.3. Negligible parasitic capacitance

In the case of negligible damping of high-frequency current fluctuations in the input coil, Martinis and Clarke [1] show that the SQUID behaves as if its inductance were equal to the reduced inductance

$$L^r = \left(1-\alpha_e^2\right)L \tag{4.15}$$

where

$$\alpha_e^2 = M_i^2/L_T L = \alpha^2 L_i/L_T\,. \tag{4.16}$$

The voltage measured across the SQUID is

$$V(\omega) = V_N^r(\omega) + M_i V_\Phi^r \frac{V_i(\omega) + M_i J_N^r(\omega)\left(R_i + 1/j\omega C_i\right)/L_T}{Z_T(\omega) - J_\Phi^r M_i^2\left(R_i + 1/j\omega C_i\right)/L_T}, \tag{4.17}$$

where $V_N^r(\omega)$, $V_N^r(\omega)$, V_Φ^r, and J_Φ^r refer to the respective parameters of a SQUID with inductance L^r. Substituting $R_i = 1/C_i = 0$ and $V_i(\omega) = j\omega A_p B(\omega)$, for an untuned magnetometer, I obtain

$$V(\omega) = V_N^r(\omega) + M_i V_\Phi^r \frac{A_p B(\omega)}{L_T}. \tag{4.18}$$

The effects of the circulating current and current noise have vanished, so the reduced parameters $V_N^r(\omega)$ and V_Φ^r are the only formal difference between this case and that of Sec. 4.1.2.1. The field noise can therefore be expressed as

$$S_B'^{1/2} = \frac{\sqrt{S_V^r}}{V_\Phi^r}\frac{L_T}{A_p M_i}, \tag{4.19}$$

where S_V^r is the spectral density of the voltage noise of a SQUID with inductance L^r. Assuming that the results of Sec. 4.1.1 still hold for a SQUID with inductance L^r, I estimate $S_V^r = S_V$ and

$$V_\Phi^r \approx \frac{R}{L}\left(1-\alpha^2 L_i/L_T\right)^{-1} \tag{4.20}$$

yielding a magnetic field noise

$$S_B'^{1/2} \approx \frac{1}{A_p}\sqrt{\frac{16k_BTL}{R}}\sqrt{\frac{\left[\left(1-\alpha^2\right)L_i + L_p\right]^2}{\alpha^2 L_i}}. \tag{4.21}$$

Like the previous case, the presence of interactions between the SQUID and input coil lowers the magnetic field noise.

4.1.2.4. Magnetic field noise comparison of input coil models

Table 4.1 compares the optimal input coil inductance and magnetic field noise of SQUIDs connected to input coils with high and low parasitic capacitance by evaluating Eqs. (4.13) and (4.21) for different values of α and η. The field noise is normalized to that obtained in Section 4.1.2.1 by dividing by Eq. (4.14) evaluated with $L_i = L_p$. In all cases, the interactions between the SQUID and input coil lower the magnetic field noise and the noise is minimized by choosing an input coil inductance $L_{i,optimal} > L_p$. However, fabrication constraints limit the number of input coil turns that can be placed on top of the SQUID washer, thereby limiting L_i. I therefore also calculate the noise with $L_i = L_p$; only in the last two entries of Table 4.1 does this noise exceed the optimal noise by more than 10%. For $L_i = L_p$, the models of Martinis and Clarke predict a magnetic field noise of 0.11-0.12 fT $Hz^{-1/2}$ for $\alpha = 0.7$ and 0.087-0.11 fT $Hz^{-1/2}$ for $\alpha = 0.9$.

Table 4.1: Comparison of magnetic field noise using different input coil models.

Input coil model	α	η	$L_{i,optimal}$ / L_p	$S_B'^{1/2}/S_B^{1/2}$, $L_i = L_{i,optimal}$	$S_B'^{1/2}/S_B^{1/2}$, $L_i = L_p$
Large $C_{parasitc}$	0.7	0	1.52	0.80	0.82
Large $C_{parasitc}$	0.7	0.3	1.94	0.71	0.75
No $C_{parasitc}$	0.7	-	1.96	0.71	0.76
Large $C_{parasitc}$	0.9	0	2.06	0.66	0.71
Large $C_{parasitc}$	0.9	0.3	3.10	0.49	0.59
No $C_{parasitc}$	0.9	-	5.26	0.44	0.60

4.2. Measured magnetic field noise of SQUID untuned detection

The theory presented in the previous section suggested that it might be possible to achieve more than an order of magnitude improvement in MRI voxel SNR by replacing the installed proprietary Quantum Design (QD) SQUID. When operated in the MRI system, this SQUID exhibited a flux noise of 6.5 $\mu\Phi_0$ $Hz^{-1/2}$ and had a measured effective area of 7.5 mm^2 yielding a field noise of 1.7 fT $Hz^{-1/2}$. In contrast, the theoretical 63-turn

SQUID considered in Sec. 4.1.2.1 achieves a flux noise of 2 $\mu\Phi_0$ Hz$^{-1/2}$. For $\alpha = 0.9$, its effective area 26 mm^2 when connected to the L_p = 1.3 μH gradiometer, yielding a field noise of 0.15 fT Hz$^{-1/2}$. Taking into account the interaction between the SQUID and input coil lowers the predicted field noise still further. Quantum Design sales literature specifies a flux noise < 5 $\mu\Phi_0$ Hz$^{-1/2}$ and I am not certain why the QD SQUID exhibits such high flux noise.

In our search for lower-noise SQUIDs, we purchased five 1.2-mm square-washer SQUIDs with 200 μm square washer holes and N = 60-turn input coils from Michael Mück (ez SQUID Mess- und Analysegeräte, Germany). For these SQUIDs, I measure M_i = 20 nH and estimate $L_i = NM_i$ = 1.2 μH, an excellent match for the L_p = 1.3 μH second-generation gradiometer. I also tested a SQUID employing a circular washer with 200-μm inner diameter and 1400-μm outer diameter fabricated by Vasili Semenov; the input coil of this SQUID also has 60 turns. This SQUID has M_i = 16.6 nH, so L_i = 1.0 μH. While the SQUIDs fabricated by Mück were basically 60-turn versions of an old Clarke group design [8], Semenov used an advanced design in an attempt to minimize the input coil resonances that typically cause increased flux noise in SQUIDs coupled to many-turn input coils. For example, Semenov replaced the solid washer found in most SQUIDs with a series of concentric rings in order to minimize the area in which the SQUID washer and input coil overlap, thereby minimizing the capacitance between these components. Section 4.2.1 describes measurements of the flux noise of these SQUIDs, and Sec. 4.2.2 describes the performance of one of M. Mück's SQUIDs when installed in the low-field MRI system.

4.2.1. Measurements of SQUID flux noise

Because connecting a SQUID to the MRI gradiometer and measuring the magnetic field noise involves delicate niobium wire bonding and typically renders the SQUID MRI system inoperable for a few days, I began by measuring the flux noise of possible replacement SQUIDs attached to a separate cryogenic probe. I could then predict the magnetic field noise of the SQUID installed in the MRI system from its measured flux noise and mutual inductance using the theory of Sec. 4.1.2.

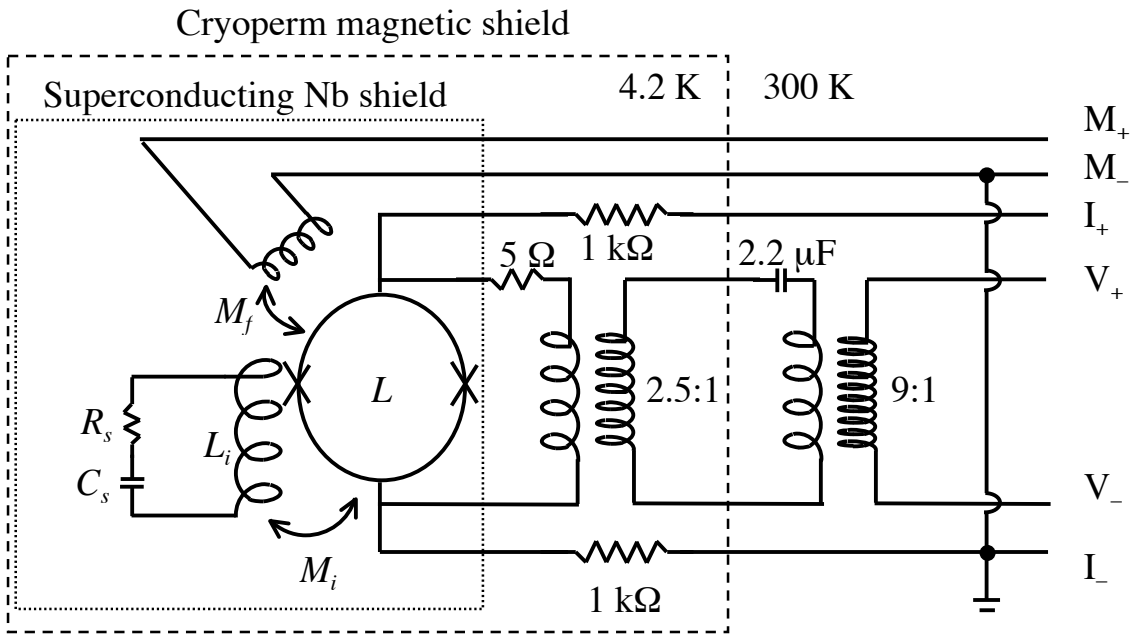

Figure 4.4: Circuit employed to measure SQUID flux noise. The I_+ and I_- leads supply bias current, the M_+ and M_- leads apply flux modulation and feedback, and the V_+ and V_- leads measure the voltage across the SQUID.

4.2.1.1. Measurement apparatus

Figure 4.4 shows the circuit used to measure SQUID flux noise. I attach the SQUID to a fiberglass circuit board with rubber cement, and then attach current and voltage leads to the SQUID using aluminum wire bonds to copper pads patterned on the circuit board. I then insert the circuit board into a cylindrical niobium shield manufactured by Quantum Design. I attach the niobium shield to the end of a cryogenic probe with yellow 3M® tape and then enclose it within a Cryoperm® magnetic shield. Finally, I lower the end of the probe into a liquid helium cryostat. The SQUID must be measured within a radiofrequency-shielded room to obtain optimal flux-modulation amplitude.

Three pairs of twisted copper leads contained within copper-nickel tubes provide bias current, allow flux modulation, and measure the voltage across the SQUID. The leads I_+ and I_- provide bias current to the SQUID; the stray capacitance of the twisted leads and the two 1 kΩ resistors form a low-pass filter to attenuate radiofrequency noise. M_+ and M_- are connected to a 10-turn wire-wound niobium modulation coil that is attached to the side of the circuit board opposite the SQUID. I measure the SQUID voltage by connecting the primary of a cryogenic transformer across the SQUID; a 5 Ω

resistor prevents the bias current from being completely shunted through the transformer primary. The secondary of the cryogenic transformer is connected to the primary of a room-temperature transformer. The preamplifier of the SQUID flux-locking electronics measures the voltage across the secondary of the room-temperature transformer.

The SQUID input coil is wire-bonded to two niobium foil plates attached to the circuit board with Miller-Stevenson epoxy. Each niobium plate has a single screw terminal. One can measure M_i by attaching wires to these terminals and measuring the SQUID response to an applied current; since these connections can couple additional noise to the SQUID, they are not used during noise testing and not shown in Fig. 4.4. A shunt formed by soldering a surface-mount resistor R_s and a surface-mount capacitor C_s across the screw terminals damps high-frequency resonances in the SQUID input coil. Although some SQUIDs have significantly higher flux noise in the absence of this shunt, the Nyquist noise of the shunt resistor contributes to the measured flux noise. Section 4.2.1.3 calculates the magnitude of this noise and its dependence on the flux modulation frequency.

4.2.1.2. Transformers and impedance matching

The proper choice of transformers is essential to match the impedance of the SQUID to the impedance of the preamplifier. Figure 4.5 shows a schematic of a SQUID connected to a preamplifier with voltage noise V_{NA}, current noise J_{NA} and gain G via a transformer with primary and secondary coil inductances of L_1 and L_2, respectively. For a transformer with N_1 primary turns and N_2 secondary turns wound on a core with inductance L_0 per turn squared, $L_1 = N_1^2 L_0$, $L_2 = N_2^2 L_0$, and the mutual inductance between the transformer coils is $M = N_1 N_2 L_0$. The SQUID is represented by a voltage source V_{SQ} in series with a resistor R_D representing the dynamic impedance of the SQUID at its operating point (the SQUID inductance can be neglected compared to that of the transformer). The preamplifier input voltage V_2 is related to V_{SQ} through the coupled equations

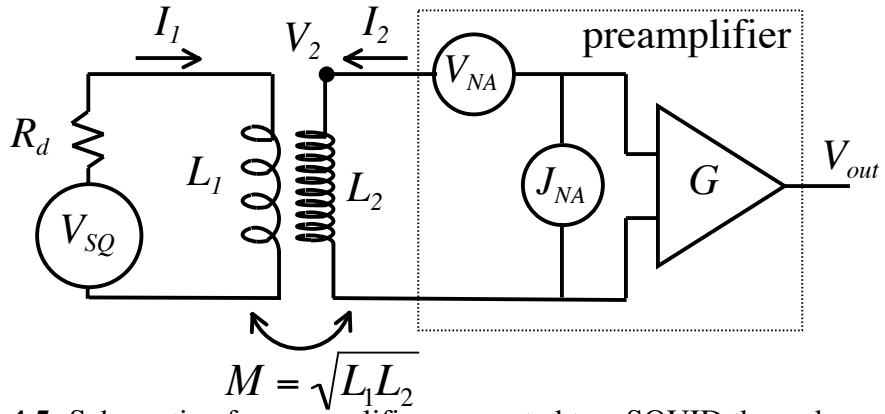

Figure 4.5: Schematic of a preamplifier connected to a SQUID through a transformer showing the preamplifier voltage and current noise.

$$\begin{aligned} V_{SQ} - I_1 R_D - L_1 \frac{dI_1}{dt} - M \frac{dI_2}{dt} &= V_{SQ} - I_1 R_D - j\omega L_1 I_1 - j\omega M I_2 = 0 \\ V_2 - L_2 \frac{dI_2}{dt} - M \frac{dI_1}{dt} &= V_2 - j\omega L_2 I_2 - j\omega M I_1 = 0 \end{aligned}, \tag{4.22}$$

where I_1 is the current in the transformer primary and I_2 is the current in the transformer secondary caused by preamplifier current noise. If the transformer primary has enough turns so that $\omega L_1 >> R_D$, then in the absence of noise

$$V_2 = M \frac{dI_1}{dt} = M \frac{V_{SQ}}{L_1} = \sqrt{\frac{L_2}{L_1}} V_{SQ} = \frac{N_2}{N_1} V_{SQ}. \tag{4.23}$$

This is the familiar equation for transformer operation. To calculate the effect of the amplifier current noise, I set $V_{SQ} = 0$ and solve Eq. (4.22) for V_2 in terms of I_2 to obtain

$$V_2 = \frac{\omega^2 L_1 L_2 + j\omega R_D L_2}{R_D^2 + \omega^2 L_1^2} R_D I_2 \cong \frac{L_2}{L_1} R_D I_2 = \frac{N_2^2}{N_1^2} R_D I_2, \tag{4.24}$$

where I have substituted $M^2 = L_1 L_2$ and then assumed $\omega L_1 >> R_D$. Equations (4.23) and (4.24) show that the effect of the transformer is to increase the output voltage of the SQUID by a factor N_2/N_1 and its impedance by a factor N_2^2/N_1^2.

Assuming uncorrelated voltage and current noise, the total preamplifier noise of the circuit shown in Fig. 4.5 referred to the voltage at the SQUID is therefore

$$\sqrt{V_{NA}^2 + \left(G_T^2 R_D J_{NA}\right)^2} \Big/ G_T = \sqrt{\left(V_{NA}/G_T\right)^2 + \left(G_T R_D J_{NA}\right)^2}, \tag{4.25}$$

where $G_T = N_2/N_1$ is the transformer voltage gain. The minimum voltage noise of $(2R_D J_{NA} V_{NA})^{1/2}$ occurs for $G_T = (V_{NA}/R_D J_{NA})^{1/2}$. Setting this minimum noise equal to $(4k_B T_N R_D)^{1/2}$ yields $T_N = V_{NA} J_{NA}/2k_B$, the noise temperature of the preamplifier. Since R_D is

a property of the SQUID rather than the preamplifier and transformers can be used to trade voltage noise for current noise and vice-versa, T_N is the figure of merit for preamplifier noise.

The most versatile and lowest-noise flux-locking electronics in the Clarke group operates at a modulation frequency f_m = 100 kHz and has voltage noise V_{NA} = 1.8 nV Hz$^{-1/2}$ and 30 pF input capacitance. From measurements of the preamplifier output noise with its input connected to varying resistive and capacitive impedances, I estimate the current noise J_{NA} to be between 0.1 and 0.3 pA Hz$^{-1/2}$, corresponding to a noise temperature between 6.5 and 20 K. The signal source connected to this preamplifier should have impedance V_{NA}/J_{NA} to achieve the best possible performance; given the uncertainty in the measurement of J_{NA}, the optimal input impedance of the preamplifier ranges from 18 kΩ to 6 kΩ. The dynamic impedance of a SQUID can be determined by measuring the slope of its voltage versus bias current curve at the operating point; the resulting value of R_D is usually several times $R/2$, the parallel resistance of the shunt resistors. The SQUIDs measured in this section display dynamic resistances of up to 30 Ω. The optimal transformer gain is therefore between 24 and 14, again depending on the value of J_{NA}, and one requires $L_1 >> R_D/2\pi f_m$ = 48 μH to assure proper transformer operation.

In order to minimize the effect of Nyquist noise originating from the resistance of the probe leads, I employ a cryogenic transformer as shown in Figure 4.4. Ferrite core transformers have the highest values of L_0 for a given geometry, but such transformers fail at cryogenic temperatures. Molypermalloy powder (MPP) cores operate at cryogenic temperatures, but have substantially lower values of L_0. For example, the FerroxCube® TX13/7.1/4.8-3E27 ferrite transformer core has inner diameter 7 mm, outer diameter 13 mm, and height 5 mm and has L_0 = 2.75 μH/turn^2, while the Magnetics® 55046 MPP core has comparable dimensions but only L_0 = 0.255 μH/turn^2. I therefore employ two transformers as shown in Fig. 4.4: a cryogenic MPP-core transformer and a room-temperature ferrite-core transformer. For the measurements described in this chapter, I employed a G_T = 2.5 cryogenic transformer with L_1 = 120 μH wound on a core obtained from BTi, Inc. in the distant past and a G_T = 9, L_1 = 600 μH warm transformer wound on an Epcos® B64290-K45-X830 N30 ferrite core for a total transformer gain of 22.5. For

an R_D = 30 Ω SQUID connected to the preamplifier described in the previous paragraph through a transformer network of gain 22.5, Eq. (4.25) predicts a total amplifier noise contribution between 0.10 and 0.22 nV Hz$^{-1/2}$ referred to the voltage across the SQUID.

4.2.1.3. Noise generated by the input circuit shunt resistor

Although the shunting resistor and capacitor placed across the input circuit damp input coil resonances near the Josephson frequency, thereby reducing noise, the shunting resistor itself produces Nyquist current noise which couples flux noise into the SQUID through the input coil. The RMS flux noise coupled into the SQUID from a shunt consisting of a resistor R_s and a capacitor C_s at angular frequency ω is

$$S_{\Phi}^{1/2} = M_i \frac{\sqrt{4k_B T R_s}}{|Z_T|} = M_i \sqrt{\frac{4k_B T R_s}{R_s^2 + \left(\omega L_i - 1/\omega C_s\right)^2}}, \tag{4.26}$$

where $Z_T = R_i + j(\omega L_i - 1/\omega C_s)$ is the total impedance of the input circuit. My initial measurements used an R_s = 47 Ω, C_s = 10 nF shunt. Connecting this shunt to one of Mück's 60-turn SQUIDs with L_i = 1.2 μH and M_i = 20 nF yields $S_{\Phi}^{1/2}$ = 0.36 μΦ_0 Hz$^{-1/2}$ at the $\omega_0/2\pi$ = 5.6 kHz MRI precession frequency. This flux noise can be neglected compared to the 2 μΦ_0 Hz$^{-1/2}$ predicted flux noise of the SQUID. However, when operated in a flux-locked loop, the SQUID not only mixes low-frequency signals up to f_m, but also mixes noise at $2f_m$ down to f_m. Equation (4.26) indicates that the SQUID is exposed to a flux noise of 11 μΦ_0 Hz$^{-1/2}$ at $\omega/2\pi = 2f_m$ = 200 kHz. Luckily, not all this noise appears at the output of the flux-locked loop.

To calculate the contribution from this high-frequency noise, I begin by calculating the ratio of the lock-in detector (shown in Fig. 1.4) response to a flux signal at frequency $2f_m$ to its response to a constant applied field. Assuming that the oscillator applies a sinusoidal flux modulation (square wave modulation can also be used) with amplitude $\Phi_0/4$ and the SQUID voltage is a sinusoidal function of the total applied flux, when exposed to an external flux $\Phi_a(t)$, the oscillating component of the SQUID output is given by

$$V_{SQ}(t) = -\frac{\Phi_0 V_{\Phi}}{2\pi} \cos\left[\frac{\pi}{2}\sin[\omega_m t] + \frac{2\pi}{\Phi_0}\Phi_a(t)\right], \tag{4.27}$$

where $\omega_m = 2\pi f_m$. Assuming that $\Phi_a(t) << \Phi_0$, Eq. (4.27) becomes

$$V_{SQ}(t) = -\frac{\Phi_0 V_\Phi}{2\pi}\cos\left[\frac{\pi}{2}\sin(\omega_m t)\right] + V_\Phi \Phi_a(t)\sin\left[\frac{\pi}{2}\sin(\omega_m t)\right]. \quad (4.28)$$

The first term in Eq. (4.28) contains only even harmonics of ω_m, so it produces no response from the lock-in detector. If Φ_a represents a constant flux, the second term in Eq. (4.28) contains $\sin(\omega_m t)$ terms but not $\cos(\omega_m t)$ terms. Therefore, the phase of the lock-in detector is set so that it produces a voltage

$$V_L \propto \int_{-\pi/\omega_m}^{\pi/\omega_m} V_{SQ}(t)\sin(\omega_m t)dt = V_\Phi \Phi_a \int_{-\pi/\omega_m}^{\pi/\omega_m} \sin\left[\frac{\pi}{2}\sin(\omega_m t)\right]\sin(\omega_m t)dt. \quad (4.29)$$

Using the formula [9]

$$\frac{1}{\pi}\int_0^\pi \sin(\alpha \sin s)\sin(ns)ds = \begin{cases} 0, & n \text{ even} \\ J_n(\alpha), & n \text{ odd} \end{cases}, \quad (4.30)$$

I obtain $V_L \propto V_\Phi \Phi_a J_1(\pi/2)/f_m$; $J_1(\pi/2) = 0.567$. Now suppose that $\Phi_a(t) = \Phi_a \cos(2\omega_m t)$. In this case, Eq. (4.29) becomes

$$V_L \propto \frac{V_\Phi \Phi_a}{2}\int_{-\pi/\omega_m}^{\pi/\omega_m} \sin\left[\frac{\pi}{2}\sin(\omega_m t)\right]\left[-\sin(\omega_m t) + \sin(3\omega_m t)\right]dt, \quad (4.31)$$

which evaluates to

$$V_L \propto \frac{V_\Phi \Phi_a}{2 f_m}\left[-J_1(\pi/2) + J_3(\pi/2)\right] = \frac{V_\Phi \Phi_a}{2 f_m}\left[-0.567 + 0.069\right]. \quad (4.32)$$

The ratio of the lock-in detector response to $\cos(2\omega_m t)$ flux signals to its response to a constant flux of the same amplitude is therefore

$$\frac{V_L(f = 2f_m)}{V_L(f = 0)} = \frac{\left[J_1(\pi/2) - J_3(\pi/2)\right]/2}{J_1(\pi/2)} = 0.439. \quad (4.33)$$

Since the lock-in detector produces no response to an applied flux $\Phi_a \sin(2\omega_m t)$, but the resistor voltage noise is split evenly between both phases, the response to flux noise is an additional factor of $\sqrt{2}$ lower than the ratio given in Eq. (4.33). The mixed-down flux noise contribution is thus 0.31 times the applied flux noise at frequency $2f_m$ calculated from Eq. (4.26). For the SQUID and shunt considered in the previous paragraph, this noise is 3.4 $\mu\Phi_0$ $\text{Hz}^{-1/2}$.

The flux noise produced by the shunt resistor is substantially higher than the 2 $\mu\Phi_0$ $\text{Hz}^{-1/2}$ flux noise of a bare SQUID calculated in Sec. 4.1.1 and therefore dominates the measured noise Sec. 4.2.1.5. I chose $R_s = 47\ \Omega$ and $C_s = 10$ nF because Mück

recommended these values, and I did not realize that he had chosen them to measure SQUIDs with substantially lower values of M_i. When I calculated the magnitude of the flux noise produced by this shunt, I reduced C_s to 1 nF in subsequent measurements, which reduces the calculated shunt noise to 0.4 $\mu\Phi_0$ Hz$^{-1/2}$. Since the impedance of a 1 nF capacitor at the ~10 GHz Josephson frequency is negligible compared to the R_s = 47 Ω resistor, reducing C_s to this value does not diminish the resonance-damping properties of the shunt.

4.2.1.4. Measurement procedure

To measure the flux noise of a SQUID connected as shown in Fig. 4.4, I begin by measuring the output of the preamplifier on an oscilloscope. I adjust the bias current applied through the I_+/I_- leads and the flux modulation and constant flux applied through the M_+/M_- leads to maximize the SQUID modulation amplitude. I then close the feedback loop shown in Fig. 1.4. From Eq. (1.4), the voltage across the feedback resistor R_f is given by $V_f = \Phi_a R_f/M_f$. The feedback loop can maintain the flux through the SQUID at any integer multiple of Φ_0. Therefore, if I open and close the feedback loop while maintaining the same applied flux, its output may change by an integer multiple of $\Phi_0 R_f/M_f$. I perform this operation multiple times to determine the ratio R_f/M_f, thereby calibrating the flux-to-voltage coefficient of the flux-locked loop (FLL). The f_m = 100 kHz flux-locking electronics used to perform these measurements has an R_f = 5 kΩ; M_f depends on the position of the wire-wound feedback coil relative to the SQUID. A typical value is M_f ~ 10 pH yielding R_f/M_f = ~1 V/Φ_0. After determining R_f/M_f, I measure the SQUID flux noise in the frequency range of interest by connecting the output of the FLL to a spectrum analyzer.

The measured SQUID flux noise often depends sensitively on the bias current, flux modulation amplitude, and lock-in detector phase. In addition, the gain of the secondary amplifier after the fixed-gain preamplifier must be set to provide the appropriate signal amplitude to the lock-in detector. Often the lowest-noise settings do not produce the highest SQUID modulation amplitude at the preamplifier output and must be determined empirically. While the spectrum analyzer produces the best measurements of the SQUID flux noise, its slow speed hinders the rapid measurements required to optimize the noise with respect to the four parameters described above. The peak-to-peak amplitude of the

FLL loop output displayed on an oscilloscope provides a rapid estimate of the total noise, but the total noise depends on the FLL bandwidth. Since the FLL bandwidth scales with the amplitude of the signal reaching the lock-in detector, which depends on both the SQUID modulation amplitude and the secondary amplifier gain, minimizing the peak-to-peak amplitude of the FLL output with respect to these four parameters does not result in the lowest flux noise per unit bandwidth. To measure the noise in a fixed bandwidth, I employ a Princeton Applied Research® 113 amplifier as a relatively narrow bandpass filter by setting both its high-pass and low-pass filters to 1 kHz. Minimizing the amplitude of the filtered FLL output with respect to these four parameters reliably locates the minimum flux noise of a particular SQUID.

4.2.1.5. Experimental results

Table 4.2 summarizes the measurements of two SQUIDs obtained from Mück and one SQUID obtained from Semenov. The mutual inductance M_i, maximum peak-to-peak modulation amplitude V_{pp}, and flux noise $S_\Phi^{1/2}$ are measured as described above. I estimate the maximum flux-to-voltage transfer function as $V_\Phi \approx \pi V_{pp}/\Phi_0$; this expression is exact in the case of sinusoidal SQUID modulation. The voltage noise across the SQUID is estimated to be $S_V^{1/2} = S_\Phi^{1/2} V_\Phi$; in all three cases, this noise is substantially larger than the 0.10 to 0.22 nV $Hz^{-1/2}$ amplifier noise contribution calculated in Sec. 4.2.1.2. The effective area and predicted field noise when attached to the $L_p = 1.3$ μH gradiometer are calculated from Eqs. (4.3) and (4.4). The flux noise generated by the shunt resistor R_s is calculated from Eq. (4.26) multiplied by the 0.31 mixing factor. Only the measurement of Mück #1 has a substantial contribution from resistor shunt noise; subtracting the shunt noise from the measured flux noise results in an estimated SQUID noise of 6.7 $\mu\Phi_0$ $Hz^{-1/2}$.

Table 4.2: Summary of SQUID flux noise measurements. Semenov #1 was measured without an input coil shunt. Mück #2 had a flux noise of 20 $\mu\Phi_0$ Hz$^{-1/2}$ and is not shown.

SQUID	Mück #1	Mück #3	Semenov #1
M_i (nH)	20	20	16.6
L_i (μH)	1.2	1.2	1.0
Maximum modulation amplitude V_{pp} (μV)	30	57	91
Estimated V_Φ (μV/Φ_0)	94	180	290
Measured flux noise $S_\Phi^{1/2}$ ($\mu\Phi_0$ Hz$^{-1/2}$)	7.5	4.1	2.4
Voltage noise across SQUID $S_V^{1/2}$ (nV Hz$^{-1/2}$)	0.7	0.7	0.7
A_{eff} when attached to gradiometer (mm^2)	27	27	24
Predicted field noise $S_B^{1/2}$ (fT Hz$^{-1/2}$)	0.59	0.32	0.21
R_s (Ω)	47	47	-
C_s (nF)	10	1	-
Shunt flux noise ($\mu\Phi_0$ Hz$^{-1/2}$)	3.4	0.4	0

It is instructive to compare these results to the theoretical predictions of Sec. 4.1.1. While I did not measure the voltage versus bias current of the SQUIDs shown in Table 4.2, a SQUID with identical junction dimensions obtained from Mück had $R = 12$ Ω junctions. The SQUID inductance can be expressed as $L = L_h + L_s$, where L_h is the inductance of the square washer hole and L_s is the inductance of the slit. These inductances can be estimated from the formulas $L_h = 1.25\mu_0 d_h$, and $L_h = 0.35$ pH/μm l_s, where d_h is the hole dimension and l_s is the slit length. For the SQUIDs obtained from Mück, $d_h = 200$ μm, $l_s = 500$ μm, and $L \approx 500$ pH. For these parameters, the theory of Sec. 4.1.1 predicts $V_\Phi = R/L = 50$ μV/Φ_0, $S_V^{1/2} = 0.11$ nV Hz$^{-1/2}$, and $S_\Phi^{1/2} = 2.1$ $\mu\Phi_0$ Hz$^{-1/2}$. The SQUIDs measured in Table 4.2 show somewhat higher V_Φ and substantially higher $S_V^{1/2}$ than predicted. Both these effects could result from the input coil resonances that typically occur SQUIDs with many-turn input coils. Both SQUIDs obtained from Mück have substantially higher flux noise than predicted. Because of its smaller washer hole, I would expect Semenov's SQUID to have somewhat lower L than Mück's SQUIDs. Although I did not measure the junction resistance of this SQUID, it is probably not too far from 10 Ω, so the predicted flux noise of Semenov's SQUID is probably ~2 $\mu\Phi_0$ Hz$^{-1/2}$, and the measured flux noise nearly achieves this value.

When connected to the second-generation gradiometer, all three SQUIDs shown in Table 4.2 are predicted to achieve substantially lower field noise than the 1.7 fT Hz$^{-1/2}$ achieved by the QD SQUID attached to the first-generation gradiometer. Semenov's

SQUID is particularly remarkable; not only does it nearly reach the predicted flux noise with a 60-turn input coil patterned above the SQUID, it does so without the benefit of an input coil shunt. Not only would it make an excellent low-field MRI detector, a 0.21 fT $Hz^{-1/2}$ second-order gradiometer based on such a SQUID would be a truly world-class measurement device in its own right.

4.2.2. Measurements of gradiometer magnetic field noise

Because bonding niobium wire to the small, slotted bond pads on Semenov #1 would be a substantial challenge and we anticipated that external noise would negate the effects of its additional sensitivity, we chose to install Mück #3 in the MRI system. As we expected, the total noise measured in the MRI system was higher than the predicted value shown in Table 4.2; we attributed the excess noise to the deleterious effects of radiofrequency noise on the SQUID. The second-generation aluminum shield described in Sec. 5.3 has much higher conductivity between aluminum plates, which substantially increases the radiofrequency attenuation compared to the first-generation shield. Unfortunately, while we were building the second-generation MRI system, Mück #3 failed for unknown reasons, and we replaced it with Mück #1. We then moved the gradiometer into the second-generation MRI system. This section describes how we connect the SQUID to the gradiometer and the noise measurements performed on Mück #1 installed in the second-generation MRI system.

4.2.2.1. SQUID and gradiometer configuration

When we moved the SQUID from the noise measurement probe to the MRI dewar, we replaced the QD niobium shield with a cryogenic SQUID package with integrated cold transformer obtained from Star Cryoelectronics. Figure 4.6(A) shows a diagram of the resulting circuit. The circuit is essentially the same as that of Fig 4.4 with the addition of the gradiometer and current-limiting Josephson junction array. Figure 4.6(B) shows the physical layout of these components within the SQUID package. The components are attached to two fiberglass circuit boards that are connected by copper wire and solder joints. The circuit board containing the transformer came with the Star Cryoelectronics package; we replaced the original 1 Ω resistor in series with the transformer with a 5 Ω resistor because of the high impedance of our SQUID but did not modify any other components. The V_+, V_-, I_+, and I_- leads pass through the niobium

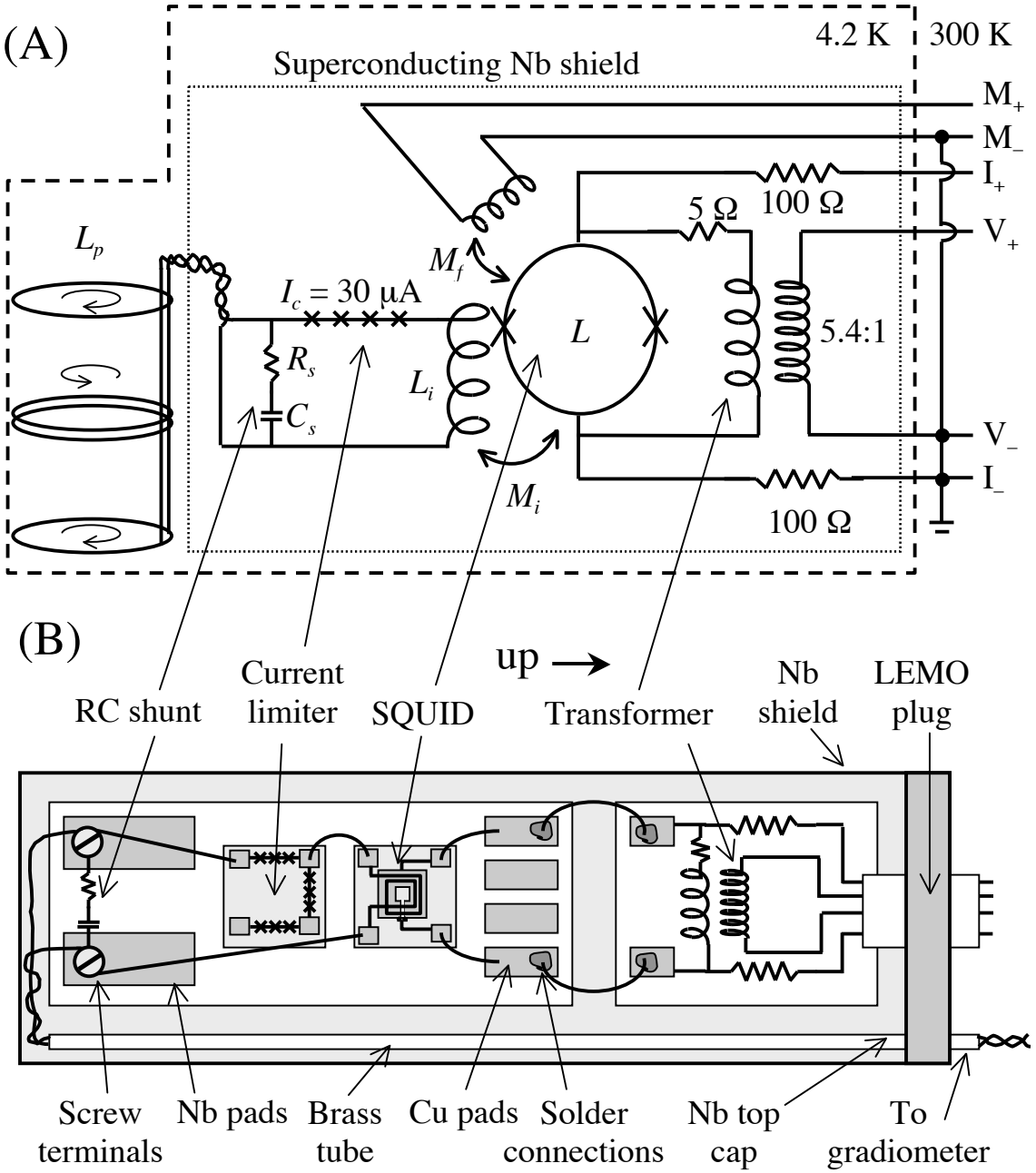

Figure 4.6: SQUID as installed in the microtesla MRI system. (A) Circuit diagram. (B) Physical location of components inside the Star Cyroelectronics niobium shield. The modulation coil, which is attached to the circuit board opposite the SQUID is not shown for clarity in (B).

shield inside a 10-pin LEMO connector. Figure 4.6(B) does not show the modulation coil, which is identical to the one described in Sec. 4.2.1.1; the M_+ and M_- leads also pass through the LEMO connector.

The circuit board containing the SQUID and current limiter is nearly identical to the circuit board used for the flux noise measurements. We originally tried to wire-bond the

input coil and current limiter to the Nb pads and reserve the screw terminals to connect the gradiometer leads. However, we find that screwing the annealed niobium wire into the screw terminals to hold it in place, and then bonding these wires to the input coil and current limiter produces the most reliable superconducting connections. When assembling the gradiometer, we loosen the screw terminals, place the gradiometer leads on top of the annealed niobium wires, and then tighten the screw terminal to press the wires together. The gradiometer leads exit the niobium shield through a thin brass tube, which shields them from the SQUID leads.

4.2.2.2. Transformer impedance and modulation frequency

Before connecting it to the SQUID, we measured the cold transformer in the Star Cryogenics package to have a gain of 5.4 and an input impedance of 18 Ω at 100 kHz. This input impedance is too low to connect to a SQUID with a dynamic resistance of up to 30 Ω. Rather than replace the pre-installed transformer, we connected the SQUID to flux-locking electronics operating at $f_m = 2$ MHz; if the permeability of the transformer core is frequency-independent, this leads to a 360 Ω input impedance. These flux-locking electronics contain an integrated gain 5 transformer before the preamplifier, for a total gain of 27. While we had previously used these flux-locking electronics to operate the QD SQUID, because they lack a preamplifier output connection, it is difficult to estimate the voltage and current noise.

4.2.2.3. Input circuit shunt resistor noise

In order to calculate the flux noise from the input circuit shunt resistor shown in Fig. 4.6(A), Eq. (4.26) must be modified to account for the pickup coil inductance L_p. The noise current generated by R_s flows through an effective inductance $L_{eff}^{-1} = L_i^{-1} + L_p^{-1}$, but only current flowing through L_i contributes flux noise to the SQUID. The flux noise is therefore

$$S_\Phi^{1/2} = M_i \frac{L_p}{L_i + L_p} \sqrt{\frac{4k_B T R_s}{R_s^2 + \left(\omega L_{eff} - 1/\omega C_s\right)^2}}. \tag{4.34}$$

For the $L_i = 1.2$ μH, $M_i = 20$ nH 60-turn input coil connected to the $L_p = 1.3$ μH gradiometer, $L_{eff} = 0.62$ μH. In order to reduce the shunt resistor noise despite the higher 2 MHz flux modulation frequency, we chose $R_s = 500$ Ω and $C_s = 1$ nF. These values yield $S_\Phi^{1/2} = 0.06\ \mu\Phi_0$ Hz$^{-1/2}$ at $\omega/2\pi = 5.6$ kHz and $S_\Phi^{1/2} = 3.4\ \mu\Phi_0$ Hz$^{-1/2}$ at

$\omega/2\pi = 2f_m = 4$ MHz. Multiplying by the mix-down factor of 0.31 derived in Sec. 4.2.1.3, the contribution of resistor shunt noise at frequency $2f_m$ to flux locked loop output is 1.1 $\mu\Phi_0$ Hz$^{-1/2}$.

Equation (4.34) can also be used to calculate the flux noise of the shunt of the QD SQUID when connected to the old $L_p = 1.7$ μH gradiometer. The Quantum Design SQUID package contains a $R_s = 10$ Ω, $C_s = 1$ nF shunt across the input coil [10]. Since $L_i = 1.9$ μH and $M_i = 11$ nH for this SQUID, the mixed-down flux noise is 1.9 $\mu\Phi_0$ Hz$^{-1/2}$ for the $f_m = 2$ MHz flux-locked loop. While this flux noise is not insignificant, does not explain the measured 6.5 $\mu\Phi_0$ Hz$^{-1/2}$ flux noise of the QD SQUID connected to the gradiometer. The QD SQUID is designed to be used in the $f_m = 500$ kHz flux-locked loop sold by QD; lowering the modulation frequency to this value would reduce the mixed-down shunt resistor noise to 0.24 $\mu\Phi_0$ Hz$^{-1/2}$.

4.2.2.4. Measurement procedure

To measure the effective area of the installed gradiometer, we wound a single 167-mm diameter turn of wire around the bottom of the cryostat such that it was 20 mm below the bottom loop of the gradiometer. The inductance between two concentric wire loops of radius r_1 and r_2 separated by an axial distance d is given by [11]

$$M_{12} = \mu\sqrt{r_1 r_2}\left[\left(2/k - k\right)\mathrm{K}\left(k^2\right) - 2\mathrm{E}\left(k^2\right)/k\right], \tag{4.35}$$

where $k^2 = 4r_1r_2/[(r_1 + r_2)^2 + d^2]$ and K and E are the complete elliptic integrals of the first and second kind, respectively. Using Eq. (4.35) to compute the mutual inductance between each of the gradiometer loops and the test coil yields a total mutual inductance of 12 nH. By measuring the flux detected by the SQUID produced by a current of known amplitude passing through this coil, we calculated an effective area of 25 mm^2. Using the inductance of the second-generation gradiometer, Eq. (4.3) predicts $A_{eff} = 27$ mm^2; stray inductance in the gradiometer leads probably explains the difference between the measured and calculated values.

To measure the magnetic field noise of the gradiometer (referred to the bottom pickup loop), we first place the cryostat in a shielded room to reduce the effects of radiofrequency and 5.6 kHz noise. We move the polarizing coil (a source of Nyquist noise) away from the gradiometer and disconnect all signal lines from the shielded room

except those necessary to operate the SQUID. The flux-locked loop is configured to produce $R_f/M_f = 0.66$ V/Φ_0. The output of the flux-locked loop is connected to a Krohn-Hite 3320 operating as a 3 kHz high-pass filter with gain 1, followed by a ~10x attenuator and a PAR® 113 operating as a 10 kHz low-pass filter with gain 10. The PAR output is measured by either a Hewlett-Packard 3561A spectrum analyzer or the 16-bit analog-to-digital converter of the TecMag Orion™ MRI console set to a 50 μs sampling time. The overall gain of the filter chain is 0.89, yielding 0.58 V/Φ_0 measured at the MRI console. We measure the voltage noise over a bandwidth of several hundred Hz centered at the 5.6 kHz MRI frequency, then convert the voltage noise to field noise using the measured flux-to-voltage coefficient and effective area.

4.2.2.5. Experimental results

Table 4.3 shows the lowest field noise measurements we have made of SQUIDs connected to the second-order gradiometer in various shielded rooms. Table 4.4 describes the attenuation properties of the shielded rooms. The measured field noise depends on the intrinsic flux noise of the SQUID, the effects of radiofrequency noise on the SQUID performance, and the amplitude of 5.6 kHz noise seen by the gradiometer. We measured the lowest field noise of 0.6 fT $Hz^{-1/2}$ from Mück #3 in the Birge B275 shielded room; the flux noise measurements shown in Table 4.2 predict a field noise of 0.32 fT $Hz^{-1/2}$. The lowest field noise obtained with Mück #1 was 0.75 fT $Hz^{-1/2}$ when measured in the second-generation Al shield described in Sec. 5.3; the predicted field noise is 0.59 fT $Hz^{-1/2}$. We expect higher preamplifier noise at 2 MHz than at 100 kHz, and this additional preamplifier noise is one possible cause of the additional field noise. Unfortunately, the low inductance of the cold transformer in the Star Cryoelectronics® SQUID package prevents us from testing the existing SQUID and gradiometer configuration with the 100 kHz flux-locked loop.

Table 4.3: Measured magnetic field noise of SQUIDs connected to the second-order gradiometer. The QD SQUID was connected to the first-generation gradiometer, while M. Mück's SQUIDs were connected to the second-generation gradiometer.

SQUID	Shielded room	Measured field noise (fT $Hz^{-1/2}$)
Quantum Design	First-generation Al shield	1.7 [a]
Mück #3	First-generation Al shield	1.1 [a]
Mück #3	Birge B203 Cu mesh room	1.1 [b]
Mück #3	Birge B275 shielded room	0.6 [b]
Mück #1	First-generation Al shield	0.9 [a]
Mück #1	Second-generation Al shield	0.75 [a]

[a] noise measured with the TecMag™ Orion console
[b] noise measured with the spectrum analyzer

Table 4.4: Attenuation characteristics of the shielded rooms shown in Table 4.3. The 5.6 kHz attenuation of the Al shields is calculated from their thickness. The B275 shielded room uses a combination of silicon steel and copper sheets to achieve 30 dB of attenuation at 60 Hz and 110 dB of attenuation at 15 kHz; I interpolate to estimate the 5.6 kHz value.

Shielded room	5.6 kHz attenuation	Radiofrequency attenuation
First-generation Al shield	17 dB	Poor
Second-generation Al shield	35 dB	Very good
Birge B203 Cu mesh room	None	Very good
Birge B275 shielded room	95 dB	Excellent

Table 4.3 shows that we measured lower field noise with Mück #1 in the first-generation Al shield than with the superior Mück #3. This seeming anomaly can be explained by improvements in the aluminum foil wrapping procedure between the measurements of Mück #3 and Mück #1. We wrapped the cryostat in aluminum foil as described in Sec. 1.4.4 for all field noise measurements. However, when testing Mück #1, Michael Mößle discovered that attaching a piece of conducting tape to the metal neck of the cryostat and running this tape all the way down the aluminum foil shielding decreased the resistance between the foil shield and electrical ground and improved the radiofrequency shielding. This enhancement produces radiofrequency shielding nearly equal to that achieved by the second-generation Al shield.

Mück #1 operated in the second-generation MRI system has 2.3 times lower magnetic field noise than the QD SQUID operated in the first-generation MRI system. Achieving the flux noise shown in Table 4.2 with Mück #1 connected to the gradiometer would produce a field noise 30% lower than the value shown in Table 4.3. Table 4.1 indicates that the interaction between the SQUID and its input coil connected to the gradiometer could lower the field noise by an additional 20-40%. These results could be

achieved by some combination of reducing amplifier noise and improving shielding. More substantial noise reduction would require replacing Mück #1 with a lower noise SQUID like Mück #3 or Seminov #1. However, Nyquist noise generated by the polarizing coil (Sec. 5.1.3) must also be taken into account to determine the overall performance of the MRI system.

4.3. Signal-to-noise ratio comparison of MRI detection modalities

After calculating and measuring the magnetic field noise of a SQUID connected to an untuned gradiometer, I now compare the magnetic field noise and MRI signal-to-noise ratio (SNR) of this detection modality to two others: a SQUID connected to a tuned superconducting input circuit and a semiconductor amplifier connected a room-temperature pickup coil (conventional Faraday detection).

4.3.1. Sample and detector geometry

I begin this calculation by choosing the sample and detector geometry for comparison. For the case of SQUID untuned detection, I choose the 65-mm diameter, 75-mm baseline second-generation gradiometer second-order gradiometer described in Sec. 5.2. Because Faraday detection is most effective at frequencies higher than 1 MHz and environmental noise can be easily screened at such frequencies, gradiometers are rarely employed in conventional MRI detection. I therefore choose a single 65-mm pickup loop in this case. In order to compare SQUID tuned detection to both SQUID untuned detection and room temperature Faraday coils, I consider SQUID tuned amplifiers connected to either a gradiometer or a magnetometer. In all cases I calculate the signal originating from a 1 mm^3 voxel of water; the sample is positioned 25 mm below the center of the pickup coil to allow space for the vacuum gap between the superconducting pickup coil and the room temperature sample.

The amplitude of the magnetic field detected at the pickup loop from a precessing spin-polarized voxel can be evaluated from Eq. (2.25) as

$$B_{det} = \frac{\mu_0 \beta_\perp}{4\pi A_p} M V_{voxel} \tag{4.36}$$

where M is the voxel magnetization, V_{voxel} is the voxel volume, and $\beta_\perp$ is defined by Eq. (2.24). The magnetic field generated by a loop of radius a carrying current I a distance d along the axis of the loop is parallel to the axis and has magnitude $\mu_0 I a^2 \Big/ 2\left(a^2 + d^2\right)^{3/2}$, so

$$\beta_\perp = 2\pi a^2 \Big/ \left(a^2 + d^2\right)^{3/2}. \tag{4.37}$$

Using Eq. (1.7) to calculate the equilibrium magnetization in a polarizing field B_p, Eq. (4.36) becomes

$$B_{det} = \frac{\mu_0}{4\pi} \frac{2V_{voxel}}{\left(a^2 + d^2\right)^{3/2}} \rho \frac{\gamma^2 \hbar^2}{4 k_B T_S} B_p = 9.0 \times 10^{-15} B_p, \tag{4.38}$$

where ρ is the voxel spin density and the equation has been evaluated using a = 32.5 mm, d = 25 mm, V_{voxel} = 1 mm^3, T_S = 310 K, and $\rho = 6.7 \times 10^{28}$ m^{-3}, the proton density of water. This equation demonstrates the inherent low-signal nature of MRI; applying a 1 T magnetic field to polarize the protons yields only 9 fT at the detector.

Unlike SQUID untuned detection, tuned detection has a limited bandwidth. Since detection bandwidth and noise can be traded off against each other, I choose the smallest possible bandwidth consistent with the MRI experiment to minimize noise. To perform frequency encoding on a sample of length $2a$ with resolution Δl and NMR FWHM linewidth δf requires a bandwidth $2a\delta f/\Delta l$. I assume that the detector must have twice this bandwidth to achieve sufficiently flat frequency response in the MRI bandwidth. Using Eq. (1.12) to express δf in terms of T_2^*, the required detector bandwidth is

$$BW_{det} = 4a \Big/ \pi T_2^* \Delta l. \tag{4.39}$$

For representative human tissue $T_2 \sim 60$ ms, yielding $\delta f \sim 5$ Hz. Using a = 32.5 mm and Δl = 1 mm, $BW_{det} \sim 700$ Hz. For the purposes of the SNR calculation, I assume that sufficient magnetic field homogeneity can be achieved so that $T_2^* = T_2$.

4.3.2. Field noise of SQUID tuned detection

Because calculating the sensitivity of SQUID tuned detection is rather complicated, I choose not to employ each of the assumptions about the interaction between the SQUID and input coil described in Sections 4.1.2.1-4.1.2.3. I instead neglect the influence of the input coil on the SQUID parameters and vice-versa but account for correlated voltage and current noise in the SQUID and the corresponding noise induced in the input coil. This corresponds to the case of large parasitic capacitance with $\eta = 0$; for $\eta \neq 0$, simply

substitute $L_T' = L_i + L_p - \eta M_i^2/L$ for L_T. Treating the case of negligible parasitic capacitance would require reworking the entire calculation.

To perform SQUID tuned detection, one inserts a tuning capacitor C_i in series with the input coil as shown in Fig. 4.7. Although the circuit is fully superconducting, the resistor R_i represents a combination of eddy current losses in the dewar and dielectric loss in the capacitor at the resonant frequency plus any intentionally added resistance. Applying a magnetic field B at angular frequency ω will cause a current

$$I_p = \frac{\omega^2 C_i A_p B}{\omega R_i C_i + j\left[\omega^2 L_T C_i - 1\right]} \qquad (4.40)$$

to flow in the input coil of the SQUID, where $L_T = L_i + L_p$. If C_i is chosen such that $\omega_0^2 L_T C_i = 1$, the reactive portion of the denominator vanishes at the MRI frequency. The effective area of the detector at $\omega = \omega_0$ is then

$$A_{eff} = M_i I_p / B = \omega_0 M_i A_p / R_i . \qquad (4.41)$$

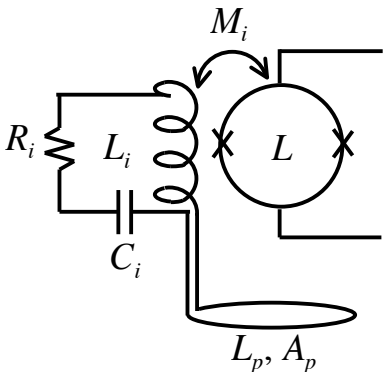

Figure 4.7: Schematic of SQUID tuned detection.

For $\omega_0 > R_i/L_T$, the effective area is greater than that of an untuned magnetometer, suggesting that tuned detection is relatively more effective at high frequencies. However, this analysis neglects the bandwidth of the detector, the interaction between the SQUID current noise and the tuned input circuit, and the current noise of the resistor R_i.

4.3.2.1. Resistively damped gradiometer

I begin by calculating the bandwidth of the tuned input circuit. Examining Eq. (4.40) shows that the half-width-half-maximum (HWHM) bandwidth of the stored energy of the pickup circuit (proportional to I_p^2) is $\Delta\omega = R_i/L_T$. In order to achieve the bandwidth BW_{det} required for MRI, one requires $\Delta\omega = \pi BW_{det}$ and thus $R_i = 4aL_T/lT_2$. Using the previous values for a, Δl, and T_2 and taking $L_T = 2.5$ μH one requires $R_i = 5.4$ mΩ. Assuming that the eddy current and dielectric losses of the superconducting resonator do not provide sufficient damping, additional damping must be added to the circuit. The most straightforward way to provide this damping is to add additional cold resistance in

series with the pickup coil. In this case, R_i represents the total resistance of the circuit, which contributes Nyquist voltage noise V_{RN} with spectral density $4k_BTR_i$.

Nyquist noise can be added to the SQUID tuned amplifier circuit shown in Fig. 4.3 by setting $V_i = V_{RN}$. The spectral density of the voltage noise across the SQUID can be calculated by evaluating the spectral density of Eq. (4.6) with $\eta = 0$ to obtain

$$S_V^{tot} = \frac{M_i^2 V_\Phi^2}{|Z_T|^2} 4k_B T R_i + S_V + \frac{\omega^2 M_i^4 V_\Phi^2}{|Z_T|^2} S_J - \frac{2\omega M_i^2 V_\Phi (\omega L_T - 1/\omega C_i)}{|Z_T|^2} S_{VJ}. \quad (4.42)$$

Seton *et al*. [2] arrive at an identical expression for the noise spectral density. An applied field $B(\omega)$ causes a voltage $V_i(\omega) = -j\omega A_p B(\omega)$ across the pickup loop. Using Eq. (4.6) again to evaluate the SQUID voltage response to this field I obtain

$$V = -j\omega M_i V_\Phi A_p B(\omega) / Z_T(\omega). \quad (4.43)$$

Dividing Eq. (4.42) by the square of the magnitude of the field-to-voltage transfer function yields the spectral density of the magnetic field noise

$$S_B = \frac{1}{A_p^2}\left[\frac{4k_BTR_i}{\omega^2} + \frac{|Z_T|^2}{\omega^2 M_i^2 V_\Phi^2} S_V + M_i^2 S_J - \frac{2(\omega L_T - 1/\omega C_i)}{\omega V_\Phi} S_{VJ}\right]. \quad (4.44)$$

Substituting $C_i = (\omega_0^2 L_T)^{-1}$ and $R_i = \Delta\omega L_T$ yields

$$S_B = \frac{1}{A_p^2}\left\{\frac{4k_BT\Delta\omega L_T}{\omega^2} + \frac{L_T^2\left[\Delta\omega^2\omega^2 + (\omega^2 - \omega_0^2)^2\right]}{\omega^4 M_i^2 V_\Phi^2} S_V + M_i^2 S_J - \frac{2L_T(\omega^2 - \omega_0^2)}{\omega^2 V_\Phi} S_{VJ}\right\}. \quad (4.45)$$

To compare the contributions of resistor noise and SQUID noise to the computed magnetic field noise, I consider the case of an L = 400 pH SQUID with a 60-turn input coil (α = 0.9, L_i = 1.2 μH, M_i = 19 nH) connected to the L_p = 1.3 μH second-order gradiometer. For definiteness I choose the $\omega_0/2\pi$ = 400 kHz precession frequency of Seton *et al*. and $BW_{det} = \Delta\omega/\pi$ = 700 Hz from the previous calculations. Using the expressions for V_Φ, S_V and S_J in Section 4.1.1 for an R = 10 Ω SQUID and evaluating the magnetic field noise at the resonant frequency, the resistor noise contributes 1.3×10^{-16} T $Hz^{-1/2}$, the SQUID voltage noise contributes 1.2×10^{-19} T $Hz^{-1/2}$, and the SQUID current noise contributes 4.6×10^{-17} T $Hz^{-1/2}$. The term containing S_{VJ} vanishes when $\omega = \omega_0$.

The contribution from the resistor dominates the total noise. Since A_p scales linearly with the number of turns on the gradiometer while L_p (and thus L_T for many turns) scales as its square, adding multiple turns to the gradiometer would not significantly decrease S_B.

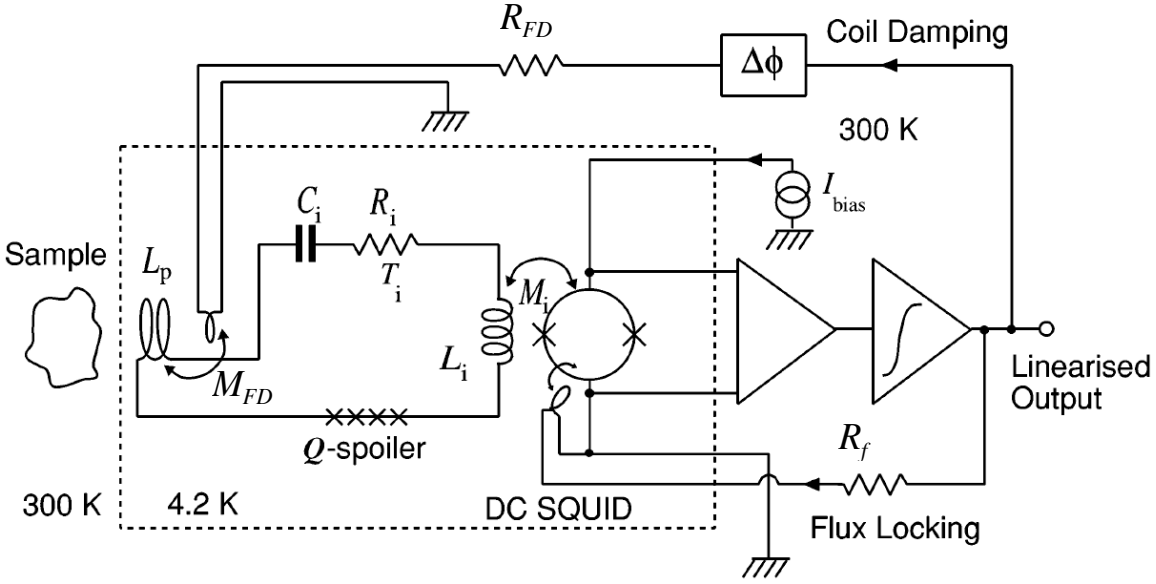

Figure 4.8: Schematic of the SQUID tuned MRI system of Seton *et al*. showing the flux locked loop and feedback damping circuits. Adapted from [12] with permission.

4.3.2.2. Feedback damped gradiometer

The above discussion suggests that one could substantially improve the noise of a SQUID tuned magnetometer or gradiometer by finding a way to damp the input circuit without introducing noise. Seton *et al*. [2] followed the lead of Simmonds, Fertig and Gifford [13] by applying feedback damping to the input coil. Figure 4.8 shows their most recent feedback damping circuit. To damp oscillations in the pickup coil, they apply the phase-shifted output of the flux-locked SQUID electronics as a flux to the pickup coil and adjust the phase shift to cancel the applied flux. The feedback damping introduces an effective resistance [2]

$$\Delta R_i = \omega M_i M_{FD} V_\Phi A / R_{FD}\,, \tag{4.46}$$

where R_{FD} is the resistance in the feedback damping line, M_{FD} is the mutual inductance between the pickup loop and the feedback damping coil, and A is the total gain of all amplification stages past the SQUID. The bandwidth with feedback damping becomes $\Delta\omega = (R_i + \Delta R_i)/L_T$, where R_i represents eddy current and dielectric loss. Because ΔR_i is included in Z_T but does not contribute resistor noise, Eq. (4.45) can be rewritten as

$$S_B = \frac{1}{A_p^2}\left\{\frac{4k_B T R_i}{\omega^2} + \frac{L_T^2\left[\Delta\omega^2\omega^2 + \left(\omega^2 - \omega_0^2\right)^2\right]}{\omega^4 M_i^2 V_\Phi^2} S_V + M_i^2 S_J - \frac{2L_T\left(\omega^2 - \omega_0^2\right)}{\omega^2 V_\Phi} S_{VJ}\right\}. \quad (4.47)$$

As written, this equation describes only a single-turn gradiometer. Equation (4.47) can be modified to represent a gradiometer with N_p turns by replacing A_p with $N_p A_p$ and L_p with $N_p^2 L_p$, where A_p and L_p represent the pickup coil area and inductance of a single-turn gradiometer. In order to optimize the number of turns on the input coil, the intrinsic coil resistance R_i must be split into eddy current losses R_e and dielectric losses R_d. As further discussed in Sec. 4.3.4, the fluctuation-dissipation theorem indicates that R_e can also be modeled as magnetic field noise from the environment that is picked up at the detector. Since external magnetic field noise does not depend on N_p, R_e contributes a constant term to S_B which can be included in the sample noise discussed in Sec. 4.3.4 but does not influence the optimal number of pickup coil turns. In contrast, R_d depends on the construction of the tuning capacitor and potentially on its value.

The dielectric loss of a capacitor C_i can be described by the dimensionless quantity $\delta = \omega C_i R_d$, where ω is the frequency at which the loss is measured. If this capacitor is installed in a resonant circuit with inductance L_T and no other sources of dissipation, the resulting intrinsic quality factor will be $Q_0 = \omega_0 L_T / R_d = 1/\delta$. Table 4.5 summarizes the quality factors measured in resonant circuits employing a variety of cryogenic capacitors. Hugh Seton expressed confidence that one could construct a 0.1 to 1 μF lead/PFTE capacitor that would achieve $Q_0 > 10{,}000$ [14]. I therefore assume that one can build resonant circuits with $1/\delta = Q_0$ ranging from 10,000 to 50,000 over a wide range of frequencies and employing capacitance up to $C_i = 100$ nF.

Table 4.5: Intrinsic quality factor of resonance circuits. Measured at 4.2 K unless noted.

Capacitor type	Capacitance	Frequency	Quality factor Q_0	Reference
Ceramic	0.1 and 1 μF	1 - 100 kHz	100 - 700[a]	Hammoud 1998 [15]
Lead/mylar	125 nF	3.15 kHz	6,400	Simmonds 1979 [13]
Silver mica	11 pF	30 MHz	7,320	Sleator 1987 [16,17]
Polystyrene	10 nF	425 kHz	42,000	Seton 1995 [2]
Lead/PFTE	1.2 nF	425 kHz	55,500	Seton 1997 [18]

[a] Measured at -200 °C.

I begin by calculating the magnetic field noise with no constraints on the value of C_i. Substituting $\omega = \omega_0$ and $R_i = R_d = \delta\omega_0 L_T$ into Eq. (4.47), replacing A_p with $N_p A_p$ and L_p with $N_p^2 L_p$ to represent a multi-turn pickup coil, and minimizing S_B with respect to N_p yields

$$S_B = \frac{2L_p}{A_p^2}\left[\frac{2k_B T\delta}{\omega_0} + \frac{L_i(\Delta\omega)^2}{\omega_0^2 M_i^2 V_\Phi^2} S_V + \frac{\Delta\omega}{\omega_0}\left(\frac{4k_B T L_i \delta}{\omega_0 M_i^2 V_\Phi^2} + \frac{(\Delta\omega)^2 L_i^2}{\omega_0^2 M_i^4 V_\Phi^4} S_V + \frac{1}{V_\Phi^2} S_J\right)^{1/2} S_V^{1/2}\right], \quad (4.48)$$

where the optimal number of turns is

$$N_p = \sqrt{\frac{M_i V_\Phi}{\Delta\omega L_p}}\left(\frac{4k_B T L_i \omega_0 \delta}{S_V} + \frac{(\Delta\omega)^2 L_i^2}{M_i^2 V_\Phi^2} + M_i^2\omega_0^2\frac{S_J}{S_V}\right)^{1/4}. \quad (4.49)$$

Following Sec. 4.1.2, I substitute $L_i = \alpha^2 N^2 L$ and $M_i = \alpha^2 N L$ to obtain

$$S_B = \frac{2L_p}{A_p^2}\left[\frac{2k_B T\delta}{\omega_0} + \frac{(\Delta\omega)^2}{\alpha^2\omega_0^2 L V_\Phi^2} S_V + \frac{\Delta\omega}{\omega_0 V_\Phi}\left(\frac{4k_B T\delta}{\alpha^2\omega_0 L} + \frac{(\Delta\omega)^2}{\alpha^4\omega_0^2 L^2 V_\Phi^2} S_V + S_J\right)^{1/2} S_V^{1/2}\right]. \quad (4.50)$$

Since L_i and M_i appear in Eq. (4.48) only in the ratio $L_i/M_i^2 = (\alpha^2 L)^{-1}$, if N_p is chosen according to Eq. (4.49), the resulting magnetic field noise does not depend on the number of input coil turns. However, the optimal value of N_p depends on N through the L_i and M_i terms appearing in Eq. (4.49). In order to estimate the relative magnitude of the terms in Eq. (4.50), I substitute $S_V = 16k_B TR$ and $S_J = 11k_B T/R$, and factor out all quantities except ω_0, $\Delta\omega$, and $V_\Phi = R/L$ to obtain

$$S_B = \frac{2L_p}{A_p^2}\frac{2k_B T}{\omega_0}\left[\delta + \frac{8(\Delta\omega)^2}{\alpha^2 V_\Phi \omega_0} + 2\sqrt{\frac{4\delta(\Delta\omega)^2}{\alpha^2 V_\Phi\omega_0} + \frac{16(\Delta\omega)^4}{\alpha^4 V_\Phi^2\omega_0^2} + \frac{11(\Delta\omega)^2}{V_\Phi^2}}\right]. \quad (4.51)$$

Since $\Delta\omega/V_\Phi = 9 \times 10^{-8}$, $\Delta\omega/\omega_0 << 1$, and $\alpha \sim 1$, while δ ranges from 2×10^{-5} to 2×10^{-4} depending on the quality of the capacitor, noise originating from dissipation in the capacitor overwhelms the SQUID voltage and current noise, and I can approximate Eq. (4.50) by its first term:

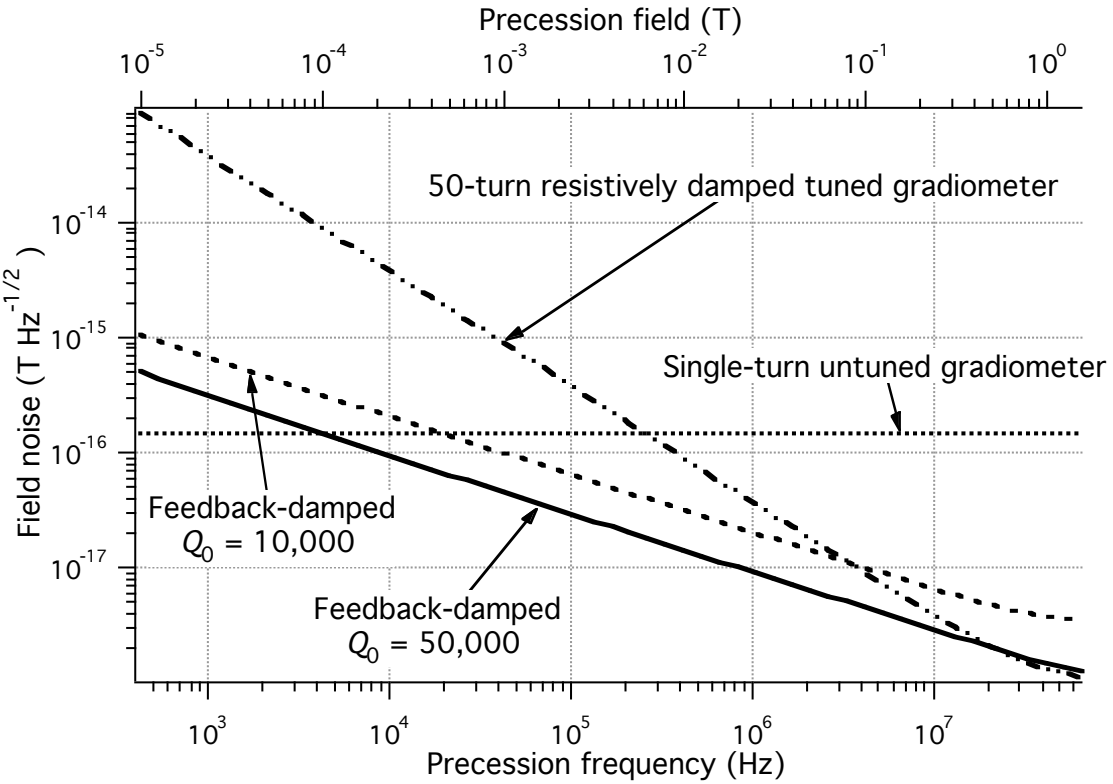

Figure 4.9: Magnetic field noise of SQUID tuned detection with feedback damping [Eq. (4.50)] compared to resistively damped tuned detection and SQUID untuned detection. The SQUID noise is evaluated using the equations of Sec. 4.1.1 with $L = 400$ pH and $R = 10$ Ω. The field noise is calculated assuming an $\alpha = 0.9$, $N = 60$ turn input coil connected to a multi-turn version of the $L_p = 1.3$ μH, $A_p = 3.3 \times 10^{-3}$ m^2 second-generation gradiometer. The untuned field noise is calculated from Eq. (4.4).

$$S_B \cong \frac{4k_B T L_p}{A_p^2 \omega_0}\delta. \tag{4.52}$$

Figure 4.9 shows Eq. (4.50) plotted over five decades of precession frequency for two different values of $Q_0 = 1/\delta$ and compares it to the magnetic field noise of resistively damped tuned detection and SQUID untuned detection. Feedback-damped tuned detection becomes superior to untuned detection at frequencies above 5 to 20 kHz, depending on the value of Q_0. Comparing the first term of Eq. (4.45) with Eq. (4.52) shows that the magnetic field noise of resistively damped tuned detection scales as ω_0^{-1}, while that of feedback-damped tuned detection scales as $\omega_0^{-1/2}$. The magnetic field noise of resistively damped detection crosses that of feedback-damped detection when $\Delta\omega/\omega_0 = \delta$ and feedback damping is no longer necessary to increase the detector bandwidth. The high-frequency region in Fig. 4.9 in which resistive damping produces lower noise than feedback damping occurs because my treatment of resistive damping

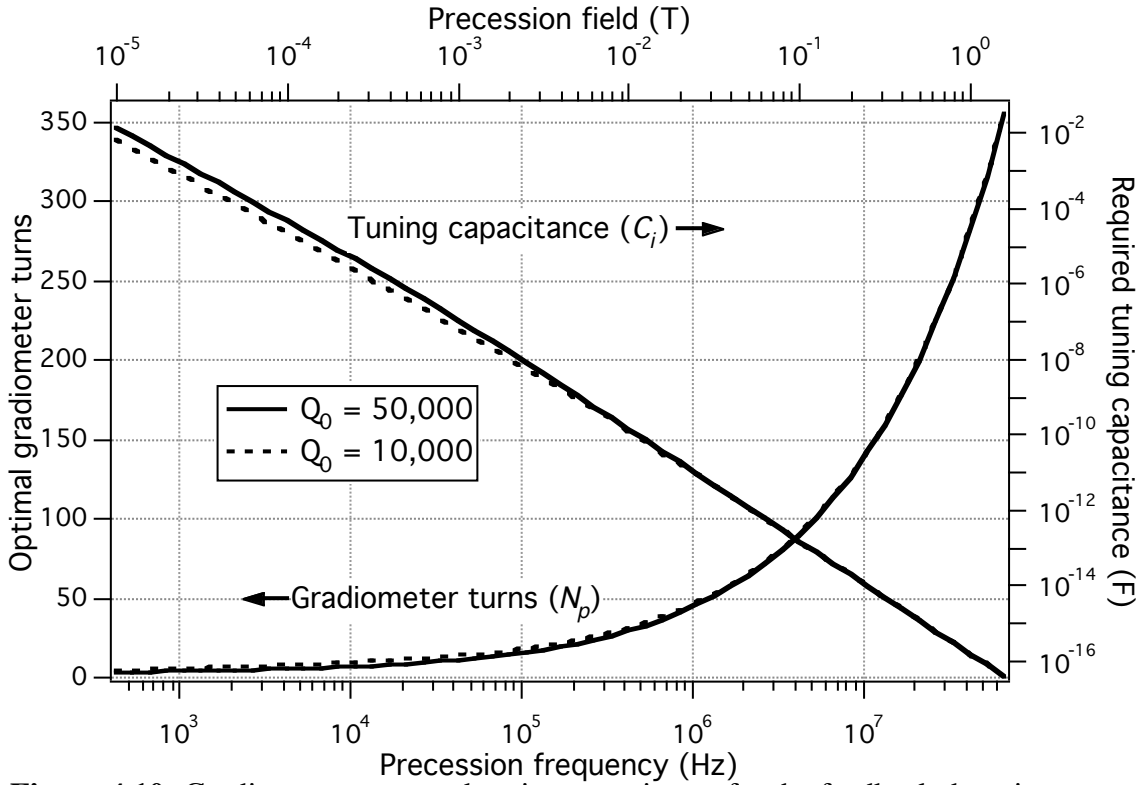

Figure 4.10: Gradiometer turns and tuning capacitance for the feedback damping detectors considered in Fig. 4.9 connected to an $L = 400$ pH, $N = 60$ turn SQUID.

neglects capacitor losses; such low-noise detection can only be achieved with a resonator Q_0 which exceeds Q_0 of the feedback-damped detector. I therefore consider only feedback damping for the remainder of this chapter.

However, while Eq. (4.50) minimizes the field noise with respect to N_p, it does not consider whether this results in physically realizable values for C_i. Figure 4.10 plots N_p computed from Eq. (4.49) and the resulting required C_i as functions of precession frequency for the two values of Q_0 shown in Fig. 4.9. The required tuning capacitance ranges from less than 0.1 fF to 10 mF. Both extremes are unphysical; the smallest tuning capacitance will be swamped by the stray capacitance of the gradiometer, while none of the cryogenic capacitors described Table 4.5 has a value anywhere near 10 mF. I therefore repeat this calculation, optimizing N and N_p while maintaining C_i between the limits $C_{i,min}$ and $C_{i,max}$, where $C_{i,min}$ represents the constraints of stray capacitance and $C_{i,max} = 100$ nF accounts for the previously-discussed capacitor fabrication constraints.

4.3.2.3. Feedback damped gradiometer with constrained tuning capacitance

The total stray capacitance in the input circuit can expressed as

$$C_{stray} = C_{stray}^{leads} + C_{stray}^{grad} + C_{stray}^{input}, \tag{4.53}$$

where C_{stray}^{leads} is the capacitance of the leads between the gradiometer and the SQUID, C_{stray}^{grad} is the capacitance of the gradiometer, and C_{stray}^{input} is the capacitance between the input coil and the SQUID washer. The stray capacitance acts as a shunt across the inductive elements of the circuit, so its effect can be neglected if the magnitude of the inductive impedance of the input circuit $\omega_0 L_T$ is much smaller than that of the stray capacitance $1/\omega_0 C_{stray}$. Since $C_i = 1/(\omega_0^2 L_T)$, this condition can be expressed as $C_{stray} << C_i$. I now proceed to estimate C_{stray}^{leads} and C_{stray}^{grad}. Since C_{stray}^{input} depends on the number of input coil turns, which is an output of the model, I temporarily neglect this term, then calculate its effects self-consistently in Sec. 4.3.2.4.

In order to maximize the balance of the superconducting gradiometer against uniform external fields, the superconducting shield of the SQUID package must be located far from the gradiometer and the leads between the gradiometer and SQUID package must be tightly twisted. In our MRI cryostat, the SQUID package is located a distance ~5a above the top loop of the gradiometer. The stray capacitance of the leads can be approximated by the capacitance of two wires of conducting radius ϕ and length 5a separated by twice the insulated wire radius ϕ_I:

$$C_{stray}^{leads} = \pi(5a)\varepsilon_0\varepsilon_r \big/ \cosh^{-1}(\phi_I/\phi) = 12 \text{ pF}, \tag{4.54}$$

where 5a = 160 mm, ϕ = 37.5 μm, and ϕ_I = 62.5 μm are the relevant lengths for our gradiometer, and I assumed the insulation has a relative permeability $\varepsilon_r = 3$.

Figure 4.11 shows a schematic of the stray capacitance of a multi-turn second-order gradiometer, where C_{Np} is the capacitance of upper and lower the N_p-turn loops, C_{2Np} is the capacitance of the center $2N_p$-turn loop, and C_b is the capacitance of the twisted leads between the loops. Assuming tightly

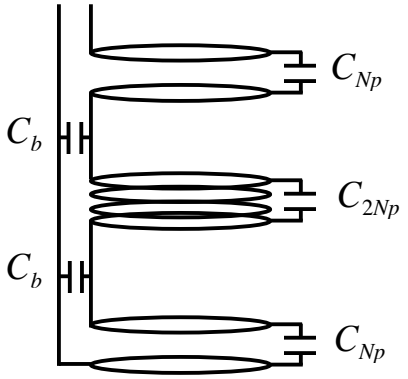

Figure 4.11: Stray capacitance model of a second-order gradiometer.

twisted wire over the $b = 75$ mm gradiometer baseline, $C_b = 5.7$ pF. Massarini and Kazimierczuk [19] show that the stray capacitance of an N_p-turn single layer inductor is $C_{Np} \approx C_{tt}/(N_p - 1)$, where C_{tt} is the capacitance between adjacent turns, and that the stray capacitance of double and triple layer inductors converges to $1.37C_{tt}$ and $0.57C_{tt}$, respectively, for $N_p \geq 10$. They also warn not to use multi-layer windings for high-frequency applications. Although one would need to wind multiple layers to accommodate the number of gradiometer turns shown in Fig. 4.10, one can easily reduce the number of gradiometer turns by decreasing the number of input coil turns; as described above, this does not increase the magnetic field noise. I therefore estimate C_{stray}^{grad} assuming single-layer coils and then later verify that this assumption is realistic.

For two gradiometer turns of radius a coils separated by a distance d,

$$C_{tt} = \pi(2\pi a)\varepsilon_0\varepsilon_r \big/ \cosh^{-1}(d/2\phi). \tag{4.55}$$

For tightly packed turns with $d = 2\phi_I$, $C_{tt} = 16$ pF, so a tightly packed $N_p = 10$ turn coil has $C_{Np} = 1.8$ pF. For $N_p < 10$, I would increase d to minimize the stray capacitance; a $N_p = 2$ turn coil with turns separated by $d = 2$ mm has $C_{Np} = C_{tt} = 4.3$ pF; the center coil of such a gradiometer would have $C_{2Np} = C_{tt}/3 = 1.4$ pF. Assuming $N_p = 2$ ($N_p = 2$ gives the highest stray capacitance), and using the formulas for series and parallel capacitors, the capacitance of the network shown in Fig. 4.11 is

$$C_{stray}^{grad} = \left\{ C_{Np}^{-1} + \left[C_b + \left(C_{2Np}^{-1} + \left(C_b + C_{Np} \right)^{-1} \right)^{-1} \right]^{-1} \right\}^{-1} = 2.7 \text{ pF}. \tag{4.56}$$

Based on the above results, I choose $C_{i,min} = 10\left(C_{stray}^{leads} + C_{stray}^{grad}\right) = 150$ pF. If the constraint $C_{i,min} \leq C_i \leq C_{i,max}$ fixes C_i at either $C_{i,min}$ or $C_{i,max}$, the total inductance is fixed by $L_T = (\omega_0^2 C_i)^{-1}$. However, one can allocate this inductance between the input coil inductance and the gradiometer inductance by choosing the number of turns on each to minimize the magnetic field noise. Substituting $\omega = \omega_0$, $A_p \rightarrow N_p A_p$, $L_T = N_p^2 L_p + \alpha^2 N^2 L$, and the tuning capacitance constraint $L_T = (\omega_0^2 C_i)^{-1}$ or $N_p^2 = [(\omega_0^2 C_i)^{-1} - \alpha^2 N^2 L]/L_p$ into Eq. (4.47) and minimizing the total magnetic field noise with respect to N, the optimal number of input coil turns is

$$N = \frac{1}{\alpha^2 \omega_0 L}\left\{\frac{\Delta\omega S_V^{1/2}}{C_i V_\Phi\left(4k_B T\delta + \alpha^2\omega_0 L S_J\right)} \cdot \left[\sqrt{\frac{(\Delta\omega)^2}{\omega_0^2 V_\Phi^2} S_V + \frac{4k_B T\delta\alpha^2 L}{\omega_0} + \alpha^4 L^2 S_J} - \frac{\Delta\omega}{\omega_0 V_\Phi} S_V^{1/2}\right]\right\}^{1/2}. \quad (4.57)$$

The corresponding optimal magnetic field noise is given by

$$S_B = \frac{L_p}{A_p^2}\left\{\frac{4k_B T\delta L_p}{\omega_0} + \frac{2}{\omega_0\alpha^2 L}\left[\frac{(\Delta\omega)^2}{\omega V_\Phi^2} S_V + \frac{\Delta\omega}{V_\Phi} S_V^{1/2}\sqrt{\frac{(\Delta\omega)^2}{\omega_0^2 V_\Phi^2} S_V + \frac{4k_B T\delta\alpha^2 L}{\omega_0} + \alpha^4 L^2 S_J}\right]\right\}. \quad (4.58)$$

Figure 4.12 plots N, N_p and C_i as a function of precession frequency with these constraints in place and assuming the SQUID fabrication constraint $4 \le N \le 60$. At low frequencies, hundreds of gradiometer turns are required to maintain $C_i \le C_{i,max}$. For precession frequencies between 40 kHz and 400 kHz, Eq. (4.49) determines N_p. At higher frequencies, N and N_p decrease to keep $C_i \ge C_{i,min}$. Although the constraints of stray capacitance considered in this model allow a single-turn gradiometer to operate at frequencies up to 10 MHz, causality dictates that flux-locking and feedback damping will fail unless the signal transmission time between the SQUID and the feedback damping electronics is much shorter than $2\pi/\omega_0$. For signals traveling at one-third the speed of light through a total transmission length of 2 m from the SQUID to the electronics and back, this constraint becomes $\omega_0/2\pi << 50$ MHz. Since $N_p < 30$ for all frequencies above 20 kHz, it is realistic to assume single-layer gradiometer windings at all frequencies at which C_{stray}^{grad} becomes significant. Figure 4.13 plots the magnetic field noise as a function of precession frequency for the constrained solution. As expected, the magnetic field noise matches that shown in Fig. 4.9 between 40 kHz and 400 kHz. It is higher than Fig. 4.9 below this range where the constraint $N \le 60$ prevents the optimal relationship between N_p and N described in Eq. (4.49). The noise remains equal to that shown in Fig. 4.9 above 400 kHz until the constraint $N \ge 4$ becomes operative, at which point it rises above this level.

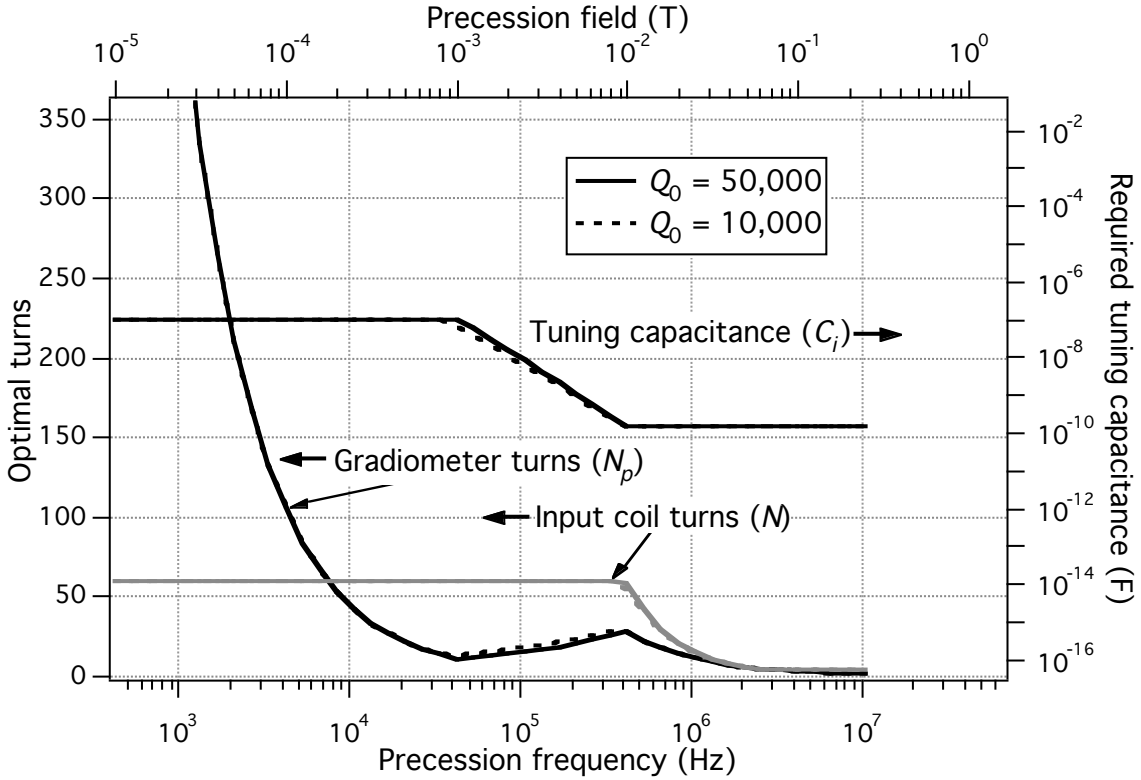

Figure 4.12: Optimal tuning capacitance, gradiometer turns, and SQUID input coil turns (gray) with the constraints 150 pF ≤ C_i ≤ 100 nF and 4 ≤ N ≤ 60.

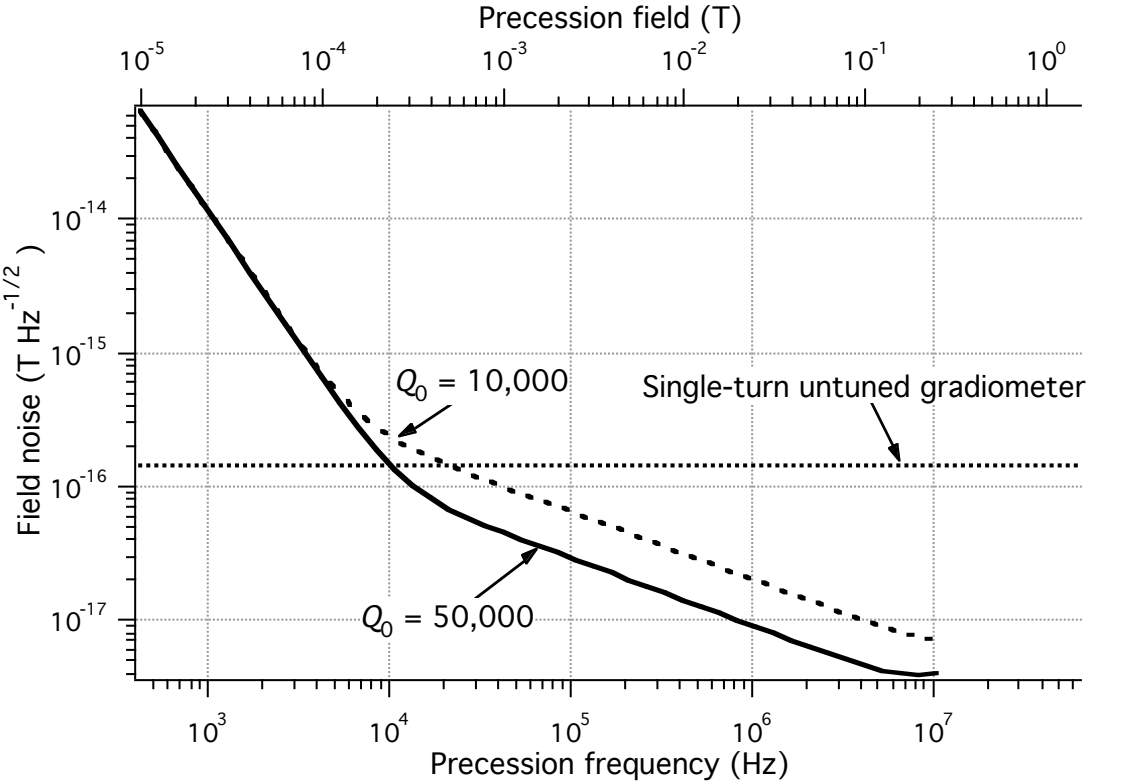

Figure 4.13: Magnetic field noise of SQUID tuned detection with the constraints described in Fig. 4.12.

4.3.2.4. Feedback damped gradiometer including input coil impedance

For a 5-μm wide input coil separated from the niobium SQUID washer by a 400 nm SiO insulating film, Mück and Clarke [20] estimate a capacitance per unit length of $C_0 \approx 0.6$ nF/m and an inductance per unit length $L_0 \approx 175$ nH/m. If the innermost turn of the input coil is a square of side length l_{t0}, and the side length of each successive turn increases by $2\Delta l_t$, the length of an N-turn input coil is

$$l_{coil} = 4(Nl_{t0} + N(N - 1)\Delta l_t). \tag{4.59}$$

Assuming $l_{t0} = 200$ μm and $\Delta l_t = 10$ μm, a 60-turn input coil has $l_{coil} = 0.19$ m, $C_{stray}^{input} = 110$ pF, and a stripline inductance $L_{input} = 33$ nH, while a 4-turn input coil has $l_{coil} = 3.7$ mm, $C_{stray}^{input} = 2.2$ pF, and $L_{input} = 0.65$ nH. Since the inductance of a single-turn gradiometer is 1.2 μH, I can neglect the stripline inductance of even a 60-turn input coil. In order to account for C_{stray}^{input}, I begin by calculating the optimal value of N neglecting C_{stray}^{input}, calculate $C_{stray}^{input} = l_{coil}C_0$, and then set $C_{i,min} = 10\left(C_{stray}^{leads} + C_{stray}^{grad} + C_{stray}^{input}\right)$. If required tuning capacitance with the optimal value of N exceeds $C_{i,min}$, I recalculate N using Eq. (4.57), then calculate the corresponding value for $C_{i,min}$. I repeat this procedure until the value of N no longer changes to obtain a self-consistent solution. Since the magnetic field noise including the effects of C_{stray}^{input} differs only slightly from that shown in Fig. 4.13, I plot the results of this calculation in the next section.

4.3.2.5. Feedback damped magnetometer

At frequencies above a few hundred kilohertz, enclosing the experiment in a thin conducting enclosure is sufficient to screen external noise, so gradiometric detection is no longer necessary. A magnetometer has approximately four times lower inductance than a second-order gradiometer with equal A_p, yielding lower magnetic field noise. Since gradiometer balance is no longer an issue, the superconducting shield around the SQUID can be located closer to the magnetometer to reduce stray capacitance. I estimate a lead length $2a$ yielding $C_{stray}^{leads} = 4.9$ pF. The stray capacitance of an N_p-turn magnetometer is just C_{Np}; I again assume the worst-case scenario of a 2-turn pickup coil with $C_{Np} = 4.3$ pF.

Figure 4.14 plots the optimal values of C_i, N_p, and N for an $a = 32.5$ mm tuned magnetometer with $L_p = \mu_0 a[\ln(8a/\phi) - 2] = 0.28$ μH and compares these values to the

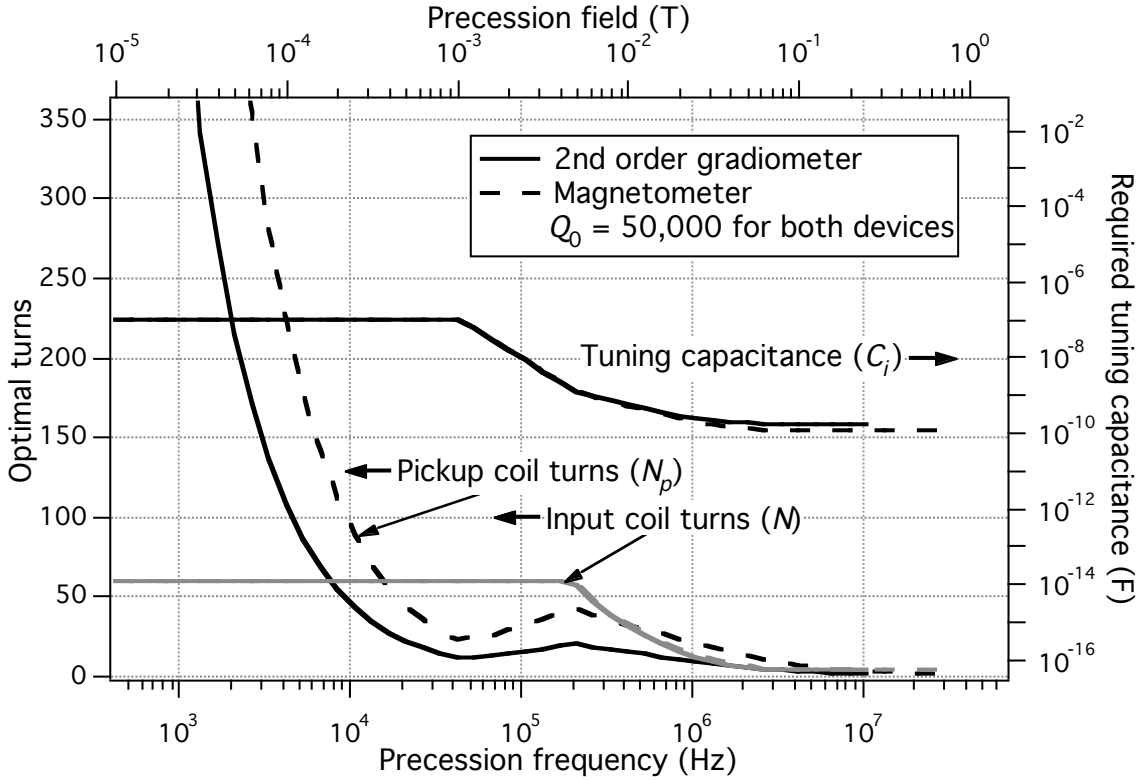

Figure 4.14: Optimal tuning capacitance, pickup coil turns, and input coil turns for the gradiometer and magnetometer. $C_{i,min}$ includes the effects of input coil capacitance.

tuned gradiometer. The effects of input coil capacitance are computed self-consistently as described in the previous section. Since the magnetometer is designed for high-frequency operation, I assume that one can achieve Q_0 = 50,000 as shown in Table 4.5 at 425 kHz and do not plot the Q_0 = 10,000 case. Because of its lower inductance, the optimal number of magnetometer turns exceeds the number of gradiometer turns. In addition, the lower inductance and lower stray capacitance of the magnetometer allow it to be operated at higher frequencies.

Figure 4.15 compares the magnetic field noise the magnetometer and gradiometer. The thin lines show the noise of these devices connected to the modeled R = 10 Ω, L = 400 pH SQUID considered in Figs. 4.9 to 4.14, while the thicker lines represent the noise when connected a SQUID with the same $S_V^{1/2}$ and V_Φ as the measurements of Mück #3 shown in Table 4.2. To model the effect of changing the number of input coil turns on Mück #3, I use the measured value of M_i = 20 nH for N = 60 turns, and assume $M_i \propto N$ and $L_i = NM_i$. As expected from Eq. (4.48) and the lower inductance of the magnetometer, the magnetometer field noise is approximately half the gradiometer field

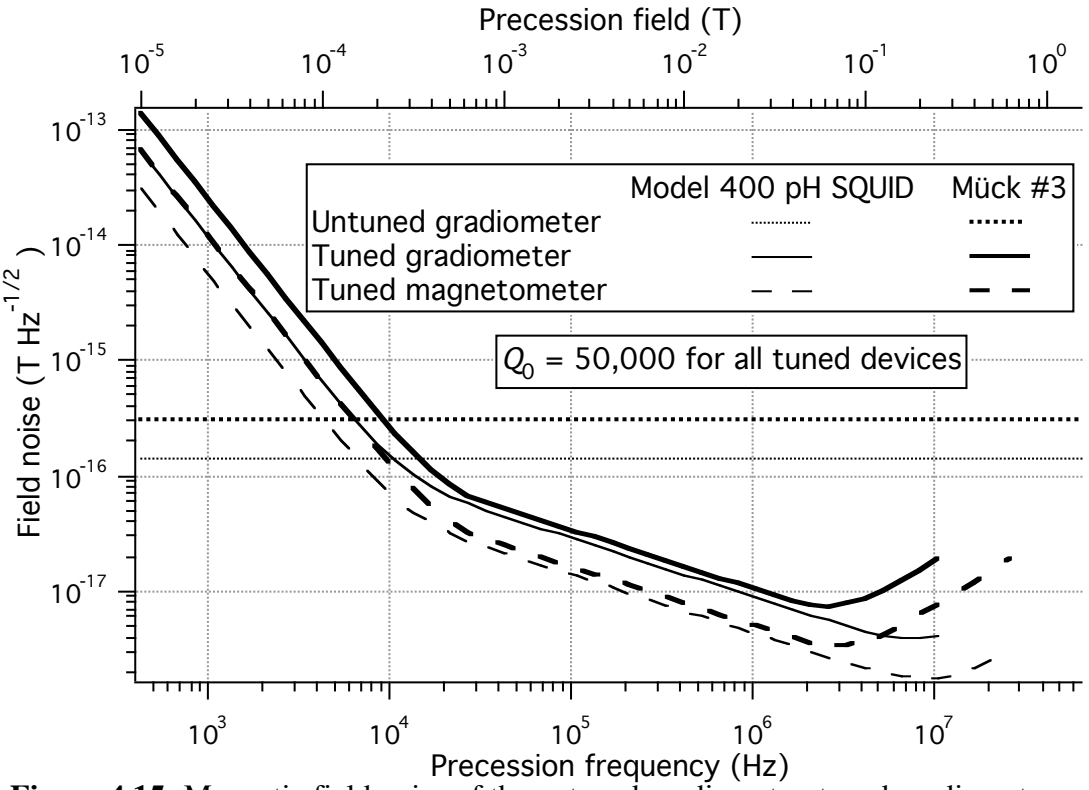

Figure 4.15: Magnetic field noise of the untuned gradiometer, tuned gradiometer, and tuned magnetometer including the effects of input coil capactance. These devices are attached to a SQUID with either the parameters of the R = 10 Ω, L = 400 pH SQUID considered in Sec. 4.1.1 or those of Mück #3 described in Table 4.2.

noise. The lower inductance and stray capacitance of the magnetometer also allow somewhat higher-frequency detection compared with the gradiometer. The higher voltage noises of Mück #3 increase the magnetic field noise by a factor of ~2 compared to the modeled 400 pH SQUID in the low-frequency range where $C_{i,max}$ constrains C_i. Capacitor dissipation is the dominant noise source in the mid-frequency regime where C_i is not constrained, and replacing the modeled SQUID with Mück #3 only raises the noise by ~15%. The increased current noise of Mück #3 becomes significant above ~3 MHz where $C_{i,min}$ constrains C_i, leading to substantially increased noise in this regime.

4.3.3. Field noise of conventional Faraday detection

Three types of noise must be considered in conventional Faraday detection: Nyquist noise from the room-temperature resistive copper coil, noise originating in the semiconductor amplifier, and the noise from Nyquist noise currents in the conducting sample. Because low-noise semiconductor amplifiers have noise temperatures well below 298 K, an impedance-matched amplifier will produce negligible noise compared to

the Nyquist noise of the pickup coil. I therefore neglect amplifier noise in this discussion. Since sample noise contributes equally to all detection schemes, I defer the treatment of sample noise to Sec. 4.3.4. Although a multi-turn pickup loop is generally required to match the amplifier impedance in low-frequency Faraday detection, here I consider only a single-turn pickup coil because I anticipate that SQUID detection will yield lower noise at low frequencies. Finally, I note that the tuning capacitor and matching circuit can be placed very close to the pickup coil to minimize stray capacitance; therefore conventional Faraday coils can be tuned to substantially higher frequencies than can wire-wound SQUID-detected superconducting coils.

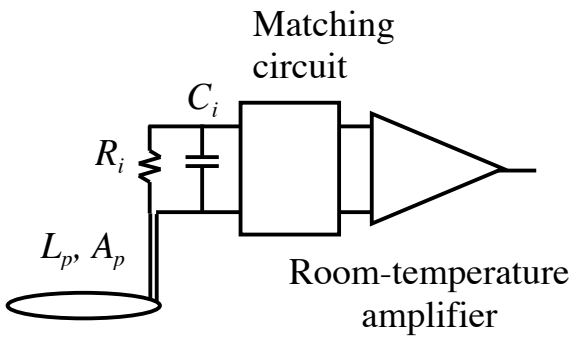

Figure 4.16: Schematic of conventional Faraday detection.

Figure 4.16 shows a schematic of a pickup coil with resistance R_i, inductance L_p, and area A_p connected to a tuning capacitor C_i and a matched semiconductor amplifier. Unlike the SQUID, which measures the current in the input circuit, the semiconductor amplifier measures the voltage across the tuning capacitor. I have intentionally left the matching circuit and amplifier as black boxes in order to focus on the dynamics of the tuned circuit. The voltage across the capacitor is given by

$$V_C(\omega) = \frac{-\omega A_p B(\omega) + jV_{RN}(\omega)}{\omega R_i C_i + j\left(\omega^2 L_p C_i - 1\right)}, \tag{4.60}$$

where $B(\omega)$ is the applied magnetic field and $V_{RN}(\omega)$ is the Nyquist voltage noise of the resistor. The magnetic field noise resulting from $V_{RN}(\omega)$ at the resonant frequency $\omega_0 = (L_p C_i)^{-1/2}$ is thus

$$S_B^{1/2}(\omega_0) = \sqrt{4k_B T R_i}\,/\omega_0 A_p\,, \tag{4.61}$$

where $T = 298$ K is the pickup coil temperature. Because alternating current of frequency $\omega_0/2\pi$ travels only within a skin depth $\delta = (2\rho/\mu_0\omega_0)^{1/2}$ of the surface of a material with resistivity ρ, R_i depends on ω_0. The resistance of a pickup coil of radius a and wire radius ϕ is thus

$$R_i = \rho \frac{2\pi a}{2\pi\phi\delta} = \frac{a}{\phi}\sqrt{\frac{\mu_0 \rho \omega_0}{2}}. \quad (4.62)$$

This resistance provides a bandwidth $\Delta\omega = R_i/L_i$. If $\Delta\omega \geq \pi BW_{det}$, the noise is given by substituting Eq. (4.62) into Eq. (4.61):

$$S_B^{1/2}(\omega_0) = \frac{1}{\omega_0^{3/4} A_p}\sqrt{4k_B T \frac{a}{\phi}}\sqrt[4]{\frac{\mu_0 \rho}{2}}. \quad (4.63)$$

In this case, the magnetic field noise scales as $\omega_0^{-3/4}$; if additional resistance must be added to achieve the required bandwidth, $R_i = \Delta\omega L_i$ and the field noise scales as ω_0^{-1}. The crossover between these two regimes occurs at

$$\omega_{crossover} = \frac{2}{\mu_0 \rho}\left(\frac{\phi}{a}\Delta\omega L_i\right)^2; \quad (4.64)$$

for a = 32.5 mm, ϕ = 3.25 mm, $\rho = 1.7 \times 10^{-8}$ Ωm, $\Delta\omega = 2\pi\cdot 350$ Hz, and $L_i = \mu_0 a[\ln(16a/\phi) - 7/4] = 0.14$ μH, the crossover frequency is 14 kHz.

4.3.4. Nyquist noise from a warm conducting sample

If Nyquist noise from originating from the conducting sample exceeds the detector noise, further reducing the detector noise will not improve the MRI SNR. Therefore, before comparing the noise of conventional Faraday detection to the two SQUID detection modalities, I estimate the field noise originating generated by a conducting sample near the pickup loop. This derivation follows that of Suits, Garroway, and Miller [21], but extends their results to calculate field noise from cylinders of finite radius.

Their derivation begins by calculating the electrical power dissipated in the sample from the oscillating field generated by a current $I\sin(\omega t)$ flowing in the pickup coil. The time-averaged dissipated power can be expressed as an integral over the sample volume V:

$$P_{loss} = \frac{1}{2}\sigma\omega^2 \int_V \mathbf{A}\cdot\mathbf{A}\ \ d\mathbf{r}, \quad (4.65)$$

where **A** is the vector potential in the Coulomb gauge resulting from a static current I in the pickup coil and σ is the sample conductivity. This expression assumes the radiation wavelength is much longer than the sample and detector sizes. If the sample is cylindrically symmetric about the pickup coil axis, the changing magnetic field caused by the circular pickup coil will induce cylindrically symmetric currents to flow in the sample

and no electrical charge will build up. If, in addition, the sample is non-magnetic and much smaller than the radiation skin depth, the vector potential in the sample can be approximated by its value in free space. For a circular loop of radius a in the $z = 0$ plane centered at the origin and carrying a current I,

$$\mathbf{A} = \frac{1}{2}\mu_0 I a \hat{\mathbf{a}}_\theta \int_0^\infty e^{-k|z|}\, \mathrm{J}_1(kr)\, \mathrm{J}_1(ka)\, dk, \tag{4.66}$$

where $\hat{\mathbf{a}}_\theta$ is the azimuthal unit vector. In order to calculate the power lost in the cylindrical sample of radius R and height H a distance h below the pickup coil shown in Fig. 4.17, I substitute Eq. (4.66) into Eq. (4.65) and integrate over the cylindrical volume. After integrating over the azimuthal coordinate and substituting $\lambda = ka$, I obtain

$$P_{loss} = \frac{1}{4}\pi\sigma\mu_0^2 I^2\omega^2 \int_0^R \int_h^{h+H} r\left(\int_0^\infty e^{-\lambda|z|/a}\, \mathrm{J}_1(\lambda r/a)\, \mathrm{J}_1(\lambda)\, d\lambda\right)^2 dz\, dr = \frac{1}{2}\sigma\mu_0^2 I^2\omega^2 V_{loss}, \tag{4.67}$$

where I have lumped all the geometrical factors into a single volume V_{loss}. This power is equivalent to a series resistance

$$R_{loss} = P_{loss}/I_{rms}^2 = 2P_{loss}/I^2 = \sigma\mu_0^2\omega^2 V_{loss} \tag{4.68}$$

in the pickup coil, where I_{rms} is the root mean square current flowing in the pickup coil. The fluctuation-dissipation theorem states that all dissipative losses produce identical noise at the same temperature, so the magnetic field noise from can be evaluated by substituting $R_i = R_{loss}$ and $T = T_{samp}$ in Eq. (4.61) to obtain

$$S_B^{1/2} = \mu_0\sqrt{4k_B T_{samp}\sigma V_{loss}}/A_p\,. \tag{4.69}$$

Gabriel, Lau, and Gabriel [3] measure σ of biological tissue at frequencies ranging from 10 Hz to 10 GHz. For internal tissue at the precession frequencies considered in this chapter, they measure σ between 0.05 and 1.0 $(\Omega\mathrm{m})^{-1}$ depending on the tissue type and frequency. For all tissue, the conductivity increases gradually with frequency. For the purposes of this chapter I assume that $\sigma(\omega/2\pi)$ can be approximated by a power law interpolation between σ(1 kHz) = 0.1 $(\Omega\mathrm{m})^{-1}$ and σ(10 MHz) = 0.5 $(\Omega\mathrm{m})^{-1}$.

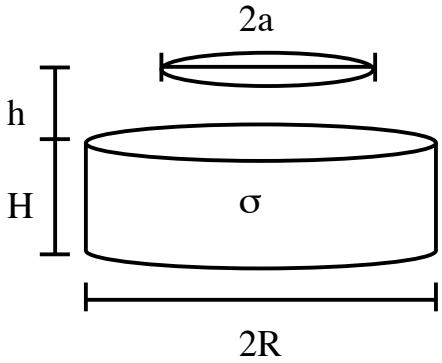

Figure 4.17: Sample and pickup coil geometry.

To evaluate Eq. (4.69), I integrate Eq. (4.67) numerically to find V_{loss} in the case of an infinite planar sample and two cylindrical samples approximating medically relevant samples. Table 4.6 shows the sample noise in each of these cases assuming $\sigma = 0.5\ (\Omega\text{m})^{-1}$. While the noise from the "torso" model is nearly the same as the half-plane sample, the smaller "arm" model produces half the noise of the larger samples.

Table 4.6: Sample noise evaluated with h = 25 mm, T_{samp} = 310 K, and $\sigma = 0.5\ (\Omega\text{m})^{-1}$.

Model	R (m)	H (m)	V_{loss} (m^3)	$S_B^{1/2}$ (fT Hz$^{-1/2}$)
Half-plane	∞	∞	3.8×10^{-6}	0.068
"Torso"	0.2	0.2	2.6×10^{-6}	0.056
"Arm"	0.05	0.05	0.6×10^{-6}	0.027

4.3.5. SNR comparison of detection modalities

Figure 4.18 summarizes the magnetic field noise values calculated in this chapter. If the spin magnetization is independent of precession frequency (as in the case of prepolarized protons), the optimal detection modality at a given precession frequency is that which has the lowest magnetic field noise. A SQUID attached to an untuned second-order gradiometer has the lowest magnetic field noise at frequencies below 10 kHz. Assuming one can fabricate a low-frequency 100 nF cryogenic capacitor with Q_0 = 50,000, SQUID detection with a tuned gradiometer becomes superior to untuned detection for $\omega_0/2\pi$ > 10 kHz. The crossover frequency is remarkably insensitive to Q_0 and increases only to 13 kHz for Q_0 = 5,000 (this calculation is not shown in Fig. 4.18). SQUID tuned detection provides the lowest noise above this frequency until the constraints $C_i \geq C_{i,min}$, $N \geq 4$, and $N_p \geq 1$ can no longer be satisfied; this condition occurs at $\omega_0/2\pi$ = 10 MHz for the tuned gradiometer and $\omega_0/2\pi$ = 25 MHz for the tuned magnetometer. These constraints cause a minimum in the magnetic field noise of SQUID tuned detection at 3 MHz that is well below the calculated sample noise. While one could almost certainly reduce the stray capacitance of the tuned magnetometer and SQUID input coil to allow SQUID tuned detection at frequencies above 25 MHz, this would not reduce the total magnetic field noise below the sample noise. Since the magnetic field noise of conventional Faraday detection falls below the sample noise in this regime, the versatility and convenience of a room-temperature pickup coil make it the superior choice.

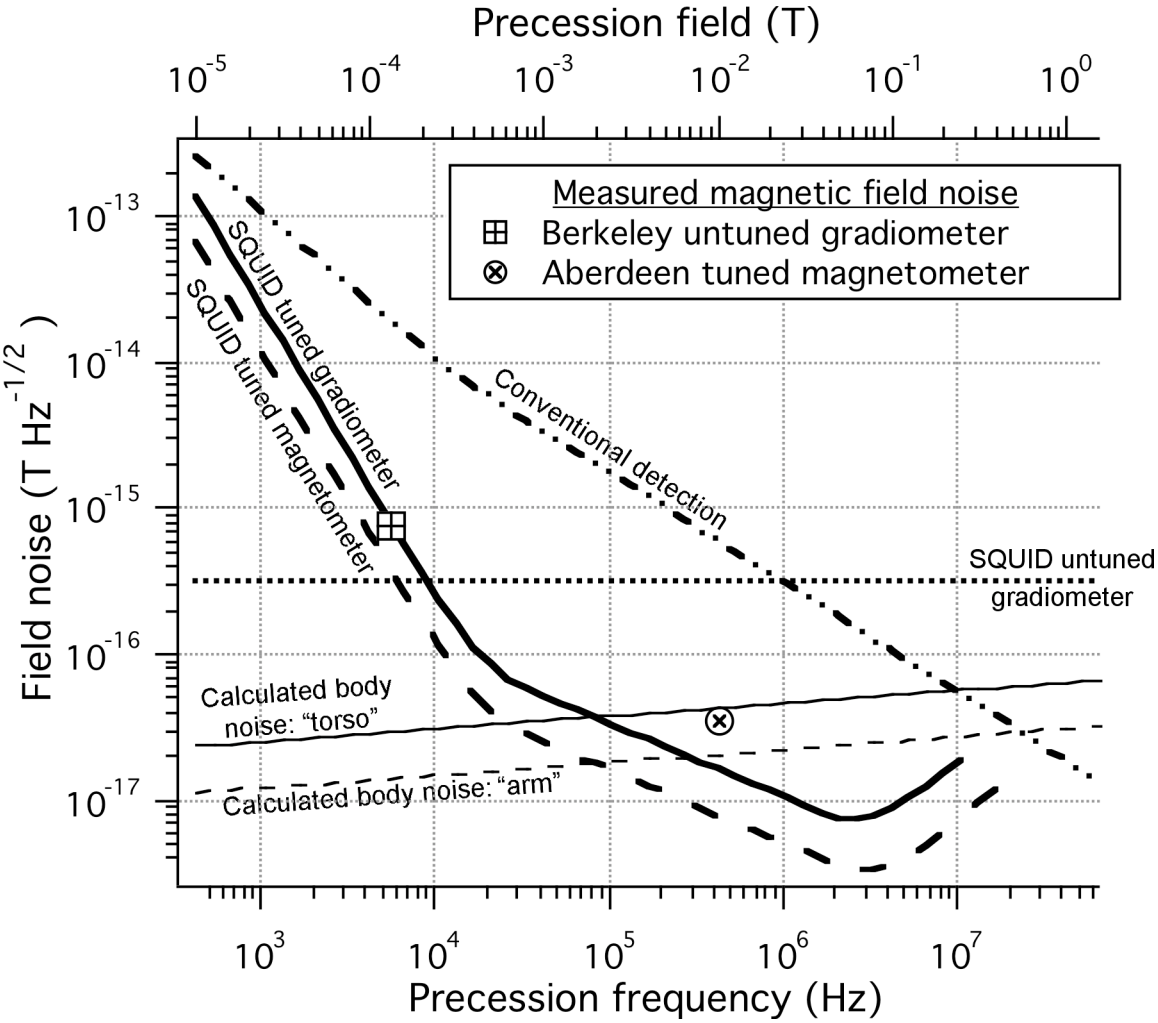

Figure 4.18: Calculated and measured magnetic field noise of SQUID tuned and untuned detection and conventional Faraday detection compared to modeled sample noise. The SQUID noise parameters are those of Mück #3 described in Table 4.2; I assume Q_0 = 50,000 for SQUID tuned detection. The measured noise of the 425-kHz SQUID tuned magnetometer comes from [22].

Figure 4.18 also plots the experimentally measured 0.75 fT $Hz^{-1/2}$ field noise of the Clarke group SQUID untuned gradiometer and the 0.035 fT $Hz^{-1/2}$ field noise of the 29-turn 425-kHz SQUID tuned magnetometer of Seton, Hutchison, and Bussel [22]. The measured noise is substantially greater than the predicted noise in both cases. In the case of the Clarke group gradiometer, much of the difference between the measured and predicted magnetic field noise results from using the Mück #1 SQUID instead of Mück #3; the preamplifier of the 2 MHz flux-locking electronics may also contribute excess noise. Seton *et al.* attribute the excess noise in their measurements to dielectric losses, particularly in the cryostat end cap.

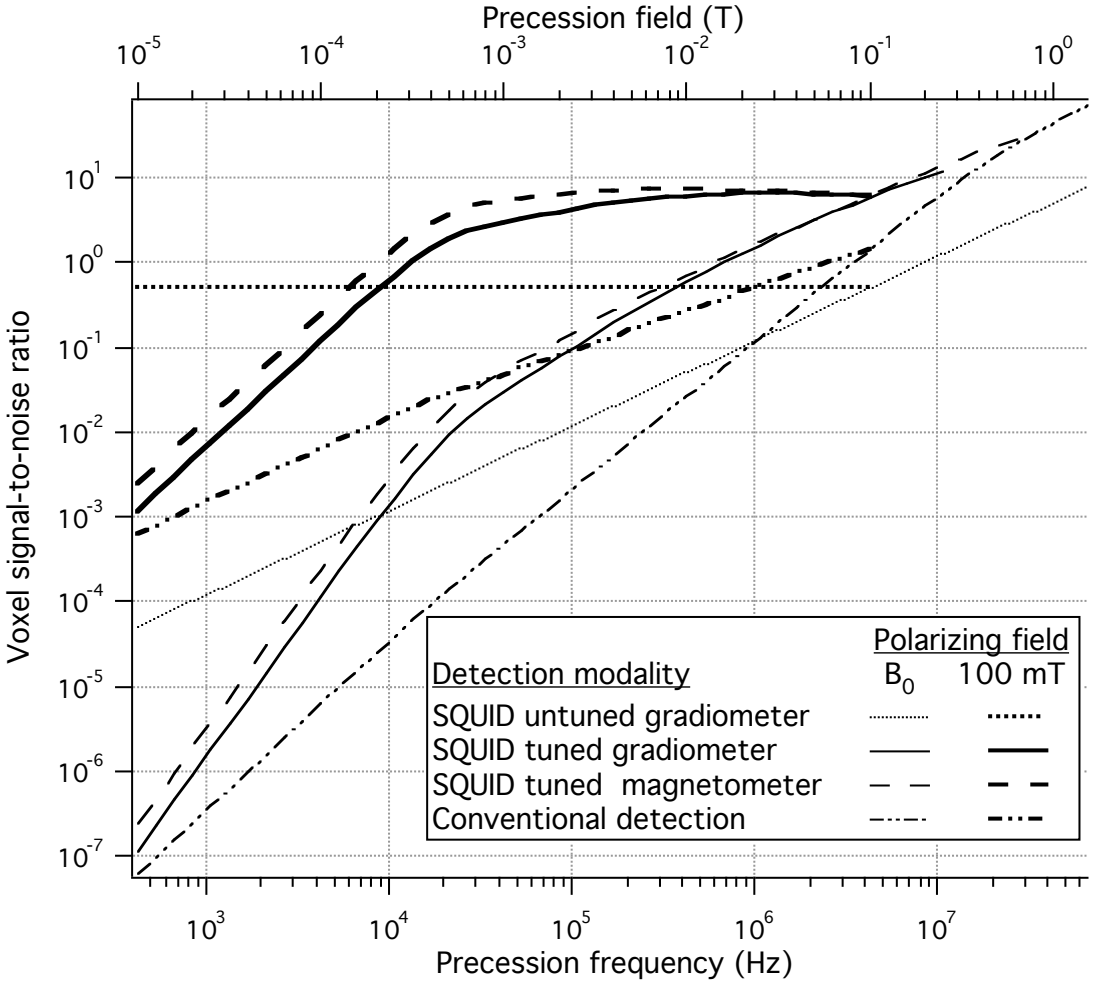

Figure 4.19: SNR comparison of the three different detection modalities with and without prepolarization. The SQUID noise parameters are those of Mück #3, and Q_0 = 50,000 for SQUID tuned detection. The prepolarized traces end at 100 mT since one would always choose to polarize in B_0 for $B_0 > B_p$.

However, in non-prepolarized MRI, the precession field is also used to polarize the protons, so there is an additional incentive to employ higher fields. From Eq. (2.40), the signal-to-noise ratio of a voxel obtained from a single acquisition step is given by

$$SNR_{voxel} = B_{det}\sqrt{T_s/2}\,\big/ S_B^{1/2}, \tag{4.70}$$

where B_{det} is given by Eq. (4.38) and T_s is the data acquisition time. Figure 4.19 plots the signal-to-noise ratio of the 1 mm^3 voxel of water described in Sec. 4.3.1 measured using the modalities shown in Fig. 4.18 with $T_s = T_2$ = 60 ms. The polarizing field B_p is set to either B_0 for conventional polarization or to a 100 mT prepolarizating field. The sample noise from the "arm" model has been added in quadrature to the detector noise. At frequencies below 10 kHz, prepolarized SQUID untuned detection provides the highest

SNR. Between 10 kHz and 4 MHz, prepolarized SQUID tuned detection is best. Above the 4 MHz precession frequency corresponding to the 100 mT prepolarization field, higher SNR can be achieved by using the precession field to polarize the spins. Although Fig. 4.19 indicates that conventional detection surpasses SQUID tuned detection at precession frequency of 25 MHz, it does not include the causality constraints that make it difficult to operate flux-locked loops and feedback damping at frequencies above a few megahertz.

Figure 4.19 also reveals much about the potential of these detection modalities to make 1-mm resolution three-dimensional images of biological ($T_2 \sim 60$ ms) samples. Prepolarized MRI detected using Mück #3 attached to an untuned second-order gradiometer achieves a single-shot voxel SNR of 0.5. Therefore, 400 acquisition steps (either phase encoding steps or averages) are required in order to take an image with a voxel SNR of 10; assuming a 0.5 s repetition time, an image would take ~3 minutes. Employing a SQUID with the voltage noise calculated in Section 4.1.1 would increase the single-shot SNR to 1.1 and would require only 83 acquisition steps (41 s) to achieve a SNR of 10. Therefore, assuming that external noise could be reduced below 0.1 fT, SQUID untuned detection would greatly benefit from reduced SQUID noise. In contrast, prepolarized SQUID tuned detection at 500 kHz achieves a single-shot voxel SNR of 7. The magnetic field noise is dominated by sample noise, so further improvements in SQUID technology would not increase SNR. While multiple phase encoding steps would be required to form an image, these additional acquisition steps would further increase the voxel SNR.

Comparing these methods to conventional MRI detection, prepolarized SQUID untuned detection achieves a SNR equivalent to 50 mT conventional detection without prepolarization, while prepolarized SQUID tuned detection at 500 kHz is equivalent to 250 mT conventional detection. One can see immediately that low-field SQUID detection will never surpass the SNR of conventional detection at the 1.5 T clinical standard. Therefore, the lower cost, more open geometry, and potentially higher contrast of low-field MRI must compensate for its inferior SNR in any successful medical application of low-field MRI. Chapter 6 continues this comparison between conventional

and SQUID-detected MRI and identifies potential applications of low-field SQUID-detected MRI.

---

[1] J. M. Martinis and John Clarke, Signal and noise theory for a DC SQUID amplifier, *J. Low Temp. Phys.* **61** (1985) 227.
[2] H. C. Seton, D. M. Bussel, J. M. S. Hutchison, and D. J. Lurie, Use of a DC SQUID receiver preamplifier in a low field MRI system, *IEEE Trans. Appl. Supercon.* **5** (1995) 3128.
[3] S. Gabriel, R. W. Lau, and C. Gabriel, The dielectric properties of biological tissues. 2. Measurements in he frequency range 10-20 GHz. *Phys. Med. Biol.* **41** (1996) 2251.
[4] C. Tesche and J. Clarke, dc SQUID: Current Noise, *J. Low Temp. Phys.* **37** (1979) 397.
[5] T. Ryhänen and H. Seppä, SQUID magnetometers for low-frequency applications, *J. Low Temp. Phys.* **76** (1989) 287.
[6] M. B. Ketchen and J. M. Jaycox, Ultra-low-noise tunnel junction DC SQUID with a tightly coupled planar input coil, *Appl. Phys. Lett.* **40** (1982) 736.
[7] C. Hilbert and John Clarke, Measurements of the dynamic input impedance of a DC SQUID, *J. Low Temp. Phys.* **61** (1985) 237.
[8] F. Wellstood, C. Heiden, and John Clarke, Integrated dc SQUID magnetometer with a high slew rate, *Rev. Sci. Instrum.* **55** (1984) 952.
[9] G. B. Arfken and H. J. Weber, *Mathematical Methods for Physicists, 4th ed.* (San Diego: Academic Press, 1995) p. 632.
[10] R. Fox, Quantum Design, personal communication, March 7, 2006.
[11] J. D. Jackson, *Classical Electrodynamics, 3rd ed.* (New York: John Wiley & Sons) p. 232.
[12] H. C. Seton, J. M. S. Hutchision, and D. M. Bussel, Gradiometer pick-up coil design for a low field SQUID-MRI system, *Magn. Reson. Mater. Phys., Biol. Med.* **8** (1999) 116.
[13] M. B. Simmonds, W. A. Fertig, and R. P. Gifford, Performance of a resonant input SQUID amplifier system, *IEEE Trans. Mag.* **15** (1979) 478.
[14] H. Seton, private communication, 5 April 2006.
[15] A. Hammoud, S. Geerber, R. L. Patterson, and T. L. MacDonald, Performance of surface-mount ceramic and solid tantalum capacitors for cryogenic applications, *1998 Annual Report Conference on Electrical Insulation and Dielectric Phenomena, IEEE,* vol. 2 (1998) 572.
[16] T. Sleator, E. L. Hahn, C. Hilbert, and John Clarke, Nuclear-spin noise and spontaneous emission, *Phys. Rev. B*, **36** (1987) 1969.
[17] C. Hilbert, John Clarke, T. Sleator, and E. L. Hahn, Nuclear quadrupole resonance detected at 30 MHz with a dc superconducting quantum interference device, *Appl. Phys. Lett.*, **47** (1985) 637.
[18] H. C. Seton, J. M. S. Hutchison, and D. M. Bussel, A 4.2 K receiver coil and SQUID amplifier used to improve the SNR of low-field magnetic resonance images of the human arm, *Meas. Sci. Technol.* **8** (1997) 198.
[19] A. Massarini and M. K. Kazimierczuk, Self-capacitance of inductors, *IEEE Trans. Power Electron.* **12** (1997) 671.

[20] M. Mück and John Clarke, The superconducting quantum interference device microstrip amplifier: computer models, *J. Appl. Phys.* **88** (2000) 6910.
[21] B. H. Suits, A. N. Garroway, and J. B. Miller, Surface and gradiometer coils near a conducting body: the lift-off effect, *J. Magn. Reson.* **135** (1998) 373.
[22] H. C. Seton, J. M. S. Hutchison, and D. M. Bussel, Liquid helium cryostat for SQUID-based MRI receivers, *Cryogenics* **45** (2005) 348.

5. Second-generation SQUID MRI system

Our microtesla MRI system has been constantly upgraded since its initial construction. Section 1.4 describes the state of the MRI system two and one-half years ago when I began to work on this project. This chapter describes both the improvements to the first-generation MRI system made since that time and the construction of the second-generation MRI system.

We have employed three generations of polarizing coils since the coil described in Sec. 1.4.3. With each generation, we either reduced the Nyquist noise coupled to the gradiometer from the copper coil windings and/or improved the coil cooling system to allow longer operating times. Section 5.1 describes the guiding principles behind these improvements and the geometry and performance of each polarizing coil. In our quest for lower magnetic field noise, we first replaced the gradiometer installed by McDermott and co-workers with one designed to improve the gradiometer balance. Section 5.2 describes the second-generation gradiometer and our measurements of its balance against uniform external fields. We next replaced the QD SQUID with Mück #3 as described in Sec. 4.2. The combination of these improvements reduced the measured magnetic field noise from 1.7 fT $Hz^{-1/2}$ to 1.1 fT $Hz^{-1/2}$. Since the flux noise measurements of Mück SQUID #3 indicated that we should obtain ~0.3 fT $Hz^{-1/2}$, we suspected that the additional noise arose from some combination of external radiofrequency and 5.6 kHz noise. We therefore constructed a second-generation MRI system with improved shielding against both types of noise. Section 5.3 describes the second-generation aluminum shield, and Sec. 5.4 describes the magnetic field coils of the second-generation MRI system. As described in Sec. 4.2.2.5, Mück #1 connected to the second-generation gradiometer in the second-generation MRI system achieves a magnetic field noise of 0.75 fT $Hz^{-1/2}$. Section 5.5 presents images taken with the second-generation microtesla MRI system.

5.1. Polarizing coils

Since MRI SNR scales directly with B_p, the performance of the polarizing coil is as critical as that of the SQUID-based gradiometer in producing fast, high-resolution images. An ideal polarizing coil would produce high magnetic fields at the sample, be able to operate indefinitely without overheating, and couple negligible Nyquist magnetic

field noise to the gradiometer. Since the coil design strategies mandated by these requirements conflict with each other, one must balance the importance of each of these factors to design an optimal polarizing coil. This section describes each of these requirements in turn, and then compares the performance of the four polarizing coils used since I joined the microtesla MRI project.

5.1.1. Field strength

The magnetic field generated by a polarizing coil can be calculated using the Biot-Savart law. The magnetic field from a circular wire loop of radius R in the xy plane carrying current I at a point $\mathbf{r} = (r,z)$ can be expressed in cylindrical coordinates as

$$B_r = \frac{\mu_0 I}{4\pi}\frac{\sqrt{2}z}{R^2}\left(\frac{R}{r}\right)^{3/2}\frac{\sqrt{\xi-1}}{\xi^2-1}\left[\xi \mathrm{E}\left(\frac{2}{1-\xi}\right)-(1+\xi)\mathrm{K}\left(\frac{2}{1-\xi}\right)\right] \tag{5.1}$$

and

$$B_z = \frac{\mu_0 I}{4\pi}\frac{\sqrt{2}}{R}\left(\frac{R}{r}\right)^{3/2}\frac{\sqrt{\xi-1}}{\xi^2-1}\left[\left(1-\frac{r}{R}\xi\right)\mathrm{E}\left(\frac{2}{1-\xi}\right)+\frac{r}{R}(1+\xi)\mathrm{K}\left(\frac{2}{1-\xi}\right)\right], \tag{5.2}$$

where

$$\xi = \frac{R}{2r}\left(1+\frac{r^2}{R^2}+\frac{z^2}{R^2}\right) \tag{5.3}$$

and K and E represent the complete elliptic integrals of the first and second kind, respectively. If $r = 0$, $B_r = 0$ and

$$B_z = \frac{\mu_0 I R^2}{2\left(R^2+z^2\right)^{3/2}}. \tag{5.4}$$

For the purposes of coil design, it is particularly useful to calculate the magnetic field in terms of intrinsic rather than extrinsic properties. Figure 5.1 shows a solenoid of rectangular cross-section with inner radius R_1, outer radius R_2, and height H carrying current density J. The magnetic field at the point $\mathbf{r} = (r,z)$ can be evaluated by integrating Eqs. (5.1) and (5.2) over the rectangular solenoid cross-section. For $r > 0$, the integral must be evaluated numerically; if $r = 0$,

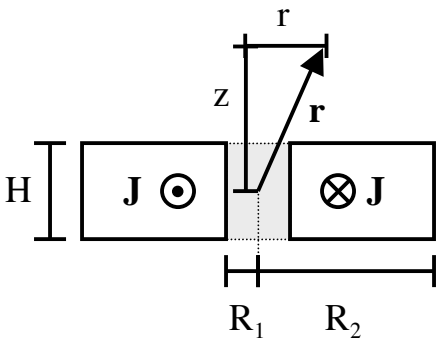

Figure 5.1: Polarizing coil geometry.

$$B_z = \frac{\mu_0 J}{2}\left[z' \ln\left(\frac{R_2 + \sqrt{R_2^2 + z'^2}}{R_1 + \sqrt{R_1^2 + z'^2}} \right) \right]_{z'=z-H/2}^{z'=z+H/2}, \tag{5.5}$$

where I have used the notation $\left[f(x) \right]_{x=a}^{x=b} = f(b) - f(a)$. At the center of the solenoid,

$$B_z = \frac{\mu_0 J H}{2} \ln\left(\frac{R_2 + \sqrt{R_2^2 + H^2/4}}{R_1 + \sqrt{R_1^2 + H^2/4}} \right). \tag{5.6}$$

If $H >> R_2$, this equation reduces to $B_z = \mu_0 J(R_2 - R_1)$, the familiar formula for a long solenoid. In all cases, the magnetic field is linear in J.

For a copper coil of volume $V = H(R_2^2 - R_1^2)$, the dissipated power can be expressed in terms of the current density as

$$P = \rho_{Cu} J^2 V / \lambda, \tag{5.7}$$

where $\rho_{Cu} = 1.7 \times 10^{-8}$ Ωm is the resistivity of copper and λ is the fraction of the coil volume which carries current. Choosing λ close to 1 minimizes the power dissipated to achieve a given current density. However, the coolant requires space to flow through the coil, so one must optimize the geometry of the coil turns and coolant channels to maximize J in steady-state operation. While aspects of this optimization procedure are patently empirical, a coil winding and cooling scheme can be characterized by the intrinsic parameters J and λ. For fixed J and λ, the capacity of the power supply sets the maximum coil volume. Equations. (5.1)-(5.6) can then be employed to optimize the dimensions of the coil to produce the maximum field at the sample.

While employing intrinsic parameters simplifies the optimization of the polarizing coil geometry, one must know the resistance of the coil to connect it to an amplifier. If the solenoid is wound out of wire with current-carrying cross-sectional area A_w, the wire length can be expressed as $L_w = \lambda V / A_w$ and the coil resistance is given by $\rho_{Cu} L_w / A_w = \lambda \rho_{Cu} V / A_w^2$. The coil current is $I = J A_w / \lambda$, and the voltage across the coil is $V = \rho_{Cu} J V / A_w$. For a coil of cross-sectional area A_C wound with N turns of wire carrying a current I, the intrinsic properties can be expressed as $\lambda = N A_w / A_C$ and $J = NI / A_C$.

5.1.2. Cooling techniques

The first polarizing coils constructed by McDermott and coworkers consisted of tightly wound copper wire solenoids with no special cooling apparatus. While these coils

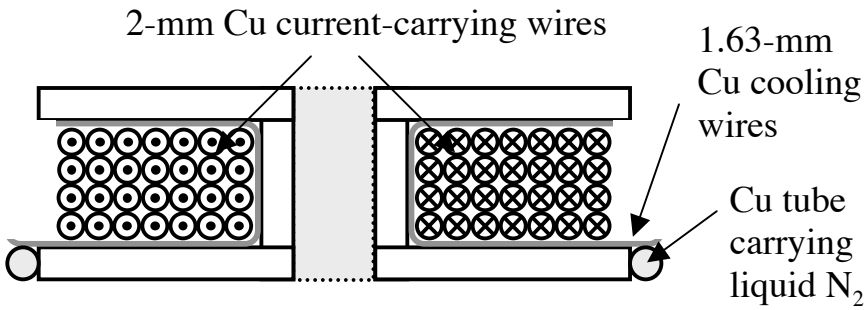

Figure 5.2: Cross-section of a polarizing coil that uses copper wires (gray) to conduct heat to a hollow copper tube cooled by liquid-nitrogen.

achieved λ of 0.7-0.8, waiting for them to cool drastically slowed experimental progress. Therefore, they used 102 1.63-mm diameter sections of copper wire to conduct heat away from the polarizing coil described in Secs. 1.4.3 and 5.1.4.1. These wires completely surround the inner diameter of the solenoid and fan out in an angularly symmetric pattern. As shown in Fig. 5.2, the cooling wires conduct heat from the top, bottom, and inner diameter of the solenoid to a hollow copper tube. The wires are soldered to the copper tube to minimize the thermal resistance of the contact. Flowing liquid nitrogen through the copper tube cooled the coil significantly faster than air-cooling alone.

However, even with the improvements to this basic design made in the open bore Litz wire polarizing coil described in Sec. 5.1.4.2, the heat flow through the copper cooling wires was much lower than the power dissipated by the coil, and cooling the coil still required ~15 minutes after executing an imaging sequence. In addition, the copper cooling wires couple Nyquist noise into the gradiometer as described in Sec. 5.1.3. We therefore cooled the subsequent coils by flowing liquid nitrogen or water directly through the coil windings. Although the volume of the channels required for coolant flow reduces λ, the direct physical contact between the coolant and the current-carrying wires dramatically improves cooling performance. I call this technique internal cooling as opposed to external cooling as described in the previous paragraph.

Table 5.1 compares the properties of liquid nitrogen and water that are relevant to their use as polarizing coil cooling fluids. The primary advantage of liquid nitrogen is that one can pre-cool the polarizing coil to substantially below room temperature, thereby reducing its resistance and lowering the power required to achieve a given current density. However, we found that when we tried to operate the polarizing coil while cooling it with liquid nitrogen, hot spots developed within the coil windings, and the coil

insulation failed at these points. These hot spots form in places where the coil windings are cooled relatively inefficiently by gaseous nitrogen. Since liquid nitrogen cools other parts of the coil to below 100 K, the overall coil resistance decreases far below its room-temperature value, and one cannot discern the presence of such hot spots from the measured polarizing coil resistance. We therefore pre-cooled the liquid nitrogen-cooled coil described in Sec. 5.1.4.3, but stopped cooling it before executing an MRI pulse sequence to avoid the risk of coil failure.

Table 5.1: Cooling properties of liquid nitrogen and water. Enthalpy and viscosity values are from [1] unless noted.

Coolant	Liquid nitrogen	Water
Advantages	Low temperature reduces coil resistance	Readily available coolant; continuous cooling possible
Disadvantages	Continuous cooling problematic	Must be doped to shorten T_1 to prevent it from contributing an NMR signal
Initial temperature	77 K	10-20 °C
Enthalpy per liter	160 kJ to boil; ~160 kJ to heat resulting gas by 200 K	42 kJ to raise temperature by 10 °C
Viscosity	Liquid: 0.15 mPa s [2] Gas: 13 μPa s at 200 K 18 μPa s at 300 K	0.89 mPa s at 25 °C 0.55 mPa s at 50 °C
Hazard to human subject from coolant leak	Frostbite from leaking liquid; suffocation from slow gas leak inside the shielded room	Electrical shock transmitted from break in polarizing coil insulation through water leak to subject.

In contrast, the temperature of cooling water rises by only 10-25 °C when passing through the coil turns, so water cooling maintains a relatively stable coil temperature and can be used continuously. However, water contains NMR-active protons, so the cooling water must be doped to prevent it from appearing in the MRI image. Sections 5.1.4.3 and 5.1.4.4 provide additional details about internal cooling with liquid nitrogen and water.

5.1.3. Magnetic field noise

As described in Sec. 4.3.4, the presence of conducting material near the pickup coil produces Nyquist noise. While the noise from poorly conducting biological samples is well below the detection limit of a SQUID untuned gradiometer, polarizing coils fabricated from copper wire can generate substantial Nyquist noise. To illustrate this effect, I calculate the magnetic field noise coupled into the bottom loop of the $2a$ = 65-

mm diameter gradiometer by a single $r = a = 32.5$ mm loop of $2\phi = 2$-mm diameter wire a distance $d = 50$ mm below the gradiometer. This loop represents a typical turn of the polarizing coil described in Sec. 5.1.4.1.

If this loop is an unbroken conductor, Eq. (4.69) can be used to estimate the resulting magnetic field noise. Although the small dimensions of this loop result in $V_{loss} = 6.0 \times 10^{-10}$ m^3, the conductivity of copper ($\sigma = 1/\rho_{Cu} = 5.9 \times 10^7$ Ω^{-1}m^{-1}) is orders of magnitude higher than that of biological tissue, resulting in $S_B^{1/2} = 9.2$ fT Hz$^{-1/2}$ for a coil temperature $T_C = 300$ K. A more sophisticated calculation following the approach of Sec. 4.3.4, including the inductive impedance of the loop but still neglecting skin depth effects, yields

$$S_B^{1/2} = \frac{\sqrt{4k_B T_C}}{\pi a^2} M_{pl} \sqrt{\frac{R_l}{R_l^2 + \omega^2 L_l^2}}, \tag{5.8}$$

where $M_{pl} = 7.8$ nH is the mutual inductance between the pickup coil and the loop calculated using Eq. (4.35), $R_l = 1.1$ mΩ is the resistance of the loop and $L_l = 0.18$ μH is its inductance. Evaluated at $\omega/2\pi = 5.6$ kHz, Eq. (5.8) yields $S_B^{1/2} = 1.6$ fT Hz$^{-1/2}$. Thus a single closed turn of wire produces magnetic field noise comparable to or greater than the SQUID noise. We therefore always open the leads to the polarizing coil with a relay when measuring spin precession.

However, breaking the continuity of the conducting loop does not eliminate magnetic field noise generated by currents flowing around the inner radius of the loop and back around the outer radius. To calculate the magnetic field noise from this current path, I calculate the power dissipated in the conducting loop when a current $I\sin(\omega t)$ flows in the pickup coil, then use Eq. (4.68) to calculate the equivalent resistive loss. Since the loop and pickup coil are concentric and $\phi << d$, the magnetic field produced by the pickup coil is perpendicular to the loop and has a constant magnitude over the loop. I can therefore simplify the geometry by straightening the loop into a wire of length $2\pi r$ without changing the dissipated power. Figure 5.3 shows a cross-section of the resulting straight wire of width w oriented perpendicular to the applied magnetic field. The changing magnetic field induces a current flowing around the loop. The amplitude of this current can be calculated by applying Faraday's law

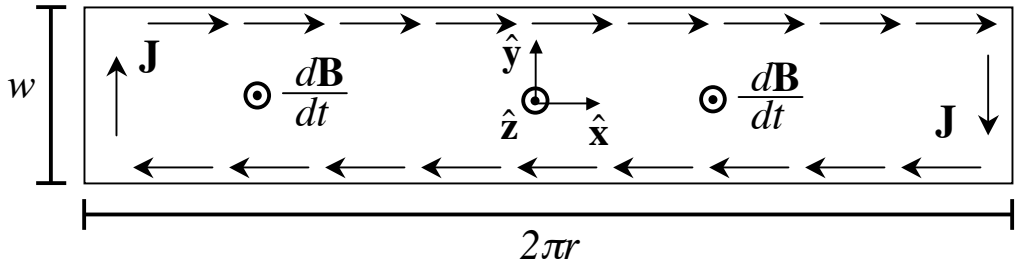

Figure 5.3: Current path in the straightened section of the broken conducting loop.

$$\nabla \times \mathbf{E} = -d\mathbf{B}/dt = -dB/dt\,\hat{\mathbf{z}}, \tag{5.9}$$

which becomes

$$\partial E_y/\partial x - \partial E_x/\partial y = -dB/dt = -j\omega B. \tag{5.10}$$

Far from the ends of the straight wire, symmetry requires $\partial E_y/\partial x = 0$. Equation (5.10) can then be solved to obtain

$$E_x = j\omega y B + C, \tag{5.11}$$

where C is the constant of integration. This electric field results in a current density

$$\mathbf{J} = j\omega y B/\rho_{Cu}\,\hat{\mathbf{x}}, \tag{5.12}$$

where I have set $C = 0$ so that no charge accumulates at the ends of the wire. The average power dissipated can be found by integrating $\mathrm{Re}[\rho_{Cu}\mathbf{J}^* \cdot \mathbf{J}]/2$ over the volume of the wire:

$$P_{loss} = \frac{1}{2}\int_0^{2\pi r} dx \int_{-\phi}^{\varphi} dz \int_{-\sqrt{\phi^2-z^2}}^{\sqrt{\phi^2-z^2}} dy\, \frac{\omega^2 y^2 B^2}{\rho_{Cu}} = \frac{\pi^2 r \phi^4 \omega^2 B^2}{4\rho_{Cu}}. \tag{5.13}$$

Comparing this result to Eq. (4.68) yields

$$R_{loss} = \frac{\pi^2 r \phi^4 \omega^2}{2\rho_{Cu}}\left(\frac{B}{I}\right)^2 \tag{5.14}$$

and

$$S_B^{1/2} = \frac{\sqrt{4k_B T_C R_{loss}}}{\pi a^2 \omega} = \sqrt{\frac{2k_B T_C r}{\rho_{Cu}}}\,\frac{\phi^2}{a^2}\left(\frac{B}{I}\right). \tag{5.15}$$

Using Eqs. (5.1) and (5.2) to evaluate the field from the pickup coil, I obtain $B/I = 2.2$ μT/A, resulting in a magnetic field noise $S_B^{1/2} = 0.26$ fT Hz$^{-1/2}$. While this noise is an order of magnitude lower than the noise from a continuous conducting loop of the same dimensions, the noise from 100 such turns will add in quadrature to produce 2.6 fT Hz$^{-1/2}$, so that a polarizing coil wound from 2-mm diameter copper wire is too

noisy to be used near a low-noise SQUID gradiometer. However, dividing the single conductor of radius ϕ into N conductors of radius $N^{-1/2}\phi$ maintains the same cross-sectional conducting area but reduces the magnetic field noise by a factor $N^{1/2}$. Upon realizing this, we replaced the polarizing coil wound from 2-mm diameter copper wire used by McDermott and co-workers with coil of similar dimensions wound from 30-strand 0.32-mm diameter Litz wire as described in Sec. 5.1.4.2, anticipating that the sixfold reduction in wire diameter would produce a sixfold reduction in coil Nyquist noise. Although this strategy reduces Nyquist noise, the additional insulating layers that separate the 30 strands of wire reduce λ, so that Eq. (5.7) indicates that a coil wound from Litz wire dissipates more power to achieve a given current density than one wound from solid wire.

The 1.63-mm copper wires used for external polarizing coil cooling, shown in Fig. 5.2, also couple Nyquist noise to the gradiometer. The field generated by a current flowing in the pickup coil changes in magnitude and direction over the length of these wires. In the radial sections of these wires, B_z generates currents traveling along the length of wire as shown in Fig. 5.3, and B_r generates currents traveling around the circumference of the wire. Using methods similar to those described above and integrating from the solenoid inner radius R_1 to the its outer radius R_2, the total magnetic field noise from both current paths over a radial section of wire can be expressed as

$$S_B^{1/2} = \sqrt{\frac{k_B T_C}{\pi \rho_{Cu}}} \frac{\phi^2}{a^2} \left\{ \int_{R_1}^{R_2} \left[B_z(r)/I \right]^2 + \frac{2}{3} \left[B_r(r)/I \right]^2 dr \right\}^{1/2}. \tag{5.16}$$

Over the vertical section of the wires, B_r generates currents traveling along the length of wire, and B_z generates currents traveling around the circumference of the wire. The total magnetic field noise over a vertical section of wire can therefore be expressed as

$$S_B^{1/2} = \sqrt{\frac{k_B T_C}{\pi \rho_{Cu}}} \frac{\phi^2}{a^2} \left\{ \int_{h}^{h+H} \left[B_r(z)/I \right]^2 + \frac{2}{3} \left[B_z(z)/I \right]^2 dz \right\}^{1/2}, \tag{5.17}$$

where h is the distance between the pickup coil and the top of the solenoid and H is the solenoid height.

5.1.4. Fabricated polarizing coils

Table 5.2 summarizes the measured and calculated parameters of the four polarizing coils used since I began working on the microtesla MRI project. It shows the

Table 5.2: Comparison of the geometry, field strength, cooling performance, and Nyquist noise of the polarizing coils described in this section. I measured the geometrical dimensions, wire specifications, and number of turns of each coil. These parameters serve as inputs to a model that produces the coil resistance, copper volume fraction, current density, dissipated power, and magnetic field strengths. All magnetic field strengths assume a coil current of 35 A.

Coil	Solid-wire 50-mm bore	Litz-wire 50-mm bore	Liquid N_2-cooled flat	Small water-cooled test
Inner diameter ($2R_1$)	57 mm	59 mm	32 mm	32 mm
Outer diameter ($2R_2$)	137 mm	200 mm	230 mm	174 mm
Height (H)	90 mm	70 mm	50 mm	36 mm
Top cap height	6.4 mm	15 mm	6.4 mm	7 mm
Wire strands	1	30	30	30
Strand diameter (2ϕ)	2 mm	0.32 mm	0.32 mm	0.32 mm
Coil turns	810	800	650	240
Coil resistance	1.3 Ω	2.3 Ω	1.9/1.0[d] Ω	0.56 Ω
Copper fraction (λ)	0.71	0.39	0.32	0.23
Current density at 35 A	7.9 A/mm^2	5.7 A/mm^2	4.65 A/mm^2	3.3 A/mm^2
Power at 35 A	1.6 kW	2.8 kW	2.3/1.2[d] kW	0.68 kW
Field at coil center	270 mT	250 mT	240 mT	110 mT
Av. field in bore[a]	230 mT	215 mT	-[e]	-[e]
Av. field over arm[b]	45 mT	52 mT	57 mT	28 mT
Av. field over specimen[c]	100 mT	100 mT	110 mT	55 mT
Cooling method	External liquid N_2	External liquid N_2	Internal liquid N_2	Internal water
Operating time	~15 s	~65 s	~250 s	Continuous
Cooling time	~5 min	~15 min	~15 min	-
Measured Nyquist noise	3 fT Hz$^{-1/2}$[f]	<1.5 fT Hz$^{-1/2}$[h]	0.8 fT Hz$^{-1/2}$[h]	-
Calc. Nyquist noise	2.9 fT Hz$^{-1/2}$[g]	0.7 fT Hz$^{-1/2}$[h]	0.6 fT Hz$^{-1/2}$[h]	0.5 fT Hz$^{-1/2}$[h]

[a] The 50-mm diameter cylindrical region starting at the coil top and extending down 50 mm into the bore.
[b] The 60-mm diameter cylindrical region starting above the insulation and extending upwards 80 mm.
[c] The 20-mm diameter cylindrical region starting above the insulation and extending upwards 20 mm.
[d] Values given for room temperature and the initial average cooled temperature of ~180 K.
[e] The bores of these coils are closed and used for coolant transport.
[f] Unknown coil location relative to gradiometer, likely 10 mm beneath cryostat.
[g] Coil top 10 mm beneath cryostat.
[h] Coil placed directly beneath cryostat, 25 mm from bottom gradiometer loop.

calculated magnetic field from each coil over three cylindrical regions with the approximate dimensions of a phantom within the coil bore, a human arm on top of the coil, and a specimen of prostate tissue on top of the coil. When imaging the human arm, we placed 10 mm of Styrofoam on top of the polarizing coil to insulate the arm from the cryogenically cooled coil; since we wanted to keep the prostate samples cold, we used only 5-mm insulation in this case. Since the water-cooled coil remains at room temperature, I calculate its magnetic field in the absence of this insulation. The following sections describe the details of these coils in turn.

5.1.4.1. Solid-wire 50-mm bore coil

This coil featured a 50-mm diameter inner bore. The low resistance of this coil allowed us to apply a current of 40 A to achieve a 300 mT polarizing fields within its bore. At the time we were using this coil, we had not yet configured the MRI system to vary the gradients while acquiring an image. We would typically apply current to the coil for a total of ~15 s while acquiring ~3 projection-reconstruction angles, then run liquid nitrogen through the copper cooling tube for ~5 minutes before acquiring subsequent angles.

Although this coil produced the highest polarizing fields we have yet achieved, its high Nyquist noise cancels any SNR advantage it has over the other coils. By modeling this coil as an array of 800 equally spaced broken wire loops, computing the magnetic field noise of each loop using Eq. (5.15), and then taking the quadrature sum, I estimated the magnetic field noise of the coil windings to be 2.8 fT $Hz^{-1/2}$. Using Eqs. (5.16) and (5.17) I estimate the magnetic field noise generated by the 102 0.16-mm diameter cooling wires to be 0.7 fT $Hz^{-1/2}$. The quadrature sum of these values yields, 2.9 fT $Hz^{-1/2}$, in excellent agreement with the 3 fT $Hz^{-1/2}$ measured by McDermott and coworkers.

5.1.4.2. Litz-wire 50-mm bore coil

In an attempt to reduce this Nyquist noise, we wound a coil with similar dimensions with 800 turns of 30-strand Litz wire. Each strand had a diameter of 0.32 mm, for a total cross-sectional area nearly equal to that of the 2-mm solid wire of the previous coil. The resulting coil had 75% greater resistance and power dissipation than the original solid-wire coil but produced comparable fields for the same applied current. In order to increase the effectiveness of the cooling wires and reduce the likelihood of freezing the

sample in the bore, we wound current-carrying Litz wire onto the coil until it reached a diameter of 90 mm, installed 174 0.32-mm diameter cooling wires, and then wound the coil to its final diameter. After upgrading the MRI system to enable automated gradient switching, we began to operate the polarizing coil for longer stretches of time before cooling it. With this polarizing coil, we could apply ~65 1-s polarizing pulses before the coil required cooling for ~15 minutes, but the ratio of operating time to cooling time did not substantially increase compared to the previous coil.

For this coil, I estimate 0.4 fT $Hz^{-1/2}$ magnetic field noise generated by the Litz-wire turns. I calculate that the cooling wires generate a field noise of 0.6 fT $Hz^{-1/2}$, for a total field noise of 0.7 fT $Hz^{-1/2}$. Our first measurements of the Nyquist noise of this coil were made against a background of 2.4 fT $Hz^{-1/2}$ (radiofrequency noise leaking through the shield raised the noise above the 1.7 fT $Hz^{-1/2}$ SQUID noise), so we can only conclude that the coil noise was less than 1.5 fT $Hz^{-1/2}$.

We recently attempted to measure the Nyquist noise of this polarizing coil more accurately by measuring it in the second-generation MRI system and found that the coil generated 2.4 fT $Hz^{-1/2}$ of noise. Additional current paths within the Litz-wire coil that are not included in the calculation above are the most likely cause of the excess noise in the later measurement. During the two and one-half years between these measurements, we burned through the wire insulation of this coil at least twice while attempting to increase the maximum coil operating time between cooling periods. Each time, we removed the defective wire from the coil and then joined new Litz wire to the remaining wire with a solder junction. Because the solder junctions make an electrical connection between all 30 strands of the Litz wire, electrical current can flow from one solder junction to the next solder junction through one strand of Litz wire and then back through a different strand, effectively increasing the diameter of the wire in the magnetic field noise calculation. In addition, such damage to the wire insulation may have caused a short between adjacent turns in the coil, thereby producing a circular current loop without noticeably changing the coil resistance. As shown in Sec. 5.1.3, even one such closed loop can generate more Nyquist noise than the rest of the Litz-wire coil combined.

5.1.4.3. Liquid nitrogen-cooled flat coil

The third-generation coil substantially improves the cooling performance and eliminates the copper cooling wires by using the internal cooling scheme shown in Fig. 5.4. We flow liquid nitrogen through a manifold that distributes it between eight nozzles located in the center of the coil. The nitrogen flows radially inwards to the center bore of the coil and radially outwards to the edge of the coil through a series of gaps created by G-10 fiberglass spacing rods. The liquid nitrogen vaporizes within the coil, and tubes connected to the inner bore and outer edge of the coil vent the resulting nitrogen gas outside the aluminum shield. We pre-cool this coil for 10-15 minutes until its resistance drops from 1.9 Ω to 1.0 Ω, corresponding to an average coil temperature of ~180 K. Since the coil contains 5.8 kg of copper, and the heat capacity of copper is approximately 0.37 J/g K between 200 and 300 K [1], 260 kJ of heat is required to raise the coil temperature to 300 K. Passing 35 A through the cold coil dissipates 1.2 kW of power, so

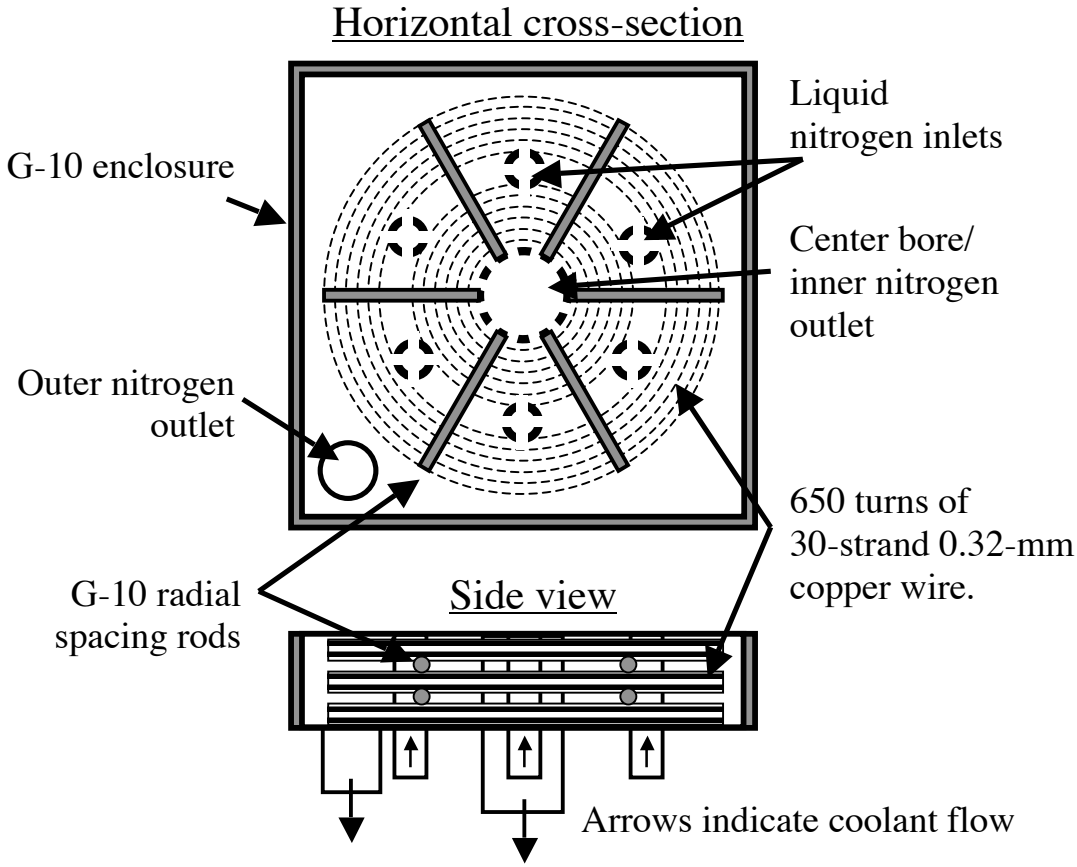

Figure 5.4: Schematic of the internally cooled liquid nitrogen coil. While this figure shows six nitrogen inlets for clarity, the coil itself contains eight.

that one would predict an operating time of 260 kJ/1.2 kW = 220 s. Since we attach the coil to a constant-voltage power supply, the applied current and dissipated power decrease as the coil warms. On the other hand, the nitrogen flow pattern causes the inner and outer edges of the coil to be warmer than average when we begin to operate the coil; since these regions have correspondingly higher resistance, their temperature will increase rapidly during operation. Experimentally, we find that we can apply current for ~250 s before stopping to cool the coil again. During this time, the total resistance of the polarizing coil circuit (including 0.3 Ω of contact and lead resistance) rises from 1.3 Ω to 1.9 Ω, such that the average current through the coil is 30 A. In the descriptions of the images taken using this polarizing coil, I calculate B_p using the 30 A time-averaged current.

Because of its long operating time, low Nyquist noise, and moderately high magnetic fields, we have used this coil to polarize almost all of our samples during the last year and a half of low-field MRI research. However, for the reasons described in Sec. 5.1.2, we cannot cool this coil during continuous operation without generating hot spots and potentially destroying the wire insulation. Furthermore, while liquid nitrogen is readily available in the laboratory, one would prefer to use a water-cooled solenoid in a hospital environment.

5.1.4.4. Small water-cooled test coil

We therefore began to investigate water-cooled solenoids. We encountered an electrical anomaly (coil resistance rising and falling much more rapidly than could be explained by coil heating) when attempting to water-cool the coil described in the previous section. Therefore, we chose to build a small (and possibly sacrificial) test coil to determine the current density that could be achieved with a continuously water-cooled Litz-wire coil. To optimize the cooling efficiency, we decided that each Litz-wire turn should be in contact with cooling water, and thus wound 8 vertical layers of wire separated by G-10 fiberglass spacing rods in a 1:2:2:2:1 pattern, where each colon represents a spacing layer. Although this winding scheme reduced λ to 0.23, we hoped that the enhanced cooling would allow us to run more current through the wires.

In order to prevent the cooling water from producing a detectable NMR signal, we doped it with 0.05 M $MnCl_2$ to reduce its T_1 to 0.45 ms [3]. We pumped 1.6 L/min of

cooling water through the coil, cooling the recirculating doped water by passing it through a heat exchanger along with 7.6 L/min of ~15 °C tap water. Using this arrangement, we could apply 55 A of current for 30 minutes without damaging the coil, corresponding to a continuous current density J_c = 5.2 A/mm^2. Since the coil is cooled continuously, but prepolarized MRI sequences require only pulsed polarizing fields, one can achieve a pulsed current density $J_p = J_c\sqrt{\left(T_p + T_{other}\right)/T_p}$, where T_p is the polarizing time and T_{other} is the sum of the encoding, acquisition, and delay times. Assuming a 50% duty cycle yields J_p = 7.3 A/mm^2. The larger, liquid-nitrogen-cooled coil described in Sec. 5.1.4.3 produces higher magnetic fields than this coil even with J_p = 7.3 A/mm^2. However, if we built a polarizing coil with dimensions equal to the liquid-nitrogen-cooled coil and used the winding geometry and cooling scheme of the small water-cooled test coil, we could hope to achieve an average field of 110 mT over the arm.

5.2. Higher-balance, lower-inductance gradiometer

Besides the polarizing coil changes described above, the first change we made to the microtesla MRI system built by McDermott and co-workers was to replace its superconducting gradiometer. As described in Sec. 1.1.4, we employ a second-order gradiometer to reduce the response to distant sources of magnetic field noise. Since we did not know how much external noise contributed to the measured 1.7 fT Hz$^{-1/2}$ magnetic field noise, we believed that improving the balance of the gradiometer against uniform external fields might reduce this noise.

The first-generation gradiometer installed in the MRI system consisted of four loops of 2ϕ = 75-μm diameter superconducting niobium wire wound in grooves machined on the outside of a hollow Phenolic cylinder. The loops had a diameter $2a$ = 65 mm and were wound in the configuration shown in Fig. 1.6(B) with baseline b = 75 mm. The two center loops were wound within the same groove. The inductance of a single loop is given by $L_1 = \mu_0 a[\ln(8a/\phi) - 2]$ = 0.28 μH. Assuming that the two center loops contribute an inductance of $4L_1$, a first-order estimate of the gradiometer inductance is $L_p = 6L_1$ = 1.7 μH. Using Eq. (4.35) to compute the mutual inductance between the center loop and either the upper or lower loop yields M_{cu} = 3.3 nH, so $L_p = 6L_1 - 8M_{cu}$ =

1.65 μH, a somewhat better estimate of the gradiometer inductance. The mutual inductance between the top and bottom gradiometer loops is 0.6 nH and can be neglected.

The imbalance of a gradiometer against uniform fields is defined as the ratio of its response to a uniform field divided by the response of a magnetometer with identical loop area perpendicular to the applied field; its balance is the inverse of this quantity. We estimated the balance of the gradiometer by measuring the SQUID response to 5.6 kHz magnetic fields applied by the cancellation coils in the *x*, *y*, and *z* directions. We obtained apparent balances of 130, 420, and 520 in the *x*, *y*, and *z*-directions, respectively. Since wire-wound superconducting gradiometers commonly have balances of 1000 or more, we were somewhat surprised by these results.

The poor balance in the *x* (axial) direction originates from two factors. First, since the two center loops were wound within the same groove, the diameter of the outer loop is approximately $2(a + 2\phi_I)$, where $\phi_I = 62.5$ μm is the insulated radius of the wire. Second, the square cancellation coils used to apply the test field have poor homogeneity and produce a relatively strong second-derivative magnetic field. If the field produced by these coils at their geometric center is $B\hat{\mathbf{x}}$, I calculate the field at a distance $b = 75$ mm above or below this point to be $B'\hat{\mathbf{x}} = 1.0058B\hat{\mathbf{x}}$. The expected measured imbalance can be calculated by summing the flux through each of the four gradiometer loops and dividing by the flux through an equal-area magnetometer to obtain

$$\frac{\pi a^2 B' - \pi a^2 B - \pi\left(a + 2\phi_I\right)^2 B + \pi a^2 B'}{\pi a^2 B} = 0.0039 = (260)^{-1}. \qquad (5.18)$$

This imbalance is a factor of two smaller than the measured imbalance of 1/130. Since the effects of the mismatched center loops and inhomogeneous magnetic field partially cancel each other, this discrepancy could be explained if the radii of the center loops differed by either more or less than $2\phi_I$.

When we examined the gradiometer, we found that the wires connecting the turns of the gradiometer were not twisted. Assuming that these wires are separated by a distance $2\phi_I$, the area between the wires connecting adjacent gradiometer coils is $2\phi_I b = 9.4$ mm^2, producing an imbalance of $2\phi b/\pi a^2 = 1/350$. This effect could explain the poor transverse (*y* and *z*) balance.

In order to improve the balance against uniform fields and hopefully reduce the contribution of external noise, we fabricated a gradiometer with identical dimensions but an improved winding scheme compared to the gradiometer used by McDermott and co-workers. The center two loops of this gradiometer were wound in two grooves separated by a 2.5-mm gap, and we twisted the niobium wires that formed the 75-mm baseline segments. Separating the center loops by 2.5 mm reduces the gradiometer inductance to $L_p = 4L_1 + 2M_{cc} - 8M_{cu} = 1.31$ μH, where $M_{cc} = 0.11$ μH is the mutual inductance between the two center loops computed using Eq. (4.35).

When we measured the balance of this gradiometer using the fields generated by the cancellation coils, we obtained apparent values of 120, 8300, and 2800 in the x, y, and z-directions, respectively. As expected, twisting the gradiometer leads results in much higher transverse balance. Setting both center loop areas equal to πa^2 in Eq. (5.18) but retaining the field inhomogeneity terms predicts an axial imbalance of 1/86. The best estimate of the axial balance of the gradiometer itself is therefore $(86^{-1} - 120^{-1})^{-1} = 300$. We would need to wind a coil that produces a more homogeneous field in the x-direction (vertical) in order to estimate the axial balance of the gradiometer more accurately.

When we measured the magnetic field noise after installing this gradiometer, we found it to be virtually unchanged at 1.7 fT $Hz^{-1/2}$ despite the lower inductance and improved balance of the gradiometer. Applying Eq. (4.3) to the $L_i = 1.9$ μH Quantum Design SQUID, one would expect reducing L_p from 1.7 μH to 1.3 μH to increase the effective area by 11%, thereby reducing the magnetic field noise. We did not make careful measurements of effective area as described in Sec. 4.2.2.4 after installing the second-generation gradiometer, and thus have no record of the change in effective area[*]. Since changing A_{eff} does not change the flux noise of the SQUID, and we calculate the magnetic field noise by dividing the measured flux noise by A_{eff}, our subsequent measurements of magnetic noise did not reflect the change in gradiometer inductance.

[*] We separated the two center loops of the second-generation gradiometer in order to increase the gradiometer balance. Only after installing Mück #3 did we realize that this would also increase A_{eff}, so we made no measurements of A_{eff} with the Quantum Design SQUID attached to the second-generation gradiometer. The measured values of magnetic field noise in this configuration (May through August 2005) are therefore up to 11% too high.

Improving the gradiometer balance only decreases the contribution of magnetic field noise picked up by the gradiometer from distant external sources. Since we did not measure lower magnetic field noise, we concluded that SQUID noise and radiofrequency noise picked up by the copper probe leads made the largest contributions to the measured 1.7 fT $Hz^{-1/2}$ noise. We therefore replaced the Quantum Design SQUID with a lower-noise SQUID fabricated by Michael Mück as described in Sec. 4.2. Although the predicted field noise of Mück #3 was 0.32 fT $Hz^{-1/2}$, we measured a magnetic field noise of 1.1 fT $Hz^{-1/2}$. Based on the measurements shown in Table 4.3, we concluded that the excess noise resulted from some combination of 5.6 kHz noise and radiofrequency noise.

5.3. Second-generation aluminum shield

To reduce the magnetic field noise still further, we embarked on a project to build a second-generation aluminum shield to decrease the level of both 5.6 kHz and radiofrequency noise. The first-generation aluminum shield was located in Birge B260 and was 2.4 m wide, 2.4 m high, and 3.6 m long; the extra length accommodated the Golay coils shown in Fig. 1.12. In order to fit the second-generation shield into the smaller space available in Birge B203, we reduced the size of the shield to a 2.4-m cube. While this change substantially reduced the construction effort, it required us to redesign the dB_z/dx and dB_z/dy gradient coils as described in Sec. 5.4.3.

5.3.1. Physical description

The sides of the second-generation aluminum shield are 6.4-mm thick 5052 aluminum plates, double the thickness of the first-generation shield. The floor, back three sides, and ceiling are each composed of two 1.2 m by 2.4 m such plates bolted to a frame built from 38-mm square hollow extruded aluminum supports with 1/4-20 brass bolts. The front side features two 0.76-m wide vertical plates on either side of a 1.0 m wide by 2.0 m high door made from the same plate. Flexible nickel-coated copper-beryllium “fingers” riveted to the inside of the door provide a low-resistance electrical connection between the door and the aluminum plate comprising the cube.

The construction of this shield was a monumental effort, involving nearly one ton of aluminum and one thousand brass bolts. Since Michael Hatridge designed the shield, ordered the aluminum, and supervised the undergraduates who drilled the holes for the

bolts and put the cube together, I will let him describe the details of its design and construction in his dissertation.

5.3.2. Shielding performance

Since the radiation skin depth in 5052 aluminum is 1.5 mm at 5.6 kHz, we expect the 6.4-mm thick walls to attenuate such radiation by a factor of $e^{6.4/1.5} \approx 70$. As described in Sec. 4.2.1.5, we measured a magnetic field noise of 1.1 fT $Hz^{-1/2}$ with the gradiometer connected to Mück #3 in the Birge B203 copper mesh screen room. This noise level represents the relatively noise-free region of the magnetic field spectrum around 5.6 kHz[†]; the spectrum outside this region contained peaks with approximately ten times higher amplitude. When we replaced the screen room with the second-generation aluminum shield, these peaks disappeared, and we measured 0.75 fT $Hz^{-1/2}$ noise between 3 kHz and 10 kHz. These results indicate that the second-generation shield attenuates 5.6-kHz noise by at least a factor of 15.

Since the SQUID does not directly measure the amplitude of radiofrequency noise, it is more difficult to quantify the radiofrequency screening of the second-generation aluminum shield. As described in Sec. 1.1.3, the most noticeable effect of radiofrequency radiation is the reduction in SQUID modulation amplitude. The SQUID can also mix noise at twice the modulation frequency of the flux-locked loop down to MRI frequencies as described in Sec. 4.2.1.3. When we moved the SQUID gradiometer from the first-generation shield to the second-generation shield, the SQUID modulation amplitude increased, but we did not make quantitative measurements of this effect. A qualitative indication of the improved radiofrequency shielding is that the measured SQUID noise barely increases when the Birge B203 fluorescent lights are turned on, whereas the first-generation MRI system could not be operated with the room lights on. However, the radiofrequency shielding of the second-generation shield is not perfect, since we must still wrap the cryostat in aluminum foil as described in Sec. 4.2.2.5 to obtain the lowest magnetic field noise.

By far the most important measure of the performance of the second-generation aluminum shield is the 0.75 fT $Hz^{-1/2}$ magnetic field noise measured with Mück #1 in this

[†] McDermott and co-workers chose the 5.6 kHz precession frequency to take advantage of this low-noise region in the Birge basement electromagnetic spectrum.

enclosure. Since Table 4.2 shows that flux noise of this SQUID after subtracting the calculated shunt noise is equivalent to a magnetic field noise of 0.51 fT $Hz^{-1/2}$, the combination of 5.6 kHz noise and radiofrequency noise contribute at most 0.55 fT $Hz^{-1/2}$ to the observed magnetic field noise. Since the preamplifier noise of the 2 MHz flux-locking electronics has not been measured and could contribute substantially to the total field noise, the environmental contribution might be significantly lower.

5.3.3. Eddy currents induced by the polarizing field

After measuring the magnetic field noise of Mück #1 connected to the second-generation gradiometer inside the second-generation aluminum shield, we began to apply polarizing pulses to acquire MRI images. We immediately noticed that the SQUID detected a multi-exponential relaxation signal with a flux amplitude of ~60 Φ_0 when measured ~70 ms after the polarizing pulse; the longest time constant was ~60 ms. This relaxation signal exceeded the ±15 Φ_0 dynamic range of the flux-locked loop, thereby preventing data acquisition. At first we were unsure of the origin of this relaxation: did the polarizing coil magnetize steel rebar in the floor of Birge B203, or did it induce eddy currents in the second-generation magnetic shield?

I decided to model the eddy-current behavior of the new shield to determine whether it could be responsible for this relaxation. For ease of calculation, I approximate the shield as a 2.4-m tall, 2.8-m diameter closed cylinder; the circular ends of this cylinder have the same area as the 2.4-m square top and bottom plates of the shield. I represent the nitrogen-cooled flat polarizing coil by an equivalent point dipole at the center of this cylinder; applying 35 A of current produces a 370 A m^2 dipole. I divide the top of this cylinder up into 67 6.4-mm thick annuli with inner and outer radii differing by 20 mm and do the same for the cylinder bottom. The cylinder walls are divided into 120 20-mm tall cylinders, each of radius 1.2 m. I estimate the inductance of each loop by modeling them as normal metal wires with radius $\phi = 3.2$ mm (half the shield thickness) and applying the formula $L = \mu_0 R[\ln(16R/\phi) - 7/4]$ [4]. For two such loops in the presence of an applied magnetic field that couples a flux $\Phi_1(t)$ into the first loop and $\Phi_2(t)$ into the second loop, the current through the loops obeys the coupled differential equations

$$\begin{aligned} \frac{d\Phi_1}{dt} + I_1 R_1 + L_1 \frac{dI_1}{dt} + M_{12} \frac{dI_2}{dt} &= 0 \\ \text{and } \frac{d\Phi_2}{dt} + I_2 R_2 + L_2 \frac{dI_2}{dt} + M_{12} \frac{dI_1}{dt} &= 0, \end{aligned} \tag{5.19}$$

where $I_1(t)$, R_1, and L_1 are the time-varying current, resistance, and inductance of the first loop, $I_2(t)$, R_2, and L_2 are the same quantities for the second loop, and M_{12} is the mutual inductance between the two loops. Equation (5.19) can be generalized to many loops and expressed in vector notation as

$$\frac{d\mathbf{\Phi}}{dt} + \mathbf{R}\mathbf{I} + \mathbf{L}\frac{d\mathbf{I}}{dt} = 0, \tag{5.20}$$

where $\mathbf{I}(t)$ and $\mathbf{\Phi}(t)$ are vectors representing the current flowing around and external applied flux to each loop, respectively, $\mathbf{R}$ is a diagonal matrix describing the resistance of each loop, and $\mathbf{L}$ is a matrix that contains the self and mutual inductance terms found in Eq. (5.19). Rearranging Eq. (5.20) and multiplying by the inverse of $\mathbf{L}$ yields

$$\frac{d\mathbf{I}}{dt} = -\mathbf{L}^{-1}\left(\mathbf{R}\mathbf{I} + \frac{d\mathbf{\Phi}}{dt}\right). \tag{5.21}$$

Assuming the polarizing field is turned off in a time much shorter than the eddy-current time constants, the initial current is given by

$$\mathbf{I}_0 = -\mathbf{L}^{-1}\mathbf{\Phi}_0, \tag{5.22}$$

where $\mathbf{\Phi}_0$ is a vector representing the flux through each of the loops produced by the polarizing coil. Taking the time derivative of Eq. (5.21) shows that the circulating currents decay with time constants given by inverse of the eigenvalues of $\mathbf{L}^{-1}\mathbf{R}$; the four longest time constants are 91 ms, 60 ms, 39 ms, and 28 ms. Rather than attempting to express $\mathbf{I}_0$ as a sum of the eigenvectors of $\mathbf{L}^{-1}\mathbf{R}$, I set $d\mathbf{\Phi}/dt = 0$ and integrate Eq. (5.21) numerically to find $\mathbf{I}(t)$. The magnetic field at the center of the cylinder that results from these currents is a good fit to the exponential function $\mathbf{B} = B_0 \exp(-t/\tau)\hat{\mathbf{x}}$, where $B_0 = 23$ μT and $\tau = 84$ ms. Neither decreasing the numerical integration time step by a factor of five nor doubling the number of loop elements representing the cylindrical shield changes this result.

Since the joints between the aluminum panels and the support frame increase the resistance seen by currents circulating around the shield compared to the continuous cylinder modeled above, one would expect the observed relaxation times to be shorter

than 84 ms. The ~60 ms time constant of the observed relaxation is therefore consistent with such circulating currents. Multiplying the predicted 23-μT-relaxation amplitude by the 25 mm^2 effective area of the gradiometer and dividing by its estimated axial balance of 300 yields a predicted flux amplitude of 930 Φ_0. Extrapolating experimental measurements of the relaxation back to the time that we turned off the polarizing coil yields an amplitude of ~900 Φ_0. Not only does relaxation of this magnitude make it nearly impossible to acquire data, but a 23-μT magnetic field perpendicular to the 132-μT precession field will increase the spin precession frequency by 85 Hz, potentially disrupting the MRI image.

The most obvious way to reduce the effect of these eddy currents is to increase the resistance seen by currents flowing around the aluminum shield. However, we explicitly designed the shield to have low resistance connections between the plates to improve its screening performance. We therefore decided to cancel the magnetic flux that the polarizing coil applies to the aluminum shield by applying a counter-field. By applying ~1.5 A through the 20-turn coil described in Sec. 5.4.5 and ramping down this current at the same time that we turn off the polarizing coil, we are able to reduce the detected magnitude of the eddy-current relaxation to ~4 Φ_0, within the dynamic range of the flux-locked loop.

5.4. Second-generation magnetic field coils

The second-generation magnetic field coils follow the basic design of the first-generation coils: copper wire wound on wooden coil forms. As in the first-generation system, four 38-mm diameter wooden dowels passing through holes drilled in the coil forms support the coils that produce precession field and imaging gradients. Diagonal wood beams attached to the 1.8-m wooden cubic frame support the dowels. The cancellation coils are wound directly on the cubic frame. Figure 5.5 shows the magnetic field coils of the second-generation MRI system. We made two major coil design changes compared to the first-generation system. First, we replaced the Helmholtz B_0 coils with a four-coil biplanar design [5] in order to improve magnetic field homogeneity. Second, we replaced the dB_z/dx and dB_z/dy Golay coils with more compact planar gradient coils so that the coils would fit within the smaller second-generation shield.

Table 5.3 summarizes the design of the second-generation magnetic field coils. The following sections describe each of the coils in turn.

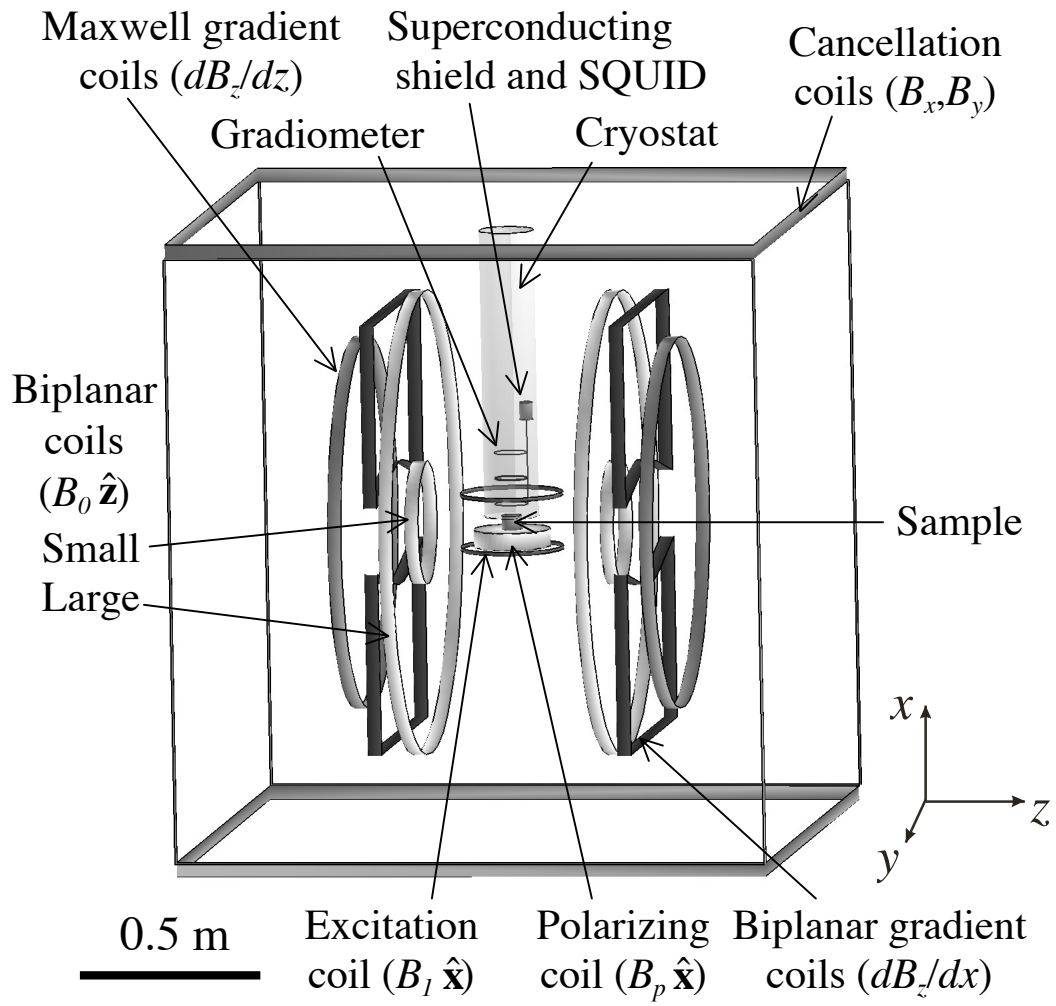

Figure 5.5: Coil geometry of the second-generation microtesla MRI system. The cryostat has been rendered translucent to reveal the superconducting shield containing the SQUID and the gradiometer. For clarity, the G_y biplanar gradient coils and the eddy-current cancellation coil are not shown and the gradiometer radius is exaggerated.

Table 5.3: Calculated properties of the second-generation magnetic field coils.

Function	Geometry	Turns, wire dia. Inductance Resistance	Coil constant Coil inhomogeneity[a]
Cancellation field B_x, B_y	Square coils on opposite sides of the 1.8 m cube	100, 1.0 mm 110 mH [a] 31 Ω	51 μT/A 2.6×10^{-3} [d]
Precession field B_z (large coils)	Four-coil biplanar; 1.37 m diameter large coils, 0.36 m diameter small coils, 0.594 m separation	20, 1.0 mm 5.9 mH [b] 3.8 Ω	28.6 μT/A [e]
Measurement field B_z (small coils)		10, 0.72 mm 0.3 mH [b] 0.95 Ω	6×10^{-8} [f]
Excitation field B_x	Helmholz pair; 155 mm radius	15, 0.8 mm 0.63 mH [b] 1.0 Ω	87 μT/A 1.8×10^{-2} [f]
Encoding gradient dB_z/dx	Biplanar; 0.9 m wide, 1.28 m high, 0.76 m separation	20, 1.15 mm ~4.5 mH [c] 3.8 Ω	78 μT/m/A 5.9×10^{-5} m [d,g]
Encoding gradient dB_z/dy	Biplanar; 1.45 m wide, 1.02 m high, 0.86 m separation	20, 1.15 mm ~5 mH [c] 4.3 Ω	60 μT/m/A 4.3×10^{-5} m [d,g]
Encoding gradient dB_z/dz	Maxwell pair; diameter 1.13 m	26, 1.0 mm 6.8 mH [b] 4.0 Ω	66 μT/m/A 3.3×10^{-6} m [f,g]
Eddy current cancellation coil B_x	Square 1.8 m coil wound in the $x = 0$ plane	20, 1.0 mm 3.1 Ω	12.6 μT/A 4.0×10^{-3} [d]

[a] Measured quantity
[b] I assume the inductance scales as the number of turns squared, which overestimates the true inductance.
[c] Inductance estimated by scaling the measured inductance of the biplanar coils in Table 1.1.
[d] Field inhomogeneity is calculated within a 0.1-m cubic volume in the center of the coils.
[e] The coil constant refers to the field per unit current through the outer coils.
[f] Field inhomogeneity is calculated within a 0.1-m diameter, 0.1-m long cylinder in the center of the coils.
[g] As in Sec. 5.4.3, I describe the field inhomogeneity of a gradient coil as $\Delta B/G$, which has units of length.

5.4.1. Cancellation field coils

As in the first-generation system, pairs of 100-turn 1.8-m square coils generate the cancellation fields. Since the measurement field coils produce a constant B_z field which is much more homogeneous than the field generated by these square coils, we eliminated the redundant B_z cancellation coil to reduce construction effort.

The B_x and B_y cancellation coils combined with the B_z measurement field coil are sufficient to cancel any homogeneous external magnetic field in the imaging volume. However, one would like to cancel external gradients as well, leaving only the desired

imaging gradients. Maxwell's equations ($\nabla \cdot \mathbf{B} = 0$ and $\nabla \times \mathbf{B} = 0$) reduce the number of independent first-derivative gradient components from nine to five. Neglecting coil inhomogeneity, the dB_z/dx, dB_z/dy, and dB_z/dz coils are sufficient to produce a constant B_z field over the sample volume, but two more independent gradient controls are required to produce a gradient-free imaging volume. By applying different currents to the two coils comprising a cancellation field pair, one could generate dB_x/dx and dB_y/dy gradients without winding additional magnetic field coils. We have not yet implemented such independent current control because none of our MRI experiments so far has required this degree of background field homogeneity.

5.4.2. Precession field coils

A 0.6-m radius Helmholtz pair (separation equal to radius) generated the B_0 field of the first-generation MRI system. I calculate the maximum magnetic field inhomogeneity $\Delta B_0/B_0$ of this coil to be 9×10^{-5} within a 0.1-m diameter, 0.1-m long cylinder centered within the coil and 1.4×10^{-3} within a 0.2-m diameter, 0.2-m long cylinder. A field inhomogeneity of 1.4×10^{-3} corresponds to a frequency shift of 8 Hz at 132 μT, which produces a 3 mm spatial distortion with a 60 μT/m frequency-encoding gradient. We therefore decided to redesign the B_0 coil to increase its magnetic field homogeneity.

Following the lead of Tsai *et al.* [6], we chose the 4-coil biplanar geometry developed by Morgan, Conolly, and Macovski [5]. Table 5.4 shows their design expressed as the ratios of the large coil radius R_1 and the small coil radius R_2 to the spacing between the coils z and the ratio of the currents carried by these coils I_1/I_2. I calculate the magnetic field inhomogeneity of a $z = 0.6$ m implementation of this coil to be 2.4×10^{-5} over the 0.2-m diameter cylinder. We could never produce a coil with dimensions as precise as the specifications shown Table 5.4, so I calculated the effect of varying the dimensions. An error of ±7 mm in the radius of the inner or outer coils raises the inhomogeneity to $\sim 2 \times 10^{-4}$, while an error of ±2% in the current flowing through the inner coil raises the inhomogeneity to $\sim 1 \times 10^{-4}$. Even with these relatively gross errors, the 4-coil biplanar design still produces a substantially more homogeneous field than the original Helmholtz pair.

Table 5.4: Calculated dimensions and coil currents of the 4-coil biplanar B_0 coil.

R_1/z	1.15025
R_2/z	0.30510
I_1/I_2	40.7631

In order to perform field-cycling experiments in the first-generation MRI system [7], we maintained a constant current through the B_0 coil and applied field-cycling pulses to the B_z cancellation coil. We did not perform field-cycling using the B_0 coil because we could not find a way to maintain a constant current through the B_0 coil during data acquisition without coupling noise into the SQUID and yet rapidly change this current during the field-cycling steps. Since the cancellation coils have poor homogeneity and high inductance, employing them to apply field cycling pulses does not work well for MRI. We therefore chose to eliminate the B_z cancellation coil in favor of a second coil wound on top of the B_0 coil that could be used for field cycling in the second-generation MRI system.

We wound these coils on a two circular forms cut from 3/4-inch thick premium grade A1 oak plywood. Since the 54-inch coil diameter exceeds the dimensions of 4 by 8 foot plywood sheets, we used a plate joiner to attach additional plywood to form ~58-inch squares. We marked these circles with a divider, made a rough cut with a jigsaw, and then sanded the circles to their final diameter. We used a router to cut grooves in the outside of the circles for the large coils and circular 0.36-m diameter grooves for the small coils, and then wound the wire within these grooves. We drilled four 1.5-inch holes forming a 24-inch square for the support dowels to pass through, and then attached the coils to the wooden frame.

Because the smallest integer approximation of the ratio $I_1/I_2 = 40.7631$ is 163/4, and we did not want to wind 163-turn coils, we decided to apply different currents to the large and small coils and wound 20 turns on the large coils and 10 turns on the small coils. In this configuration, the simplest way to ensure the required ratio of currents is to attach constant-current power supplies to both the large and small coils, measure the current applied to the large coil, and then apply the appropriate current to the small coil. However, this arrangement makes it inconvenient to change B_0 by hand and is incompatible with automated B_0 field cycling. In order to overcome these limitations, we could insert a small current-measuring resistor in series with the large coils and use the voltage across this resistor as the input to a voltage-controlled, constant-current power supply connected to the small coils.

5.4.3. Image encoding gradient coils

We were unable to find suitable designs for a biplanar gradient coil that would fit within the smaller second-generation shielded room, so I began with the approximate layout of the planar gradient coils employed by Tsai *et al.* [6], and then optimized the geometry to minimize the magnetic field inhomogeneity. The inhomogeneity of a dB_z/dy gradient coil can be described as

$$\Delta B/G = \max_{\mathbf{r}} \left| B_z(\mathbf{r}) - yG_y \right| / G_y , \tag{5.23}$$

where $B_z(\mathbf{r})$ is the z-component of the magnetic field generated by the coil at a point $\mathbf{r}$, G_y is the magnetic field gradient generated by the coil, and $\max_{\mathbf{r}}$ denotes the spatial maximum over the region of interest; $\Delta B/G$ has units of length. For the Golay gradient coils installed in the first-generation system, I calculate $\Delta B/G$ = 17 μm over the 0.1-m diameter, 0.1-m long cylinder in the center of the gradient coils. Because the first-generation dB_z/dz coils have a ratio of coil separation to radius of 1.54 rather than the ideal value of $\sqrt{3}$ [‡], I calculate $\Delta B/G$ = 78 μm over the same region. For an applied gradient of 1 mT/m, this inhomogeneity corresponds to a maximum frequency shift of 0.7 Hz and 3.3 Hz for the Golay and Maxwell coils, respectively.

I began optimizing the planar gradient coils by describing the coils by the coordinates X_1, Y_1, Y_2, A_x, A_y, B_x, and B_y as shown in Fig. 5.6(A). Fixing the coil spacing at $2Z_1$ = 0.7 m, I chose the initial values of the parameters shown in Table 5.5 to approximate the coil of Tsai *et al.* I then calculated the gradient of the magnetic field inhomogeneity over a 0.1-m cube at the center of the coils with respect to each of the coordinates and minimized the inhomogeneity repeatedly with respect to each coordinate. This process decreased $\Delta B/G$ from an unacceptably large 920 μm to 74 μm, comparable to the inhomogeneity of the dB_z/dz coils of the first-generation system. I calculated that a 2.5-mm error in any of the coordinates would increase $\Delta B/G$ to at most 110 μm and a 5-mm error would produce a maximum inhomogeneity of 150 μm.

[‡] When McDermott and co-workers built the first-generation MRI system, they installed a properly spaced Maxwell coil. However, they later moved the coils apart to accommodate a larger cryostat. We subsequently restored the Helmholz B_0 coil to its proper spacing, but did not modify the Maxwell coil.

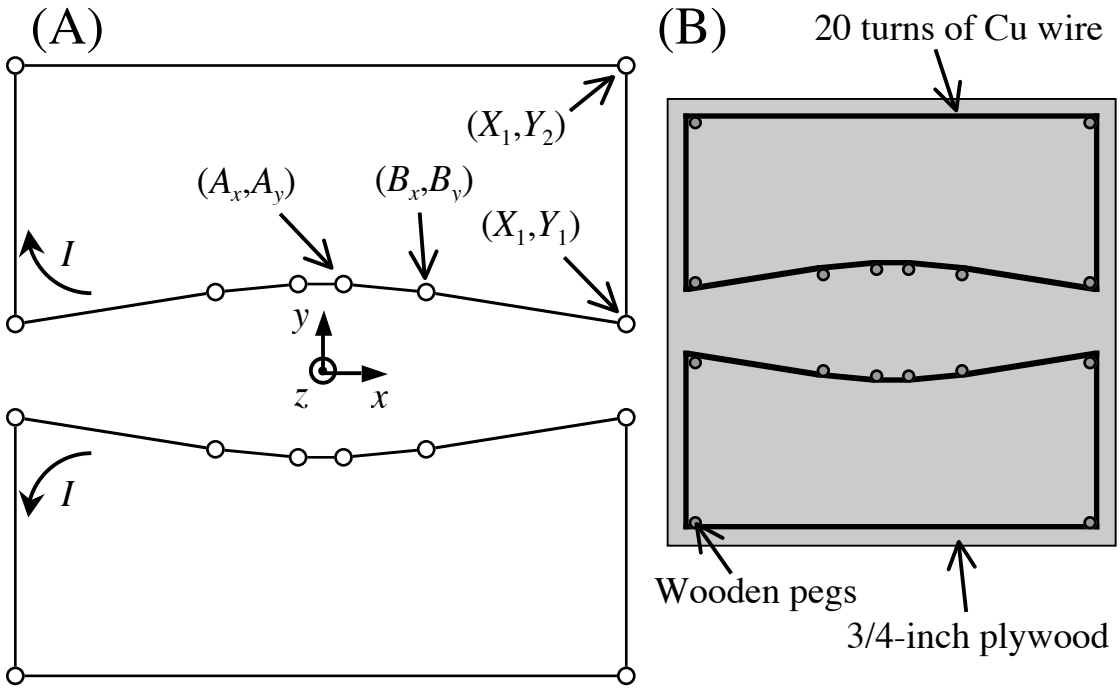

Figure 5.6: Custom-designed planar gradient coils. (A) A side view of one of the halves of a dB_z/dy planar gradient coil showing the coordinate definitions and direction of the electrical current. (B) A schematic of the constructed magnetic field coil in which copper wire is wound around wooden pegs inserted into holes in the plywood coil form.

We built the planar gradient coils by winding wire around 1/4-inch diameter wooden pegs (Woodworks, Ltd.) inserted into holes in the 3/4-inch thick plywood coil form as shown in Fig. 5.6(B). In order to accurately position the coil holes, we printed 42-inch by 60-inch graph paper with grid lines every 0.1 inch (2.5 mm) on an inkjet poster printer. We placed the graph paper on top of the plywood, marked the calculated hole locations, and used a center punch to mark the center of the holes. We laid out the locations of the 1.5-inch holes for the support dowels to pass through in the same way. We then glued the pegs in the holes and wound 20 turns of wire around the pegs. To prevent the wires from sagging under the influence of gravity, we added extra support pegs that are not shown in Fig. 5.6(B). We placed the plywood

Table 5.5: Coordinates, gradient per unit current, and inhomogeneity of initial and optimized planar gradient coils.

	Initial values	Optimized values
X_1	0.438 m	0.413 m
Y_1	0.097 m	0.091 m
Y_2	0.583 m	0.586 m
A_x	0.035 m	0.032 m
A_y	0.097 m	0.075 m
B_x	0.117 m	0.143 m
B_y	0.169 m	0.060 m
Z_1	0.350 m	0.350 m
G/I	3.0 μT/m	4.6 μT/m
$\Delta B/G$	920 μm	74 μm

forms of the dB_z/dx and dB_z/dy coils back-to-back and supported them on the 1.5-inch dowels within the wooden cube. In order to fit the planar gradient coils between the B_0 and dB_z/dz coils, we chose $Z_1 = 0.38$ m for the dB_z/dx coils and 0.43 m for the dB_z/dy coils and scaled the other dimensions accordingly. This somewhat greater center-to-center spacing decreases the gradient per unit current and increases the magnetic field homogeneity compared to the values shown in Table 5.5.

Maxwell gradient coils of comparable diameter to the B_0 coil produce homogeneous dB_z/dz gradients in a compact space, so we kept this design in the second-generation system. I calculate $\Delta B/G = 3.3$ μm for the 1.13-m diameter Maxwell coil; the superior homogeneity of the Golay coils in the first-generation MRI system and the correctly-spaced Maxwell coils in the second-generation MRI system compared to the planar gradient coils probably originates from the cylindrical geometry of these coils.

5.4.4. Excitation coils

In order to obtain a more homogeneous excitation field, we replaced the single-loop excitation coil shown in Fig. 1.12 with the Helmholz pair shown in Fig. 5.5 and described in Table 5.3. We also constructed a planar excitation coil to image the large, flat grid phantom described in Sec. 3.2. This coil consists of a 10-turn, 425-mm diameter outer coil and a counter-wound, 4-turn, 340-mm diameter inner coil, and is wound from 0.72-mm diameter wire. I calculate a resistance of 0.8 Ω, an inductance of 0.21 mH, and a field inhomogeneity of 3.5% in a 220-mm diameter circular plane.

5.4.5. Eddy-current cancellation coil

As described in Sec. 5.3.3, we reduced the eddy currents induced in the aluminum shield when the polarizing coil is turned off by simultaneously turning off a counter-field to reduce the net change in magnetic flux threading the walls of the shield. The coil generating the eddy-current cancellation field should be comparable to the size of the aluminum shield to maximize the mutual inductance between the coil and the shield. We therefore wound a 20-turn horizontal coil around the vertical center of the wooden cube. Each coil turn is connected to either side of a 20-pin connector that can be disconnected to allow access to the cryostat and sample. By applying ~1.5 A to this coil while applying the polarizing field, we drastically reduce the amplitude of the eddy-current

relaxation signal produced by the aluminum shield while reducing the amplitude of the polarizing field by less than 20 μT.

5.5. Images taken with the second-generation MRI system

Figure 5.7 shows an image of an array of plastic 8.2-mm diameter columns with 0.85-mm thick walls submerged in 10-mm deep water taken with the second-generation MRI system. We acquired this image with the eight-echo pulse sequence described in Sec. 2.5.1 using 64 T_p = 1.7 s polarizing pulses with an average field of B_p = 85 mT over the sample to obtain N_z = 127 k-space lines with frequency encoding gradient G_y = 150 μT/m and maximum phase encoding gradient $G_{z,max}$ = 140 μT/m. The image has a resolution of 0.8 x 0.8 mm; taking two averages yields an SNR of 6.0 in a total imaging time T_T = 477 s. Although the SNR of this image is a factor of 3.6 lower than the multi-echo water phantom image shown in Fig. 2.14, the voxel volume is a factor of 15 larger in Fig. 2.14 than in Fig. 5.7. In order to compare these images, I define a figure of merit obtained by dividing the SNR efficiency [Eq. (2.42)] by the voxel volume to obtain

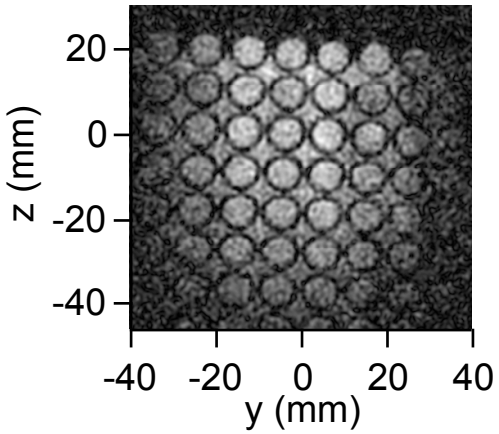

Figure 5.7: Eight-echo image of plastic columns in water with τ = 108 ms and T_{phase} = 106 ms. The image processing uses 4x interpolation and sqrt(cos) smoothing with k_c = 5000 m^{-1}.

$$FOM \equiv \frac{\Upsilon}{V_{voxel}} = \frac{SNR_{voxel}}{V_{voxel}\sqrt{T_T}}. \tag{5.24}$$

This figure of merit is 1.9 times higher for Fig. 5.7 than for Fig. 2.14, indicating that one can obtain higher quality water images for a given imaging time with the second-generation MRI system. However, since these two images have different sample geometries, polarizing fields, and polarizing times, it is difficult to assess how much of the image improvement results from the decreased magnetic field noise in the second-generation MRI system.

Figure 5.8 shows a series of six 14-mm thick cross-sections of a three-dimensional image of a bell pepper taken with B_p = 60 mT, T_p = 600 ms, frequency-encoding gradient G_z = 120 μT/m and maximum phase encoding gradients $G_{y,max}$ = 2.0 μT/m and

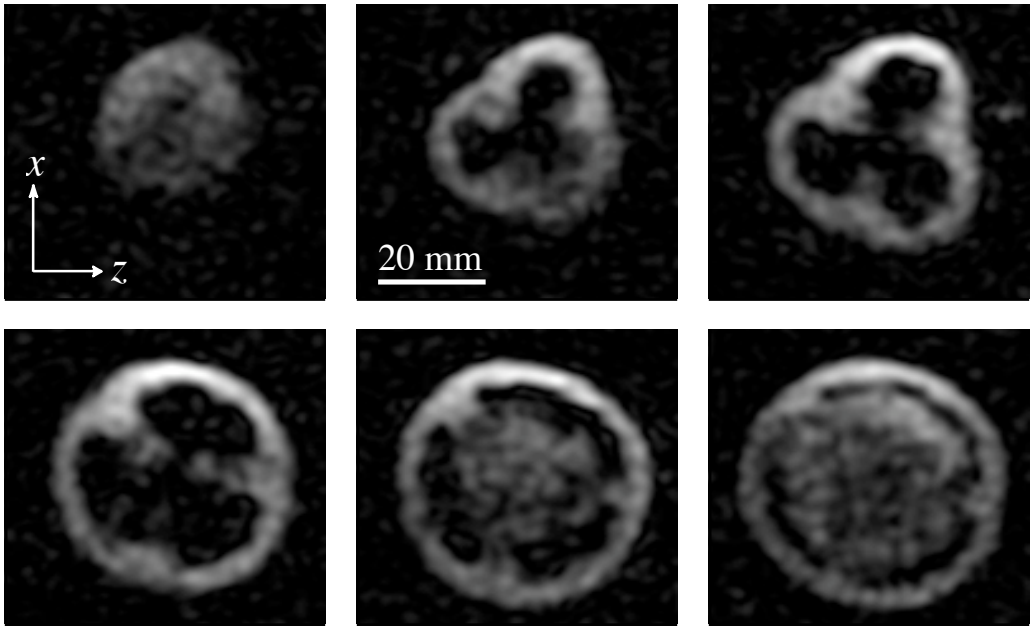

Figure 5.8: Six cross-sections of an image of a green pepper taken with $\tau = 38$ ms and $T_{phase} = 36$ ms. The image processing uses 4x interpolation and sqrt(cos) smoothing with $k_c = 2200$ m^{-1}.

$G_{x,max} = 20$ μT/m. The total imaging time was 341 s. The cross-sections have an in-plane resolution of 1.9 mm x 1.6 mm. Since the polarizing field, polarizing time, voxel volume, and imaging times of Fig. 5.8 and the three-dimensional pepper image presented in Chapter 2 (Fig. 2.18) are all comparable, we can compare the SNR of these images directly. Figure 5.8 has a voxel SNR of 17, while Fig. 2.18 has a voxel SNR of 8.9. The factor of 2 increase in SNR is roughly consistent with the 2.3 times lower magnetic field noise measured in the second-generation MRI system.

Since we have not yet incorporated the changes made in the second-generation aluminum shield into our human subjects protocol, I do not present *in vivo* images taken in the second-generation MRI system.

---

[1] *CRC Handbook of Chemistry and Physics 85th ed.*, (Boca Raton, Florida: CRC Press, 2005).
[2] Film coefficient and pressure drop calculator, Advanced Photon Source, Argonne National Laboratory, www.aps.anl.gov/asd/me/Calculators/film_coeff_dp_nitro.html, accessed April 3, 2006.
[3] R. B. Lauffer, Paramagnetic metal complexes as proton relaxation agents for NMR imaging: theory and design, *Chem. Rev.* **87** (1987) 901.
[4] J. D. Jackson, *Classical Electrodynamics, 3rd ed.* (New York: John Wiley & Sons) p. 234.

[5] P. Morgan, S. Conolly, A. Macovski, Proc. 5th ISMRM, Vancouver (1997) 1477.
[6] L. L. Tsai, M. S. Rosen, R. W. Mair, and R. L. Walsworth, Construction of an optimized open-access human-scale MRI magnet for orientational lung study, Abstract submitted to 46th ENC (2005).
[7] S-K. Lee, M. Mößle, W. Myers, N. Kelso, A. H. Trabesinger, A. Pines, and John Clarke, SQUID-detected MRI at 132 μT with T_1-weighted contrast established at 10 μT-300 μT, *Magn. Reson. Med.* **53** (2005) 9.

6. Potential applications of microtesla SQUID-detected MRI

In the preceding chapters, I have explained the principles that govern the detectors, magnetic field coils, and pulse sequences employed in low-field SQUID-detected MRI and employed these principles to calculate resolution, SNR, and imaging time. I also described the design and construction of a second-generation SQUID-detected untuned MRI system. In this chapter, I apply the principles and practical knowledge of the preceding chapters to discern the most promising applications of this novel imaging technique. Since Faraday-detected (conventional) medical MRI is a mature technology, SQUID-detected MRI will only be adopted in applications where it provides demonstrably higher image quality or dramatically reduced costs compared to conventional MRI or in applications in which conventional MRI cannot be used at all.

In order to narrow the field of potential applications of SQUID-detected untuned MRI, Sec. 6.1 compares this detection modality to both high and low field conventional MRI and eliminates applications for which conventional MRI is clearly superior. One unique property of microtesla SQUID-detected MRI is the ease with which single-sided MRI can be performed by winding the polarizing coil around the bottom of the cryostat, leaving the half-plane below the cryostat open. Section 6.2 describes the design and calculated performance of an optimized single-sided SQUID-detected MRI system. Such a system could potentially be used for low-field T_1-contrast imaging to detect or monitor prostate cancer. Section 6.3 describes preliminary *in vitro* measurements of T_1 of healthy and cancerous prostate tissue and uses the results of these measurements to estimate the *in vivo* contrast-to-noise ratio (CNR) between healthy and cancerous prostate tissue that could be obtained using a single-sided MRI system. Microtesla MRI could also be combined with existing multichannel SQUID arrays used for magnetoencephalography (MEG) to create a combined MEG/MRI brain imaging system. Section 6.4 calculates the resolution, imaging time, SNR, and CNR between gray and white brain tissue of MRI detected using an existing of 275-SQUID MEG system.

6.1. Comparison with conventional MRI

Figure 4.19 shows that prepolarized MRI with B_p = 100 mT detected with an untuned second-order gradiometer connected to a low-noise SQUID (Mück #3) yields a

SNR equivalent to 50 mT conventional non-prepolarized MRI with the same pickup coil geometry. While Fig. 4.19 provides a rough estimate of the relative performance of untuned SQUID and conventional detection, it ignores the details of both detection methodologies. In this section, I consider the detailed advantages and disadvantages of SQUID-detected MRI compared to conventional MRI.

6.1.1. Advantages of conventional MRI

In order to narrow the field of potential applications of SQUID-detected untuned MRI, I begin by considering the advantages of high-field conventional MRI. First, microtesla MRI will never be able to employ effectively contrast mechanisms that scale with the strength of the precession field. These include MRI spectroscopy based on the proton chemical shift and blood-oxygen-level-dependent (BOLD) [1] contrast for functional MRI (fMRI) of the brain. Trabesinger *et al.* [2] demonstrated *J*-coupling spectroscopy in microtesla NMR, but we have yet to find a specific application for *J*-coupling MRI spectroscopy. Since they rely on contrast mechanisms that do not scale with B_0, fMRI based on direct detection of neuronal currents [3] or on vascular space occupancy (VASO) [4] might be possible at microtesla fields provided that one could achieve sufficient SNR.

Another advantage of conventional MRI is that the pickup coil is not constrained within a cryostat, so its geometry can be optimized for maximum sensitivity. For ease of comparison, Fig. 4.19 shows the voxel SNR of conventional and SQUID-detected MRI assuming a $2a = 65$-mm diameter pickup loop $d = 25$ mm above the sample, so it underestimates the SNR achievable from optimized conventional detection. To estimate how much the SNR of conventional detection can be improved by optimizing the coil geometry, I combine Eqs. (4.70), (4.36), and (4.61) to express the SNR of conventional detection from a single acquisition step as

$$SNR_{voxel} = \frac{\mu_0 \beta_\perp}{4\pi} \frac{\omega_0}{\sqrt{4 k_B T R_i}} M V_{voxel} \sqrt{T_s/2}\,, \tag{6.1}$$

where $\mu_0\beta_\perp/4\pi$ is the field perpendicular to B_0 produced per unit current flowing through the pickup coil at the location of the sample, ω_0 is the detection frequency, $T = 298$ K is the coil temperature, R_i is the coil resistance, M is the voxel magnetization, V_{voxel} is the voxel volume, and T_s is the data acquisition time. The only factors that depend on coil

geometry are $\beta_\perp$ and R_i. Since R_i is proportional to the length of the pickup coil l_{coil}, the SNR of conventional detection depends on pickup coil geometry as

$$SNR_{voxel} \propto \beta_\perp \Big/ \sqrt{l_{coil}} \,. \tag{6.2}$$

For definiteness, I consider the case of *in vivo* arm imaging. If B_0 is parallel to the arm, a saddle coil (one-half of the Golay gradient coils shown in Fig. 1.12) enclosing the arm can be used as the pickup coil. A saddle coil with radius r = 60 mm, length l = 120 mm, and angle θ = 120° has an average value of $\beta_\perp$ of 126 m^{-1} over the 60-mm cubic region in the center of the coil and a total length of $4(l + \theta r)$ = 0.98 m. The average value of $\beta_\perp$ in the 60 mm cubic region beginning d = 25 mm below the a = 32.5 mm pickup loop considered in Fig. 4.19 is 27 m^{-1}, and $l_{coil} = 2\pi a$ = 0.20 m. Evaluating Eq. (6.2) for both coils shows that the saddle coil achieves 2.1 times greater average SNR over this region. Furthermore, $\beta_\perp$ of the saddle coil varies between 84% and 128% of its average value over this cubic volume while $\beta_\perp$ of the single pickup loop varies between 22% and 357% of its average value over the same region. The saddle coil will therefore produce a substantially more uniform image than the single pickup loop. While Sec. 6.2.1 shows that increasing the pickup loop radius to a dimension comparable to the coil-sample spacing could increase the average value of $\beta_\perp$ somewhat and make the detector response more homogeneous, the versatility of room-temperature pickup coils remains a substantial advantage.

6.1.2. Competing low-cost MRI technologies

Even without including the effects of pickup coil geometry, Fig. 4.19 shows that 1.5 T conventional MRI achieves approximately two orders of magnitude higher SNR than SQUID-detected untuned MRI. Since a full-body high-field MRI system can image any part of the human body, it is clear that SQUID-detected untuned MRI cannot match the versatility of these systems either. However, because full-body high-field MRI systems cost approximately $1 million per tesla of precession field, there is a market for low-cost specialized MRI systems with lower SNR. While a SQUID-detected untuned MRI system would cost substantially less than a 1.5 T full-body MRI system, SQUID-detected MRI is not the only low-cost MRI technology. In this section, I compare SQUID-detected MRI to two other approaches to low-cost MRI.

6.1.2.1. Permanent magnet MRI systems

One strategy to reduce the cost of an MRI system is to replace the costly 1.5 T superconducting magnet with smaller, lower-field permanent magnets. Although other vendors sell similar devices, I will focus on two products manufactured by Esaote S.p.A (Genoa, Italy), who claim to have sold over 1,000 MRI systems [5].

The Esaote E-Scan XQ is an open-bore 0.2 T MRI system that is designed for musculoskeletal imaging of the peripheral limbs and shoulders. The patient lies within the ~0.3 m gap between two ~1 m diameter cylinders which contain the permanent magnets and magnetic field gradient coils. A different close-fitting transmit/receive* coil is used to image each limb or joint. The E-Scan XQ must be enclosed in an external radiofrequency shield. The smaller Esaote C-Scan can be used to image peripheral limbs and joints within an approximately 0.2 m by 0.4 m rectangular magnet bore and does not require an external radiofrequency shield.

Figure 4.19 shows that 0.2 T conventional MRI achieves 9 times the SNR of SQUID-detected untuned MRI prepolarized at 100 mT for using a circular pickup loop. Since Sec. 6.1.1 shows that replacing the circular pickup loop with a saddle coil increases the SNR by a factor of 2.1, I estimate that the optimized pickup coils used in the Esaote MRI systems yield a SNR ~20 times that of SQUID-detected untuned MRI.

6.1.2.2. Resistive prepolarized MRI systems

However, the large permanent magnets employed in Esaote's MRI systems are still expensive compared to resistive copper electromagnets. In 1993, Macovski and Conolly [6] suggested that low-cost prepolarized MRI systems employing resistive polarizing and readout magnets could be designed to image specific parts of the body. More recently, Matter *et al.* [7] describe the construction and operation of a 16-kW, 0.42-T polarizing coil. The coil has an inner diameter of 127 mm and is designed to polarize a wrist within its bore. To demonstrate this coil, they perform prepolarized Faraday-detected MRI with B_p = 0.4 T and B_0 = 27 mT on a sample of water doped with copper sulfate (T_1 = 323 ms at B_p and T_2 = 170 ms at B_0), achieving a SNR of 8.7 with 0.47 mm x 0.47 mm x 12 mm voxels in a total imaging time of 87 s. This represents a figure of merit [Eq. (5.24)] 8.6

* Conventional MRI systems typically employ a single tuned coil that both produces the excitation field and detects the precessing spins.

times higher than the microtesla MRI water phantom image shown in Fig. 5.7. Since we polarized our water phantom in an average field B_p = 85 mT, most of the increased SNR of the Faraday-detected phantom image can be attributed to its higher polarizing field. Although the polarizing coil used by Matter *et al.* has a volume three times larger than our polarizing coil, the more fundamental issue is that we polarize the sample in the fringing field of our coil; Table 5.2 shows that the nitrogen-cooled flat coil used to polarize our water phantom achieves a field of 240 mT in the center of its bore. Unfortunately, the constraint that the cryogenic pickup loop contained within the helium cryostat must be as close to the sample as possible prevents us from imaging limbs within the bore of the polarizing coil.

Like prepolarized SQUID-detected MRI [8], prepolarized Faraday-detected MRI can be used to make T_1-contrast images in any magnetic field between the polarizing field and the background field of the experiment. For example, Ungersma *et al.* [9] demonstrate that T_1 dispersion contrast between 50 mT and 58 mT can be used to distinguish protein from fat and water. Furthermore, since both techniques require large polarizing coils, but prepolarized Faraday-detected MRI requires no cryogenics, prepolarized Faraday-detected MRI systems will always be less expensive than SQUID-detected MRI systems.

6.1.3. Advantages of SQUID-detected microtesla MRI

After this survey of low-cost conventional MRI systems, it might seem as if there are no applications for which SQUID-detected microtesla MRI is superior to the other available options. However, as described in Sec. 6.2, a SQUID-detected microtesla MRI system can be configured for single sided imaging by winding the polarizing coil around the bottom of the cryostat. There are few constraints on the position of the microtesla magnetic field and gradient coils, so the single sided configuration leaves the lower half-plane available for the subject. Neither permanent magnet MRI nor resistive field-cycling MRI allow for this imaging geometry. Furthermore, while larger permanent magnet MRI machines such as the Esoate E-Scan XQ have a relatively open imaging geometry, permanent magnets are incompatible with low-field or field-cycling measurements. Thus an ideal application of SQUID-detected microtesla MRI would be to image a part of the body accessible only to single-sided imaging using low-field or

field-cycling T_1-contrast. As described in Sec. 6.3, non-invasive detection or monitoring of prostate cancer using low-field T_1-contrast MRI might be one such application.

Another potential application of SQUID-detected microtesla MRI is to add MRI capabilities to existing biomagnetic diagnostic tools. The two primary SQUID-based biomagnetic diagnostic tools are magnetocardiography (MCG), which is used to detect ischemia of the heart [10], and magnetoencephalography (MEG) [11], which is used to localize epileptic foci within the brain and for presurgical mapping of brain function. Since the magnetic fields generated by neuronal currents in the brain are ~100 times weaker than those generated by depolarization currents flowing in the heart, MEG systems must have lower magnetic field noise and higher geometrical coupling factors than MCG systems and are therefore better candidates to combine with SQUID MRI. Furthermore, the interpretation of the magnetic source map obtained from MEG requires that it be superimposed over an MR image of the brain, so performing MRI using the MEG system would eliminate the need for a separate high-field brain MRI. Section 6.4 calculates the MRI performance of a commercial 275-channel MEG system.

6.2. Design of a single-sided imaging system

Figure 6.1 shows a schematic of a single-sided SQUID MRI system with a water cooled polarizing coil. The second-order gradiometer has radius a and baseline b; the sample is positioned a distance d below the bottom loop of the gradiometer. The polarizing coil has inner radius R_1, outer radius R_2 and height H; the sample is a distance h below the lowest turn of the polarizing coil. I assume the precession field is perpendicular to the gradiometer axis. In order to maximize SNR, the bottom loop of the gradiometer and polarizing coil should both be as close to the sample as possible and the radius of the gradiometer and polarizing coil should be optimized based on their distance from the sample. The distance between the bottom of the gradiometer and the bottom of the cryostat (Δd) sets a minimum bound for d. Although our present cryostat has Δd = 25 mm, Seton, Hutchison, and Bussel [12] describe a low-noise cryostat with Δd = 17 mm, so I assume we could achieve Δd = 20 mm. The distance between the lowest turn of the polarizing coil and the bottom of the polarizing coil (Δh) sets the minimum bound on h. Assuming the polarizing coil has a 6-mm thick bottom plate and a

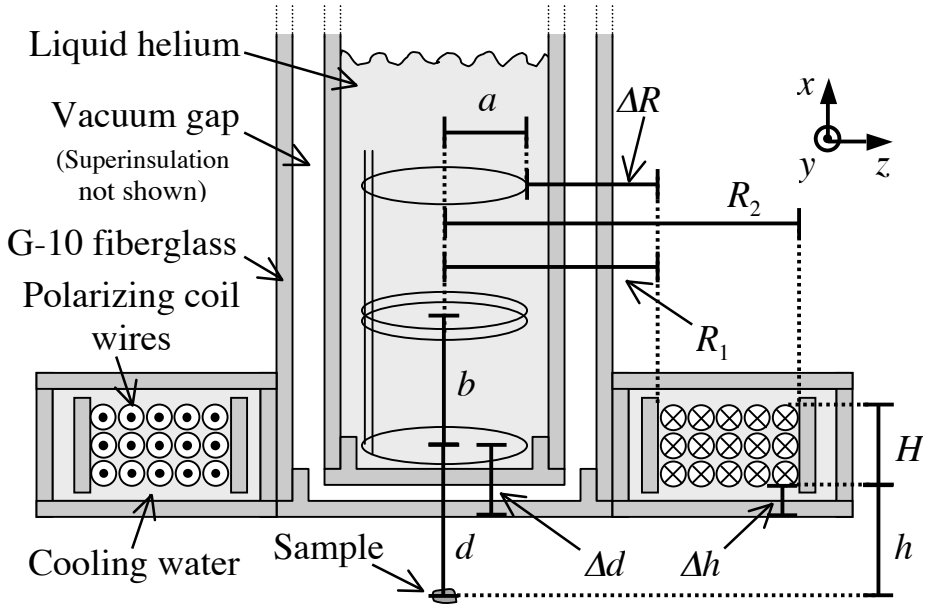

Figure 6.1: Cross-section of a single-sided SQUID MRI system.

3-mm thick channel for cooling water below the bottom turn, Δh = 10 mm. Finally, ΔR is the radial distance between the gradiometer and the innermost turn of the polarizing coil. Our cryostat can accommodate gradiometers with radii up to 41 mm and has an outer radius of 82.5 mm. Assuming a 10 mm radial space between outer wall of the cryostat and the innermost polarizing coil turn, ΔR = 51.5 mm; I use ΔR = 50 mm in the calculation below.

In order to optimize the dimensions of the gradiometer and polarizing coil, one must choose a region over which to optimize the MRI SNR. Since prostate imaging is the most promising application of a single-sided SQUID MRI we have yet identified, and the relatively small prostate gland is located ~50 mm from the surface of the perineum, I optimize the SNR at a point 50 mm below the bottom of the cryostat. Given the constraints described in the previous paragraph, d = 70 mm and h = 60 mm.

6.2.1. Optimal gradiometer baseline and radius

I begin by choosing the gradiometer baseline. In order to maximize the coupling between the sample and gradiometer, the gradiometer baseline should be several times the sample-gradiometer spacing. However, a longer baseline gradiometer discriminates against external noise less effectively than a shorter baseline gradiometer and must be contained within a taller cryostat. Given these constraints, I choose a b = 150 mm baseline gradiometer for the d = 70 mm sample distance.

I next optimize the gradiometer radius, which determines the minimum inner diameter of the cryostat and which in turn determines the inner radius of the polarizing coil. Combining Eqs. (2.37) and (4.4) shows that the voxel SNR of SQUID untuned detection from a single acquisition step is given by

$$SNR_{voxel} = \frac{\mu_0 \beta_\perp}{4\pi} \frac{1}{S_\Phi^{1/2}} \frac{M_i}{L_p + L_i} MV_{voxel} \sqrt{T_s/2}\,, \tag{6.3}$$

where $S_\Phi^{1/2}$ is the flux noise of the SQUID, L_p is the gradiometer inductance, L_i is the input coil inductance, and M_i is the mutual inductance between the SQUID and input coil. Following the derivation in Sec. 4.1.2.1, I choose the optimal input coil inductance $L_i = L_p$ to obtain

$$SNR_{voxel} = \frac{\mu_0 \beta_\perp}{4\pi} \frac{\alpha}{2 S_\Phi^{1/2}} \sqrt{\frac{L}{L_p}} MV_{voxel} \sqrt{T_s/2}\,, \tag{6.4}$$

where L is the SQUID inductance and α is the coupling constant between the SQUID and input coil. Only $\beta_\perp$ and L_p depend on the gradiometer geometry. To obtain a simple expression for the optimal gradiometer radius, I assume that the gradiometer inductance scales linearly with its radius ($L_p = \Lambda a$); this approximation is equally good for magnetometers and gradiometers. Using Eq. (4.37) to express $\beta_\perp$ for a sample a distance d below bottom gradiometer loop, I obtain

$$SNR_{voxel} \propto \frac{\beta_\perp}{\sqrt{L_p}} = \frac{2\pi a^2}{\left(a^2 + d^2\right)^{3/2} \sqrt{\Lambda a}} = \frac{2\pi}{\sqrt{\Lambda}} \left(\frac{a}{a^2 + d^2} \right)^{3/2}; \tag{6.5}$$

this expression considers only the coupling to the bottom gradiometer loop. Maximizing Eq. (6.5) with respect to a yields $a = d$, so in this approximation, the optimal pickup coil radius is equal to its distance from the sample. However, an $a = 70$ mm second-order gradiometer has $L_p \approx 3$ μH, and matching $L_i = L_p$ would require a 96-turn input coil on the SQUID. Figure 6.2 shows the optimal gradiometer radius as a function of sample-gradiometer distance obtained by maximizing Eq. (6.3) assuming an $L = 400$ pH, $\alpha = 0.9$ SQUID and fixing the maximum number of input coil turns at 60. Figure 6.2 shows an optimal gradiometer radius $a = 54$ mm for $d = 70$ mm and $b = 150$ mm. However, since the gradiometer radius determines the inner diameter of the polarizing coil, I consider the optimal polarizing coil geometry before determining the final gradiometer radius.

6.2.2. Optimal polarizing coil geometry

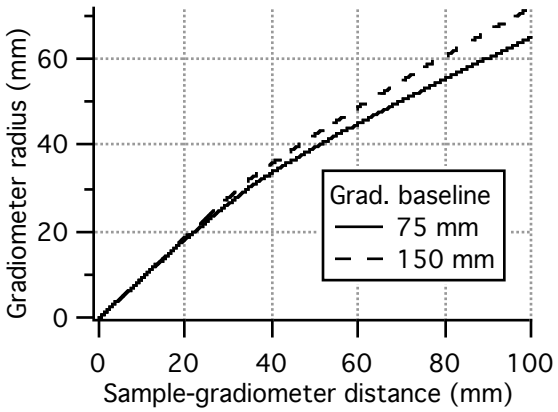

Figure 6.2: Optimal second-order gradiometer radius as a function of sample-gradiometer spacing. The gradiometer inductance is calculated as in Sec. 5.2 with a baseline of either 75 or 150 mm and a 2.5-mm gap between the middle turns. This calculation includes the coupling between the sample and the upper gradiometer loops.

Just as there is an optimal gradiometer radius for a given value of d, there is an optimal radius for a single-turn polarizing coil for a given value of h. This optimal radius provides the highest magnetic field per unit power applied to the coil. Since the power scales as the resistance of the coil, which in turn scales with its length, the optimal radius can be found by maximizing the magnetic field per unit current divided by the coil circumference. The quantity can be calculated for a coil of radius R by substituting $z = h$ into Eq. (5.4) and dividing the result by $2\pi RI$ to obtain

$$\frac{\mu_0 R}{4\pi\left(R^2 + h^2\right)^{3/2}}. \tag{6.6}$$

Minimizing this quantity with respect to R yields an optimal radius $R_{opt} = h/\sqrt{2}$; for $h = 60$ mm, $R_{opt} = 42$ mm. Since the optimal radius of a polarizing coil turn is much smaller than the optimal 54-mm gradiometer radius plus $\Delta R = 50$ mm, maximizing the MRI SNR [Eq. (6.3)] requires balancing the gradiometer sensitivity and polarizing field strength. Furthermore, the polarizing coil occupies a substantial volume, so the field along its axis is described by Eq. (5.5) rather than Eq. (5.4).

In order to optimize gradiometer radius and polarizing coil geometry simultaneously, I begin by fixing the volume of the polarizing coil V at either one, two, three, or four times the volume of the liquid-nitrogen cooled flat coil described in Sec. 5.1.4.3. I assume a water-cooled polarizing coil with $\lambda = 0.23$ capable of dissipating the heat from a continuous current density $J_c = 5.2$ A/mm^2; these are the intrinsic parameters of the water-cooled test coil described in Sec. 5.1.4.4. Since the inductance of the optimal gradiometer is always larger than the $L_i = 1.2$ μH inductance of a 60-turn input

coil and the voxel magnetization M scales linearly with the polarizing field B_p, the voxel SNR scales as the figure of merit

$$FOM = \beta_\perp \frac{M_i}{L_i + L_p} B_p = \frac{2\pi a^2}{\left(a^2 + d^2\right)^{3/2}} \frac{M_i}{L_i + L_p} \frac{\mu_0 J_c}{2} \left[z' \ln\left(\frac{R_2 + \sqrt{R_2^2 + z'^2}}{R_1 + \sqrt{R_1^2 + z'^2}} \right) \right]_{z'=h-H/2}^{z'=h+H/2}, \quad (6.7)$$

where M_i = 19 nH and I have used Eq. (5.5) to evaluate B_p. Maximizing Eq. (6.7) with respect to R_1 and R_2 while maintaining the constraints $H = V/\pi(R_2^2 - R_1^2)$ and $a = R_1 - \Delta R$ yield the optimal gradiometer and polarizing coil geometry. Table 6.1 shows these optimized geometries as a function of polarizing coil volume. In all four cases, taking the polarizing field into account reduces the optimal gradiometer radius below 54 mm. The figure of merit has a broad maximum; fixing a = 54 mm and V = 0.002 m^3 yields an optimal outer radius R_2 = 160 mm and a 4.7 mT m^{-1} figure of merit, only 4% lower than the figure of merit obtained by optimizing the gradiometer and polarizing coil together. Table 6.2 summarizes the electrical and physical properties of the polarizing coils shown in Table 6.1; either increasing the number of Litz wire strands or wiring sections of the coil in parallel would raise the applied current and lower the applied voltage.

Table 6.1: Optimized gradiometer radius and polarizing coil geometry for four different polarizing coil volumes. The gradiometer baseline is 150 mm, and the gradiometer inductance is calculated assuming a 2.5 mm gap between the middle turns.

V (m^3)	Power	a (mm)	R_1 (mm)	R_2 (mm)	H (mm)	B_p (mT)	FOM (mT m^{-1})
0.002	4 kW	46	96	154	44	39	4.9
0.004	8 kW	47	97	179	56	65	8.2
0.006	12 kW	48	98	194	68	86	11.0
0.008	16 kW	48	98	208	76	105	13.4

Table 6.2: Physical and electrical properties of the optimized polarizing coils described in Table 6.1, assuming that the coils are wound from 30-strand, 0.32-mm diameter Litz wire and that the entire coil is wired in series.

V (m^3)	Power	Copper mass	Wire length	Resistance	Current	Voltage
0.002	4 kW	4.1 kg	191 m	1.4 Ω	55 A	73 V
0.004	8 kW	8.2 kg	382 m	2.7 Ω	55 A	145 V
0.006	12 kW	12.3 kg	572 m	4.0 Ω	55 A	218 V
0.008	16 kW	16.4 kg	763 m	5.4 Ω	55 A	291 V

Since the optimal gradiometer radius for this single-sided system is larger than the 32.5 mm radius of our existing gradiometer, its magnetic field noise will be somewhat lower. An a = 47 mm, b = 150 mm gradiometer has L_p = 2.05 μH and

$A_p = 6.94 \times 10^{-3}$ m^2. If connected to this gradiometer, Mück SQUID #3 (Table 4.2) would have an effective area $A_{eff} = 43$ mm^2 and a magnetic field noise of 0.20 fT Hz$^{-1/2}$.

6.2.3. Polarizing coil Nyquist noise

Table 6.3 shows the Nyquist noise generated by the copper windings of the polarizing coils described in Table 6.1 calculated using the methods of Sec. 5.1.3. The Nyquist noise is slightly higher than the calculated SQUID noise using Mück SQUID #3. The higher Nyquist noise of the larger coils somewhat offsets their higher polarizing fields; the largest coil generates a magnetic field 2.7 times the smallest coil, but produces 40% more Nyquist noise.

Table 6.3: Nyquist noise of the optimized polarizing coils assuming that they are wound from 30-strand, 0.32-mm diameter Litz wire at 300 K.

V (m^3)	Power	Nyquist noise
0.002	4 kW	0.20 fT Hz$^{-1/2}$
0.004	8 kW	0.24 fT Hz$^{-1/2}$
0.006	12 kW	0.27 fT Hz$^{-1/2}$
0.008	16 kW	0.28 fT Hz$^{-1/2}$

6.2.4. Cooling water spin precession amplitude

Because of the proximity of the water-cooled polarizing coil to the gradiometer, the protons in the cooling water are better coupled to the detector than the protons in the sample. The cooling water protons will be efficiently polarized by the polarizing field and will align along B_0 as this field is turned off adiabatically. If the excitation field reaches the polarizing coil, the cooling water protons will precess around B_0 and contribute to the detected NMR signal. To estimate the magnitude of the worst-case spin-precession amplitude, I assume that the polarizing coil receives a uniform 90° excitation pulse. The magnetic field within the polarizing coil varies depending on the proximity to the nearest wire; I approximate it as a uniform field B_p^{int} equal in strength to the field at the vertical center of the coil at a radius 5 mm within the inner bore. Since the water-cooling jacket occupies a larger volume than the polarizing coil windings, I model it as an annulus with inner radius R_1 - 7 mm, outer radius R_2 + 7 mm, and height H + 6 mm. I assume a proton density half that of water to accommodate the volume of the coil windings and fiberglass spacers. Table 6.4 shows the precession amplitude of the cooling water assuming that it begins in equilibrium with the estimated average internal polarizing coil field at a temperature of 300 K. For each polarizing coil, the calculated precession amplitude of the cooling water B_{det}^{cw} is ~40,000 times B_{det}^{voxel}, the precession

signal of a (3 mm)^3 voxel of water 70 mm below the gradiometer, although B_{det}^{cw} is not high enough to exceed the dynamic range of the SQUID flux-locking electronics.

Table 6.4: Estimated polarizing coil average internal magnetic field and spin precession amplitude of the cooling water calculated for each of the four polarizing coils. The precession amplitude from a (3 mm)^3 voxel of water polarized in B_p is listed for comparison. The spin precession amplitudes are expressed as a magnetic field referred to the bottom loop of the gradiometer and as a magnetic flux detected by the SQUID.

V (m^3)	Power	Estimated average internal field (B_p^{int})	Precession amplitude of cooling water (B_{det}^{cw})	Precession amplitude of a voxel (B_{det}^{voxel})
0.002	4 kW	120 mT	41 pT / 0.89 Φ_0	1.1 fT / 2.4 μΦ_0
0.004	8 kW	180 mT	75 pT / 1.5 Φ_0	1.8 fT / 3.9 μΦ_0
0.006	12 kW	220 mT	100 pT / 2.1 Φ_0	2.4 fT / 5.2 μΦ_0
0.008	16 kW	260 mT	120 pT / 2.5 Φ_0	2.9 fT / 6.3 μΦ_0

The easiest way to prevent the the precession signal from the cooling water from obscuring the precession signal from the sample is to dope the cooling water with a paramagnetic ion to reduce its T_1 relaxation time and wait a time

$$T_d + \tau > T_1 \ln\left(B_{det}^{cw} / B_{det}^{voxel}\right) \approx 11 T_1 \tag{6.8}$$

before beginning data acquisition. The T_1 relaxation data compiled by Lauffer [13] indicate that Mn^{2+} is the most effective paramagnetic relaxation agent in aqueous solutions at NMR frequencies of 20 kHz. The longitudinal relaxivity of Mn^{2+} is $R_1 = 44$ mM^{-1} s^{-1}, so cooling water doped with 50 mM $MnCl_2$ has $T_1 = 1/([Mn^{2+}]R_1) =$ 0.45 ms, and could be used in MRI pulse sequences with $T_d + \tau \geq 5$ ms. Doping the cooling water with 50 mM $MnCl_2$ increases its conductivity to 0.66 (Ω m)$^{-1}$ [14]; Nyquist currents in the conducting cooling water contribute less than 0.03 fT Hz$^{-1/2}$ additional noise in all four coil geometries (I assume that the cooling water occupies half the volume of the water-cooling jacket described above). Other strategies to reduce the contribution of the cooling water to the NMR signal include applying slice-selective excitation pulses to prevent excitation of the cooling water spins and choosing the frequency-encoding direction along the axis of the polarizing coil to discriminate between cooling water and sample protons based on their precession frequency.

6.2.5. Calculated SNR

Combining Eqs. (4.70) and (4.38) yields the SNR of a single acquisition step,

$$SNR_{voxel} = \frac{\mu_0}{4\pi} \frac{2V_{voxel}}{\left(a^2 + d^2\right)^{3/2}} \rho \frac{\gamma^2 \hbar^2}{4 k_B T_S} \frac{B_p}{S_B^{1/2}} \sqrt{T_s/2}\,, \tag{6.9}$$

where $S_B^{1/2}$ is the SQUID magnetic field noise, ρ is the spin density, and $T_S = 310$ K is the sample temperature. Table 6.5 shows Eq. (6.9) evaluated using B_p given in Table 6.1, $S_B^{1/2}$ given by the quadrature sum of the SQUID noise and the polarizing coil Nyquist noise, $\rho = 6.7 \times 10^{28}$ m^{-3} (the spin density of water), $T_s = 60$ ms, and a voxel volume $V_{voxel} = (1\text{ mm})^3$; these parameters are chosen to match the SNR calculations in Sec. 4.3.5.

Table 6.5: Polarizing field, total noise, and voxel SNR of a single acquisition step of the optimized single-sided MRI system as a function of polarizing coil volume.

V (m^3)	Power	B_p (mT)	$S_B^{1/2}$ (total)	(1 mm)^3 voxel SNR	(3 mm)^3 voxel SNR
0.002	4 kW	39	0.28 fT Hz$^{-1/2}$	0.023	0.61
0.004	8 kW	65	0.31 fT Hz$^{-1/2}$	0.034	0.92
0.006	12 kW	86	0.33 fT Hz$^{-1/2}$	0.042	1.12
0.008	16 kW	105	0.35 fT Hz$^{-1/2}$	0.048	1.31

In Sec. 4.3.5, I calculate a SNR of 0.51 for a (1 mm)^3 voxel polarized in a 100 mT field detected with a 0.31 fT Hz$^{-1/2}$ SQUID untuned gradiometer. Although the magnetic field noise is nearly identical in both cases and the 0.008 m^3 polarizing coil produces the 100 mT polarizing field assumed in Sec. 4.3.5, the geometric factor $(a^2 + d^2)^{-3/2}$ in Eq. (6.9) leads to a factor of 10 lower SNR for the single-sided MRI system. If I decrease the sample-gradiometer spacing from $d = 70$ mm to $d = 25$ mm as in Sec. 4.3.5, the 0.008 m^3 polarizing coil produces $B_p = 150$ mT and SNR_{voxel} increases to 0.28; the remaining difference in SNR can be attributed to polarizing coil Nyquist noise and the larger gradiometer radius of the single-sided system, which is not optimized for the smaller 25–mm sample-gradiometer spacing. Table 6.5 also shows the SNR of the single-sided MRI system for the more realistic $V_{voxel} = (3\text{ mm})^3$, which yields SNR values of order unity.

6.3. Detection or monitoring of prostate cancer

As discussed in Sec. 6.1.3, one potential application of single-sided SQUID-detected MRI is to detect or monitor prostate cancer using low-field T_1-contrast imaging. MRI detection of prostate cancer has been studied for more than twenty years. Early studies at 0.15 T [15], 0.26 T [16], and 1.5 T [17] could not distinguish between normal prostate tissue and prostate tumors based using T_1-contrast; the T_2-contrast results were

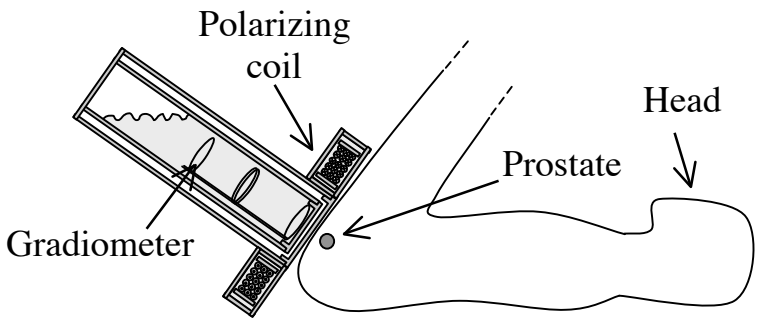

Figure 6.3: Potential geometry of a single-sided prostate MRI system.

ambiguous. More recently, Liney *et al*. [18] measured $T_2 = 96 \pm 15$ ms in normal prostate tissue and $T_2 = 65 \pm 6$ ms in prostate tumors at 1.5 T; the uncertainties represent the standard deviations over the 16 patients studied. Although benign prostate hyperplasia (BPH) can sometimes be mistaken for prostate cancer, this study measured T_2 of BPH to be 128 ± 39 ms. The ratio of choline to citrate concentration measured using magnetic resonance spectroscopic imaging (MRSI) [19] can be used to supplement T_2-contrast MRI. The use of endorectal MRI receive coils instead of body coils has been shown to improve image quality and diagnostic confidence in prostate imaging [20]. In part because of its high cost, MRI is only employed to diagnose prostate cancer after negative biopsy results following a blood test showing a high level of prostate specific antigen (PSA) [21].

The primary advantages of low-field MRI of the prostate are that it costs less than high-field MRI and is entirely non-invasive; in contrast prostate biopsy is extremely invasive. As discussed in Sec. 6.1.3, other low-cost MRI technologies cannot be used in the single-sided imaging geometry required for prostate MRI. To our knowledge, the low-field relaxation properties of human prostate tissue have not been previously investigated. However, because T_1 converges to T_2 in the low-field limit, there is reason to believe that a combination of T_1 and T_2 contrast imaging might be able to distinguish between normal prostate tissue and tumors in low magnetic fields.

6.3.1. Possible designs for a microtesla prostate MRI system

Figure 6.3 shows one possible geometry for prostate imaging with the single-sided MRI system. In this configuration, the patient lies on his back with his legs supported in stirrups and the bottom of the cryostat is placed flush against the perineum. The patient could be made more comfortable by completely inverting the gradiometer so that he

could sit on top of it. While sitting atop this "MRI chair" is one of the least invasive prostate examinations imaginable, an inverted cryostat would not hold liquid helium, so recirculating helium gas from an external cryocooler would be required to cool the gradiometer and SQUID. Although a cryocooler would almost certainly be desirable for any commercial application of low-field MRI, a prototype *in vivo* prostate imaging system would probably employ the geometry of Fig. 6.3.

6.3.2. Low-field *in vitro* measurements of prostate tissue T_1

In order to measure the low-field T_1 relaxation time of normal and cancerous prostate tissue, we collaborated with Jeffry Simko, Lars Schmidt, and Kevin Chew to obtain specimens of fresh prostate tissue from prostatectomy patients through the University of California, San Francisco (UCSF) Prostate SPORE Tissue Core. Less than one hour after the prostate blood supply had been cut off, Lars Schmidt or Kevin Chew divided the prostate tissue into regions of normal tissue and tumor based on a preliminary visual inspection and provided us with ~8-mm diameter, ~2-mm thick sections of each region. They placed the tissue in plastic centrifuge tubes within closed biohazard bags. We transported the tissue on ice to our low-field MRI system in Birge Hall and measured its spin relaxation properties; the elapsed time between receiving the tissue at UCSF and measuring it in Berkeley ranged from 2 to 4 hours. When we finished the measurements, we froze the tissue in dry ice and returned it to UCSF the next day, where Jeffry Simko subsequently classified the fraction of tumor in each sample and its Gleason grade.

We measured T_1 of the prostate tissue using spin-echo NMR with a variable delay time T_d between turning off the polarizing field and applying the 90° excitation pulse. We have optimized the measurement procedure over the course of measuring nine samples of prostate tissue; here I describe the most recent procedure. We begin by placing both samples of prostate tissue ~35 mm apart within their biohazard bags under the cryostat inside a Styrofoam® sample chamber. The sample is cooled by heat conduction to the liquid-nitrogen cooled polarizing coil and warmed by room-temperature nitrogen gas flowing through the sample chamber. We monitor the sample temperature by measuring the resistance of a long, thin copper wire in the sample chamber and adjust the gas flow to maintain a constant temperature of 4 °C. We apply a 25 μT/m gradient to separate the NMR peaks of the samples by 40 Hz. The pulse

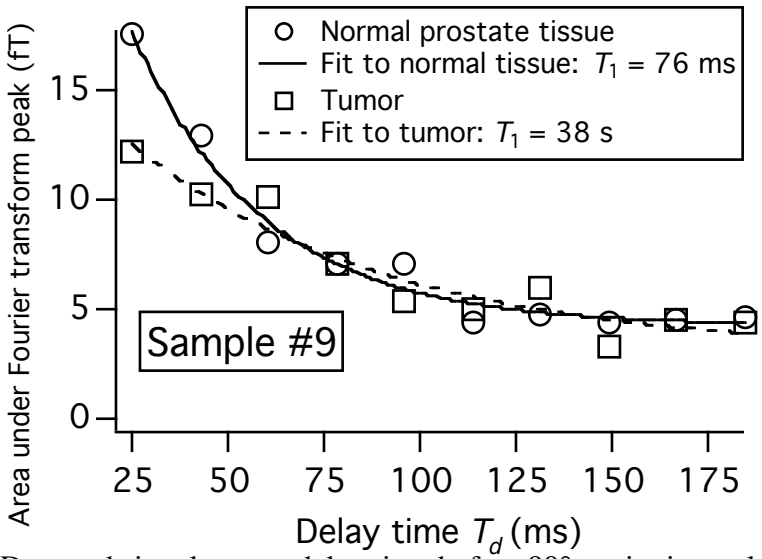

Figure 6.4: Detected signal versus delay time before 90° excitation pulse for simultaneously measured samples of normal prostate tissue and prostate tumor. Each data point represents the sum of 60 acquisition steps.

sequence polarizes the samples in a B_p = 90 mT[†] field for a time T_p = 500 ms. After a variable delay time T_d ranging from 25 ms to 184 ms (T_d includes the T_{off} = 22 ms time to turn off the polarizing coil), we apply a 90° excitation pulse, causing the spins to precess in B_0 = 132 μT. The 180° pulse follows a time τ = 8 ms later, and we begin data acquisition 5 ms after the 180° pulse. We sum together 60 data acquisition steps for each value of T_d. We quantify the signal from each sample by taking the area under the magnitude of the Fourier transform of the acquired data within ±20 Hz of the peak corresponding to each sample. Figure 6.4 shows the signal amplitude plotted versus T_d for one pair of samples. We fit the data to the exponential relaxation function

$$B_{det}(T_d) = B_{noise} + B_{sig}\exp(-T_d/T_1), \tag{6.10}$$

where B_{noise} represents the area under the magnitude of the Fourier transform in the absence of any signal, B_{sig} is the signal extrapolated to $T_d = 0$, and T_1 is the longitudinal relaxation time of the sample. The best fits to the data in Fig. 6.4 yield T_1^{normal} = 76 ms and T_1^{tumor} = 38 ms.

During the course of our measurements, we discovered that the prostate samples degrade over time, causing the T_1 values of normal tissue and tumors to converge. Figure 6.5 shows the longitudinal relaxation rates ($1/T_1$) of the prostate tissue samples that we

[†] This is the polarizing field at the average current of 30 A. See Sec. 5.1.4.3 for more details.

measured less than four hours after receiving them from UCSF. The uncertainty in $1/T_1$ is calculated by estimating the error in the data by the deviation of the data from the exponential fit. Taking the mean and standard deviation of the $1/T_1$ values shown in Fig. 6.5 yields 13 ± 3 s^{-1} ($T_1 = 77 \pm 18$ ms) for the normal tissue and 22 ± 3 s^{-1} ($T_1 = 46 \pm 6$ ms) for the tumors. Although these are preliminary measurements and require *in vivo* confirmation, they are sufficient to estimate the T_1 contrast that could be achieved in microtesla fields.

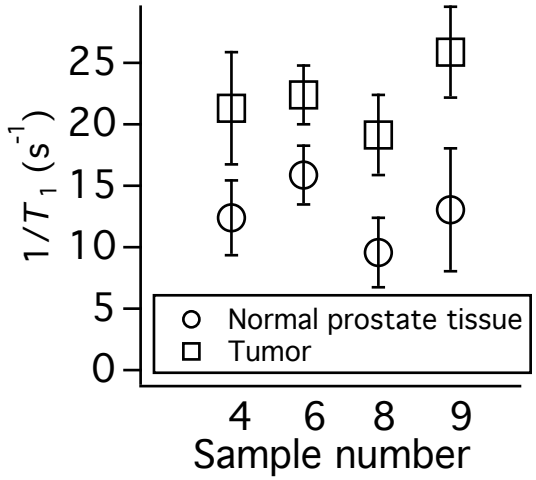

Figure 6.5: Measured $1/T_1$ values of normal prostate tissue and prostate tumors at 132 μT.

In order to estimate the SNR and contrast that could be obtained from microtesla prostate MRI, one also needs to know T_1 in the polarizing field B_p and T_2 at B_0. Poon *et al.* [15] measured $T_1 \approx 500$ ms *in vivo* for both normal prostate tissue and prostate tumors at 0.15 T, so I use this value for T_1 in the polarizing field. We measured a single pair of prostate tissue samples and obtained $T_2 = 48 \pm 9$ ms for normal tissue and $T_2 = 40 \pm 8$ ms for tumors. Because the samples may have degraded somewhat prior to making these measurements, we suspect the true value of T_2 of normal tissue may be closer to T_1 (higher) than indicated by this measurement.

6.3.3. Prostate imaging pulse sequence

In this section, I assume that B_0 points along the z-axis, the gradiometer loops and prostate form a line along the x-axis, and the prostate is located $d = 70$ mm below the bottom loop of the gradiometer. For definiteness and symmetry, I choose the frequency-encoding gradient along the x-direction and employ phase encoding in the y- and z-directions. Maximizing the voxel SNR requires minimizing the time between turning off the polarizing pulse and the echo top. In this section, I estimate the minimum encoding time that yields 5 x 3 x 3 mm resolution with a 70 mm x 70 mm phase-encoding field of view (FOV); Sec. 6.3.4 shows that these parameters yield reasonable image SNR and contrast. Figure 2.12 shows the pulse sequence timing definitions used in this section.

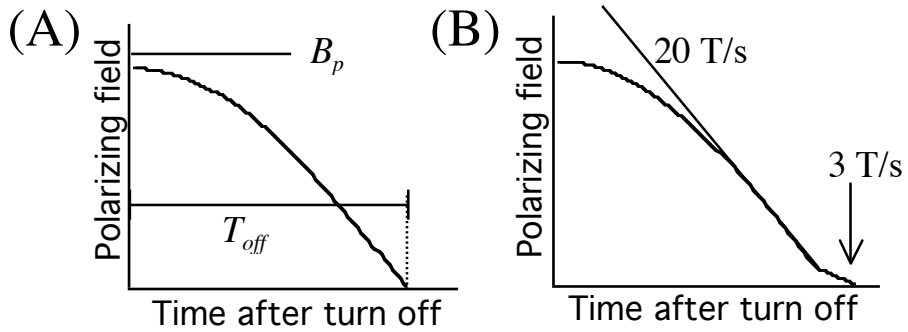

Figure 6.6: Polarizing coil current versus time after turning off the polarizing coil. (A) Quarter-sine waveform. (B) Quarter-sine waveform modified to satisfy dB/dt < 20 T/s and the adiabatic turn-off criterion.

6.3.3.1. Precession field strength

Maximizing the signal at the echo top requires a phase encoding time $T_{phase} < \tau << T_2$. Equation (2.20) indicates that the phase encoding resolution in the z-direction is $\Delta l_z = \pi/(\gamma T_{phase} G_{z,max})$, where $G_{z,max}$ is the maximum phase encoding gradient in the z-direction (the same is true in the y-direction). To maintain $\varepsilon = L_z G_{z,max}/B_0 \leq 0.2$ to prevent significant concomitant gradient blurring in the phase encoding direction, I require

$$B_0 \geq 5\pi L_z/(\gamma T_{phase} \Delta l_z), \tag{6.11}$$

where L_z is the image FOV. Assuming $T_{phase} = 4$ ms, $L_z = 70$ mm, and $\Delta l_z = 3$ mm requires $G_z = 980$ μT/m and $B_0 \geq 340$ μT. I therefore assume $B_0 = 350$ μT for the prostate imaging sequence, corresponding to a precession frequency $\omega_0/2\pi \geq 14.9$ kHz.

6.3.3.2. Polarizing pulse shape and ramp time

In order to minimize the total sequence time and to maximize the signal remaining at the echo top, one should turn the polarizing field on and off as fast as possible. Matter *et al*. [7] have constructed custom switching circuitry that allows them to switch a 16-kW, 0.006-m^3 polarizing coil with comparable current density on or off in 6.5 ms; the coil current follows the quarter-sine waveform show in Fig. 6.6(A). However, two additional constraints limit dB_p/dt. First, exposing human subjects to rapidly changing magnetic fields can cause peripheral nerve stimulation; for the purposes of this calculation, I restrict the change in the maximum exposed polarizing field to the old FDA

limit of 20 T/s[‡]. Second, since B_p is perpendicular to B_0, it must be turned off slowly so that the spin magnetization adiabatically follows the direction of the total applied field and the spins end up aligned with B_0. The spins will follow the direction of the applied field when angle of the applied field changes much more slowly than the spin precession angular velocity. This criterion can be expressed as

$$\frac{d\theta_B}{dt} = \frac{d}{dt}\left\{\tan^{-1}\left[\frac{B_p(t)}{B_0}\right]\right\} = \frac{dB_p/dt}{\left[B_0 + B_p^2(t)/B_0\right]} << \omega = \gamma\sqrt{B_0^2 + B_p^2(t)}, \qquad (6.12)$$

where θ_B is the angle between the total applied field and the z axis, and ω is spin angular precession frequency. This angle θ_B only changes significantly when B_p becomes comparable to B_0; assuming dB_p/dt is constant, $d\theta_B/dt$ has a maximum at $B_p = 0$ and Eq. (6.12) becomes $dB_p/dt << \gamma B_0^2 = 33$ T/s for $B_0 = 350$ μT. Therefore the quarter-sine waveform would need to be modified as shown in Fig. 6.6(B) to be compatible with microtesla imaging fields. Alternatively, one could raise B_0 to ~900 μT while turning off the polarizing coil. Table 6.6 shows the maximum exposed field and the polarizing coil turn-off time for each of the four polarizing coils. I assume that the field profile follows the 20 T/s quarter-sine waveform until it drops to a field $B_p = 1$ mT at the prostate, after which the field decreases linearly at 3 T/s.

Table 6.6: Maximum exposed field and minimum turn-off time for each of the four polarizing coils.

V (m^3)	Power	Maximum exposed field	Polarizing coil turn-off time (T_{off})
0.002	4 kW	84 mT	7 ms
0.004	8 kW	125 mT	10 ms
0.006	12 kW	157 mT	13 ms
0.008	16 kW	184 mT	15 ms

6.3.3.3. Slab-selective excitation pulses

Since the gradiometers described in Table 6.1 are sensitive to spins precessing within a yz region somewhat larger than their $2a \approx 95$ mm diameters, the phase encoding FOV must be at least this large to avoid image aliasing. Since the prostate gland is only ~30 mm in size, many more phase encoding steps must be spent to prevent aliasing than are required to image the prostate. While the additional acquisition steps required to prevent aliasing increase the image SNR, eliminating them reduces the total imaging

[‡] The current FDA standard specifies no numerical limit to dB/dt but requires that the changing magnetic field must not cause peripheral nerve stimulation.

time. One method to select an L_y x L_z FOV is to apply a combination of frequency-selective excitation pulses and gradients as described in Sec. 2.2. Because phase encoding is used to further divide the selected region into voxels, this procedure is called slab selection rather than slice selection.

In order to select a rectangular column of spins with coordinates $-L_y/2 \le y \le L_y/2$ and $-L_z/2 \le z \le L_z/2$, one can apply slab-selection in the y-direction with the 90° excitation pulse and slab-selection in the z-direction with the 180° pulse used to generate the spin echo. In order to minimize the encoding time, the refocusing gradients required for these pulses can be applied simultaneously with the phase encoding gradients. A 5-lobe sinc function excitation pulse (shown in Fig. 2.4) employed to select a slab of width L_z has a duration

$$T_{ss} = 3/\Delta f = 6\pi/(\gamma G_{ss} L_z) \tag{6.13}$$

where Δf is the bandwidth of the pulse and G_{ss} is the amplitude of the slice-selection gradient. In order to minimize T_{ss}, G_{ss} should be chosen as large as possible given the constraints of concomitant gradients. However, because the refocusing pulses are applied during the phase encoding step, the relevant gradient strength is $G_{z,max} + G_{ss}$. Since $G_{z,max}$ = 980 μT/m is already close to the concomitant gradient limit, I choose the relatively weak G_{ss} = 340 μT/m, which yields Δf = 1 kHz and T_{ss} = 3 ms. In sequence timing calculations, I assume that the spins rotate instantaneously a time $T_{ss}/2$ after the beginning of the pulse.

6.3.3.4. Pulse sequence timing

The minimum delay time between beginning to turn off the polarizing pulse and the center of the 90° pulse is given by $T_d = T_{off} + T_{ss}/2$. For the slice-selection and phase-encoding times described above, the minimum echo time is $\tau = T_{ss}/2 + T_{phase} + T_{ss}/2$ = 7 ms. Adding an additional 2 ms to allow for gradient ramping times yields τ = 9 ms. These minimum times produce the highest voxel SNR, but one can increase T_d to enhance T_1 contrast or increase τ to enhance T_2 contrast.

Equation (2.19) shows that the resolution in the frequency-encoding direction in the absence of T_2^* decay is given by $\Delta l_x = \pi/[\gamma(T_s - t_{echo})G_x])$, where T_s is the data acquisition time, t_{echo} is the time between the beginning of data acquisition and the echo top, and G_x is the frequency-encoding gradient. One must choose $T_s - t_{echo} < T_2^*$ to prevent T_2^* decay

from significantly degrading the resolution. I assume sufficient field homogeneity such that $T_2^* = T_2$ and choose $T_s - t_{echo} = 45$ ms based on the estimates of low-field prostate T_2 given in Sec. 6.3.2. Assuming a 1 ms delay after the end of the slab-selective 180° pulse and the beginning of data acquisition yields $t_{echo} = \tau - T_{ss}/2 - 1$ ms = 6.5 ms and $T_s = 51.5$ ms. Choosing $G_x = 52.5$ μT/m yields the desired $\Delta l_x = 5$ mm resolution.

Assuming that ramping up the polarizing coil field takes the same time as turning it off, the total sequence time that not spent polarizing is given by

$$T_{other} = T_{off} + T_d + 2\tau + T_s - t_{echo} = 7 \text{ ms} + 8.5 \text{ ms} + 18 \text{ ms} + 45 \text{ ms} = 78.5 \text{ ms}, \quad (6.14)$$

where I substituted $T_{off} = 7$ ms for the smallest coil. Dividing T_{other} by T_1 of the prostate in the polarizing field yields 0.16. Figure 2.20 indicates that the optimal polarizing time is $T_p = 1.4T_1 = 700$ ms. The polarizing coil has a duty factor $T_p/(T_p + T_{other}) = 90\%$, so one cannot raise its pulsed operating power much above the limit set by continuous water cooling.

6.3.4. Calculated SNR and CNR of prostate images

The voxel SNR is given by Eq. (2.40):

$$SNR_{voxel} = \frac{\mu_0 \beta_\perp}{4\pi A_p S_B^{1/2}} M_{echo} V_{voxel} \sqrt{N_{av} N_y N_z T_s/2}\,, \quad (6.15)$$

where M_{echo} is the spin magnetization at the echo top, N_y and N_z are the number of phase encoding steps in the y and z directions, respectively, and N_{av} averages are taken of each phase encoding step. To obtain a 3 mm x 3 mm phase-encoding resolution in a 70 mm x 70 mm FOV, I require $N_y = N_z = 24$. Since the sequence yields a frequency-encoding resolution of 5 mm, $V_{voxel} = 4.5 \times 10^{-8}$ m^3. For an $a = 46$ mm pickup loop a distance $d = 70$ mm above the prostate, $A_p = \pi a^2 = 6.6 \times 10^{-3}$ m^2 and $\beta_\perp = 22.6$ m^{-1}; these values differ slightly for each polarizing coil described in Table 6.1. I set $S_B^{1/2}$ equal to the combination of SQUID noise and polarizing coil Nyquist noise shown in Table 6.5. The magnetization at the echo top can be expressed in terms of the pulse sequence timing and relaxation times summarized in Table 6.7 as

$$M_{echo} = M_0[1 - \exp(-T_p/T_{1,high})]\exp(-T_{off}/T_{1,int})\exp[-(T_d - T_{off})/T_{1,low}]\exp(-2\tau/T_2), \quad (6.16)$$

where M_0 is the equilibrium magnetization in the polarizing field B_p. I assume that prostate tissue has 75% of the proton density of water. Rather than model the dynamic

spin relaxation as the polarizing field ramps down, I simply assume that the spins relax towards zero magnetization with an average time constant of $T_{1,int}$ = 200 ms.

Table 6.7: Summary of the prostate MRI pulse sequence timing described in Sec. 6.3.3 and the modeled spin relaxation times during each step.

Sequence step	Duration	Spin relaxation time
Polarizing field ramp up	$T_{on} = T_{off}$	Not modeled
Polarization	T_p = 700 ms	$T_{1,high}$ = 500 ms
Polarizing field ramp down	T_{off} (Table 6.6)	$T_{1,int}$ = 200 ms
Delay	$T_d - T_{off}$ (minimum 1.5 ms)	$T_{1,low}$ = 77 ms (normal), 46 ms (tumor)
Before echo top	2τ (minimum 18 ms)	T_2 = 48 ms (normal), 40 ms (tumor)
After echo top	$T_s - t_{echo}$ = 35 ms	T_2 as above

6.3.4.1. Sequence optimized for maximum signal-to-noise ratio

To optimize the pulse sequence for maximum SNR, I choose the minimum values for $T_d - T_{off}$ and τ shown in Table 6.7. Table 6.8 shows the calculated SNR of normal prostate tissue and tumors for each system geometry using this pulse sequence with N_{av} = 1; the total sequence time is ~7.5 minutes in each case. The contrast-to-noise ratio (CNR) is calculated as the difference between the SNR of normal tissue and the SNR of tumors. Both SNR and CNR scale roughly as the square root of the polarizing coil volume and power. Although the SNR with the three largest polarizing coils would yield adequate image quality, the CNR is low enough so that normal tissue could be mistaken for a tumor or vice-versa.

Table 6.8: Calculated SNR and CNR of a 5 mm x 3 mm x 3 mm voxel using the minimal-delay prostate imaging sequence and each of the four single-sided system geometries shown in Table 6.1.

V (m^3)	Power	SNR (normal)	SNR (tumor)	CNR
0.002	4 kW	8.0	7.3	0.7
0.004	8 kW	11.3	10.3	1.0
0.006	12 kW	13.9	12.7	1.2
0.008	16 kW	15.9	14.5	1.4

6.3.4.2. Sequence optimized for maximum contrast-to-noise ratio

One can increase the CNR by either increasing T_d to obtain additional T_1 contrast or increasing τ to obtain additional T_2 contrast. Since Table 6.7 shows that $T_{1,low}$ differs by a greater fraction between normal tissue and tumors than does T_2, greater contrast can be

obtained for the same loss of signal by increasing T_d than by increasing τ. Table 6.9 shows the SNR and CNR obtained from the prostate imaging sequence optimized to maximize CNR using a delay time T_d - T_{off} = 50 ms. The CNR has increased by a factor of 2.5 compared to Table 6.8, but the SNR of the normal tissue has decreased by 47% and the SNR of tumor has decreased by 65%. With this T_1-weighted pulse sequence, tumors will be more pronounced, but the overall image quality will be worse; none of the polarizing coils yield a SNR above 10 for normal tissue. The most useful images can probably be obtained using a pulse sequence somewhere between these two extremes.

Table 6.9: Calculated SNR and CNR of a 5 mm x 3 mm x 3 mm voxel using the maximum-contrast prostate imaging sequence and each of the four single-sided system geometries shown in Table 6.1.

V (m^3)	Power	SNR (normal)	SNR (tumor)	CNR
0.002	4 kW	4.3	2.6	1.7
0.004	8 kW	6.0	3.6	2.4
0.006	12 kW	7.4	4.4	3.0
0.008	16 kW	8.4	5.1	3.3

6.3.5. Prospects for microtesla prostate MRI

These calculations indicate that prepolarized SQUID-detected untuned MRI could produce a 5 x 3 x 3 mm image of the prostate in ~7.5 minutes and that a combination of T_1- and T_2-contrast could potentially distinguish voxels filled with prostate cancer from those filled with normal tissue. The fact that 1.5 T MRI can produce 1 x 1 x 5 mm resolution images with a pelvic coil or 0.5 x 0.5 x 3 mm images with an endorectal coil in comparable imaging times [19], yet a recent analysis [22] concludes that MRI and MRSI "…have a limited role in prostate cancer diagnosis but may be helpful for patients with a high index of suspicion and negative initial biopsy" leads me to doubt the diagnostic utility of microtesla prostate MRI. Although one might hope that low-field T_1 contrast might provide a unique contrast mechanism, our measured ratio of 1.7 between T_1 of normal tissue and T_1 of tumors at 132 μT is not much greater than the *in vivo* T_2 ratio of 1.5 measured by Liney *et al.* [18] at 1.5 T.

Given its lower cost compared to high-field MRI, the most likely application of microtesla prostate MRI would be to supplement PSA monitoring in patients with low-grade prostate cancer who have elected "watchful waiting" in place of interventional therapy. Although its efficacy would need to be demonstrated in clinical trials, a periodic

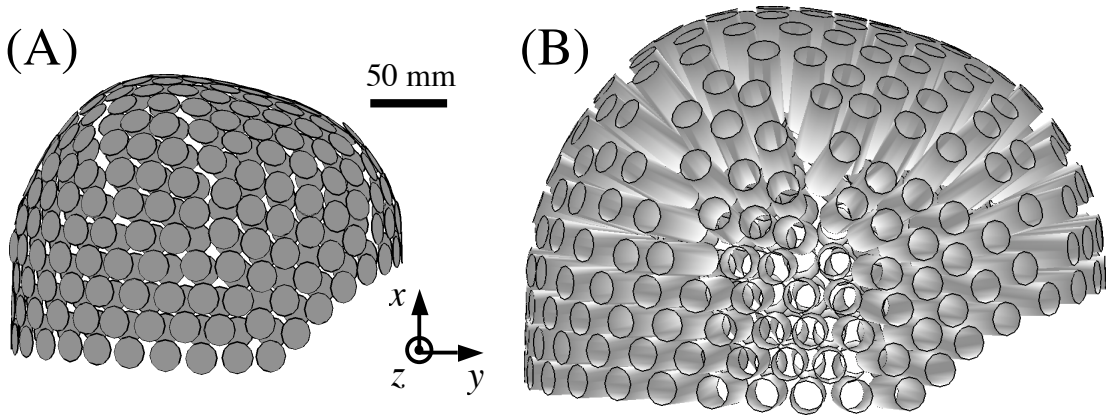

Figure 6.7: Gradiometer locations in the CTF 275-SQUID MEG system. (A) Gradiometer pickup loops drawn as circles. (B) Gradiometers drawn as open-ended tubes. The subject faces towards the positive *y* direction.

microtesla prostate MRI might be able to assess the progression of prostate cancer more accurately than PSA testing alone.

6.4. Combined magnetoencephalography and MRI of the brain

As described in Sec. 6.1.3, another potential application of SQUID-detected microtesla MRI is to combine it with SQUID-based MEG systems. Since an MEG system already contains an array of SQUIDs designed to measure magnetic fields produced in the brain and MEG data must be superimposed on an MR image of the brain for interpretation, performing MEG and SQUID-detected MRI with the same system seems quite appealing. Besides eliminating the need for a high-field MRI exam, combined MEG/MRI could eliminate the problem of matching the magnetic source image obtained from the MEG data, which is usually taken with the subject sitting up, with the high-field MR image of the brain, which is taken with the subject lying within the bore of the magnet. This section estimates the resolution, imaging time, SNR, and CNR between gray and white matter that could be obtained by using the 275-SQUID CTF/VSM Medtech® Ltd. MEG system to perform microtesla MRI of the brain.

6.4.1. MEG gradiometer geometry and sensitivity

The CTF MEG system consists of 275 untuned superconducting first-order gradiometers with diameter 18 mm and baseline 50 mm. The gradiometer pickup coils are located ~20 mm from the concave bottom wall of the cryostat, which is shaped like a helmet to accommodate a human head. Each gradiometer has magnetic field noise of ~4 fT $Hz^{-1/2}$ referred to the pickup coil. Figure 6.7 shows two depictions of this gradiometer

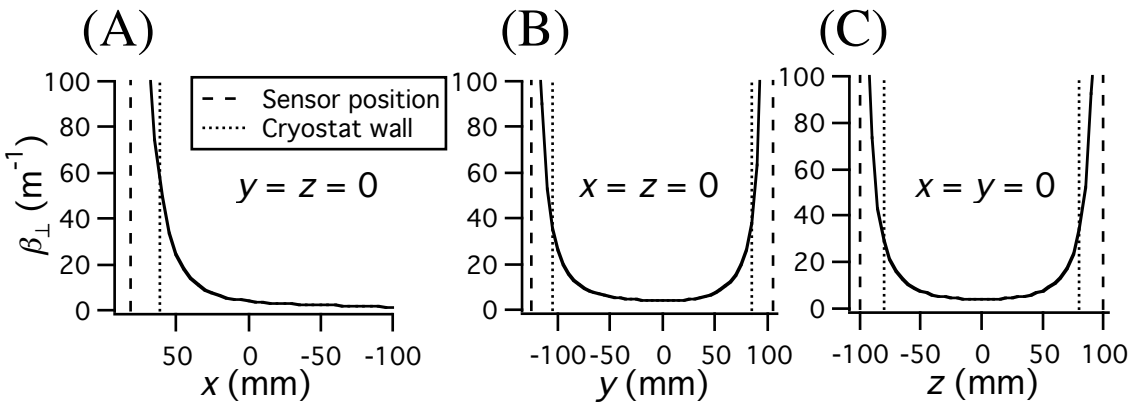

Figure 6.8: Calculated values of $\beta_\perp$ along three lines along the coordinate axes shown in Fig. 6.7. (A) Top to bottom. (B) Back to front. (C) Left to right (subject's perspective). The origin is chosen to be the average position of the pickup loops, ~80 mm below the top center pickup loop. The vertical lines show the approximate location of the pickup loops and cryostat wall.

array; Fig. 6.7(A) renders the pickup coils as filled circles, while Fig. 6.7(B) depicts the gradiometers as open-ended tubes. I have chosen the z-axis in the horizontal direction perpendicular to the subject's line of sight, because this is the most convenient direction to apply the B_0 field.

Since the gradiometers have identical size and magnetic field noise, Eq. (2.53) indicates that the SNR that can be obtained using this gradiometer array as an MRI detector can be evaluated using Eq. (6.15) with the substitution

$$\beta_\perp(\mathbf{r}) = \sqrt{\sum_{n=1}^{N_d} \beta_{\perp,n}^2(\mathbf{r})}, \tag{6.17}$$

where $N_d = 275$ is the number of detectors and $\beta_{\perp,n}(\mathbf{r})$ represents the geometrical response factor of the n^{th} detector evaluated at the point $\mathbf{r}$. Figure 6.8 shows the values of $\beta_\perp$ calculated for the gradiometer geometry shown in Fig. 6.7 using Eq. (6.17). The value of $\beta_\perp$ varies greatly over the inside of the MEG helmet, from ~40 m^{-1} at the surface of the MEG helmet to 4 m^{-1} at the geometric center of the pickup loop, to 2 m^{-1} 50 mm below the geometric center. Rather than computing SNR_{voxel} for all values of $\beta_\perp$, I choose $\beta_\perp = 10$ m^{-1} to represent the geometrical response factor at the periphery of the brain and $\beta_\perp = 3$ m^{-1} to represent the geometrical response factor at the center of the brain.

6.4.2. Polarizing coil geometry

In order to maximize the SNR of the combined MEG/MRI system, the polarizing coil should be placed as close to the brain as possible. However, the gradiometer array and its cryostat already occupy the region closest to the brain. Figure 6.9 shows the MEG gradiometers and polarizing coil in what I believe to be the optimal polarizing coil geometry given these constraints. Although the magnet wires are relatively far from the brain, the brain is located within the center of the coil and the polarizing coil provides a relatively uniform field over the entire brain. I estimate that the CTF MEG system would constrain the inner radius of the polarizing coil to a value between 0.3 and 0.4 m.

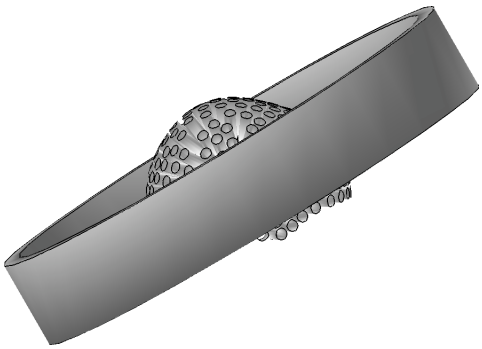

Figure 6.9: Optimized polarizing coil for combined MEG/MRI with inner radius 0.4 m.

Because the wires are far from the gradiometers and Nyquist currents in the cryostat superinsulation limit the magnetic field noise of the CTF system to ~4 fT $Hz^{-1/2}$, the polarizing coil can be wound from solid wire without raising the overall system noise level. Winding the coil from solid wire increases the copper volume fraction λ, which reduces the power dissipation at a given current density J. Since the solid-wire coil in Table 5.2 has $\lambda = 0.71$, the Litz-wire coil has $\lambda = 0.39$, and the water-cooled coil has $\lambda = 0.23$, I estimate that a water-cooled, solid-wire coil would have $\lambda = 0.23(0.71/0.39) = 0.42$. Since Eq. (5.7) indicates that the dissipated power scales as J^2/λ, increasing λ from 0.23 to 0.42 allows the current density to increase by 35% to 7.0 A/mm^2 for the same power dissipated per unit volume as the water-cooled test coil.

Table 6.10 shows the parameters of two polarizing coils designed to provide a 50 mT field at the center of the coil. The first polarizing coil has an inner radius of 0.3 m, while the second must be made 70% larger to produce the same magnetic field with has an inner radius of 0.4 m; the volume scales roughly with the inverse square of the inner radius. Both polarizing coils produce relatively homogenous fields that vary by less than 15% within the 0.1 m sphere centered within the coil.

Table 6.10: Optimal solenoid geometries to obtain a 50 mT polarizing field for combined MEG/MRI assuming two different inner radii.

J (A/mm^2)	λ	V (m^3)	Power	R_1 (m)	R_2 (m)	H (m)	B_p (mT)
7.0	0.42	0.007	13.9 kW	0.3	0.325	0.143	49
7.0	0.42	0.012	23.8 kW	0.4	0.43	0.153	48

6.4.3. NMR properties of brain tissue

Fischer *et al.* [23] found that T_1 of gray and white brain matter at precession frequencies between 10 kHz and 50 MHz could be described by the formula

$$1/T_1 = 1/T_{1,w} + D + A/\left[1 + \left(f/f_c\right)^{\beta'}\right], \tag{6.18}$$

where f is the proton Larmor frequency and $T_{1,w}$, D, A, f_c, and β' are fitting parameters; the best fit values of these parameters are shown in Table 6.11. Table 6.11 also shows their estimates of the spin density and T_2 of gray and white matter, which they found to be independent of precession field, and the calculated values of T_1 at B_p and B_0 in the sequence described in the next section.

Table 6.11: NMR properties of brain matter described by Fischer *et al.* [23] and T_1 calculated using Eq. (6.18) at the polarizing and precession fields chosen for the brain MRI pulse sequence. The spin density is given as a fraction of the spin density of water.

	$T_{1,w}$ (s)	D (s^{-1})	A (s^{-1})	f_c (kHz)	β'	T_2 (ms)	Rel. spin density	T_1 (50 mT)	T_1 (35 μT)
Gray matter	4.348	0.11	11.08	85	0.438	104	0.837	398 ms	104 ms[a]
White matter	4.348	-1.52	19.07	67	0.251	62	0.716	230 ms	80 ms

[a] Extrapolating Eq. (6.18) to f = 1.5 kHz yields T_1 = 102 ms. Since $T_1 \geq T_2$, I use $T_1 = T_2$ = 104 ms.

6.4.4. Brain imaging pulse sequence

In this section, I design a pulse sequence to obtain a (4 mm)^3 resolution image of the brain, which I estimate to have a 0.2 x 0.25 x 0.15 m FOV in the *x*-, *y*-, and *z*-directions, respectively. To minimize the total sequence time, I choose *y* as the frequency encoding direction because it has the largest FOV.

As discussed in Sec. 3.1.3, because neuronal currents in the brain change on a ~1 ms timescale, MEG systems are designed with a bandwidth of 1-2 kHz. To minimize the increase in bandwidth required to accommodate MRI, the precession field should be chosen as low as possible subject to the constraints of concomitant gradients. The

precession frequency must also be high enough so that neuronal currents do not produce a signal in the imaging bandwidth.

The T_2 times shown in Table 6.11 indicate that we can choose $T_s - t_{echo} = 60$ ms without losing frequency-encoding resolution; a $G_y = 49$ μT/m gradient yields the desired 4-mm resolution. Table 3.1 shows that a combination of phase correction and B_0 field cycling can correct concomitant gradient artifacts in two-dimensional images with $\varepsilon = GL/B_0 = 0.49$ in the frequency-encoding direction and $\varepsilon = 1.03$ in the phase encoding direction. I estimate that concomitant gradient artifacts would be a factor of $\sim\sqrt{2}$ worse in three dimensions, so I chose a precession field $B_0 = 35.2$ μT corresponding to $\omega_0/2\pi = 1.5$ kHz and $\varepsilon = 0.35$ in the frequency-encoding direction. A maximum phase-encoding gradient of 120 μT/m yields $\varepsilon = 0.68$ in the x-direction; 4-mm resolution requires $T_{phase} = 24.5$ ms.

Since the subject is exposed to a maximum polarizing field of ~50 mT, the polarizing coil can be ramped more rapidly than shown in Table 6.6 without exceeding 20 T/s. However, since the $R_1 = 0.4$ m coil is substantially larger than the polarizing coil of Matter *et al.* [7], I assume longer ramping times $T_{on} = T_{off} = 15$ ms. Slice-selective pulses are not required for brain imaging, and I reduce the delay times accordingly. The total time not spent polarizing is

$$T_{other} = T_{off} + T_d + 2\tau + T_s - t_{echo} = 15 \text{ ms} + 16 \text{ ms} + 53 \text{ ms} + 60 \text{ ms} = 144 \text{ ms}. \quad (6.19)$$

For gray matter at $B_p = 50$ mT, $T_{other}/T_1 = 0.36$, which yields an optimal polarizing time $T_p = 630$ ms. Table 6.12 summarizes the timing of this pulse sequence.

Table 6.12: Summary of the brain MRI pulse sequence timing described in Sec. 6.4.4 and the modeled spin relaxation times during each step.

Sequence step	Duration	Spin relaxation time
Polarizing field ramp up	$T_{on} = 15$ ms	Not modeled
Polarization	$T_p = 630$ ms	T_1 at 50 mT
Polarizing field ramp down	$T_{off} = 15$ ms	T_1 at 5 mT
Delay	$T_d - T_{off} = 1$ ms	T_1 at 35.2 μT
Before echo top	$2\tau = 53$ ms	T_2
After echo top	$T_s - t_{echo} = 60$ ms	T_2
Sequence step time	$T_R = 774$ ms	

6.4.5. Calculated SNR and CNR of brain images

Table 6.13 shows the SNR and CNR of gray and white brain matter calculated using the pulse sequence of the previous section and the methods developed in Sec. 6.3.4. The SNR and CNR at the periphery of the brain are excellent, and the sequence can still distinguish between gray and white matter at the center of the brain. However, the 25-minute imaging time may be clinically unacceptable. Table 6.14 shows the SNR and CNR that could be achieved using SENSE ([24], Sec. 2.8.3) to reduce the imaging time by a factor of 4 to only 6.1 minutes. This sequence could be used to image the periphery of the brain, but the SNR at the center of the brain is too low to produce acceptable image quality. While the values in Table 6.14 represent the maximum achievable SNR with SENSE, since each detector sees only a small fraction of the total image FOV, the measured SNR will be close to the optimal value as in Fig. 2.24(A).

Table 6.13: Calculated SNR and CNR of a $(4\text{ mm})^3$ voxel containing gray or white matter using the brain imaging sequence at the periphery or center of the brain.

Location	$\beta_\perp$ (m^{-1})	SNR (gray)	SNR (white)	CNR	Total time
Periphery	10	32.2	22.2	10.0	24.5 min
Center	3	9.7	6.7	3.0	24.5 min

Table 6.14: Calculated maximum SNR and CNR of the brain imaging sequence using SENSE to decrease the imaging time by a factor of 4.

Location	$\beta_\perp$ (m^{-1})	SNR (gray)	SNR (white)	CNR	Total time
Periphery	10	16.1	11.1	5.0	6.1 min
Center	3	4.8	3.3	1.5	6.1 min

6.4.6. Prospects for combined MEG/MRI

The calculations of the previous section show that the SQUID sensor array of an MEG system could be used to acquire $(4\text{ mm})^3$ resolution MR images in a polarizing field of 50 mT at a precession frequency of 1.5 kHz. A combination of field-cycling and phase correction could eliminate concomitant gradient artifacts, and SENSE could be used to reduce the imaging time. Although some technical challenges (such as preventing the polarizing coil from magnetizing the μ-metal shield that surrounds an MEG system) remain, combined MEG/MRI is feasible. Two primary questions remain. First, what is the diagnostic utility of MRI images with the resolution and SNR described in Tables 6.13 and 6.14? Would it be enough to eliminate the need for high-field brain MRI in certain circumstances? This question could be answered by generating simulated

microtesla images using high-field MR images of the brain as input data. The second question is economic: would performing combined MEG/MRI eliminate enough high-field MRI exams to repay the cost of adding MRI functionality to the MEG system?

I close by observing that Eq. (4.5) indicates that an 18-mm diameter first-order gradiometer connected to a 20-turn SQUID with the 4.1 $\mu\Phi_0$ Hz$^{-1/2}$ flux noise of Mück SQUID #3 has a magnetic field noise of 1.3 fT Hz$^{-1/2}$, a factor of 3 lower than the 4 fT Hz$^{-1/2}$ achieved in the CTF MEG system, which is limited by cryostat noise. While this additional sensitivity may not be required for MEG, it would substantially improve the MRI performance of the SQUID array. Although it might be economically infeasible, one could imagine designing a low-noise MEG/MRI cryostat based on the principles of Seton *et al*. [25] that would achieve three times the SNR and CNR described in Tables 6.13 and 6.14.

Appendix 6.A. Spin noise of cooling water

The coil noise calculations in Sec. 6.2.3 ignore the contribution of the spin noise of the cooling water to the polarizing coil noise. The equivalent pickup coil resistance of the spin noise at angular frequency ω of a volume of spins V_S with longitudinal magnetization M_L is given by [26]

$$R_{spin} = \gamma\left(\frac{\mu_0\beta_\perp}{4\pi}\right)^2\left(\frac{\omega}{\delta\omega}\right)M_L V_S, \tag{6.20}$$

where $\delta\omega$ is the NMR linewidth including the effects of applied gradients. Using Eq. (4.61) to convert equivalent resistance to field noise and Eq. (1.7) to express M_L as the equilibrium polarization in the internal field of the polarizing coil B_p^{int}, the spin noise is

$$S_B^{1/2} = \frac{\mu_0}{4\pi A_p}\sqrt{\frac{\rho\gamma^3\hbar^2 B_p^{int}}{\omega\ \ \delta\omega}\int_{V_S}\beta_\perp^2 d\mathbf{r}}, \tag{6.21}$$

where ρ is the spin density, and I have integrated $\beta_\perp{}^2$ over the spin volume to allow for non-uniform detector response. Table 6.15 shows the calculated spin noise assuming a $\delta\omega/2\pi = 1$ Hz NMR linewidth and using the values of B_p^{int} given in Table 6.4. Since we measure the intrinsic linewidth of tap water to be $1/\pi T_2 = 0.14$ Hz, spin noise dominates both SQUID noise and polarizing coil Nyquist noise unless we increase $\delta\omega$ by either doping the cooling water or applying magnetic field gradients. Doping the cooling water

with 50 mM $MnCl_2$ to decrease its T_2 to less than 0.45 ms as described in Sec. 6.2.4 yields $\delta\omega/2\pi = 1/\pi T_2 = 700$ Hz. Therefore spin noise contributes a factor of $(700)^{1/2} \approx 26$ less noise than shown in Table 6.15 and can be neglected compared to SQUID noise and polarizing coil Nyquist noise. However, spin noise could easily disrupt an NMR experiment cooled with undoped water and using slab-selective gradients to eliminate the cooling water precession spin signal.

Table 6.15: Spin noise generated at 5.6 kHz by the longitudinally polarized coil cooling water assuming a 1 Hz NMR linewidth.

V (m^3)	Power	Spin noise
0.002	4 kW	0.34 fT $Hz^{-1/2}$
0.004	8 kW	0.46 fT $Hz^{-1/2}$
0.006	12 kW	0.55 fT $Hz^{-1/2}$
0.008	16 kW	0.63 fT $Hz^{-1/2}$

[1] S. Ogawa, T. M. Lee, A. R. Kay, and D. W. Tank, Brain magnetic resonance imaging with contrast dependent on blood oxygenation, *Proc. Natl. Acad. Sci. USA*, **87** (1990) 9868.

[2] A. H. Trabesinger, R. McDermott, S-K. Lee, M. Mück, John Clarke, and A. Pines, SQUID-detected liquid state NMR in microtesla fields, *J. Phys. Chem. A*, **108** (2004) 957.

[3] D. Konn, P. Gowland, R. Bowtell, MRI detection of weak magnetic fields due to an extended current dipole in a conducting sphere: A model for direct detection of neuronal currents in the brain, *Magn. Reson. Med.* **50** (2003) 40.

[4] H. Lu, X. Golay, J. J. Pekar, and P. C. M. van Zijl, Functional magnetic resonance imaging based on changes in vascular space occupancy, *Magn. Reson. Med.* **50** (2003) 263.

[5] Esaote SpA website, www.esaote.com/products/MRI/products1.htm, accessed April 20, 2006.

[6] A. Macovski and S. Conolly, Novel approaches to low-cost MRI, *Magn. Reson. Med.*, **30** (1993) 221.

[7] N. I. Matter, G. C. Scott, T. Grafendorfer, A. Macovski, and S. Conolly, Rapid polarizing field cycling in magnetic resonance imaging, *IEEE Trans. Med. Imaging* **25** (2006) 84.

[8] S-K. Lee, M. Mößle, W. Myers, N. Kelso, A. H. Trabesinger, A. Pines, and John Clarke, SQUID-detected MRI at 132 μT with T_1-weighted contrast established at 10 μT-300 μT, *Magn. Reson. Med.* **53** (2005) 9.

[9] S. E. Ungersma, N. I. Matter, J. W. Hardy, R. D. Venook, A. macovski, S. M. Conolly, and G. C. Scott, Imaging with T_1 dispersion contrast, to be published in *Magn. Reson. Med.*

[10] J. Chen, P. D. Thomson, V. Nolan, and John Clarke, Age and sex dependent variations in the normal magnetocardiogram compared with changes associated with ischemia, *Ann. Biomed. Engin.* **32** (2004) 1088.

[11] Magnetoencephalography (MEG) and magnetic source imaging (MSI), J. W. Wheless, E. Castillo, V. Maggio, H. L. Kim, J. I. Breier, P. G. Simos, A. C. Papanicolaou, *Neurologist*, **10** (2004) 138.

[12] H. C. Seton, J. M. S. Hutchison, and D. M. Bussel, Liquid helium cryostat for SQUID-based MRI receivers, *Cryogenics* **45** (2005) 348.
[13] R. B. Lauffer, Paramagnetic metal complexes as proton relaxation agents for NMR imaging: theory and design, *Chem. Rev.* **87** (1987) 901.
[14] Landolt-Börnstein 6th ed., Vol. II, Pt. 7 (Berlin: Springer-Verlag, 1960) p. 44.
[15] P. Y. Poon, R. W. McCallum, M. M. Henkelman, M. J. Bronskill, S. B. Sutcliffe, M. A. S. Jewett, W. D. Rider, and A. W. Bruce, Magnetic resonance imaging of the prostate, *Radiology*, **154** (1985) 143.
[16] J. P. R. Jenkins, I. Isherwood, D. S. Hickey, M. Machin, J. Grant, and N. J. Blacklock, Quantitative magnetic resonance in prostatic disease, Abstract, 4th Annual Meeting of the Society of Magnetic Resonance in Medicine, London, 1985.
[17] L. Kjaer, C. Thomsen, P. Iversen, and O. Henriksen, *in vivo* estimation of relaxation processes in benign hyperplasia and carcinoma of the prostate gland by magnetic resonance imaging, *Magn. Reson. Imaging*, **5** (1987) 23.
[18] G. P. Liney, L. W. Turnbull, M. Lowry, L. S. Turnbull, A. J. Knowles, and A. Horsman, *in vivo* quantification of citrate concentration and water T_2 relaxation time of the pathologic prostate gland using ^{1}H MRS and MRI, *Magn. Reson. Imaging*, **15** (1997) 1177.
[19] J. Kurhanewicz, D. B. Vigneron, H. Hricak, P. Narayan, P. Caroll, S. J. Nelson, Three-dimesnional H-1 MR spectroscopic imaging of the *in situ* human prostate with high (0.24–0.7-cm^3) spatial resolution, *Radiology*, **198** (1996) 795.
[20] R. A. Huch Boni, C. Meyenberger, J. Pok Lundquist, F. Trinkler, U. Lutolf, and G. P. Krestin, Value of endorectal coil versus body coil MRI for diagnosis of recurrent pelvic malignancies, *Abdom. Imaging*, **21** (1996) 345.
[21] F. G. Claus, H. Hricak, and R. R. Hattery, Pretreatment evaluation of prostate cancer: Role of MR imaging and ^{1}H MR spectroscopy, *RadioGraphics*, **24** (2004) S167.
[22] F. V. Coakley, A. Qayyum, and J. Kurhanewicz, Magnetic resonance imaging and spectroscopic imaging of prostate cancer, *J. Urol.* **170** (2003) S69.
[23] H. W. Fischer, P. A. Rinck, Y. van Haverbeke, and R. N. Muller, Nuclear Relaxation of Human Brain Gray and White Matter: Analysis of Field Dependence and Implications for MRI, *Magn. Reson. Med.* **16** (1990) 317.
[24] K. P. Pruessman, M. Weiger, M. B. Scheidegger, P. Boesiger, SENSE: Sensitivity encoding for fast MRI, *Magn. Reson. Med.* **42** (1999) 952.
[25] H. C. Seton, J. M. S. Hutchison, and D. M. Bussel, Liquid-helium cryostat for SQUID-based MRI receivers, *Cryogenics* **45** (2005) 348.
[26] L. Darrasse, J.-C. Ginefri, Perspectives with cryogenic RF probes in biomedical MRI, *Biochime*, **85** (2003) 915.

7. Future directions

This chapter describes the steps required to move from the second-generation MRI system described in Chapter 5 to the single-sided imaging system described in Sec. 6.2. It also lays out the next steps required to realize the potential applications of SQUID-detected microtesla MRI described in Chapter 6.

7.1. MRI system upgrades

The first step towards building a single-sided SQUID MRI system with the performance shown in Table 6.5 is to lower the magnetic field noise of the existing SQUID gradiometer. The magnetic field noise of Mück SQUID #1 measured in the second-generation aluminum shield is 0.75 fT $Hz^{-1/2}$; as described in Sec. 5.3.2, I estimate the SQUID flux noise to contribute 0.51 fT $Hz^{-1/2}$ towards this total. The remaining noise consists of some combination of external noise and the preamplifier noise of the 2 MHz flux-locking electronics. While replacing Mück #1 with a lower-noise SQUID with higher V_Φ such as Mück #3 (now broken) or Semenov #1 would reduce both the total magnetic field noise and the contribution of preamplifier noise, it makes little sense to attach such excellent SQUIDs to a preamplifier with unknown current noise. Therefore, the first step towards reducing the magnetic field noise is to either measure the noise of the 2 MHz flux-locking electronics or to replace them with a flux-locked loop with known current noise. Since we measure spin precession at 5.6 kHz, we do not require the high bandwidth of the 2 MHz flux-locking electronics. Although reducing the flux modulation frequency to 100 kHz would likely reduce the preamplifier noise, it would also require increasing the impedance of the cold transformer to maintain proper transformer operation as described in Sec. 4.2.1.2.

The second-generation aluminum shield may reduce external noise to the point where a second-derivative gradiometer is no longer required to discriminate against external noise sources. If this is the case, one could increase the effective area and reduce the magnetic field noise by connecting the SQUID to a first-order gradiometer. I calculate the inductance of a 65-mm diameter, two-turn first-order gradiometer with 75 mm baseline and 2.5 mm spacing between two top and two bottom loops the to be 1.59 μH. Connecting this gradiometer to the installed SQUID would raise the effective

area from 27 mm^2 to 48 mm^2, yielding predicted magnetic field noise of 0.29 fT Hz$^{-1/2}$. If one continued along this path and replaced the gradiometer with a two-turn*, 0.78-μH magnetometer coupled to a 400 pH SQUID with a 49-turn input coil, the effective area would increase to 68 mm^2, corresponding to a field noise of 0.20 fT Hz$^{-1/2}$ if the SQUID had the estimated 6.7 $\mu\Phi_0$ Hz$^{-1/2}$ flux noise of Mück #1. However, I doubt that the second-generation aluminum shield attenuates external noise sufficiently to allow the use of a magnetometer. Furthermore, even if we could employ a first-order gradiometer or magnetometer in the second-generation shield, our ultimate aim is to reduce the shielding requirements of the system to allow for easy installation in a hospital environment.

Dantsker *et al.* [1] showed that one could add an asymmetric superconducting flux transformer to a planar high transition-temperature magnetometer to produce a first-order gradiometer with only a 5% reduction in its effective area. Figure 7.1 shows a schematic of an asymmetric flux transformer that converts a superconducting wire-wound magnetometer to a first-order axial gradiometer based on the work of Dantsker *et al.* The distance g between the bottom loop of the flux transformer and the pickup coil is adjusted so that their mutual inductance is such that no current flows in the pickup loop in the presence of a uniform magnetic field. Kittel *et al.* [2] fabricated a second-order gradiometer with 47% of the effective area of a magnetometer using the same principles. I leave it to future graduate students to determine whether the lower magnetic field noise that might be achieved with such devices is worth adding a mechanical feedthrough to the SQUID probe to adjust the distance g.

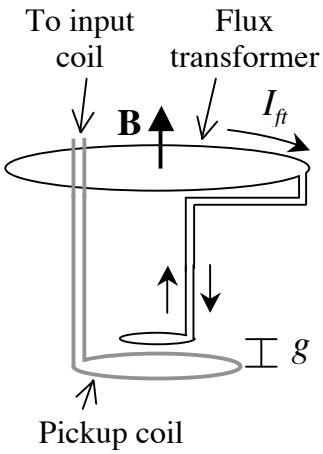

Figure 7.1: Wire-wound magnetometer and asymmetric flux transformer configured to produce a first-order gradiometer. The arrows show the direction of the current I_{ft} that flows in the flux transformer in response to an applied field **B**.

* This inductance assumes a 2.5-mm gap between the magnetometer turns. A single-turn magnetometer has A_{eff} = 56 mm^2. An N_p-turn magnetometer has the same effective area as a single-turn magnetometer if one assumes that the pickup coil inductance scales as N_p^2. Since this assumption overestimates L_p, a two-turn magnetometer achieves somewhat higher effective area than a single-turn magnetometer.

The polarizing coil must also be upgraded to realize the single-sided MRI system described in Sec. 6.2. The polarizing fields given in Table 6.5 assume a current density of 5.2 A/mm^2, which I estimate from tests conducted with the water-cooled test coil. The volume of the polarizing coils in Table 6.5 ranges from 2.5 to 10 times the volume of the water-cooled test coil, so it is possible that additional challenges will arise when attempting to scale up the water-cooling scheme described in Sec. 5.1.4.4. The operating power of these polarizing coils ranges from 1.7 to 7 times higher than the power we presently supply to the liquid-nitrogen cooled flat coil. While we might be able to produce somewhat higher power by adding additional 4 kW bipolar power supplies in parallel with our existing power supply, higher power demands will require the use of less expensive, more efficient switching power supplies. Because such power supplies cannot absorb the energy stored in the polarizing coil inductance, we would need to employ switching circuitry like that of Matter *et al*. [3], which transfers the inductive energy of the polarizing coil to a capacitor bank. Such custom switching circuitry would also be required to reduce the polarizing coil switching times to those assumed in the design of the prostate imaging sequence.

The final challenge concerning the polarizing coil is how to prevent it from disrupting the gradiometer balance and thereby increasing the contribution of external magnetic field noise. This effect occurs because oscillating uniform magnetic fields induce eddy currents in the copper windings of the polarizing coil, which in turn produce non-uniform magnetic fields that are detected by the gradiometer. While the second-generation aluminum shield reduces external noise to the point that these effects can be neglected, they could potentially dominate the magnetic field noise of an unshielded, high-balance gradiometer. The first step towards understanding and eliminating this source of noise is to measure the effect of the polarizing coil on the balance of the gradiometer. Because the gradiometer balance can not be measured accurately in the non-uniform fields generated by the square cancellation coils, vertical Helmholtz or four-coil biplanar coils should be constructed in order to make these measurements.

7.2. Progress towards applications of microtesla MRI

The *in vitro* NMR measurements of prostate tissue and designs for a prostate imaging system described in Sec. 6.3.2 represent the first steps towards microtesla MRI

of the prostate. The calculations of SNR and CNR in Sec. 6.3.4 use values of prostate tissue T_2 obtained from a preliminary measurement. We plan to measure additional samples of prostate tissue in the near future to reduce the uncertainty in T_2 and improve our estimate of the performance of a microtesla prostate imaging system. Once we have established the values of T_1 and T_2 of *in vitro* prostate tissue in our system with another half-dozen measurements, further *in vitro* measurements will yield decreasing returns. Because we are not equipped to make *in vivo* measurements of prostate tissue in our laboratory, further progress would require working with our collaborators to construct an *in vivo* microtesla MRI system at UCSF. Such an undertaking requires substantial funding, which is by no means guaranteed.

We are also investigating microtesla MRI as a potential tool to detect breast cancer. High-field MRI using an injected gadolinium contrast agent can detect malignant breast tumors with high sensitivity, but has difficulty distinguishing them from benign tumors [4]. Koenig and Brown [5] present a curve of T_1 versus magnetic field that indicates substantial low-field T_1 contrast between a specimen of normal breast tissue and a specimen of breast tumor. However, their specimen of normal tissue may represent fatty breast tissue, which should be easily distinguishable from both normal glandular breast tissue and breast tumors. Therefore, the first step towards demonstrating the feasibility of microtesla breast MRI is to measure the relaxation properties of *in vitro* breast tissue using the same procedure we have implemented for prostate tissue.

Finally, although combined MEG/MRI appears promising, developing this technology requires owning a MEG system, which would require very substantial funding. Such work would probably require collaborating with a medical devices company, preferably one of the MEG system manufacturers. In the absence of such collaboration, we could further investigate the feasibility of combined MEG/MRI by simulating the acquisition of MR images with an MEG sensor array using high-field MR images of the brain as input data. Asking clinicians who process MEG data to assess the quality of the resulting images could yield an estimate of the demand for a combined MEG/MRI system were such a device to be marketed.

[1] E. Dantsker, O. M. Froehlich, S. Tanaka, K. Kouznetsov, John Clarke, Z. Lu, V. Matijasevic, and K. Char, High-T_c superconducting gradiometer with a long baseline asymmetric flux transformer, *Appl. Phys. Lett.* **71** (1997) 1712.
[2] A. Kittel, K. A. Kouznetsov, R. McDermott, B. Oh, and John Clarke, High T_c superconducting second-order gradiometer, *Appl. Phys. Lett.* **73** (1998) 2197.
[3] N. I. Matter, G. C. Scott, T. Grafendorfer, A. Macovski, and S. Conolly, Rapid polarizing field cycling in magnetic resonance imaging, *IEEE Trans. Med. Imaging* **25** (2006) 84.
[4] P. C. Stomper, S. Herman, D. L. Klippenstein, J. S. Winston, S. B. Edge, M. A. Arredondo, R. V. Mazurchuk, L. E. Blumenson, Suspect breast lesions: Findings at dynamic gadolinium-enhanced MR imaging correlated with mammographic and pathologic features, *Radiology* **197** (1995) 387.
[5] S. H. Koenig and R. D. Brown II, Relaxation of tissue in *NMR Spectroscopy of Cells and Organisms, Vol. II*, ed. R. Gupta (Boca Raton, Florida: CRC Press, 1987) p. 95.